Bioorthogonal tools to study fatty acid uptake in immune cells

Bertheussen, K.

Citation

Bertheussen, K. (2026, January 13). *Bioorthogonal tools to study fatty acid uptake in immune cells*. Retrieved from https://hdl.handle.net/1887/4286403

Bioorthogonal Tools to Study Fatty Acid Uptake in Immune Cells

Proefschrift

ter verkrijging van
de graad van doctor aan de Universiteit Leiden,
op gezag van rector magnificus prof.dr.ir. H. Bijl,
volgens besluit van het college voor promoties
te verdedigen op dinsdag 13 januari 2026
klokke 11:30 uur

door

Kristine Bertheussen
geboren te Bergen, Noorwegen
in 1994

Promotores: Prof.dr. S.I. van Kasteren

Prof.dr. K.M. Bonger

Promotiecommissie: Prof.dr. M. Ubbink

Prof.dr. M. van der Stelt

Prof.dr. N.I. Martin

Dr. S. Kloet (Leids Universitair Medisch Centrum)

Dr. A. Schurich (King's College London)

Table of Contents

1

General Introduction

Introduction

All living cells have an inherent need for exogenous metabolites to cover their energetic needs, and to provide building block for biosynthesis.[1] The same is true for immune cells. What has been largely underappreciated over the last decades, is how the availability of metabolites to immune cells can directly impact their immunological function, activation, and differentiation.[1] This growing field, called immunometabolism, has been gaining popularity in recent years.[2,3]

This thesis focuses on the study of the metabolic requirements of T cells during their activation. T cell activation is part of the *adaptive immune response*, which is mounted by antigens presented on the surface of antigen-presenting cells (APCs) that in turn are recognised by specific T cell receptors (TCRs) on the surface of T cells. The binding of the TCR to the presented antigens, in combination with relevant costimulatory signals, forms the basis of the activation and differentiation of T cells, from quiescent cells to highly specialised effectors/orchestrators of the anti-pathogen immune response.[4]

In response to the TCR binding, a plethora of signalling cascades inside the T cells are stimulated to mount the appropriate immune response.[5,6] This includes a substantial metabolic reprogramming to, amongst others, support their increased growth and proliferation during the clonal expansion phase, and their conversion from small featureless cells to large effector cells.[7,8] Quiescent, naïve T cells maintain low biosynthetic levels and their cellular energy demands are mostly maintained by the tricarboxylic acid (TCA) cycle and oxidative phosphorylation (OXPHOS, Figure 1A).[9] Conversely, effector T cells have a large biosynthetic burden where the synthesis of nucleotides, amino acids, and fatty acids for DNA, proteins, and lipids, respectively, are needed.[10] Therefore, these T cells will upregulate their aerobic glycolysis, which will dwarf the contribution of OXPHOS to their metabolism (Figure 1B). Aerobic glycolysis generates energy faster, albeit less efficient, than OXPHOS, and is an important source for essential biosynthetic building blocks.[1]

The metabolic reprogramming of T cells is further supported by an increased uptake of exogenous nutrients such as glucose, amino acids, and fatty acids (FAs, Figure 1B). The local concentration of these nutrients in the cell's direct microenvironment is therefore a key factor in the activation of T cells. Low or high availability of these nutrients can directly modulate T cell activation and thus the immune response.[11–15] The cellular uptake of exogenous glucose and amino acids in T cells is defined by well-known, distinct membrane transporters, such as GLUT1 for glucose, and the LAT-family of solute carriers for the amino acids.[16–18] The expression of these transporters is therefore closely linked to the uptake of the nutrients, and thereby also to T cell activation.[13,19] It has been demonstrated that the knockout of these nutrient transporters impairs T cell survival and effector differentiation, highlighting their importance for proper T cell function.[13,19] However, transporter levels are not the only determining factor in how much nutrient a cell takes up. The competing transporter activity of its surrounding cells and other factors affecting local nutrient concentrations also determine the uptake (and hence activation) of T cells.[20]
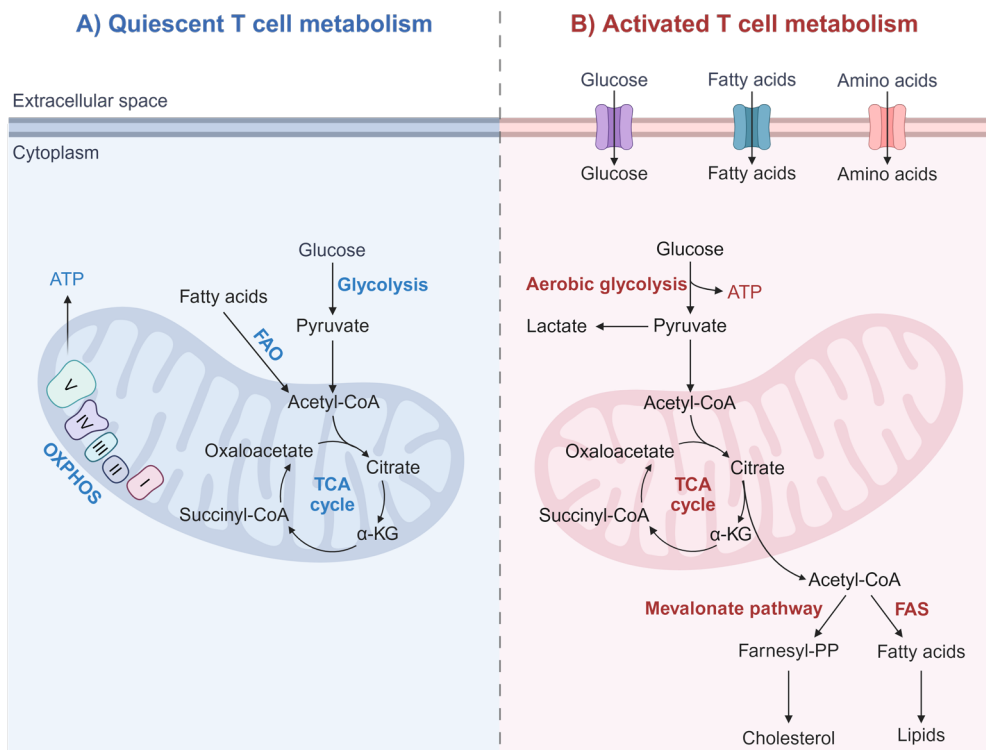
Figure 1: *Metabolic pathways that support T cells.* ***A)*** *Quiescent T cells break down glucose, via glycolysis, or fatty acids, via fatty acid β-oxidation (FAO), to acetyl coenzyme A (CoA). Acetyl-CoA enters the tricarboxylic acid (TCA) cycle in the mitochondria, which generates reducing equivalents for oxidative phosphorylation (OXPHOS) through several enzymatic reactions. Complex V in the electron transport chain generates ATP, the molecular currency of energy in the cell, from OXPHOS.* ***B)*** *Activated T cells undergo metabolic reprogramming, where aerobic glycolysis becomes increasingly important for ATP production. The uptake of extracellular nutrients such as glucose, fatty acids, and amino acids are also increased. Additionally, products of the TCA cycle form important precursors for the synthesis of several complex biomolecules which are needed for activation and proliferation. For example, citrate is transported from the mitochondria to the cytoplasm where it is converted to acetyl-CoA. Acetyl-CoA is the basis of fatty acid synthesis (FAS), leading to the biosynthesis of cellular lipids. Simultaneously, acetyl-CoA supports the production of farnesyl pyrophosphate (farnesyl-PP) via the mevalonate pathway, a precursor for cholesterol biosynthesis. The figure is made with BioRender.*

T cells also require FAs during their activation.[15] However, the uptake, intracellular transport, and function of this class of nutrients is much less defined. While there have been indications that FAs can enter T cells via passive diffusion[21], the contribution of transporters such as CD36, fatty-acid binding proteins (FABPs), or fatty acid transport proteins (FATPs) appears to be significant to control cellular FA uptake.[22] In addition to FA uptake, T cells also cover their FA need by *de novo* fatty acid synthesis (FAS), complicating the matter further.[23]

FAs are important for a number of physiological pathways in cells. They can be used as energy storage, as energy substrates that are degraded via lipolysis and fatty acid β-oxidation (FAO), or as structural membrane components in the form of phospholipids and cholesterol.[24] Additionally, they can play important roles in intracellular signal transduction[25], as messengers between cells[26], or as modulators of gene transcription.[27] However, changes in FA homeostasis and lipid storage can also lead to the accumulation of free FAs (FFAs) in cells, causing lipotoxicity.[28] The complexity and diversity of FA biology, as well as its importance for T cell function and activation, highlights the relevance of studying this class of biomolecules.

This Chapter will further focus on current knowledge of FA uptake and metabolism in different T cell subsets, emphasising the importance of the correct function and regulation of FA-related metabolic pathways for these essential immune cells. Extra attention will be given to the immunomodulatory FA oleic acid (OA), as this is one of the better-studied examples of a FA that is key during T cell activation. Lastly, the molecular tools to study exogenous FA uptake will be discussed.

Fatty acid and lipid metabolism in different T cell subsets

During metabolic reprogramming upon activation, effector T cells upregulate their FA-related anabolic pathways, including *de novo* FAS, accompanied by the aforementioned switch to aerobic glycolysis (Figure 1B). The increase in FAS supports the production of cellular lipids, such as ceramides and phospholipids, to sustain increased proliferation and growth.[29] The biosynthesis of other cellular lipids such as isoprenoids, cholesterol, and cholesterol derivatives is also upregulated in effector T cells.[29] The biosynthetic precursors of these lipids are products of the mevalonate pathway. It is therefore unsurprising that the knockout of the key enzyme 3-hydroxy-3-methylglutaryl coenzyme A (HMG-CoA) reductase (HMGCR) from this pathway ablates proper effector T cell functions.[30] At the same time, T cells take up exogenous lipids and cholesterol, either as FFAs[15], or from low-density lipoprotein (LDL) particles via the LDL receptor (LDLR), which is upregulated in early activating T cells.[31] The expression of LDLR is essential for the early activation of effector T cells, highlighting that the endogenous lipid and cholesterol biosynthesis is insufficient to cover the cell's metabolic needs during differentiation.[31]

During the early activation of CD4+ effector T cells, FA metabolism is governed by two distinct signalling pathways[15] resulting from the activation of mammalian target of rapamycin complex 1 (mTORC1). This leads to the activation of the transcription factors peroxisome proliferator-activated receptor gamma (PPARγ) and that of sterol regulatory element-binding protein 1 (SREBP1), which upregulate the expression of genes related to FA uptake and *de novo* FAS, respectively.[15] If either of these two signalling pathways are inhibited, the T cells suffer from reduced activation and proliferation, indicating that both FA uptake and FAS are essential for proper activation of effector T cells.[15] SREBPs have also been implicated as essential for the metabolic reprogramming and activation of CD8+ T cells, by regulating the lipid biosynthesis program, further supporting the essential role of these metabolic pathways for effector T cell differentiation.[32]

The picture is further complicated by the differential reliance on FA uptake and FAS

by the different T cell subsets. After activation, CD4+ effector T cells can turn into different sub-types, each with their own function in the immune system.[33] To support their immunological functions, T helper 1 (Th1), Th2, and Th17 cells show unique changes in FA metabolism. Th17 cells are heavily dependent on *de novo* FAS, and inhibition of the rate-limiting enzyme, acetyl-coenzyme A carboxylase 1 (ACC1) leads to a decline in the differentiation of this T cell subset.[34–36] *De novo* FAS is also important for Th1 and Th2 differentiation, but to a lesser extent than for Th17 cells.[35,37] Interestingly, the expression of PPARγ has been shown to be important for the function and proliferation of Th2 cells.[37,38] This could indicate that the uptake of exogenous FAs plays a more important role for Th2 cells, contrary to Th17 cells where *de novo* FAS plays a bigger role. However, the precise roles of FA uptake and FAS to the biology of T cell subsets remains to be fully elucidated. Regulatory T cells (Tregs), which can suppress immune responses in an antigen-specific manner[39], show a particularly intriguing lipid uptake and FAS phenotype.[29] Tregs show low levels of glycolysis.[40,41] Yet, they are not metabolically quiescent.[8,9] They show an increased FA uptake, and use FAO to support their immunosuppressive functions (Figure 1), distinguishing them other T cell subsets.[8,9,42] The role of this difference compared to effector T cells is, as of yet, unknown, nor is it known whether this could be exploited therapeutically, for example in treatments aimed to reactivate the immune system to fight cancer.[43,44]

After the end of the effector phase, T cells can form long-lasting memory cells that can reactivate quickly in response to encounters with the same antigen.[45] These memory T cells (both central and peripheral) are different again in their metabolic behaviour. They are metabolically quiescent, but instead of breaking down glucose to fuel OXPHOS, memory T cells rely heavily on catabolic FAO (Figure 1A).[1,7,9,46] This utilisation of FAO is believed to support memory T cell persistence and longevity by providing a stable ATP source[9], and increasing mitochondrial spare respiratory capacity.[47] Additionally, it is believed that FAO yields less oxidative damage to the cells, minimising the damage the cells accumulate over their (long) lifetimes.[48]

An example – the myriad of roles of oleic acid in T cell function

Oleic acid (OA) is a monounsaturated non-essential FA (C18:1, ω-9, Figure 2).[49] It comprises 13% of the circulating FFAs in the blood stream[50], with its serum concentration being between 30 µM and 3.2 mM in healthy adults.[51] Its main dietary source is olive oil (of which OA constitutes ~70%)[52], and like most other dietary FAs, OA can be stored in lipid droplets, metabolised by FAO, or used in the biosynthesis of other lipids.[53]
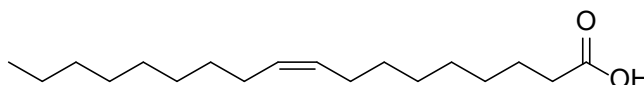

Figure 2: *Structure of the monounsaturated fatty acid oleic acid (C18:1, ω-9).*

In addition to the purely metabolic properties, OA has been described to have direct immunomodulatory properties, and it is often described as anti-inflammatory.[54–56] OA treatment has been shown to influence immunological functions in diseases like

asthma[57], sepsis[58], and cancer.[59–64]

In an ovalbumin-induced BALB/c asthma mouse model, for example, daily oral administration of 250 mg/kg OA has been shown to reduce symptoms *in vivo* by reducing cytokine secretion, reducing the amount of inflammatory cells present in the lung, and alleviating the overall pathological changes in the lung (such as epithelial cell proliferation, inflammatory cell infiltration, and mucus hypersecretion).[57]

In an experimental sepsis mouse model, the daily oral administration of 0.28 mg OA was also shown to mitigate inflammation by increasing production of the anti-inflammatory cytokine IL-10, as well as decreasing production of the pro-inflammatory cytokines IL-1β and TNFα.[58] OA also decreased systemic corticosterone levels, as well as decreasing neutrophil migration and accumulation at the site of infection. These factors were likely contributing to the increased bacterial clearance observed upon treatment with OA, and could indicate a beneficial effect of OA on sepsis outcome.[58]

Rather surprisingly, OA has also been implicated in a beneficial reduction in cancer progression and growth in cancer types such as pancreatic cancer[59], esophageal cancer[60], lung carcinomas[61,62], tongue squamous cell carcinomas[63], and human hepatocellular carcinoma cells[64]. The molecular mechanism is not known, but changes in autophagy and apoptosis have been suggested as possible mechanisms for the anti-tumour effect of OA.[62–64]

Since OA appears to impact the immune system in a wide variety of ways, and shows beneficial effects in its combat of multiple diseases, a more in-depth understanding of the cellular and molecular basis of these immunomodulatory effects are needed. Since T cells are important contributors of the immune system, and represent cells of the adaptive immune system, the uptake and use of OA by T cells is described below.

Oleic acid affects T cell proliferation, metabolism, and differentiation

OA has been shown to increase the rate of T cell proliferation both *in vitro* and *in vivo*.[65–69] However, at high concentrations, OA decreased both T cell proliferation and viability via apoptosis[65,70], indicating a dose-dependent effect of the FA. A proposed mechanism for the increased proliferation of OA-treated T cells is the incorporation of OA into membrane lipids, such as phosphatidylcholine, which appears to facilitate an increased calcium flux through the membrane.[67] There were no indications of exogenous OA altering metabolic pathways such as glycolysis and OXPHOS, suggesting OA is not used as a catabolic energy source. No changes in T cell receptor (TCR) signalling were detected either.[67] However, the exposure of T cells to OA did significantly increase the expression of several genes related to FAO, as well as genes related to cholesterol biosynthesis and *de novo* FAS.[71] This could indicate that OA serves as a substrate to generate acetyl-CoA, which can in turn be fed into biosynthetic pathways generating cholesterol, and long-chain FAs.[71]

There is further evidence that the metabolic reprogramming of OA-treated T cells appear to be the driving force of the differentiation into specific T cell subsets after exposure to OA.[71] This is supported by the upregulated production of several key

cytokines upon treatment of cells with OA. IL-9, the signature cytokine of a Th9 subset, was upregulated in T cells upon treatment with 30 µg/mL of OA *in vitro*, as was IL-17A, the cytokine produced by Th17 cells. Treatment of cells *in vitro* with exogenous OA also increased production of IL-5, IL-13, and the transcription factor GATA3, which are all associated with the Th2 subset.[71] OA-treated T cells were also shown to significantly increase their production of IL-2, IFN-γ, and TNF-α, as well as IL-4 and IL-10.[66,67] This could indicate an enrichment of the Th1 and Th2 subsets.[72] These results highlight a connection between OA uptake, cellular metabolism, and the differentiation of T cells into pro-inflammatory subsets. However, the broad subset of Th-types observed to be upregulated upon OA treatment suggest that it is a general factor in differentiation.

Regarding the immunosuppressive Treg subset, there is conflicting evidence for the role of OA in their activation. Both the decrease in Treg population upon OA-treatment[66,71], and an increase in Treg differentiation[73], have been reported. It was also shown that OA-treatment resulted in the enhanced suppressive function of Tregs.[74] Since Tregs generally rely on FAO-driven OXPHOS to generate energy for their suppressive functions[8,40,75], it could be the case that OA uptake amplified these metabolic pathways, which in turn increased FOXP3 expression and phosphorylation of STAT5.[74] This in turn enhanced the suppressive function of the OA-treated Tregs.

Although different papers describe different specific outcomes of the differentiation of T cells exposed to OA, it is clear that this FA has the potential of modulating T cell differentiation in either a pro- or anti-inflammatory manner. However, determining the exact outcome is influenced by the experimental setup, and still requires further research.

Molecular tools to study the uptake of exogenous fatty acids

Although there are substantial indications that OA, and other FAs, have strong immunomodulatory effects, it is still difficult to study the effect of FA uptake on cellular phenotype at a single-cell level.

To measure FA uptake, a FA molecule needs to be modified in a way that allows its detection and quantification. The most traditional way to achieve this would be to use ^{14}C or ^{3}H radioactively labelled FAs (Figure 3).[76–79] The major advantage of this method is that the chemical modification of the FA is negligible, as the atomic composition of the isotope-labelled lipid is identical to that of the unlabelled lipid.[79] However, this method not only requires specialised laboratory setups, personnel training, and protective equipment, there are also no methods by which the uptake data from these experiments can be correlated to the biology of a single cell.[79]

In order to obtain single cell data on FA uptake, several fluorescently labelled FAs were developed, where the FAs were covalently modified with a fluorophore such as BODIPY prior to FA uptake (Figure 3).[80–85] This allowed for the major breakthrough of single cell FA studies, as it allowed the study of FA uptake by fluorescent microscopy[80–84] and flow cytometry.[81,82,84] Unfortunately, the modifications used in these experiments significantly alter FA structure (Figure 3), which in turn impacts their biochemical properties, uptake, and cellular distribution patterns.[86] There have

e.g. been observations of fluorescently labelled universal FA probes accumulating in specific organelles or cellular compartments.[87,88]

Several other methods have been developed for measuring the uptake of FAs *in vivo* and *in vitro*. A bioluminescent FA probe was developed, where a long-chain FA was bound to luciferin via a cleavable linker.[89] Upon cellular uptake, the cleavable linker could be hydrolysed by intracellular glutathione which in turn released luciferin. By addition of the enzyme luciferase, luciferin emitted detectable light that was proportional to the FA uptake.[89] Another FA probe has been developed were FA uptake in T cells can be quantified using a FA-quantum dot conjugate (FA-Qdot).[90] Although both these FA probes have been demonstrated to be applicable *in vivo*, their large sizes could still lead to mismatched uptake and distribution patterns compared to the native FA molecules.[86]
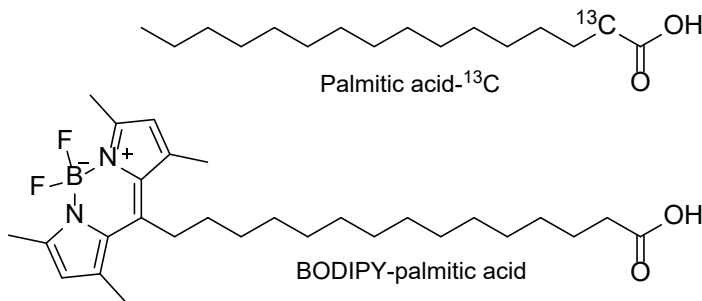

Figure 3: Structures of radioactively (palmitic acid-^{13}C) and fluorescently (BODIPY-palmitic acid) labelled fatty acid analogues, using palmitic acid (C16:0) as an example.

Applying bioorthogonal (click) chemistry to explore fatty acid uptake

The aim of this thesis is to combine the favourable properties of radiolabelling (small labels) with the single-cell compatibility of fluorophore-labelled FAs using bioorthogonal chemistry. The term bioorthogonal chemistry, sometimes also referred to as click chemistry, was initially coined for the work started by Bertozzi in 2000 for labelling of cell surface glycans.[91] The approach consists of the introduction of a small, biologically inert group into a biomolecule of interest. Then, after any biological phenomenon under investigation is complete, this group is reacted using chemistry that is selective for the introduced group and unreactive with all other chemistry found in the biological system.[92–94] The biomolecule of interest can thereby be covalently labelled with a reporter molecule (e.g. a fluorophore, Figure 4). This approach has been highly successful for studying a wide variety of biomolecules (such as proteins, DNA, RNA, carbohydrates, and lipids).[93] Many excellent review articles have been published describing different bioorthogonal click reactions and their biological applications.[92–98] The approach has also been extensively extended to the study of FA biology.[86,87,99–101] In the remainder of this Chapter, the bioorthogonal investigations of FA biology, which are relevant for this thesis, will be discussed.

Figure 4: *The principles of bioorthogonal (click) chemistry. A small chemical modification is introduced into the biomolecule of interest (diamond shape), allowing for a selective click reaction with a reporter molecule (e.g. a fluorophore, F). The figure is made with BioRender.*

Bioorthogonal FA probes can be fitted with a bioorthogonal group, either through labelling of the fatty acid head group, or of the acyl tail. However, the former approach[102], will remove the key acid moiety that lends the molecules their name. Here the focus will therefore lie on those approaches that label the FA acyl tail. Two bioorthogonal groups have been mainly used for tail-labelling: azides[103–108], and alkynes[99,101,109–111] at the ω-position (Figure 5A). Since this renders the carboxylic acid moiety in its native state, these bioorthogonal FAs can be incorporated into endogenous biological processes such as phospholipid biosynthesis and protein lipidation, and the click reaction can be used to detect or visualise them.[86,100,112]

The azide and alkyne modifications allow for detection via the copper(I)-catalysed alkyne-azide cycloaddition (CuAAC), where the reporter molecule contains the opposite modification, e.g. FA alkyne modification with an azide reporter molecule, or vice versa (Figure 5B).[100] CuAAC is widely used due to its relatively fast reaction kinetics, low unspecific reactivity, and the synthetic availability of alkyne and azide modifications to be incorporated into biomolecules.[93–95] However, the major disadvantage of this reaction is the employment of cytotoxic copper(I) ions, which means CuAAC is not live cell nor *in vivo* compatible.[93–95] Of the two groups, the alkyne is the better bioorthogonal label in FAs, as its lipophilicity is similar to that of the native, terminal ethyl group. The azide is more polar, thereby reducing the amphiphilic nature of the bioorthogonal FA analogue compared to the parent molecule. Interestingly, the alkyne/azide FAs have not yet been used to study FA uptake by activating immune cells.
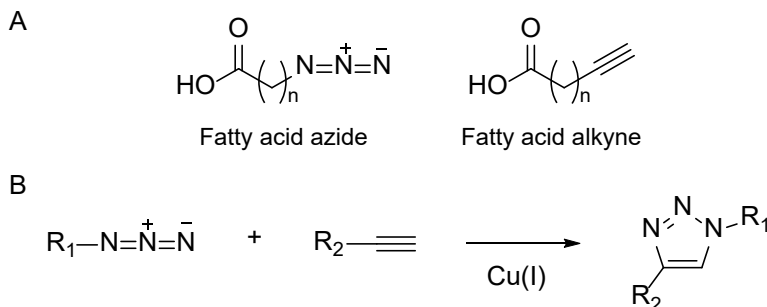

Figure 5: *Structures of **A)** general bioorthogonal fatty acid analogues with terminal azide or alkyne modifications, and **B)** the copper(I)-catalysed azide-alkyne cycloaddition (CuAAC) reaction.*

One downside of the CuAAC is that the copper catalyst used is toxic to cells, requiring the fixation of the cells prior to the click reaction.[113] The copper catalyst is also incompatible with many fluorophores used in routine flow cytometry panels.[114] These problems were negated by the development of the inverse electron-demand Diels-Alder (IEDDA) reaction – the reaction between an electron-poor diene, such as a tetrazine, and a strained or electron-rich dienophile – as a novel click reaction (Figure 6).[115,116] This reaction has opened up a world of live-cell compatible chemistry with exceptionally fast reaction kinetics.[96] Since tetrazines absorb light at 500-530 nm, they have an added benefit of quenching fluorophores with absorbance wavelengths in a similar range.[117] This presents an advantage for live-cell applications, where the resulting tetrazine-conjugated fluorophores only become fluorescent upon successful IEDDA ligation (Figure 6). This turn-on effect reduces background fluorescence and protects live cells from being destroyed by several washing steps.[96]
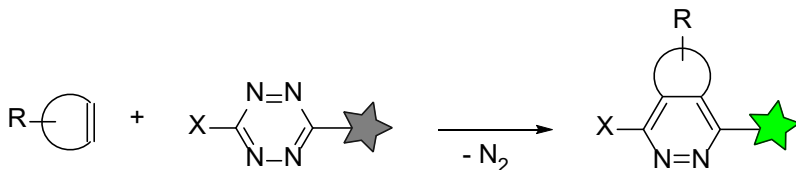

Figure 6: The inverse electron-demand Diels-Alder (IEDDA) reaction between an electron-rich dienophile and an electron-poor diene (here represented by a tetrazine-conjugated fluorophore).

While the IEDDA reaction has been used to study lipid biology before[118,119], its application to FA uptake has not been previously explored. This thesis describes the development of sterculic acid (StA) (Figure 7A) as a bioorthogonal FA analogue of OA. Contrary to the already established bioorthogonal OA analogues oleic acid alkyne (OAalk, Figure 7B) and oleic acid azide (OAaz, Figure 7C), StA was shown to react with tetrazines via an IEDDA reaction, therefore highlighting it as a live-cell compatible alternative to the azide- and alkyne-modified OA analogues (Chapter 2).
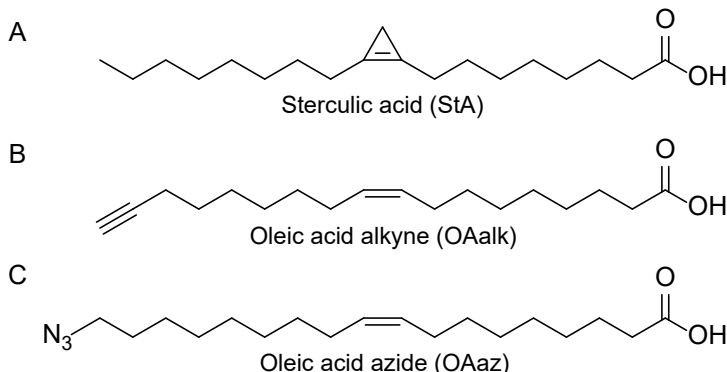
*Figure 7: Structures of bioorthogonal oleic acid analogues **A)** sterculic acid (StA), **B)** oleic acid alkyne (OAalk), and **C)** oleic acid azide (OAaz).*

Furthermore, StA was demonstrated as a versatile bioorthogonal OA analogue which could be incorporated into a plethora of methods to detect *in vitro* uptake and metabolism of OA in dendritic and T cells. This includes methods such as live-cell confocal imaging (Chapter 2), identification of post-translationally oleoylated proteins by mass spectrometry (Chapter 3), as well as the connection between phenotypic, transcriptomic, and proteomic differences, and a differential OA uptake at a single-cell level (Chapter 4).

References

1. O'Neill, L. A. J., Kishton, R. J. & Rathmell, J. A guide to immunometabolism for immunologists. *Nat Rev Immunol* **16**, 553–565 (2016).

2. Mathis, D. & Shoelson, S. E. Immunometabolism: an emerging frontier. *Nat Rev Immunol* **11**, 81–83 (2011).

3. Murray, P. J., Rathmell, J. & Pearce, E. SnapShot: Immunometabolism. *Cell Metab* **22**, 190 (2015).

4. Hwang, J.-R., Byeon, Y., Kim, D. & Park, S.-G. Recent insights of T cell receptor-mediated signaling pathways for T cell activation and development. *Exp Mol Med* **52**, 750–761 (2020).

5. Courtney, A. H., Lo, W.-L. & Weiss, A. TCR Signaling: Mechanisms of Initiation and Propagation. *Trends Biochem Sci* **43**, 108–123 (2018).

6. Shah, K., Al-Haidari, A., Sun, J. & Kazi, J. U. T cell receptor (TCR) signaling in health and disease. *Signal Transduct Target Ther* **6**, 412 (2021).

7. Chapman, N. M., Boothby, M. R. & Chi, H. Metabolic coordination of T cell quiescence and activation. *Nat Rev Immunol* **20**, 55–70 (2020).

8. MacIver, N. J., Michalek, R. D. & Rathmell, J. C. Metabolic Regulation of T Lymphocytes. *Annu Rev Immunol* **31**, 259–293 (2013).

9. Loftus, R. M. & Finlay, D. K. Immunometabolism: Cellular Metabolism Turns Immune Regulator. *Journal of Biological Chemistry* **291**, 1–10 (2016).

10. Donnelly, R. P. & Finlay, D. K. Glucose, glycolysis and lymphocyte responses. *Mol Immunol* **68**, 513–519 (2015).

11. Jacobs, S. R. *et al.* Glucose Uptake Is Limiting in T Cell Activation and Requires CD28-Mediated Akt-Dependent and Independent Pathways. *The Journal of Immunology* **180**, 4476–4486 (2008).

12. Geiger, R. *et al.* L-Arginine Modulates T Cell Metabolism and Enhances Survival and Anti-Tumor Activity. *Cell* **167**, 829–842 (2016).

13. Sinclair, L. V *et al.* Control of amino-acid transport by antigen receptors coordinates the metabolic reprogramming essential for T cell differentiation. *Nat Immunol* **14**, 500–508 (2013).

14. Carr, E. L. *et al.* Glutamine Uptake and Metabolism Are Coordinately Regulated by ERK/MAPK during T Lymphocyte Activation. *The Journal of Immunology* **185**, 1037–1044 (2010).

15. Angela, M. *et al.* Fatty acid metabolic reprogramming via mTOR-mediated inductions of PPARγ directs early activation of T cells. *Nat Commun* **7**, (2016).

16. Palmer, C. S., Ostrowski, M., Balderson, B., Christian, N. & Crowe, S. M. Glucose Metabolism Regulates T Cell Activation, Differentiation, and Functions. *Front Immunol* **6**, (2015).

17. Ren, W. *et al.* Amino-acid transporters in T-cell activation and differentiation. *Cell Death Dis* **8**, (2017).

18. Wang, W. & Zou, W. Amino Acids and Their Transporters in T Cell Immunity and Cancer Therapy. *Mol Cell* **80**, 384–395 (2020).

19. Macintyre, A. N. *et al.* The Glucose Transporter Glut1 Is Selectively Essential for CD4 T Cell Activation and Effector Function. *Cell Metab* **20**, 61–72 (2014).

20. Kedia-Mehta, N. & Finlay, D. K. Competition for nutrients and its role in controlling immune responses. *Nat Commun* **10**, 2123 (2019).

21.   Howie, D., Ten Bokum, A., Necula, A. S., Cobbold, S. P. & Waldmann, H. The Role of Lipid Metabolism in T Lymphocyte Differentiation and Survival. *Front Immunol* **8**, (2018).

22.   Schwenk, R. W., Holloway, G. P., Luiken, J. J. F. P., Bonen, A. & Glatz, J. F. C. Fatty acid transport across the cell membrane: Regulation by fatty acid transporters. *Prostaglandins Leukot Essent Fatty Acids* **82**, 149–154 (2010).

23.   Lochner, M., Berod, L. & Sparwasser, T. Fatty acid metabolism in the regulation of T cell function. *Trends Immunol* **36**, 81–91 (2015).

24.   De Carvalho, C. C. C. R. & Caramujo, M. J. The Various Roles of Fatty Acids. *Molecules* **23**, (2018).

25.   Kremmyda, L.-S., Tvrzicka, E., Stankova, B. & Zak, A. Fatty acids as biocompounds: their role in human metabolism, health and disease - a review. Part 2: fatty acid physiological roles and applications in human health and disease. *Biomedical papers* **155**, 195–218 (2011).

26.   Brennan, E., Kantharidis, P., Cooper, M. E. & Godson, C. Pro-resolving lipid mediators: regulators of inflammation, metabolism and kidney function. *Nat Rev Nephrol* **17**, 725–739 (2021).

27.   Glatz, J. Challenges in Fatty Acid and Lipid Physiology. *Front Physiol* **2**, (2011).

28.   Lipke, K., Kubis-Kubiak, A. & Piwowar, A. Molecular Mechanism of Lipotoxicity as an Interesting Aspect in the Development of Pathological States—Current View of Knowledge. *Cells* **11**, (2022).

29.   Lim, S. A., Su, W., Chapman, N. M. & Chi, H. Lipid metabolism in T cell signaling and function. *Nat Chem Biol* **18**, 470–481 (2022).

30.   Lacher, S. M. *et al.* HMG-CoA reductase promotes protein prenylation and therefore is indispensible for T-cell survival. *Cell Death Dis* **8**, (2017).

31.   Bonacina, F. *et al.* The low-density lipoprotein receptor–mTORC1 axis coordinates CD8+ T cell activation. *Journal of Cell Biology* **221**, (2022).

32.   Kidani, Y. *et al.* Sterol regulatory element–binding proteins are essential for the metabolic programming of effector T cells and adaptive immunity. *Nat Immunol* **14**, 489–499 (2013).

33.   Kaiko, G. E., Horvat, J. C., Beagley, K. W. & Hansbro, P. M. Immunological decision-making: how does the immune system decide to mount a helper T-cell response? *Immunology* **123**, 326–338 (2008).

34.   Ma, S., Ming, Y., Wu, J. & Cui, G. Cellular metabolism regulates the differentiation and function of T-cell subsets. *Cell Mol Immunol* **21**, 419–435 (2024).

35.   Berod, L. *et al.* De novo fatty acid synthesis controls the fate between regulatory T and T helper 17 cells. *Nat Med* **20**, 1327–1333 (2014).

36.   Kanno, T., Nakajima, T., Miyako, K. & Endo, Y. Lipid metabolism in Th17 cell function. *Pharmacol Ther* **245**, (2023).

37.   Kabat, A. M., Pearce, E. L. & Pearce, E. J. Metabolism in type 2 immune responses. *Immunity* **56**, 723–741 (2023).

38.   Stark, J. M., Tibbitt, C. A. & Coquet, J. M. The Metabolic Requirements of Th2 Cell Differentiation. *Front Immunol* **Volume 10**, (2019).

39.   Dikiy, S. & Rudensky, A. Y. Principles of regulatory T cell function. *Immunity* **56**, 240–255 (2023).

40.   Michalek, R. D. *et al.* Cutting Edge: Distinct Glycolytic and Lipid Oxidative Metabolic Programs Are Essential for Effector and Regulatory CD4+ T Cell Subsets. *The Journal*

of Immunology **186**, 3299–3303 (2011).

41. Shi, L. Z. *et al.* HIF1α–dependent glycolytic pathway orchestrates a metabolic checkpoint for the differentiation of TH17 and Treg cells. *Journal of Experimental Medicine* **208**, 1367–1376 (2011).

42. Endo, Y., Kanno, T. & Nakajima, T. Fatty acid metabolism in T-cell function and differentiation. *Int Immunol* **34**, 579–587 (2022).

43. Shan, F., Somasundaram, A., Bruno, T. C., Workman, C. J. & Vignali, D. A. A. Therapeutic targeting of regulatory T cells in cancer. *Trends Cancer* **8**, 944–961 (2022).

44. Hosseinalizadeh, H. *et al.* Regulating the regulatory T cells as cell therapies in autoimmunity and cancer. *Front Med (Lausanne)* **10**, (2023).

45. Kaech, S. M., Wherry, E. J. & Ahmed, R. Effector and memory T-cell differentiation: implications for vaccine development. *Nat Rev Immunol* **2**, 251–262 (2002).

46. Buck, M. D., O'Sullivan, D. & Pearce, E. L. T cell metabolism drives immunity. *Journal of Experimental Medicine* **212**, 1345–1360 (2015).

47. van der Windt, G. J. W. *et al.* Mitochondrial Respiratory Capacity Is a Critical Regulator of CD8+ T Cell Memory Development. *Immunity* **36**, 68–78 (2012).

48. Schönfeld, P., Więckowski, M. R., Lebiedzińska, M. & Wojtczak, L. Mitochondrial fatty acid oxidation and oxidative stress: Lack of reverse electron transfer-associated production of reactive oxygen species. *Biochimica et Biophysica Acta (BBA) - Bioenergetics* **1797**, 929–938 (2010).

49. Choi, S.-G., Won, S.-R. & Rhee, H.-I. Chapter 153 - Oleic Acid and Inhibition of Glucosyltransferase. in (eds. Preedy, V. R. & Watson, R. R. B. T.-O. and O. O. in H. and D. P.) 1375–1383 (Academic Press, San Diego, 2010). doi:https://doi.org/10.1016/B978-0-12-374420-3.00153-4.

50. Bicalho, B., David, F., Rumplel, K., Kindt, E. & Sandra, P. Creating a fatty acid methyl ester database for lipid profiling in a single drop of human blood using high resolution capillary gas chromatography and mass spectrometry. *J Chromatogr A* **1211**, 120–128 (2008).

51. Abdelmagid, S. A. *et al.* Comprehensive Profiling of Plasma Fatty Acid Concentrations in Young Healthy Canadian Adults. *PLoS One* **10**, (2015).

52. Lopez, S. *et al.* Membrane composition and dynamics: A target of bioactive virgin olive oil constituents. *Biochimica et Biophysica Acta (BBA) - Biomembranes* **1838**, 1638–1656 (2014).

53. Suburu, J. *et al.* Fatty acid metabolism: Implications for diet, genetic variation, and disease. *Food Biosci* **4**, 1–12 (2013).

54. Sales-Campos, H., Souza, P. R. de, Peghini, B. C., Silva, J. S. da & Cardoso, C. R. An Overview of the Modulatory Effects of Oleic Acid in Health and Disease. *Mini-Reviews in Medicinal Chemistry* **13**, 201–210 (2013).

55. Carrillo, C., Cavia, M. a del M. & Alonso-Torre, S. Role of oleic acid in immune system; mechanism of action; a review. *Nutr Hosp* **27**, 978–990 (2012).

56. Reilly, N. A., Lutgens, E., Kuiper, J., Heijmans, B. T. & Jukema, J. W. Effects of fatty acids on T cell function: role in atherosclerosis. *Nat Rev Cardiol* **18**, 824–837 (2021).

57. Lee, S.-Y. *et al.* Oleic acid attenuates asthma pathogenesis via Th1/Th2 immune cell modulation, TLR3/4-NF-κB-related inflammation suppression, and intrinsic apoptotic pathway induction. *Front Immunol* **15**, (2024).

58. Medeiros-de-Moraes, I. M. *et al.* Omega-9 Oleic Acid, the Main Compound of Olive

Oil, Mitigates Inflammation during Experimental Sepsis. *Oxid Med Cell Longev* **2018**, (2018).

59. Banim, P. J. R., Luben, R., Khaw, K.-T. & Hart, A. R. Dietary oleic acid is inversely associated with pancreatic cancer – Data from food diaries in a cohort study. *Pancreatology* **18**, 655–660 (2018).

60. Moon, H.-S., Batirel, S. & Mantzoros, C. S. Alpha linolenic acid and oleic acid additively down-regulate malignant potential and positively cross-regulate AMPK/S6 axis in OE19 and OE33 esophageal cancer cells. *Metabolism* **63**, 1447–1454 (2014).

61. Piegari, M., Soria, E. A., Eynard, A. R. & Valentich, M. A. Delay of Lung Adenocarcinoma (LAC-1) Development in Mice by Dietary Oleic Acid. *Nutr Cancer* **69**, 1069–1074 (2017).

62. Yamagata, K., Uzu, E., Yoshigai, Y., Kato, C. & Tagami, M. Oleic acid and oleoylethanolamide decrease interferon-γ-induced expression of PD-L1 and induce apoptosis in human lung carcinoma cells. *Eur J Pharmacol* **903**, (2021).

63. Jiang, L. *et al.* Oleic acid induces apoptosis and autophagy in the treatment of Tongue Squamous cell carcinomas. *Sci Rep* **7**, (2017).

64. Giulitti, F. *et al.* Anti-tumor Effect of Oleic Acid in Hepatocellular Carcinoma Cell Lines via Autophagy Reduction. *Front Cell Dev Biol* **9**, (2021).

65. Gorjão, R., Cury-Boaventura, M. F., de Lima, T. M. & Curi, R. Regulation of human lymphocyte proliferation by fatty acids. *Cell Biochem Funct* **25**, 305–315 (2007).

66. Passos, M. E. P. *et al.* Differential effects of palmitoleic acid on human lymphocyte proliferation and function. *Lipids Health Dis* **15**, 217 (2016).

67. von Hegedus, J. H. *et al.* Oleic acid enhances proliferation and calcium mobilization of CD3/CD28 activated CD4+ T cells through incorporation into membrane lipids. *Eur J Immunol* **54**, (2024).

68. Miura, S. *et al.* Increased proliferative response of lymphocytes from intestinal lymph during long chain fatty acid absorption. *Immunology* **78**, 142–146 (1993).

69. Ioan-Facsinay, A. *et al.* Adipocyte-derived lipids modulate CD4+ T-cell function. *Eur J Immunol* **43**, 1578–1587 (2013).

70. Zhu, Y. *et al.* Oleic acid causes apoptosis and dephosphorylates Bad. *Neurochem Int* **46**, 127–135 (2005).

71. Reilly, N. A. *et al.* Oleic acid triggers metabolic rewiring of T cells poising them for T helper 9 differentiation. *iScience* **27**, (2024).

72. Geginat, J. *et al.* Plasticity of Human CD4 T Cell Subsets. *Front Immunol* **5**, (2014).

73. Lin, L. *et al.* Oleic acid availability impacts thymocyte preprogramming and subsequent peripheral Treg cell differentiation. *Nat Immunol* **25**, 54–65 (2024).

74. Pompura, S. L. *et al.* Oleic acid restores suppressive defects in tissue-resident FOXP3 Tregs from patients with multiple sclerosis. *J Clin Invest* **131**, (2021).

75. Cluxton, D., Petrasca, A., Moran, B. & Fletcher, J. M. Differential Regulation of Human Treg and Th17 Cells by Fatty Acid Synthesis and Glycolysis. *Front Immunol* **10**, (2019).

76. Fredrickson, D. S. & Gordon, R. S. The metabolism of albumin bound C 14-labeled unesterified fatty acids in normal human subjects. *J Clin Invest* **37**, 1504–1515 (1958).

77. Sinclair, A. J. Incorporation of radioactive polyunsaturated fatty acids into liver and brain of developing rat. *Lipids* **10**, 175–184 (1975).

78. Pappas, A., Anthonavage, M. & Gordon, J. S. Metabolic Fate and Selective Utilization of Major Fatty Acids in Human Sebaceous Gland. *Journal of Investigative Dermatology*

118, 164–171 (2002).

79. Dubikovskaya, E., Chudnovskiy, R., Karateev, G., Park, H. M. & Stahl, A. Chapter Seven - Measurement of Long-Chain Fatty Acid Uptake into Adipocytes. in *Methods of Adipose Tissue Biology, Part B* (ed. MacDougald, O. A. B. T.-M. in E.) vol. 538 107–134 (Academic Press, 2014).

80. Huang, H., Starodub, O., McIntosh, A., Kier, A. B. & Schroeder, F. Liver Fatty Acid-binding Protein Targets Fatty Acids to the Nucleus: Real Time Confocal and Multiphoton Fluorescence Imaging in Living Cells. *Journal of Biological Chemistry* **277**, 29139–29151 (2002).

81. Liao, J., Sportsman, R., Harris, J. & Stahl, A. Real-time quantification of fatty acid uptake using a novel fluorescence assay. *J Lipid Res* **46**, 597–602 (2005).

82. Milger, K. *et al.* Cellular uptake of fatty acids driven by the ER-localized acyl-CoA synthetase FATP4. *J Cell Sci* **119**, 4678–4688 (2006).

83. Thumser, A. E. & Storch, J. Characterization of a BODIPY-labeled fluorescent fatty acid analogue. Binding to fatty acid-binding proteins, intracellular localization, and metabolism. *Mol Cell Biochem* **299**, 67–73 (2007).

84. Panagia, M. *et al.* A novel tracer for in vivo optical imaging of fatty acid metabolism in the heart and brown adipose tissue. *Sci Rep* **10**, 11209 (2020).

85. Kajiwara, K. *et al.* A negative-solvatochromic fluorescent probe for visualizing intracellular distributions of fatty acid metabolites. *Nat Commun* **13**, 2533 (2022).

86. Bumpus, T. W. & Baskin, J. M. Greasing the Wheels of Lipid Biology with Chemical Tools. *Trends Biochem Sci* **43**, 970–983 (2018).

87. Neef, A. B. & Schultz, C. Selective Fluorescence Labeling of Lipids in Living Cells. *Angewandte Chemie International Edition* **48**, 1498–1500 (2009).

88. Korotkova, D. *et al.* Fluorescent fatty acid conjugates for live cell imaging of peroxisomes. *Nat Commun* **15**, 4314 (2024).

89. Henkin, A. H. *et al.* Real-Time Noninvasive Imaging of Fatty Acid Uptake in Vivo. *ACS Chem Biol* **7**, 1884–1891 (2012).

90. Muroski, M. E. *et al.* Fatty Acid Uptake in T Cell Subsets Using a Quantum Dot Fatty Acid Conjugate. *Sci Rep* **7**, 5790 (2017).

91. Saxon, E. & Bertozzi, C. R. Cell Surface Engineering by a Modified Staudinger Reaction. *Science (1979)* **287**, 2007–2010 (2000).

92. Sletten, E. M. & Bertozzi, C. R. Bioorthogonal chemistry: fishing for selectivity in a sea of functionality. *Angew Chem Int Ed Engl* **48**, 6974–6998 (2009).

93. Bird, R. E., Lemmel, S. A., Yu, X. & Zhou, Q. A. Bioorthogonal Chemistry and Its Applications. *Bioconjug Chem* **32**, 2457–2479 (2021).

94. Scinto, S. L. *et al.* Bioorthogonal chemistry. *Nature Reviews Methods Primers* **1**, 30 (2021).

95. Patterson, D. M., Nazarova, L. A. & Prescher, J. A. Finding the Right (Bioorthogonal) Chemistry. *ACS Chem Biol* **9**, 592–605 (2014).

96. Oliveira, B. L., Guo, Z. & Bernardes, G. J. L. Inverse electron demand Diels–Alder reactions in chemical biology. *Chem. Soc. Rev.* **46**, 4895–4950 (2017).

97. Row, R. D. & Prescher, J. A. Constructing New Bioorthogonal Reagents and Reactions. *Acc Chem Res* **51**, 1073–1081 (2018).

98. Smeenk, M. L. W. J., Agramunt, J. & Bonger, K. M. Recent developments in bioorthogonal chemistry and the orthogonality within. *Curr Opin Chem Biol* **60**, 79–88 (2021).

99. Charron, G. *et al.* Robust Fluorescent Detection of Protein Fatty-Acylation with Chemical Reporters. *J Am Chem Soc* **131**, 4967–4975 (2009).

100. Hang, H. C., Wilson, J. P. & Charron, G. Bioorthogonal Chemical Reporters for Analyzing Protein Lipidation and Lipid Trafficking. *Acc Chem Res* **44**, 699–708 (2011).

101. Thiele, C. *et al.* Tracing Fatty Acid Metabolism by Click Chemistry. *ACS Chem Biol* **7**, 2004–2011 (2012).

102. Flores, J., White, B. M., Brea, R. J., Baskin, J. M. & Devaraj, N. K. Lipids: chemical tools for their synthesis, modification, and analysis. *Chem Soc Rev* **49**, 4602–4614 (2020).

103. Hang, H. C. *et al.* Chemical Probes for the Rapid Detection of Fatty-Acylated Proteins in Mammalian Cells. *J Am Chem Soc* **129**, 2744–2745 (2007).

104. Martin, D. D. O. *et al.* Rapid detection, discovery, and identification of post-translationally myristoylated proteins during apoptosis using a bio-orthogonal azidomyristate analog. *The FASEB Journal* **22**, 797–806 (2008).

105. Kostiuk, M. A. *et al.* Identification of palmitoylated mitochondrial proteins using a bio-orthogonal azido-palmitate analogue. *The FASEB Journal* **22**, 721–732 (2008).

106. Heal, W. P. *et al.* Site-specific N-terminal labelling of proteins in vitro and in vivo using N-myristoyl transferase and bioorthogonal ligation chemistry. *Chemical Communications* 480–482 (2008).

107. Heal, W. P., Wickramasinghe, S. R., Leatherbarrow, R. J. & Tate, E. W. N-Myristoyl transferase-mediated protein labelling in vivo. *Org Biomol Chem* **6**, 2308–2315 (2008).

108. Pérez, A. J. & Bode, H. B. ω-Azido fatty acids as probes to detect fatty acid biosynthesis, degradation, and modification. *J Lipid Res* **55**, 1897–1901 (2014).

109. Thinon, E. *et al.* Global profiling of co- and post-translationally N-myristoylated proteomes in human cells. *Nat Commun* **5**, 4919 (2014).

110. Thinon, E., Percher, A. & Hang, H. C. Bioorthogonal Chemical Reporters for Monitoring Unsaturated Fatty-Acylated Proteins. *ChemBioChem* **17**, 1800–1803 (2016).

111. Ticho, A. L. *et al.* S-acylation modulates the function of the apical sodium-dependent bile acid transporter in human cells. *Journal of Biological Chemistry* **295**, 4488–4497 (2020).

112. Gao, X. & Hannoush, R. N. A Decade of Click Chemistry in Protein Palmitoylation: Impact on Discovery and New Biology. *Cell Chem Biol* **25**, 236–246 (2018).

113. Meldal, M. & Tornøe, C. W. Cu-Catalyzed Azide−Alkyne Cycloaddition. *Chem Rev* **108**, 2952–3015 (2008).

114. Pelgrom, L. R. *et al.* QUAS-R: An SLC1A5-mediated glutamine uptake assay with single-cell resolution reveals metabolic heterogeneity with immune populations. *Cell Rep* **42**, (2023).

115. Blackman, M. L., Royzen, M. & Fox, J. M. Tetrazine ligation: fast bioconjugation based on inverse-electron-demand Diels-Alder reactivity. *J Am Chem Soc* **130**, 13518–13519 (2008).

116. Devaraj, N. K., Weissleder, R. & Hilderbrand, S. A. Tetrazine-Based Cycloadditions: Application to Pretargeted Live Cell Imaging. *Bioconjug Chem* **19**, 2297–2299 (2008).

117. Devaraj, N. K., Hilderbrand, S., Upadhyay, R., Mazitschek, R. & Weissleder, R. Bioorthogonal Turn-On Probes for Imaging Small Molecules inside Living Cells. *Angewandte Chemie International Edition* **49**, 2869–2872 (2010).

118. Erdmann, R. S. *et al.* Super-Resolution Imaging of the Golgi in Live Cells with a Bioorthogonal Ceramide Probe. *Angewandte Chemie International Edition* **53**,

10242–10246 (2014).

119.   Yang, J., Šečkutė, J., Cole, C. M. & Devaraj, N. K. Live-Cell Imaging of Cyclopropene Tags with Fluorogenic Tetrazine Cycloadditions. *Angewandte Chemie International Edition* **51**, 7476–7479 (2012).

2

Live-Cell Imaging of Sterculic Acid by Bioorthogonal Reaction with Tetrazine-Fluorophore Conjugates

Abstract

In the field of lipid research, bioorthogonal chemistry has made the study of lipid uptake and processing in living systems possible, whilst minimising artefacts on their biology resulting from pendant detectable groups. To allow the study of unsaturated free fatty acids in live cells, this Chapter reports the first use of sterculic acid, a naturally occurring 1,2-cyclopropene-containing fatty acid, as a bioorthogonal probe that can be reacted in the live-cell compatible Inverse Electron-Demand Diels-Alder Reaction (IEDDA). The fatty acid can be readily taken up by dendritic cells without toxic side-effects, and it can subsequently be visualised using a IEDDA reaction with quenched tetrazine-fluorophore conjugates. This reaction can also be integrated into a multiplexed bioorthogonal reaction workflow by combining it with two sequential copper-catalysed azide-alkyne cycloaddition reactions. This allows for the simultaneous study of uptake and incorporation of multiple biomolecules in the cell by multimodal confocal imaging.

Introduction

Lipids serve a myriad of roles in biology; as a catabolic carbon source[1], components of cellular and organellar membranes[2], post-translational protein modifications[3], and signalling molecules[4]. The study of their contributions in biology is complicated by their lack of direct genetic encoding, their inherent lipophilicity, and the fact that chemical modifications, e.g. with pendant fluorophores, can severely alter their structure and biochemical properties.[5]

As a result, major efforts have gone into applying bioorthogonal chemistry to the study of lipid biochemistry. By introducing small terminal alkynes and azides in fatty acid tails[6–11], phospholipids[12,13], sphingolipids[14], and cholesterol[15–17], it has been possible to study lipids with only minimal modifications compared to the endogenous molecules. This strategy reduces the chances of the modifications affecting the native function of the lipid and has successfully been used to study lipid localisation[10,12,13,17], metabolism[11,16], and trafficking[18–20], as well as post-translational lipidation of proteins (reviewed by Distefano and co-workers[21]). However, the downside of labelling lipids with alkynes/azides has been the lack of live-cell compatible chemistries that can be used with low background reactivity and fast reaction rates.[22,23] Another complicating factor when performing bioorthogonal ligation on lipids is imposed by the hydrophobic environment in which the probes reside. Optimising the fluorescent reaction partners, particularly for live-cell imaging, is thus necessary.

In 2008, the groups of Fox and Weissleder reported the inverse electron demand Diels-Alder (IEDDA) reaction – the reaction between an electron-poor diene, such as a tetrazine, and a strained or electron-rich dienophile – as a new bioorthogonal reaction.[24,25] This reaction was considered highly favourable for live-cell use due to its high reaction rates and the fluorescence quenching properties of the tetrazine (reviewed by Bernardes and co-workers[26]). The most used dienophile, *trans*-cyclooctene (TCO), is a relatively large modification compared to terminal alkynes or azides[27], but has been used successfully to label, among others, the Golgi-membrane with a TCO-modified ceramide probe.[28,29] However, for most lipids where chemical modifications to the structure can largely affect their function, smaller dienophiles are needed.[5,19] An important advance in the application of the IEDDA reaction to live-cell studies of lipid function, was the development of sterically minimal dienophiles. To this end allyl-thiols were reported by Bernardes and co-workers.[30] However, these proved to have rather slow reaction kinetics (≤ 0.002 M^{-1}s^{-1}). Devaraj and co-workers[31], and Prescher and co-workers[32] simultaneously reported cyclopropenes, so-called MiniTags, as minimal reactive dienophiles[33,34]. These cyclopropenes were incorporated into the head groups of phospholipids and were capable of reacting with rate constants of up to 13 M^{-1}s^{-1} in an IEDDA reaction[31], whilst only being slightly larger than alkynes and azides[27]. However, since the modifications were made in the phospholipid head groups, they could not be used to study fatty acid biology and the modification of proteins with fatty acids. Still, the above-mentioned properties make them an attractive alternative to TCO. Cyclopropenes are also reported to have been incorporated into glycans[32,35], lignin polymers[36], and nucleotides[37], combined with live-cell IEDDA reaction and imaging, emphasising their applicability as a bioorthogonal probe.

As discussed by Row and Prescher, it is often useful to look to nature for new bioorthogonal probes, as even rare motifs present in natural products indicate stability and compatibility in living systems.[27] In light of this, Nunn's 1952 discovery[38] of the plant metabolite sterculic acid (StA), a carbocyclic fatty acid[39] found in the kernels of *Sterculia foetida*, was intriguing. This 18-carbon *cis*-unsaturated lipid contains a naturally occurring 1,2-substituted cyclopropene-ring at C9-C10. In plants, it is synthesised by addition of a methylene unit to the double bond of oleic acid (18:1, *cis*-9), followed by enzymatic dehydrogenation to yield the cyclopropene ring.[40] It was not known whether this molecule could be used in live-cell compatible labelling chemistry as a bioorthogonal oleic acid analogue, but it is known to be biologically stable and represents a minimal structural modification of one methylene group compared to the parent oleic acid structure. Furthermore, all previously described bioorthogonal IEDDA applications have been explored for cyclopropenes with 1,3-, 3,3- or 1,2,3-substitution patterns[31,32,41], whereas there has been no report of a 1,2-substituted cyclopropene as a bioorthogonal probe.

Here, the use of StA as a bioorthogonal probe was assessed for its reaction kinetics, short-term toxicity, and live- and fixed-cell imaging capability. It was shown that the fatty acid was readily taken up by dendritic cell lines and could be used for live-cell microscopy by reaction with a tetrazine-fluorophore conjugate (Figure 1). The reaction was furthermore explored in a multiplexed reaction setup.[42] Multiple groups have previously described that it is possible to combine up to three bioorthogonal ligation reactions in a triple mutually orthogonal system, which allows the tracking of multiple bioorthogonally labelled biomolecules in a single sample.[43–45] Previous efforts in the group have focussed on the multiplexing of two copper-catalysed azide-alkyne cycloaddition (CuAAC) reactions.[46] Here, it was explored whether StA also proved compatible with the CuAAC reactions, allowing a triple-click labelling strategy. These experiments all indicate that StA is a valuable reagent to study fatty acid uptake in immune cells.
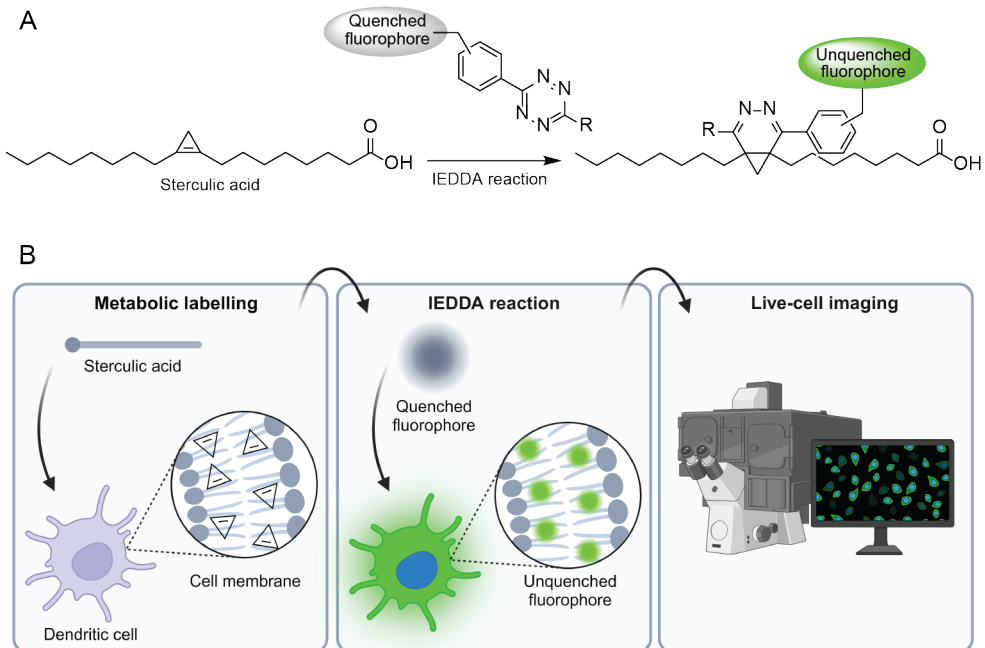
*Figure 1: Schematic overview of **A**) the inverse electron-demand Diels-Alder (IEDDA) reaction between sterculic acid and a quenched tetrazine-fluorophore conjugate. **B**) the approach to label dendritic cells with sterculic acid, followed by an IEDDA reaction with tetrazine-fluorophore conjugates to allow for live-cell confocal imaging. The figure is partially made with BioRender.*

Results & Discussion

To assess whether StA could be used in a live-cell IEDDA reaction, a library of tetrazine-conjugated turn-on fluorophores was designed and synthesised by Dr. Merel van de Plassche (Figure 2). The full description of the synthesis and characterisation of all compounds can be found in the publication by Bertheussen et al.[47] Tetrazines have a broad absorption spectrum, which peaks around 515 nm, meaning it can efficiently quench fluorescent dyes of wavelengths ≤ 550 nm via fluorescence resonance energy transfer (FRET).[48,49] Therefore, tetrazine-fluorophore conjugates are so-called turn-on fluorophores, where their fluorescent intensity increases upon ligation, and their reaction with StA can be readily quantified. Two different green fluorophores, BODIPY and Alexa Fluor 488 (AF488) were selected, and ligated to three differently substituted tetrazines (H-, methyl- or pyridyl-substituted), because of the spectrum of reactivity and stability they covered.[50] Additionally, the tetrazines were attached to the BODIPY core at two different distances, as previous research has shown that decreasing the distance between the fluorophore and the tetrazine can improve the quenching effect.[51,52] It has been suggested that the improved quenching effect occurs via an alternate mechanism, through-bond energy transfer (TBET), and not FRET.[52] Photophysical characterisations of the tetrazine-fluorophore conjugates **1**-**8** can be found in Figure S1 and Table S1.
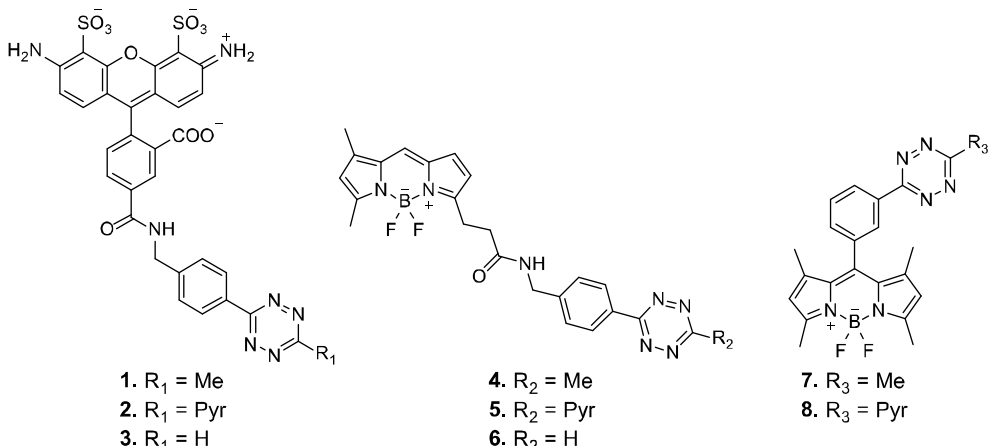
Figure 2: *Structures of tetrazine-fluorophore conjugates 1-8 that were synthesised by Dr. Merel van de Plassche (full synthesis is described in the publication by Bertheussen et al.[47])*

To investigate the fluorescence turn-on of the synthesised fluorophores **1**-**8** upon reaction with StA, the fluorophores were incubated with StA in either PBS, DMSO/ H_2O (1:1, v/v) or complete RPMI 1640 medium augmented with 10% fetal calf serum, and the fluorescent signal was measured over time (Figures 3 and S2). In line with previous reports, the two BODIPY-tetrazine conjugates **7** and **8** showed the highest turn-on ratio in PBS, followed by BODIPY FL-tetrazine conjugates **4** and **5**.[51,52] It was also found that H-substituted tetrazine **6,** and pyridyl-substituted tetrazines **5** and **8** reacted faster than methyl-substituted tetrazines **4** and **7**, in agreement with the observations of the Hilderbrand group.[53] This is also reflected in the second-order rate constant for these reactions, which are calculated for tetrazines **4**-**5** and **7**-**8** that display turn-on effects in PBS (Table S1). Surprisingly the H-substituted tetrazine **6** showed little turn-on in PBS. It has previously been suggested that H-substituted tetrazines can be too unstable to be used in biological applications.[54] Stability assessment of the tetrazine library in PBS (Figure S3A) indeed confirmed that **6** was prone to degradation over time. It was therefore possible that the reaction between StA and **6** cannot go to completion because of competition with hydrolytic degradation and unquenching of the H-substituted tetrazine. This is further supported by the observation that the relative fluorescent intensity (RFU) of tetrazines **1**-**3** and **6**, all showing little turn-on in PBS, at the starting point is high compared to the maximum RFU measured (Figure S3B). Also, tetrazines **1** and somewhat **2** show decreased stability over time, which could partially explain their low turn-on ratios. However, all AF488-tetrazine conjugates **1**-**3** showed very little quenching by the pendant tetrazines (Figure 3). This is difficult to explain, as non-sulfonated analogues such as difluorinated-fluorescein are reported to show good turn-on.[51] A possible explanation for this could either be poor resonance energy transfer[48], photo-induced electron transfer[55], or "energy transfer to a dark state" that have been reported to be important quenching mechanisms for longer bond-length tetrazines.[56] Some loss of fluorescence, likely due to photobleaching, was also observed for **7** and **8.** In DMSO/H_2O or complete medium little-to-no turn-on was observed for all the fluorophores (Figure S2). For turn-on measurements in DMSO/H_2O, this could

be explained by the high intrinsic fluorescence for almost all the fluorophores (except **8**) in the solvent, as shown in Figure S3B.
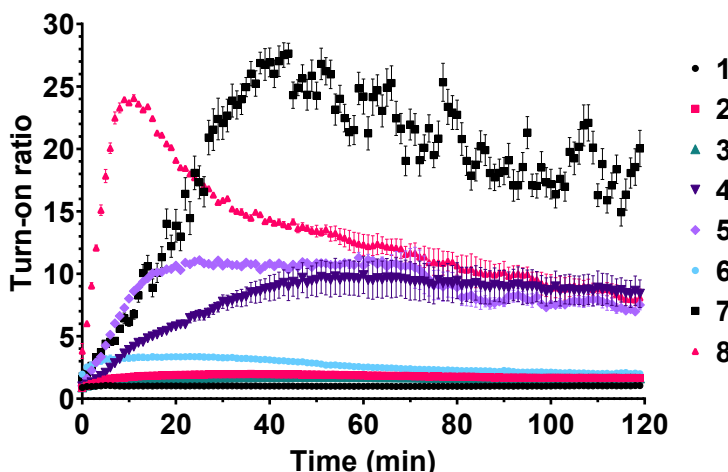

Figure 3: *Average turn-on ratio of tetrazine-fluorophore conjugates **1**-**8** upon reaction with sterculic acid in PBS at 25 °C. All conditions were measured in triplicate, and standard deviations are indicated.*

Due to the capricious turn-on behaviour of the tetrazine-fluorophore conjugates, all of conjugates were assessed in a live-cell imaging experiment with StA (Figure S4). In contrast to the cell-free medium results discussed above, **4**-**8** all exhibited successful ligation after uptake of StA by DC2.4 dendritic cells[57]. This cell line was chosen due to its excellent imaging properties and previous experience in using it as an *in vitro* model cell line for optimising bioorthogonal chemistry.[58] The Alexa Fluor-based dyes **1**-**3** were unable to react with StA in live cells. This is likely due to the hydrophilic nature of these fluorophores, caused by their sulfonation pattern, not allowing them to diffuse over the hydrophobic plasma membrane. This is in line with previously reported data.[59,60] Fluorophore **7** showed the brightest labelling with the lowest background fluorescence, allowing for imaging at lower laser intensities. As this leads to less bleaching of the sample, **7** was deemed to be the best fluorophore for live-cell imaging (Figure 4A). During live-cell labelling, H-, methyl- and pyridyl-substituted tetrazines give equally bright fluorescent signals, and the substituent on the tetrazine core thereby appears to not make a difference.
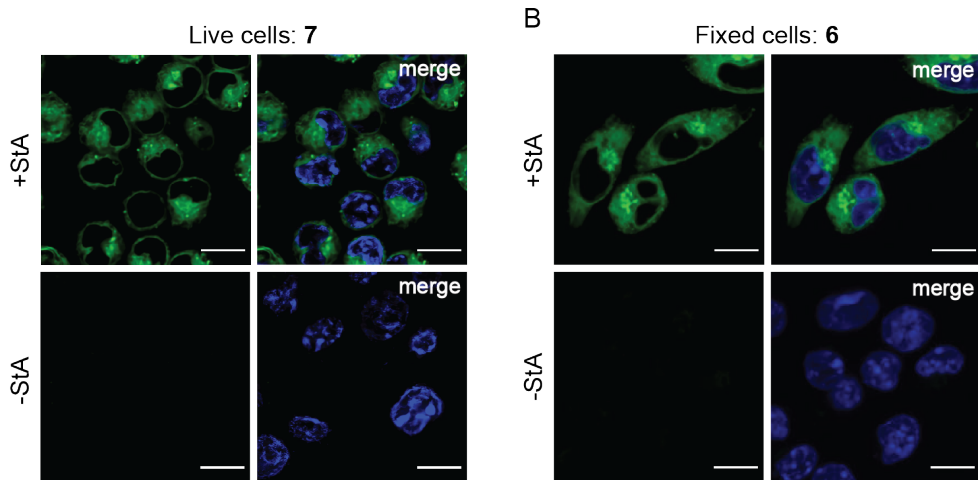
Figure 4: *Confocal imaging of DC2.4 cells incubated with sterculic acid (+StA, 50 µM) or without the probe (-StA).* **A)** *Live-cell imaging of labelled cells visualised with fluorophore* **7** *(5 µM).* **B)** *Fixed-cell imaging of labelled cells visualised with* **6** *(5 µM). The samples were washed after metabolic incorporation of StA and after ligation with the fluorophore-tetrazines and were imaged at >4 distinct locations in the same well. DNA was counterstained with Hoechst 33342 (blue) for reference. Scale bars represent 10 µm.*

To evaluate whether StA was also able to react with the tetrazine-fluorophore conjugates in fixed cells, the entire fluorophore library was also tested on fixed and permeabilised cells (Figure S5). Consistent with the results found in live cells, fluorophores **4**-**6** were able to visualise the localisation of StA. As opposed to the live-cell imaging, **1**-**3** showed labelling in fixed and permeabilised cells. However, the intensity of the signal of **1** and **2** was too low to be detected at the same laser settings as **4**-**6**. Upon increased laser intensity, these fluorophores also showed signal over background (Figure S6). The signals of **7** and **8** were the brightest of the library, but showed oversaturated spots in fixed cells, which could originate from precipitation of the fluorophores under the reaction conditions. A general trend seen from the tetrazine library in fixed cells is that the H-substituted tetrazines give the brightest signal, followed by the pyridyl tetrazines. Fluorophore **6** was deemed to be the best alternative for fixed cells, due to its bright and consistent labelling (Figures 4B & S5), despite showing low turn-on in PBS (Figure 3). A direct comparison between the turn-on study and cellular imaging is difficult, due to differing conditions in the two situations. In the turn-on study, there is an excess of StA reacting with the fluorophores, whereas the concentration of StA after metabolic incorporation for cellular imaging is the limiting factor, leading to an excess of the fluorophores instead. In addition, unreacted and potentially degraded fluorophore was routinely washed away before imaging, reducing the background signal, while this was not possible for the turn-on study.

In addition to the fluorophore library, StA was also shown to react with the commercially available (sulfo-)Cy5 tetrazine in a similar manner, allowing its use in a fixed-cell confocal imaging experiment (Figure S7). Use of the Cy5 fluorophore shows a similar labelling pattern as described for the other tetrazine-fluorophore

conjugates, even though it has no turn-on effect.

While unreacted fluorophore was routinely washed away from both live- and fixed-cell samples prior to confocal imaging to minimise background signal, sample preparation and preservation, especially for live-cell imaging, would benefit from the reduction of washing steps. Therefore, it was showed that the turn-on effect of fluorophores **4-5** and **7-8** upon ligation with StA was sufficient for wash-free live-cell imaging without any detectable background signal (Figure S8).

The metabolic fate of StA after uptake is not known, but in both live and fixed cells StA was observed throughout the cells, except for in the nucleus (Figure 4). Since exogenous free fatty acids can be readily incorporated into phospholipids and other cellular lipids via an acyl coenzyme A intermediate[61], this could indicate that StA is incorporated into plasma and organellar membranes. This is in keeping with StA serving as a mimic for oleic acid, which is known to be found ubiquitously in membrane lipids.[62] In fixed cells (Figure 4B), which are displayed as maximum intensity projections, it also appears that the fluorescent signal is stronger in the endoplasmic reticulum (ER). This can be explained by the incorporation of the free fatty acids into phospholipids through Lands' cycle and the Kennedy pathway, which occur mainly at the ER.[63] However, this would need to be verified by co-stain experiments with an ER marker.

Multiplexing of bioorthogonal reactions is growing in popularity, meaning more complex systems can be studied simultaneously.[64] Previous work has, among other things, shown that two CuAAC reactions can be combined in the same sample.[46] Here, it was explored whether the StA ligation could be included in this workflow, allowing three biomolecules to be simultaneously visualised by multimodal fluorescent imaging. DC2.4 cells were metabolically labelled with the alkyne-containing thymidine analogue 5-ethynyl-2'-deoxyuridine (EdU)[65], the azide-containing palmitic acid analogue 15-azidopentadecanoic acid (azido palmitic acid, azPA) and StA, after which the cells were fixed before performing the corresponding bioorthogonal reactions with AZDye 555 azide, AZDye 647 alkyne, and compound **5**, respectively (Figures 5 and S9). The facile inclusion of StA in both live-cell and multi-click workflows – with good signal-to-noise ratios for all three click reactions indicates that StA does not have detectable cross-reactivity with the CuAAC reagents or cellular components. This means that StA can be used in combination with other click chemistries, allowing for the simultaneous study of multiple biomolecules.

As a note of caution, StA has been reported to be an inhibitor of the enzyme stearoyl-CoA desaturase 1 (SCD1) which catalyses the transformation of saturated fatty acids such as stearic or palmitic acid to their monounsaturated counterparts oleic or palmitoleic acid, respectively.[66] Lowered activity of SCD1 has been linked to various cellular responses such as ER stress, autophagy, and apoptosis[66], which in turn poses the question if the addition of StA would be toxic to the cells by its inhibiting effect on SCD1. To ensure that this was not the case, DC2.4 cells were incubated with a concentration range of StA and cell viability after 24 h was measured by 3-(4,5-dimethylthiazol-2-yl)-2,5-diphenyltetrazolium bromide (MTT) assay (Figure S10). No significant decrease of DC2.4 cell viability was observed for concentrations of StA up to 50 µM and at higher concentrations there was no difference with vehicle-induced toxicity. This further strengthens the applicability of StA as a novel

bioorthogonal analogue of oleic acid. Nevertheless, inhibition of SCD1 should be considered in future use StA, and other cyclopropene-modified lipids.
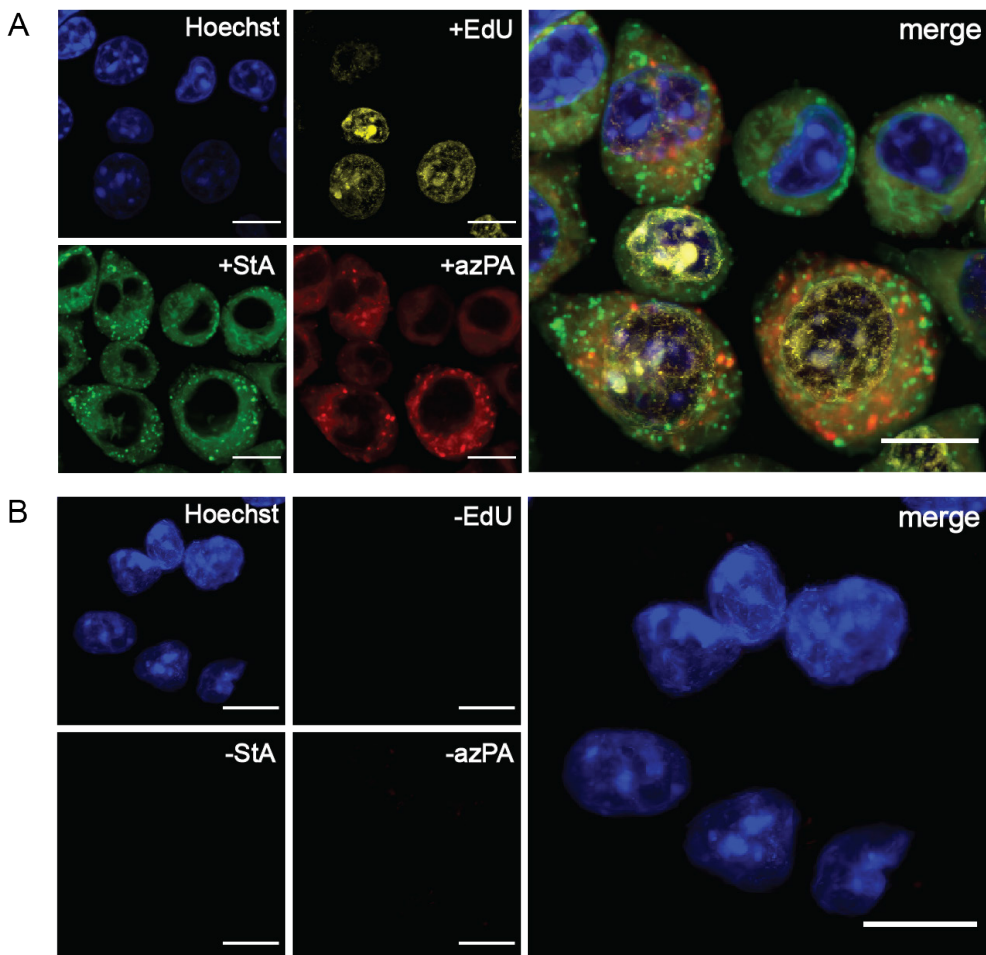

Figure 5: *Confocal imaging of triple-bioorthogonally labelled DC2.4 cells incubated with **A)** 5-ethynyl-2'deoxyuridine (EdU, 10 µM, yellow) for 20 h, followed by sterculic acid (StA, 50 µM, green) and azido palmitic acid (azPA, 100 µM, red) simultaneously for 1 h. The probes were visualised with AZDye 555 azide, compound **5**, and AZDye 647 alkyne (all 5 µM), respectively. **B)** The cells were incubated without probes and treated in the same triple-click manner as described above to show the background signal. The samples were washed between each metabolic incorporation and between each respective bioorthogonal reaction and were imaged at 3 distinct locations in the same well. DNA was counterstained with Hoechst 33342 (blue) for reference. All scale bars represent 10 µm*

Conclusion

Here, the first use of sterculic acid, a non-toxic 1,2-substituted cyclopropene-containing fatty acid, for studying lipids in both live and fixed cells has been reported. The cyclopropene moiety readily reacts with the library of tetrazine-fluorophore conjugates, allowing the study of fatty acid localisation by confocal microscopy. This reaction can occur in a mutually orthogonal manner with two subsequent CuAAC reactions, allowing the study of multiple biomolecules simultaneously. The use of sterculic acid, means that unsaturated lipids can now be visualised using live-cell microscopy; a sorely needed addition to the available tools for these elusive biomolecules.

Acknowledgements

Materials & Methods

General. Sterculic acid (#26735) was purchased from Cayman Chemical and stored as 10 mM or 100 mM stock solutions in DMSO at -20°C. Azido palmitic acid (#1346) was purchased from Click Chemistry Tools (now VectorLabs) and stored as 10 mM or 50 mM stock solutions in DMSO at -20°C. 5-ethynyl-2'-deoxyuridine (EdU, #900584) was purchased from Sigma Aldrich and stored as a 10 mM stock solution in DMSO at -20°C. The tetrazine-fluorophore conjugates **1**-**8** were synthesised in-house (as described in the publication by Bertheussen et al.[47]), and were stored as 2 mM stock solutions in DMSO at -20°C. The other fluorophores (sulpho-)Cy5 tetrazine (#1189), AZDye 555 azide (#1287), AZDye 647 alkyne (#1301) were all purchased from Click Chemistry Tools (now VectorLabs), and stored as 2 mM stock solutions in DMSO at -20°C.

Mammalian cell culture. DC2.4 cells were cultured in RPMI 1640 culture medium (Gibco, #31870025) supplemented with 10% FCS, GlutaMAX (2 mM), sodium pyruvate (1 mM), 1x non-essential amino acids (NEAA, Thermo Fisher Scientific), penicillin (100 I.U./mL), streptomycin (50 µg/mL), and 2-mercaptoethanol (50 µM, Thermo Fisher Scientific), and incubated at 37 °C, 5% CO_2. The cells were grown to 70-80% confluency and passaged every 2-3 days by trypsinisation.

Measuring turn-on of the tetrazine-fluorophore conjugates. Dilutions of the fluorophores **1**-**8** (2 µM) and StA (10 µM, Cayman Chemical) were prepared in three solvents; PBS, DMSO/H_2O (1:1, v/v), and phenol red-free RPMI 1640 culture medium (Thermo Fisher Scientific) supplemented with 10% FCS, GlutaMAX (2 mM), pyruvate (1 mM) and 1x NEAA. The solvents were analysed one at a time by adding 50 µL of the fluorophore dilutions in triplicate in a black 96-well plate, followed by addition of 50 µL StA dilution or 50 µL only solvent (negative control). This gives final concentrations of 1 µM fluorophore, and 5 µM StA. The plate was immediately scanned for fluorescence on a CLARIOstar plate reader (BMG LABTECH) with excitation/emission at 477-14/530-40 and dichroic filter 497. Fluorescence was measured once every 60 sec for 120 min. The results were processed and plotted in GraphPad Prism version 9.3.1 showing the turn-on ratio between the sample and negative control, as an average of the triplicated samples and with indicated standard deviations.

Reaction kinetics between tetrazine-fluorophore conjugates and sterculic acid. To calculate the second-order rate constants (k_2) for the reaction between tetrazines **1**-**8** and StA, the data assembled for the turn-on measurements (described earlier) were used and a previously published procedure was followed.[67] After having subtracted background fluorescence values from the data, each curve was capped at its initial plateau, after the exponential phase, to prevent photobleaching from affecting the calculations. Each replicate (n=3) was processed separately for the whole analysis. Since the experiment was performed under pseudo first-order conditions, the pseudo first-order rate constant k_1' was determined using the 'One phase decay' regression in GraphPad Prism version 9.3.1 on the data points. The second-order rate constant was then calculated as $k_2 = k_1'/c_{StA}$, and standard deviations were calculated for the replicates.

Preparation of live-cell samples. For microscopy, 6x10^5 DC2.4 cells were seeded

per well on an 8-well chamber slide (Ibidi) and allowed to attach for 2 h. The cells were incubated with StA (50 µM) or no probe (negative control) for 1 h in complete medium (as described above) with 0.1% fatty acid-free BSA (Sigma Aldrich) instead of FCS. Cells were washed with fresh medium x3, followed by incubation with the respective fluorophores **1-8** from the tetrazine library (5 µM) in complete medium for 1 h. For Figures 4A and S4, the cells were washed with fresh medium x3 after fluorophore ligation to remove unreacted probe, and DNA was counterstained with Hoechst 33342 (5 µg/mL, Sigma Aldrich) in PBS for 5-10 min followed by washing with PBS x3. For Figure S8, labelling medium was aspirated and DNA was immediately counterstained with Hoechst 33342 (5 µg/mL, Sigma Aldrich) in PBS for 5-10 min without washing steps. Each incubation step was done at 37 °C, 5% CO_2. All samples were directly imaged in phenol red-free DMEM (Sigma Aldrich) supplemented with GlutaMAX (2 mM), sodium pyruvate (1 mM), penicillin (100 I.U./mL), and streptomycin (50 µg/mL), by confocal microscopy (see below).

Preparation of fixed-cell samples. The same protocol was followed as for live-cell imaging (described above) until the point of incubation with StA, after which the cells were fixed with 4% paraformaldehyde (PFA) in PBS for 30 min at room temperature. After fixation the cells were washed with PBS followed by glycine (20 mM) in PBS to quench unreacted aldehyde. The cells were permeabilised with 0.01% saponin in PBS for 20 min and washed with PBS x2. The permeabilised sample was incubated with the tetrazine-fluorophore conjugate library (**1-8**, 5 µM) or (sulpho-)Cy5 tetrazine (20 µM) in PBS for 1 h, followed by washing with PBS x2 and blocking with 1% BSA in PBS for 30 min. DNA was counterstained with Hoechst 33342 (2 µg/mL) in PBS for 5-10 min. The incubation steps were done at room temperature and separated by intermediate washing steps with PBS. The cells were then imaged directly in glycerol/DABCO mounting medium to minimise photo bleaching.

Preparation of triple-labelled sample. For microscopy, $6x10^5$ DC2.4 cells were seeded per well on an 8-well chamber slide (Ibidi) and allowed to attach for 3 h. The triple metabolic labelling started with incubating the cells with EdU (10 µM) in complete medium for 20 h, followed by washing with PBS x2. Then a metabolic label cocktail containing StA (50 µM) and azido palmitic acid (100 µM) in medium with 0.1% fatty acid-free BSA (Sigma Aldrich) instead of FCS, was added to the sample and it was incubated for 1 h. The sample was washed with fresh medium x1 and PBS x1 and fixed in 2% PFA in 0.1M phosphate buffer pH 7.2 at room temperature overnight. Fixation solution was aspirated, and sample was washed with PBS and glycine (20 mM) in PBS, and permeabilised with 0.01% saponin in PBS for 20 min. The sample was first reacted with fluorophore **5** (5 µM) in PBS for 1 h, followed by AZDye 555 azide (5 µM) in copper-click cocktail (1 mM $CuSO_4$, 10 mM sodium ascorbate, 1 mM THPTA ligand, 10 mM amino-guanidine, 0.1 M HEPES pH 7.2) for 1 h and finally AZDye 647 alkyne (5 µM) in copper-click cocktail for 1 h. All bioorthogonal reactions were performed with intermediate washing steps with PBS x2, and after the reactions unreacted fluorophores were blocked with 1% BSA in PBS for 30 min. DNA was counterstained with Hoechst 33342 (2 µg/mL) in PBS for 5-10 min and the sample was imaged directly in glycerol/DABCO mounting medium.

Confocal microscopy. All slides were imaged on an AR1 HD25 confocal microscope (Nikon), equipped with a Ti2-E inverted microscope, LU-NV Series laser unit, and CFI Plan Apo Lambda 100x/1.45 oil objective. Hoechst, the tetrazine-fluorophore

conjugates, AZDye 555, and AZDye 647 and (sulpho-)Cy5 were excited using the 405 nm, 488 nm, 561 nm, and 647 nm laser lines, respectively, and images were acquired using the Resonant scanner and DU4 detector (495LP (450/50), 560LP (525/50), 640LP (595/50)). Poisson noise was immediately removed from the images by the built-in Nikon Denoise.ai software. Z-stacks were acquired from the fixed-cell and triple-labelled samples with 0.20-micron steps and are all presented as maximum intensity projections. Brightness and contrast were adjusted for all samples using ImageJ. Brightness and contrast were adjusted identically for samples that are directly compared to each other to make sure the relative intensity between the samples remain the same.

Assessing the cytotoxicity of sterculic acid. A 3-(4,5-dimethylthiazol-2-yl)-2,5-diphenyltetrazolium bromide (MTT) assay was performed to ensure the concentration of StA used in the following experiments was not cytotoxic. In a 96-well plate (Sarstedt), $1x10^5$ DC2.4 cells were seeded per well and allowed to attach for 2 h. Serial dilutions (1:2) of StA (stock concentration 10 mM in DMSO) in complete medium, in the range of 12.5-200 µM, were prepared. These were added in triplicate, together with the appropriate controls and blanks and incubated for 24 h. The cells were spun down (300 g, 5 min) and the culture medium was replaced with complete medium containing MTT (0.5 mg/mL). The plate was incubated for 3 h and spun down at (300 g, 5 min) before the medium was aspirated. The formed formazan crystals were dissolved in DMSO, and the plate was incubated for 2 min with 400 rpm shaking. All incubation steps were done at 37 °C, 5% CO_2. Absorbance was measured at 570 nm on a CLARIOstar plate reader (BMG LABTECH). The data were normalised against cells that had no StA added, and the normalised standard deviations are given.

Supplementary Figures & Tables
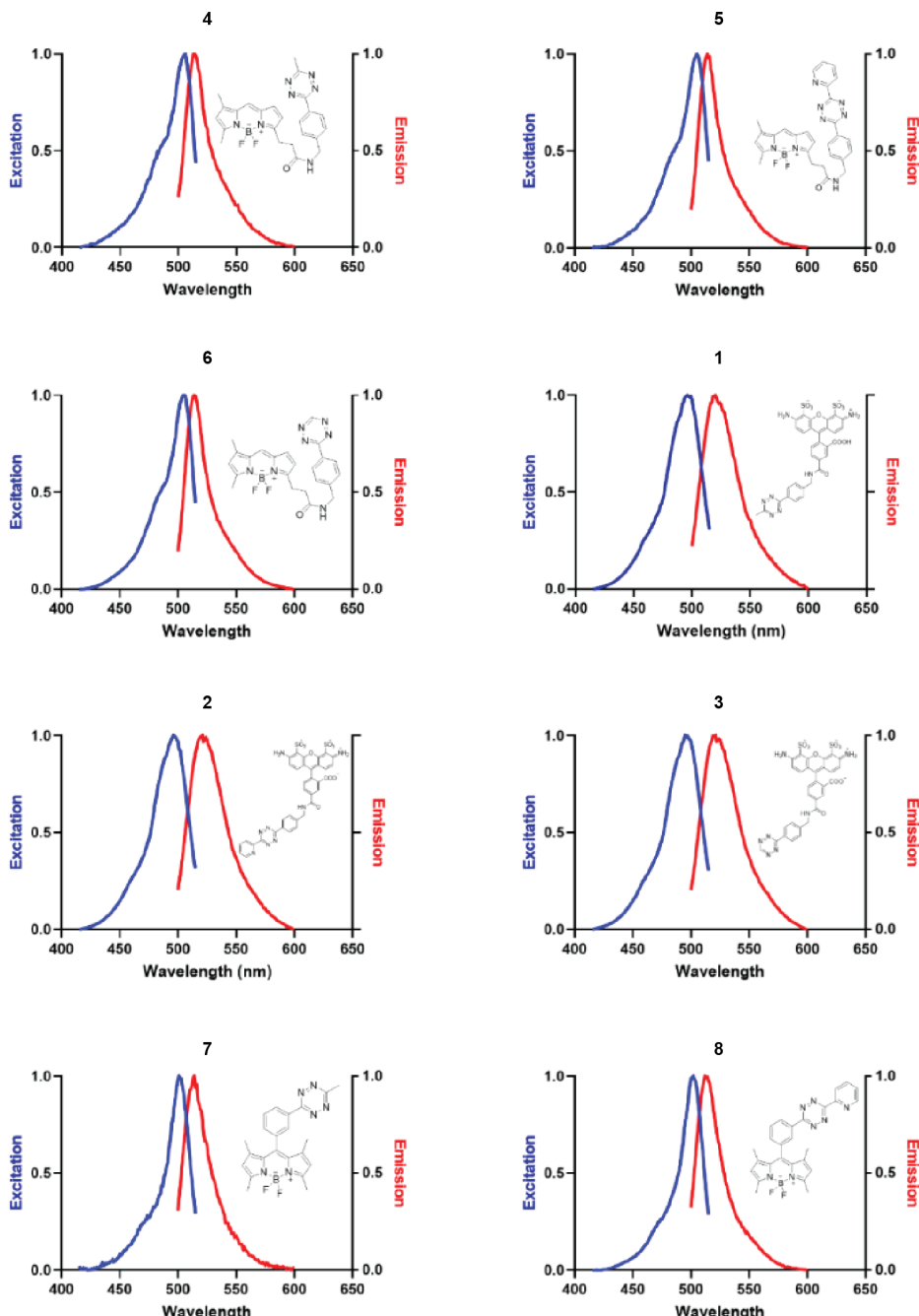
Figure S1: *Normalised excitation and emission spectra of fluorophores **1-8** measured at a final concentration of 1 µM in PBS on a CLARIOstar plate reader.*

Table S1: *Characterisations of the photophysical properties of tetrazine-fluorophore conjugates **1-8**, and their kinetics upon reaction with sterculic acid. Absorption maximum (Λ_{abs}) and extinction coefficient (E_{max}) of the tetrazine-fluorophore conjugates (1 µM) in DMSO/H_2O (1:1) and PBS. Second-order rate constants (k_2) for the conjugates (1 µM) upon reaction with sterculic acid (5 µM) in PBS.*

| Fluorophore	Λ_{abs} (nm) DMSO/H_2O (1:1)	E_{max} ($M^{-1}cm^{-1}$) DMSO/H_2O (1:1)	Λ_{abs} (nm) PBS	E_{max} ($M^{-1}cm^{-1}$) PBS	k_2 ($M^{-1}s^{-1}$)
1	500	58000	492	48000	ND
2	500	45000	492	36000	ND
3	500	39000	494	39000	ND
4	506	60000	506	34000	125 ± 41
5	508	28000	506	16000	660 ± 28
6	506	43000	506	24000	ND
7	500	59000	500	26000	658 ± 14
8	502	82000	500	26000	328 ± 36
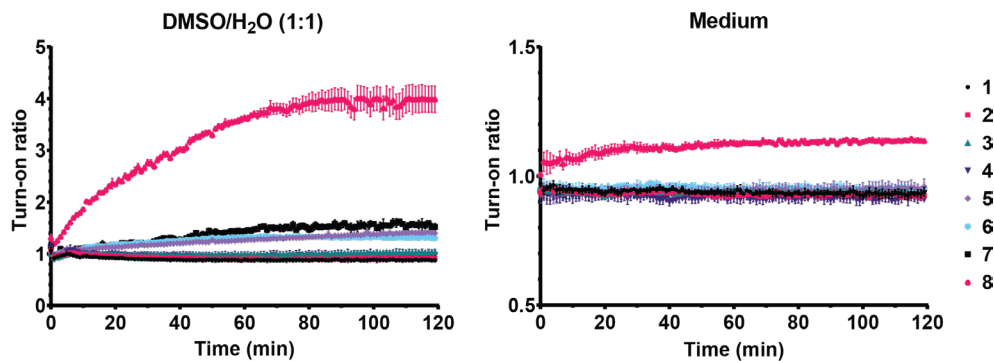
Figure S2: *Average turn-on ratio of tetrazine-fluorophore conjugates **1-8** upon reaction with sterculic acid in DMSO/H_2O (1:1, v/v) or complete medium at 25°C. All conditions were measured in triplicate, and standard deviations are indicated.*
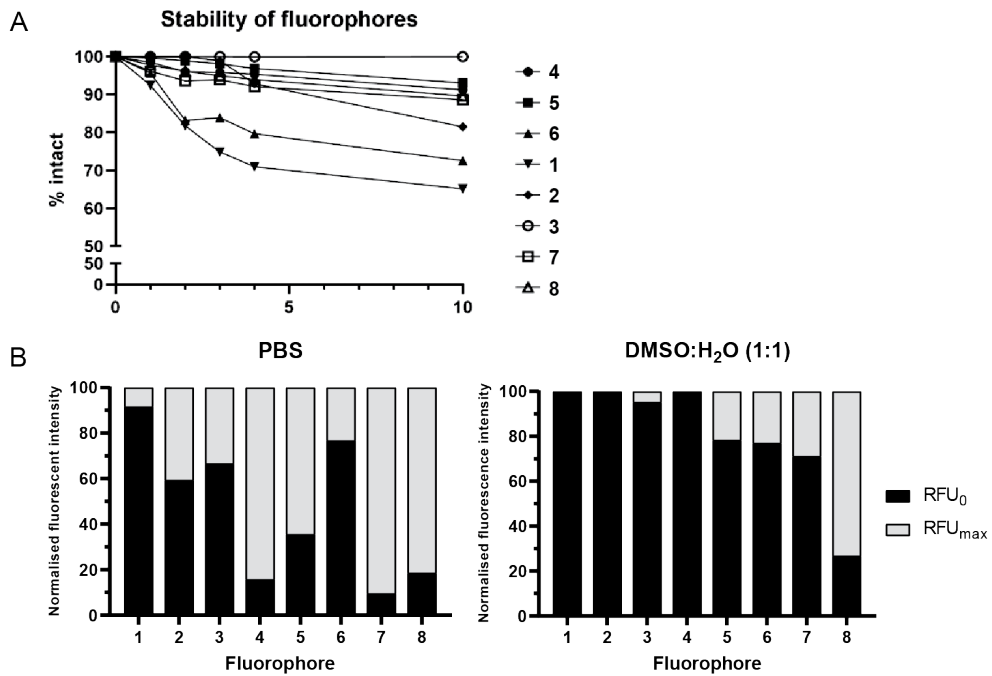
Figure S3: *Further insight into the stability and turn-on ability of tetrazine-fluorophore conjugates **1-8**. **A)** Stability of the fluorophores (10 μM) in PBS at RT for 10 h as measured by LCMS. The integral of the peak at 0 min was set as 100%. **B)** Each fluorophore (1 μM) was reacted with sterculic acid (5 μM) in PBS and DMSO:H$_2$O (1:1) at RT, and the fluorescent intensity at the start-point of measurement (RFU$_0$) is compared to the maximum fluorescent intensity (RFU$_{max}$). RFU$_{max}$ for each fluorophore is set to 100%.*
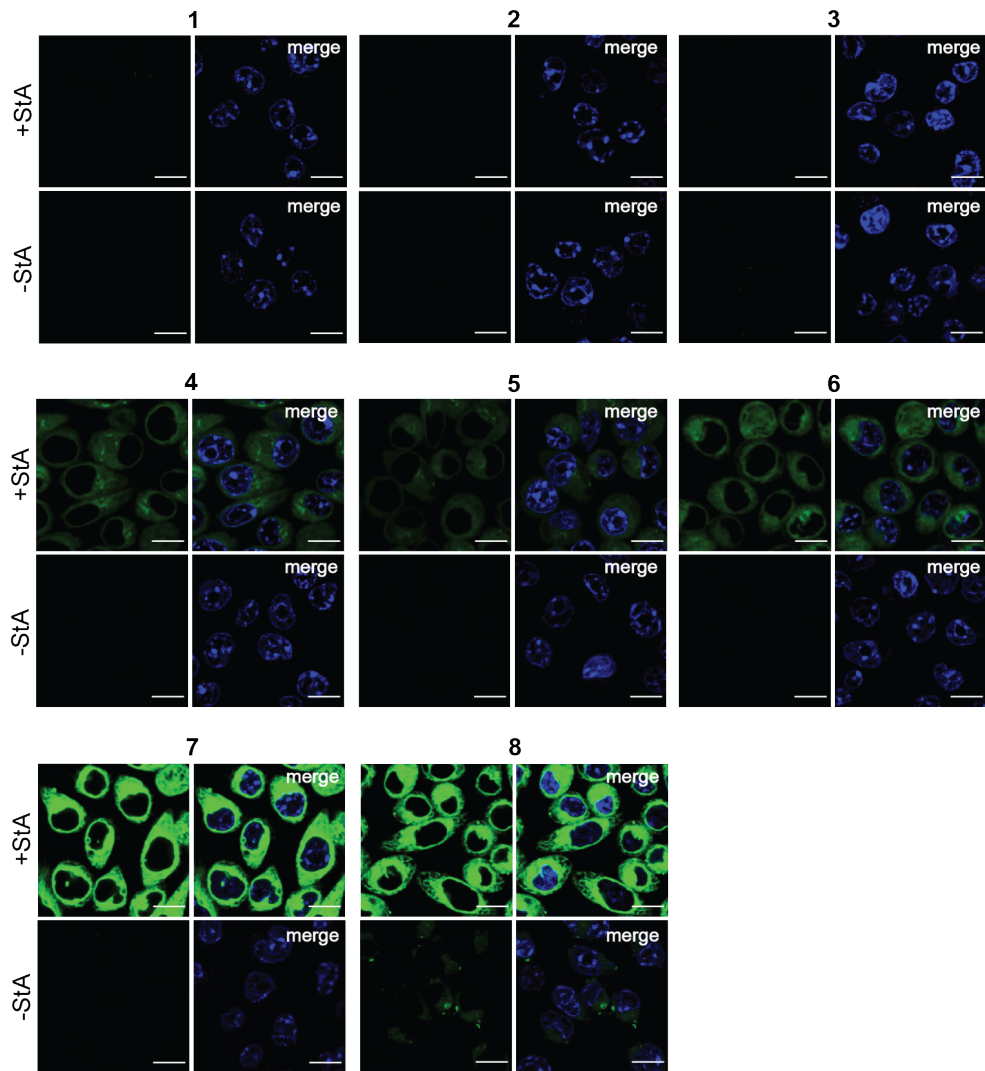
Figure S4: *Confocal live-cell imaging of tetrazine-fluorophore conjugate library (**1-8**). DC2.4 cells were incubated with sterculic acid (+StA, 50 µM) or no probe (-StA) for 1 h, followed by click reaction with the respective fluorophore (all 5 µM) for 1 h. Images are presented as single slices. All samples were routinely washed after metabolic incorporation of sterculic acid and after ligation with the fluorophores and were imaged with minimum 4 technological replicates. DNA was counterstained with Hoechst 33342. All scale bars represent 10 µm.*
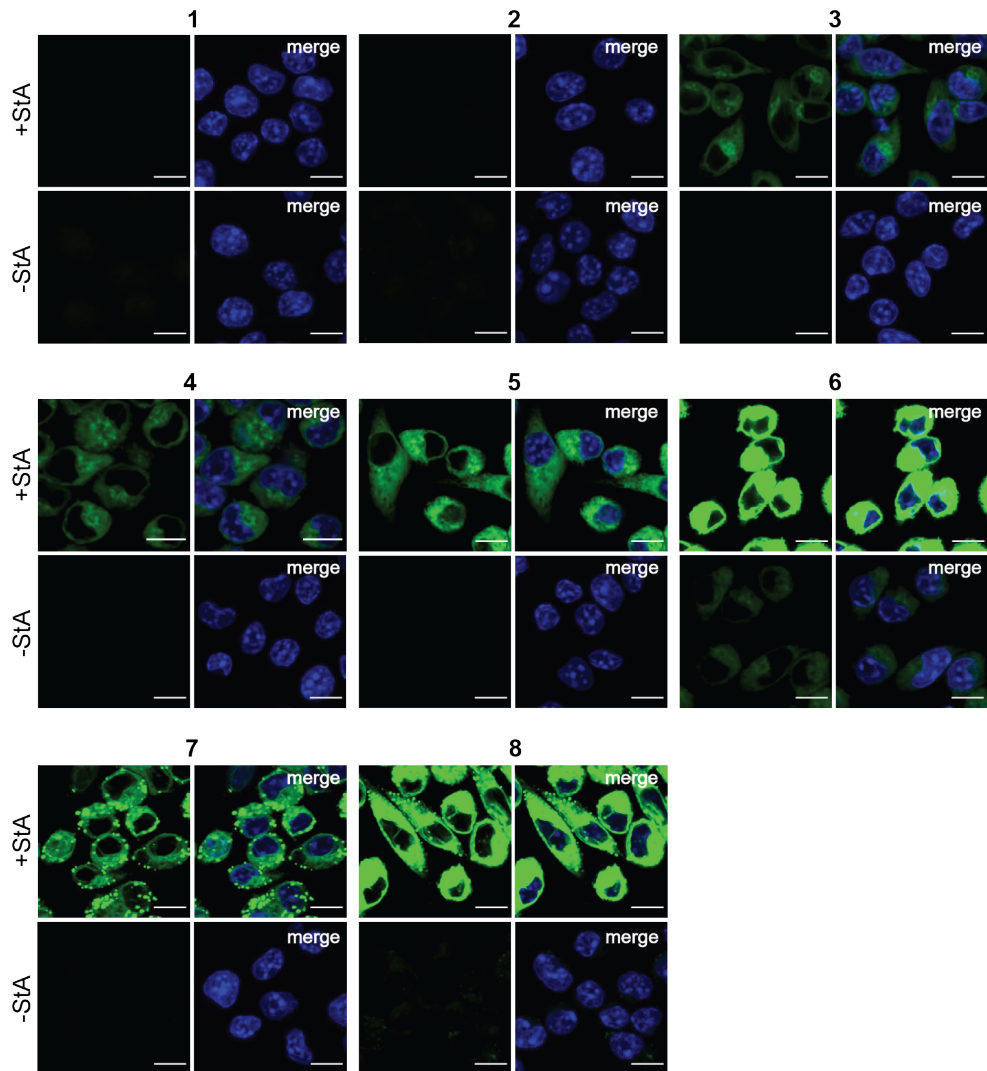
Figure S5: *Confocal fixed-cell imaging of tetrazine-fluorophore conjugate library (**1-8**). DC2.4 cells were incubated with sterculic acid (+StA, 50 µM) or no probe (-StA) for 1 h, fixed and permeabilised, followed by click reaction with the respective fluorophore (all 5 µM) for 1 h. Images are presented as maximum intensity projections of z-stacks. All samples were routinely washed after metabolic incorporation of sterculic acid and after ligation with the fluorophores and were imaged with minimum 4 technological replicates. DNA was counterstained with Hoechst 33342. All scale bars represent 10 µm.*
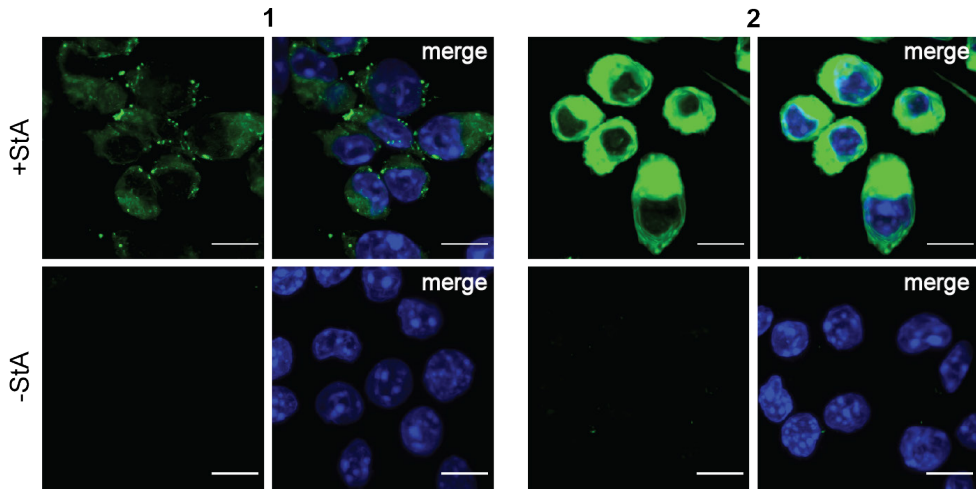
Figure S6: *Confocal fixed-cell imaging of fluorophores **1-2** with higher laser power. DC2.4 cells were incubated with sterculic acid (+StA, 50 µM) or no probe (-StA) for 1 h, fixed and permeabilised, followed by click reaction with the respective fluorophore (5 µM) for 1 h. Images are presented as maximum intensity projections of z-stacks. All samples were washed after metabolic incorporation of sterculic acid and after ligation with the fluorophores. DNA was counterstained with Hoechst 33342 (blue). All scale bars represent 10 µm.*
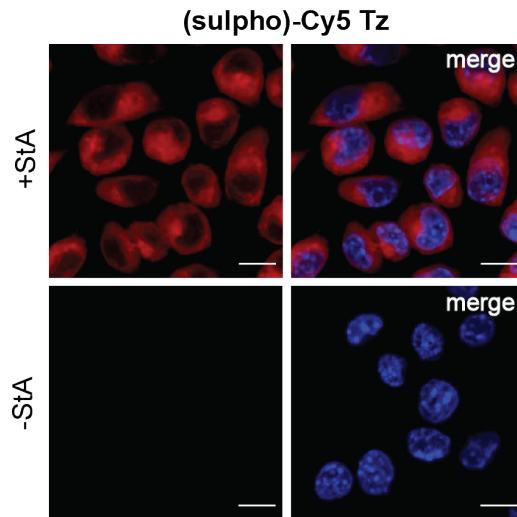
Figure S7: *Confocal fixed-cell imaging with (sulpho-)Cy5 tetrazine. DC2.4 cells were incubated with sterculic acid (+StA, 50 µM) or no probe (-StA) for 1 h, fixed and permeabilised, followed by click reaction with (sulpho-)Cy5 tetrazine (20 µM) for 1 h. Images are presented as maximum intensity projections of z-stacks. All samples were routinely washed after metabolic incorporation of sterculic acid and after ligation with the fluorophores and were imaged with 4 technological replicates. DNA was counterstained with Hoechst 33342 (blue). All scale bars represent 10 µm.*
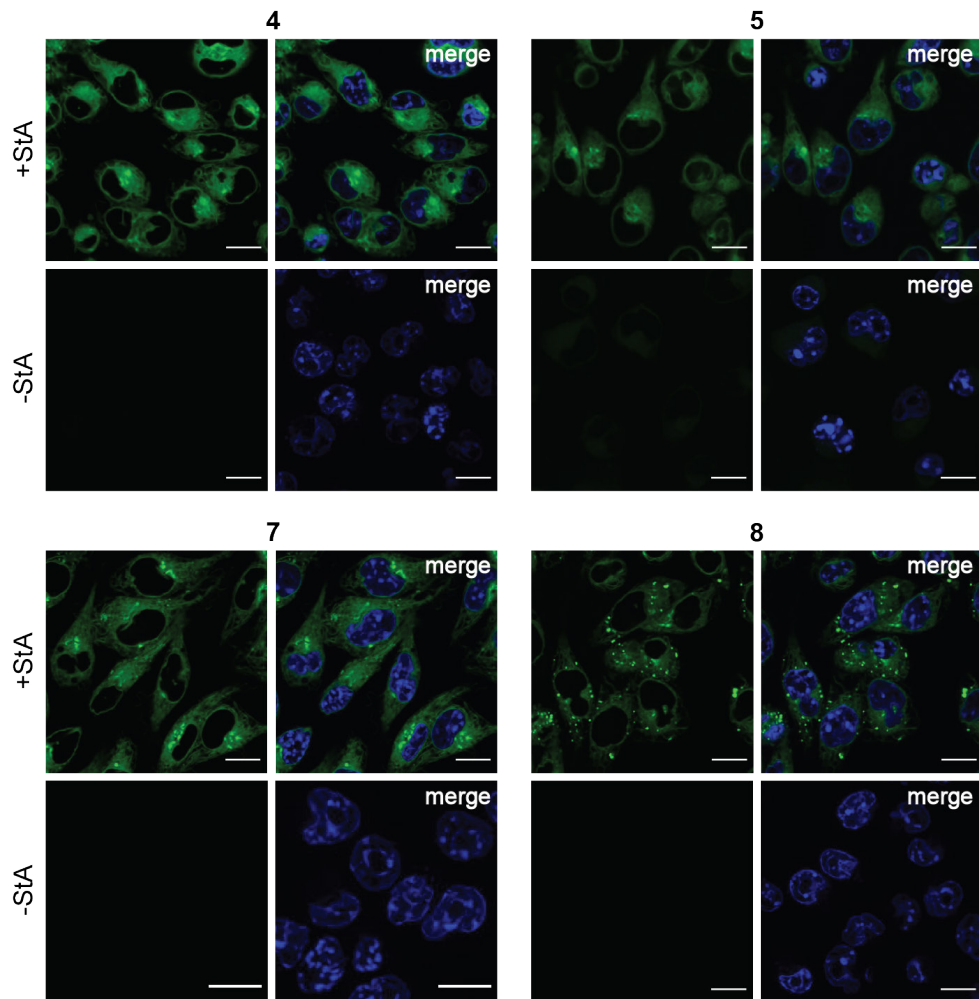
Figure S8: *Confocal live-cell imaging without washing steps after ligation between sterculic acid and fluorophores **4**-**5** and **7**-**8**. DC2.4 cells were incubated with sterculic acid (+StA, 50 µM) or no probe (-StA) for 1 h, followed by a wash step to remove excess sterculic acid, and click reaction with the respective fluorophore (all 5 µM) for 1 h. DNA was counterstained with Hoechst 33342, and samples were imaged directly without further wash steps. Images are presented as single slices and were imaged with minimum 3 technological replicates. Fluorophores **7**-**8** were imaged at a lower laser intensity than **4**-**5**. DNA was counterstained with Hoechst 33342 (blue). All scale bars represent 10 µm.*
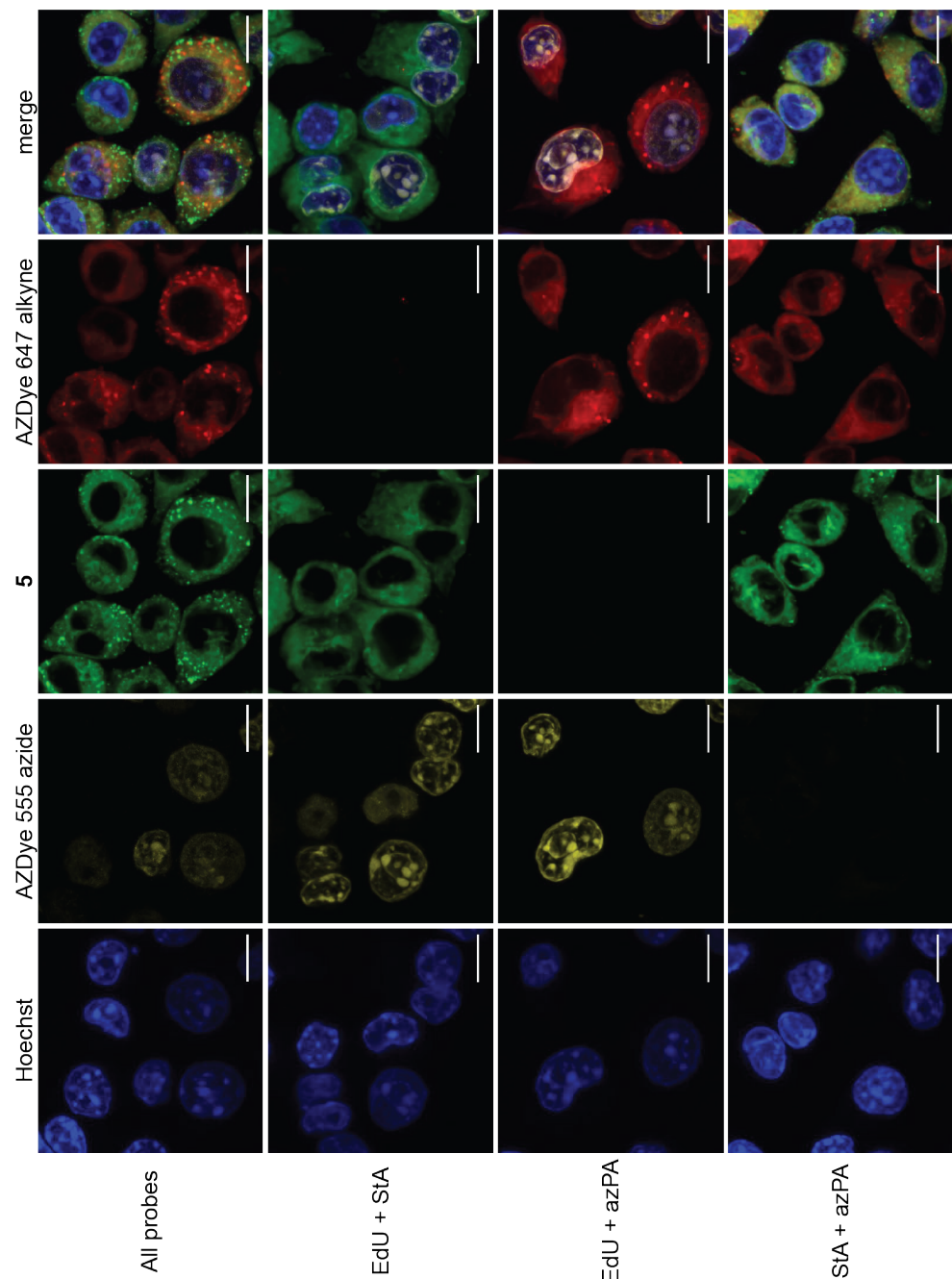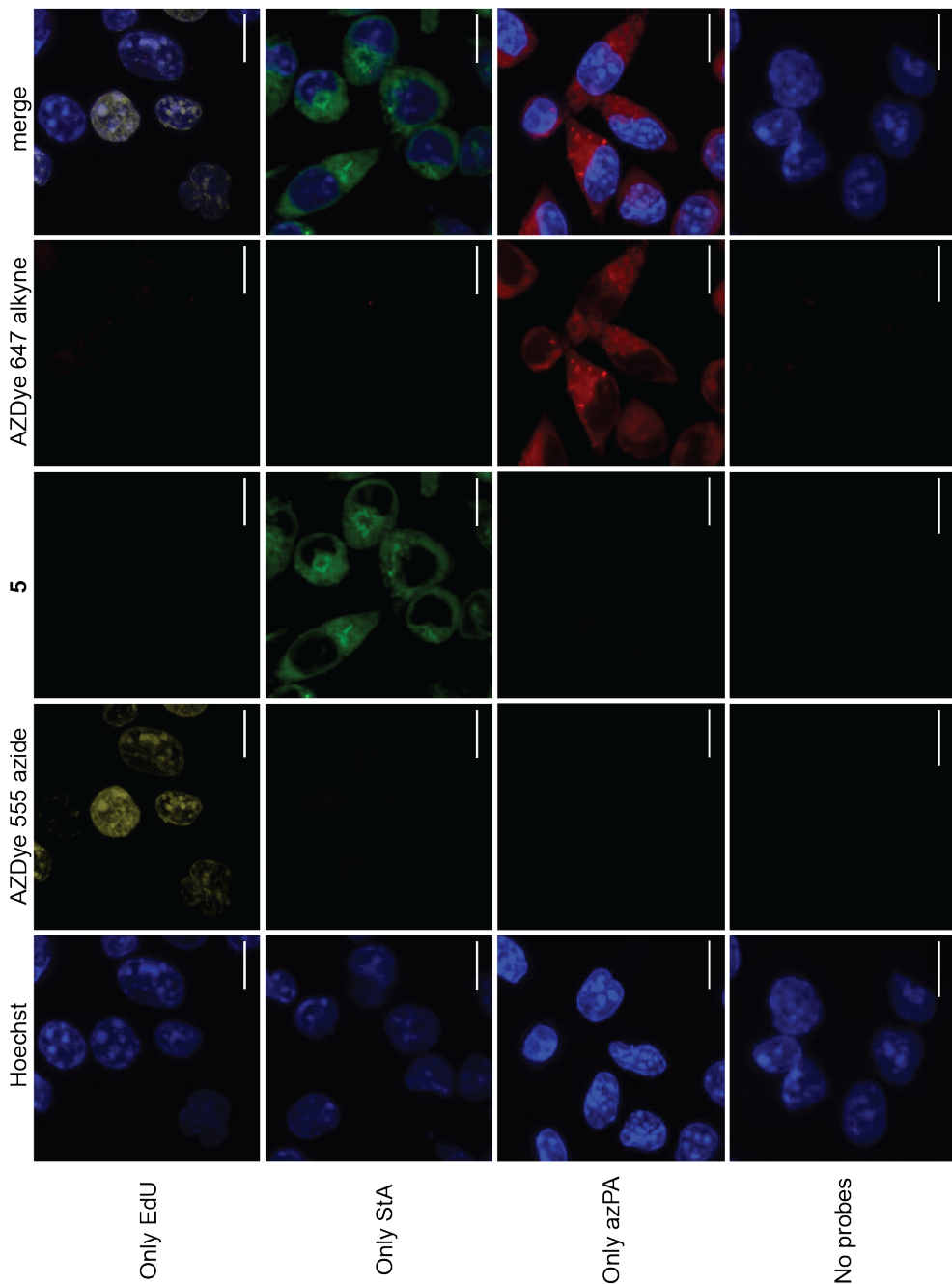
Figure S9: *Confocal imaging of triple-labelled sample with all respective controls. DC2.4 cells were incubated with EdU (10 μM) for 20 h, followed by sterculic acid (StA, 50 μM) and azido palmitic acid (azPA, 100 μM) for 1 h, or the respective combination of these probes. The cells were then fixed and permeabilised, followed by a triple-click strategy. All samples were first clicked with fluorophore **5** (5 μM) for 1 h, followed by two subsequent CuAAC reactions with AZDye 555 azide (5 μM) and AZDye 647 alkyne (5 μM) for 1 h each. All samples were routinely washed between each metabolic incorporation and between each respective bioorthogonal reaction and were imaged with 3 technological replicates. Images are presented as maximum intensity projections of z-stacks. DNA was counterstained with Hoechst 33342 (blue) as a reference. All scale bars represent 10 μm.*
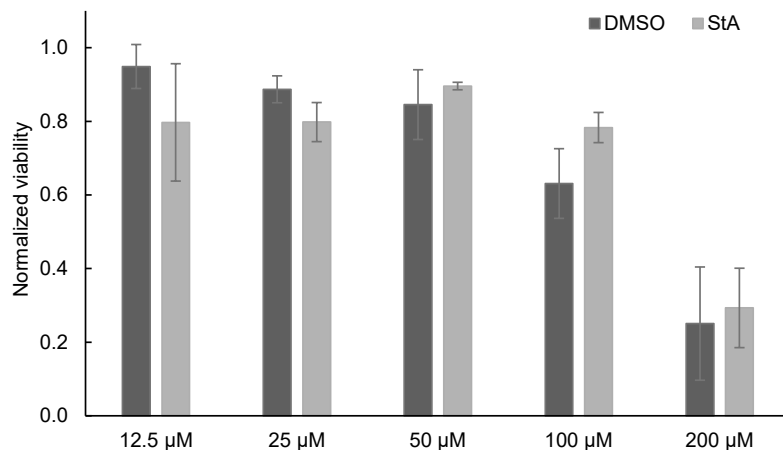
Figure S10: *Toxicity of sterculic acid (StA), as assessed by MTT assay. DC2.4 cells were incubated with given concentrations (μM) of StA in DMSO (labelled StA), or the corresponding amount of DMSO (ranging from 0.125-2%) without StA (labelled DMSO) for 24 h. Absorbance was measured at 570 nm. Absorbance values were measured in triplicate and normalised to an untreated control. Standard deviations are indicated.*

References

1.   Houten, S. M. & Wanders, R. J. A. A general introduction to the biochemistry of mitochondrial fatty acid β-oxidation. *Journal of inherited metabolic disease* **33**, 469–477 (2010).

2.   van Meer, G., Voelker, D. R. & Feigenson, G. W. Membrane lipids: where they are and how they behave. *Nature Reviews Molecular Cell Biology* **9**, 112–124 (2008).

3.   Resh, M. D. Fatty acylation of proteins: The long and the short of it. *Progress in Lipid Research* **63**, 120–131 (2016).

4.   Wymann, M. P. & Schneiter, R. Lipid signalling in disease. *Nature Reviews Molecular Cell Biology* **9**, 162–176 (2008).

5.   Bumpus, T. W. & Baskin, J. M. Greasing the Wheels of Lipid Biology with Chemical Tools. *Trends Biochem Sci* **43**, 970–983 (2018).

6.   Ticho, A. L. *et al.* S-acylation modulates the function of the apical sodium-dependent bile acid transporter in human cells. *Journal of Biological Chemistry* **295**, 4488–4497 (2020).

7.   Thinon, E., Percher, A. & Hang, H. C. Bioorthogonal Chemical Reporters for Monitoring Unsaturated Fatty-Acylated Proteins. *ChemBioChem* **17**, 1800–1803 (2016).

8.   Pérez, A. J. & Bode, H. B. ω-Azido fatty acids as probes to detect fatty acid biosynthesis, degradation, and modification. *J Lipid Res* **55**, 1897–1901 (2014).

9.   Kostiuk, M. A. *et al.* Identification of palmitoylated mitochondrial proteins using a bioorthogonal azido-palmitate analogue. *The FASEB Journal* **22**, 721–732 (2008).

10.   Charron, G. *et al.* Robust Fluorescent Detection of Protein Fatty-Acylation with Chemical Reporters. *J Am Chem Soc* **131**, 4967–4975 (2009).

11.   Thiele, C. *et al.* Tracing Fatty Acid Metabolism by Click Chemistry. *ACS Chem Biol* **7**, 2004–2011 (2012).

12.   Jao, C. Y., Roth, M., Welti, R. & Salic, A. Metabolic labeling and direct imaging of choline phospholipids in vivo. *Proceedings of the National Academy of Sciences* **106**, 15332–15337 (2009).

13.   Jao, C. Y., Roth, M., Welti, R. & Salic, A. Biosynthetic Labeling and Two-Color Imaging of Phospholipids in Cells. *ChemBioChem* **16**, 472–476 (2015).

14.   Garrido, M., Abad, J. L., Fabriàs, G., Casas, J. & Delgado, A. Azide-Tagged Sphingolipids: New Tools for Metabolic Flux Analysis. *ChemBioChem* **16**, 641–650 (2015).

15.   Jao, C. Y. *et al.* Bioorthogonal Probes for Imaging Sterols in Cells. *ChemBioChem* **16**, 611–617 (2015).

16.   Hofmann, K. *et al.* A novel alkyne cholesterol to trace cellular cholesterol metabolism and localization. *Journal of Lipid Research* **55**, 583–591 (2014).

17.   Rakers, L. *et al.* Addressable Cholesterol Analogs for Live Imaging of Cellular Membranes. *Cell Chemical Biology* **25**, 952–961 (2018).

18.   Hang, H. C., Wilson, J. P. & Charron, G. Bioorthogonal Chemical Reporters for Analyzing Protein Lipidation and Lipid Trafficking. *Acc Chem Res* **44**, 699–708 (2011).

19.   Liang, D. *et al.* A real-time, click chemistry imaging approach reveals stimulus-specific subcellular locations of phospholipase D activity. *Proceedings of the National Academy of Sciences* **116**, 15453–15462 (2019).

20.   Pérez, A. J. & Bode, H. B. "Click Chemistry" for the Simple Determination of Fatty-Acid Uptake and Degradation: Revising the Role of Fatty-Acid Transporters.

ChemBioChem **16**, 1588–1591 (2015).

21. Suazo, K. F., Park, K.-Y. & Distefano, M. D. A Not-So-Ancient Grease History: Click Chemistry and Protein Lipid Modifications. *Chemical Reviews* **121**, 7178–7248 (2021).

22. Rigolot, V., Biot, C. & Lion, C. To View Your Biomolecule, Click inside the Cell. *Angewandte Chemie International Edition* **60**, 23084–23105 (2021).

23. van Geel, R., Pruijn, G. J. M., van Delft, F. L. & Boelens, W. C. Preventing Thiol-Yne Addition Improves the Specificity of Strain-Promoted Azide–Alkyne Cycloaddition. *Bioconjugate Chemistry* **23**, 392–398 (2012).

24. Blackman, M. L., Royzen, M. & Fox, J. M. Tetrazine ligation: fast bioconjugation based on inverse-electron-demand Diels-Alder reactivity. *J Am Chem Soc* **130**, 13518–13519 (2008).

25. Devaraj, N. K., Weissleder, R. & Hilderbrand, S. A. Tetrazine-Based Cycloadditions: Application to Pretargeted Live Cell Imaging. *Bioconjug Chem* **19**, 2297–2299 (2008).

26. Oliveira, B. L., Guo, Z. & Bernardes, G. J. L. Inverse electron demand Diels–Alder reactions in chemical biology. *Chem. Soc. Rev.* **46**, 4895–4950 (2017).

27. Row, R. D. & Prescher, J. A. Constructing New Bioorthogonal Reagents and Reactions. *Acc Chem Res* **51**, 1073–1081 (2018).

28. Erdmann, R. S. *et al.* Super-Resolution Imaging of the Golgi in Live Cells with a Bioorthogonal Ceramide Probe. *Angewandte Chemie International Edition* **53**, 10242–10246 (2014).

29. Erdmann, R. S., Toomre, D. & Schepartz, A. STED Imaging of Golgi Dynamics with Cer-SiR: A Two-Component, Photostable, High-Density Lipid Probe for Live Cells. *Methods in molecular biology (Clifton, N.J.)* **1663**, 65–78 (2017).

30. Oliveira, B. L. *et al.* A Minimal, Unstrained S-Allyl Handle for Pre-Targeting Diels–Alder Bioorthogonal Labeling in Live Cells. *Angewandte Chemie International Edition* **55**, 14683–14687 (2016).

31. Yang, J., Šečkutė, J., Cole, C. M. & Devaraj, N. K. Live-Cell Imaging of Cyclopropene Tags with Fluorogenic Tetrazine Cycloadditions. *Angewandte Chemie International Edition* **51**, 7476–7479 (2012).

32. Patterson, D. M., Nazarova, L. A., Xie, B., Kamber, D. N. & Prescher, J. A. Functionalized Cyclopropenes As Bioorthogonal Chemical Reporters. *Journal of the American Chemical Society* **134**, 18638–18643 (2012).

33. Sauer, J. & Heinrichs, G. Kinetik und umsetzungen von 1.2.4.5-tetrazinen mit winkelgespannten und elektronenreichen doppelbindungen. *Tetrahedron Letters* **7**, 4979–4984 (1966).

34. Dowd, P. & Gold, A. The thermal dimerization of cyclopropene. *Tetrahedron Letters* **10**, 85–86 (1969).

35. Cole, C. M., Yang, J., Šečkutė, J. & Devaraj, N. K. Fluorescent Live-Cell Imaging of Metabolically Incorporated Unnatural Cyclopropene-Mannosamine Derivatives. *ChemBioChem* **14**, 205–208 (2013).

36. Morel, O. *et al.* REPRISAL: mapping lignification dynamics using chemistry, data segmentation, and ratiometric analysis. *Plant Physiology* **188**, 816–830 (2022).

37. Šečkutė, J., Yang, J. & Devaraj, N. K. Rapid oligonucleotide-templated fluorogenic tetrazine ligations. *Nucleic Acids Research* **41**, e148–e148 (2013).

38. Nunn, J. R. The structure of sterculic acid. *Journal of the Chemical Society (Resumed)* 313–318 (1952) doi:10.1039/jr9520000313.

39. Ahmad, M. U., Ali, S. M., Ahmad, A., Sheikh, S. & Ahmad, I. Chapter 5 - Carbocyclic Fatty Acids: Chemistry and Biological Properties. in (ed. Ahmad, M. U. B. T.-F. A.) 147–185 (AOCS Press, 2017). doi:https://doi.org/10.1016/B978-0-12-809521-8.00004-0.

40. Greenberg, A. & Harris, J. Cyclopropenoid fatty acids. *Journal of Chemical Education* **59**, 539 (1982).

41. Kumar, P. *et al.* Lipidated cyclopropenes via a stable 3-N spirocyclopropene scaffold. *Tetrahedron Letters* **59**, 3435–3438 (2018).

42. Hu, Y. & Schomaker, J. M. Recent Developments and Strategies for Mutually Orthogonal Bioorthogonal Reactions. *ChemBioChem* **22**, 3254–3262 (2021).

43. Willems, L. I. *et al.* Triple Bioorthogonal Ligation Strategy for Simultaneous Labeling of Multiple Enzymatic Activities. *Angewandte Chemie International Edition* **51**, 4431–4434 (2012).

44. Simon, C. *et al.* One, Two, Three: A Bioorthogonal Triple Labelling Strategy for Studying the Dynamics of Plant Cell Wall Formation In Vivo. *Angewandte Chemie International Edition* **57**, 16665–16671 (2018).

45. Chio, T. I., Gu, H., Mukherjee, K., Tumey, L. N. & Bane, S. L. Site-Specific Bioconjugation and Multi-Bioorthogonal Labeling via Rapid Formation of a Boron–Nitrogen Heterocycle. *Bioconjugate Chemistry* **30**, 1554–1564 (2019).

46. Bakkum, T. *et al.* Bioorthogonal Correlative Light-Electron Microscopy of Mycobacterium tuberculosis in Macrophages Reveals the Effect of Antituberculosis Drugs on Subcellular Bacterial Distribution. *ACS Central Science* **6**, 1997–2007 (2020).

47. Bertheussen, K. *et al.* Live-Cell Imaging of Sterculic Acid—a Naturally Occurring 1,2-Cyclopropene Fatty Acid—by Bioorthogonal Reaction with Turn-On Tetrazine-Fluorophore Conjugates. *Angewandte Chemie International Edition* **61**, (2022).

48. Beliu, G. *et al.* Bioorthogonal labeling with tetrazine-dyes for super-resolution microscopy. *Communications Biology* **2**, 261 (2019).

49. Wieczorek, A., Werther, P., Euchner, J. & Wombacher, R. Green- to far-red-emitting fluorogenic tetrazine probes – synthetic access and no-wash protein imaging inside living cells. *Chemical Science* **8**, 1506–1510 (2017).

50. Yang, J., Liang, Y., Šečkutė, J., Houk, K. N. & Devaraj, N. K. Synthesis and Reactivity Comparisons of 1-Methyl-3-Substituted Cyclopropene Mini-tags for Tetrazine Bioorthogonal Reactions. *Chemistry – A European Journal* **20**, 3365–3375 (2014).

51. Devaraj, N. K., Hilderbrand, S., Upadhyay, R., Mazitschek, R. & Weissleder, R. Bioorthogonal Turn-On Probes for Imaging Small Molecules inside Living Cells. *Angewandte Chemie International Edition* **49**, 2869–2872 (2010).

52. Carlson, J. C. T., Meimetis, L. G., Hilderbrand, S. A. & Weissleder, R. BODIPY–Tetrazine Derivatives as Superbright Bioorthogonal Turn-on Probes. *Angewandte Chemie International Edition* **52**, 6917–6920 (2013).

53. Karver, M. R., Weissleder, R. & Hilderbrand, S. A. Synthesis and Evaluation of a Series of 1,2,4,5-Tetrazines for Bioorthogonal Conjugation. *Bioconjugate Chemistry* **22**, 2263–2270 (2011).

54. Simon, C. *et al.* EPR imaging of sinapyl alcohol and its application to the study of plant cell wall lignification. *Chemical Communications* **57**, 387–390 (2021).

55. Knall, A.-C., Hollauf, M. & Slugovc, C. Kinetic studies of inverse electron demand Diels–Alder reactions (iEDDA) of norbornenes and 3,6-dipyridin-2-yl-1,2,4,5-tetrazine. *Tetrahedron Letters* **55**, 4763–4766 (2014).

56. Chi, W. *et al.* A unified fluorescence quenching mechanism of tetrazine-based

fluorogenic dyes: energy transfer to a dark state. Materials Chemistry Frontiers 5, 7012–7021 (2021).

57.   Shen, Z., Reznikoff, G., Dranoff, G. & Rock, K. L. Cloned dendritic cells can present exogenous antigens on both MHC class I and class II molecules. The Journal of Immunology 158, 2723–2730 (1997).

58.   van Leeuwen, T. et al. Bioorthogonal protein labelling enables the study of antigen processing of citrullinated and carbamylated auto-antigens. RSC Chemical Biology 2, 855–862 (2021).

59.   Grimm, J. B. & Lavis, L. D. Caveat fluorophore: an insiders' guide to small-molecule fluorescent labels. Nature Methods 19, 149–158 (2022).

60.   Hapuarachchige, S. et al. Design and synthesis of a new class of membrane-permeable triazaborolopyridinium fluorescent probes. Journal of the American Chemical Society 133, 6780–6790 (2011).

61.   Grevengoed, T. J., Klett, E. L. & Coleman, R. A. Acyl-CoA metabolism and partitioning. Annual review of nutrition 34, 1–30 (2014).

62.   Casares, D., Escribá, P. V & Rosselló, C. A. Membrane Lipid Composition: Effect on Membrane and Organelle Structure, Function and Compartmentalization and Therapeutic Avenues. International Journal of Molecular Sciences vol. 20 2167 Preprint at (2019).

63.   Moessinger, C. et al. Two different pathways of phosphatidylcholine synthesis, the Kennedy Pathway and the Lands Cycle, differentially regulate cellular triacylglycerol storage. BMC Cell Biology 15, 43 (2014).

64.   Smeenk, M. L. W. J., Agramunt, J. & Bonger, K. M. Recent developments in bioorthogonal chemistry and the orthogonality within. Curr Opin Chem Biol 60, 79–88 (2021).

65.   Chehrehasa, F., Meedeniya, A. C. B., Dwyer, P., Abrahamsen, G. & Mackay-Sim, A. EdU, a new thymidine analogue for labelling proliferating cells in the nervous system. Journal of Neuroscience Methods 177, 122–130 (2009).

66.   Peláez, R., Pariente, A., Pérez-Sala, Á. & Larráyoz, I. M. Sterculic Acid: The Mechanisms of Action beyond Stearoyl-CoA Desaturase Inhibition and Therapeutic Opportunities in Human Diseases. Cells vol. 9 140 Preprint at (2020).

67.   van Onzen, A. H. A. M. et al. Bioorthogonal Tetrazine Carbamate Cleavage by Highly Reactive trans-Cyclooctene. Journal of the American Chemical Society 142, 10955–10963 (2020).

3

Global Identification of Protein Oleoylation in Dendritic Cells by Pull-Down Chemical Proteomics

Abstract

Protein lipidation is a cellular process which increases protein diversity, and is important for correct protein function, signalling, transportation, and regulation. Protein lipidation has also been shown to be necessary for the correct functioning of the innate and adaptive immune responses. By incorporating a bioorthogonal modification in the fatty acyl chain of fatty acids, global protein lipidation patterns can be studied. In this Chapter, sterculic acid (StA) is used as a bioorthogonal probe to study protein oleoylation (the modification of proteins with oleic acid) in dendritic cell line DC2.4. A library of tetrazine-modified biotin molecules was synthesised and tested for their cell-permeability and reactivity with StA. Here, tetrazines **17** and **19** were identified as cell-permeable and were compared to biotin-PEG4-tetrazine in a pull-down chemical proteomics approach. Different proteins were identified as oleoylated with the three compounds. It is suggested that the physicochemical properties of the compounds, as well as spacer length between the tetrazine and biotin moieties, influence which proteins are detected. Several proteins with known immunological functions were found to be oleoylated, including proteins (e.g. SLC15A3) for which this modification had not previously been reported.

Introduction

Homo sapiens has a surprisingly low number of open reading frames (ORFs) in its genome. However, these approximately 20,000 genes form the basis for over one million proteins.[1] Multiple processes exist that increase the diversity and complexity of the proteome, compared to the original genetic information. Alternative splicing is one of these mechanisms, where a single gene can give rise to multiple mRNA transcripts, and thereby also different proteins with distinct structures and functions.[1] Proteins can also undergo various chemical modifications, which – as the name would suggest – are modifications on the peptide structure that are introduced after translation. Many distinct post-translational modifications (PTMs) exist, among others acetylation, phosphorylation, ubiquitination, glycosylation, and lipidation, and they are all important for the correct folding, function, signalling, and transportation of the modified proteins.[2]

Proteins can be modified with a number of lipids, such as fatty acids (FAs)[3], cholesterols[4], isoprenoids (such as farnesyl or geranylgeranyl)[5], or glycosylphosphatidylinositol-anchors (GPI-anchors).[6] These lipid molecules are covalently linked to cysteine, lysine, threonine, or serine sidechains, or the C- or N-terminus of the protein, via thioester, amide, thioether, or ether linkages.[2,7] Protein lipidation is associated with increased hydrophobicity of the target protein, which can be essential for regulating protein configuration, trafficking, stability, and localisation. Due to their increased hydrophobicity, lipidated proteins are often associated with biological membranes, where the lipid tail is embedded in the lipid bilayer.[7]

Protein lipidation, and especially the reversible S-palmitoylation modification, has been implicated in several functions in both innate and adaptive immunity, where it is responsible for the clustering of various important immune molecules to cellular membranes.[8] In innate immunity it has been shown that S-palmitoylation is important for the correct function and localisation of important innate immune receptors such as Toll-like receptor 2 (TLR2)[9], and MyD88 (a signalling adapter protein for TLRs).[10] Stimulator of interferon genes (STING) is a signalling protein that is involved in the immune response to DNA in the cytosol. Upon activation, STING is also S-palmitoylated, which leads to the activation of nuclear factor-κB (NF-κB) and interferon regulator factor 3 (IRF3), which in turn results in the production of proinflammatory cytokines and type-I interferons.[11]

There are also several examples of the importance of S-palmitoylation in the T-cell receptor (TCR) signal transduction pathway of adaptive immunity.[12] It has been shown that TCR coreceptors CD4 and CD8 are S-palmitoylated, and that this is necessary for the correct clustering of the TCR complex and downstream signalling subunits (such as Src family protein tyrosine kinase Lck).[13–15] Lck itself can also be S-palmitoylated, a PTM that is required for its correct plasma membrane localisation, CD4 association, and downstream signalling.[16–18]

Although these examples emphasize the importance of S-palmitoylation as an immunomodulating regulator, a proteome-wide understanding of how protein lipidation affects immune cell function, and activation, is still lacking. There is also little information about other forms of protein lipidation, and how they affect immune cell function. To elucidate this intricate balance on a global level, appropriate

chemical tools are needed that allow the selective retrieval of the lipidated part of the proteome under different biological conditions.

Bioorthogonal, or click, chemistry could serve this purpose.[2] Most bioorthogonal modifications of lipids have been applied to the modification of lipid headgroups. This offers selectivity for which lipid class the analogue will be incorporated into. There have e.g. been reports of the phospholipid class phosphatidylcholine (PC) being labelled in this way.[19] *De novo* PC biosynthesis occurs via the Kennedy pathway, where an activated choline molecule is coupled to diacylglycerol to form PC. The alkyne- and azide-containing choline analogues propargylcholine[20] and azidocholine[21], respectively, have successfully and selectively been shown to label up to 50% of the cellular pool of PC (Figure 1A).

However, since lipids react with proteins via their hydrophilic head groups, a modification in that part of the molecule will result in an impaired ability to lipidate proteins. To this end, strategies where the bioorthogonal modifications are instead located in the fatty acyl chain have been developed.[2] Perhaps the most studied bioorthogonal variants of this sort, are lipids modified with an alkyne[9,22–29] or azide[30–34] moiety at the ω-position of the fatty acyl chain (Figure 1B). This ensures a more global labelling of cellular lipids such as triglycerides, phospholipids, and glycolipids. However, these modifications also allow the study of different forms of protein lipidation (e.g. palmitoylation, myristoylation, or prenylation).[2] This approach has aided in the discovery of many new palmitoylated proteins in mammalian cells[9,22,35,36], as well as implicating the relevance of certain palmitoylated proteins in diseases like cancer[37], and bacterial or viral infections.[38]

Far less is known about the more obscure PTM, protein oleoylation (the modification of proteins with oleic acid). This PTM has previously been studied with alkyne-modified oleic acid analogues[39], but although protein oleoylation has been shown to occur in multiple proteins[39–41], not much is known about this PTM on a proteome-wide level. In Chapter 2 of this thesis, it was described how the addition of sterculic acid (StA) to dendritic cell line DC2.4, and the subsequent labelling with tetrazine-fluorophore conjugates, led to a fluorescent signal visible throughout the entire cell. This led to the conclusion that cellular membranes (including organellar membranes) were labelled with StA. However, it also posed the question if proteins could be labelled with the oleic acid analogue, StA, as a PTM, and if this bioorthogonal oleic acid analogue could be used to study protein oleoylation by chemical proteomics in immune cells. In this Chapter, by applying a library of tetrazine-modified biotin molecules, it was found that proteins can indeed be modified with StA as a PTM. It was further shown that tetrazine-modified biotins with different physicochemical properties influenced which proteins were detected as oleoylated. In addition, the comparison of live-cell versus cell lysate labelling also yielded different protein oleoylation patterns. Interestingly, several of the detected proteins are known to have key immunological functions, for example, the important immunoregulatory channel protein SLC15A3 was found to be differentially oleylated in these experiments. SLC15A3 has never been shown to be lipidated before, and therefore a novel regulatory mechanism of this protein involving protein oleoylation, is proposed.

A) Bioorthogonal modification in lipid head group
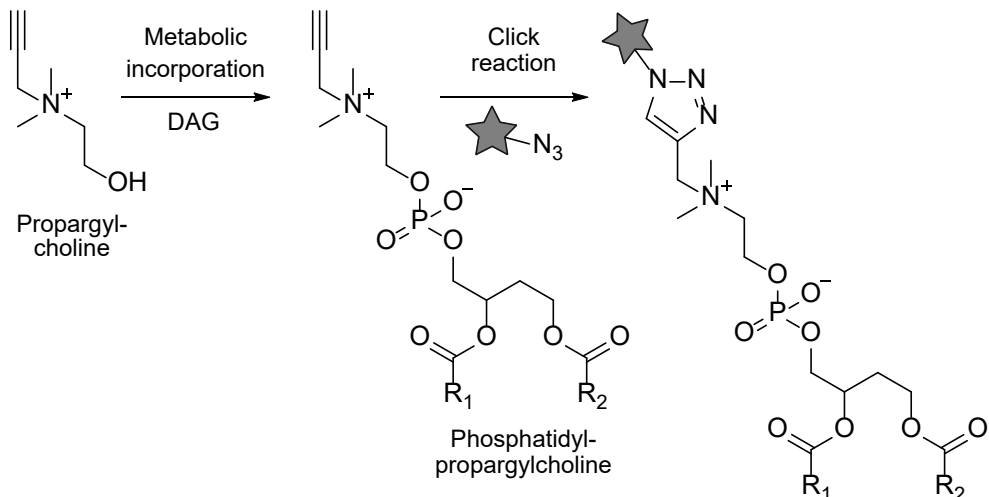
B) Bioorthogonal modification in fatty acyl chain
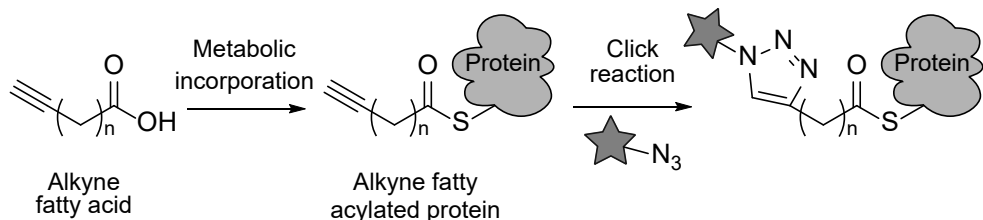
*Figure 1: Bioorthogonal modifications present in **A)** the lipid head group; allow for the metabolic incorporation of for example propargylcholine, which upon reaction with diacylglycerol (DAG) forms phosphatidylpropargylcholine, and subsequent labelling via a click reaction with an azide-tagged reporter group (star)[20], or **B)** the fatty acyl chain; allow for the metabolic incorporation of an alkyne-tagged fatty acid into a fatty acylated protein, and subsequent labelling via a click reaction with an azide-tagged reporter group (star).[9,22–29]*

Results & Discussion

Proteins can be modified with sterculic acid at a post-translational level

Here, it was first explored whether proteins can be covalently modified with StA as a PTM. DC2.4 cells were incubated with StA followed by cell lysis and click reaction with the cell-impermeable tetrazine-modified fluorophore **3** (Figure S1A, see Chapter 2). The proteins were resolved by SDS-PAGE, and the gel was fluorescently imaged (Figure 2A). However, since lipidated proteins are inherently more hydrophobic[42], and the lipid tail often resides in biological membranes[43], a live-cell click approach with the cell-permeable quenched tetrazine-modified fluorophore **7** (Figure S1B, see

Chapter 2) was also performed. In this approach, the hydrophobic fluorophore **7** could pass through cell membranes and react with the lipid in its naturally occurring location, whereafter the cells were lysed, and the proteins were resolved by SDS-PAGE (Figure 2B). In both cases fluorescent protein bands were visible. This indicates that a number of proteins were covalently modified with StA. Comparing the two approaches, it was clear that which proteins were labelled, differed under the different labelling conditions (lysate or on live cells), as indicated by the distinct labelling patterns. Upon LPS stimulation, the lipidation patterns appeared to become brighter compared to lipidation of non-stimulated DCs (Figure 2). This could indicate that protein lipidation is increased upon DC maturation but could also be caused by an increased uptake of StA by the mature DCs and subsequently more labelling of proteins by this FA analogue compared to native FAs.
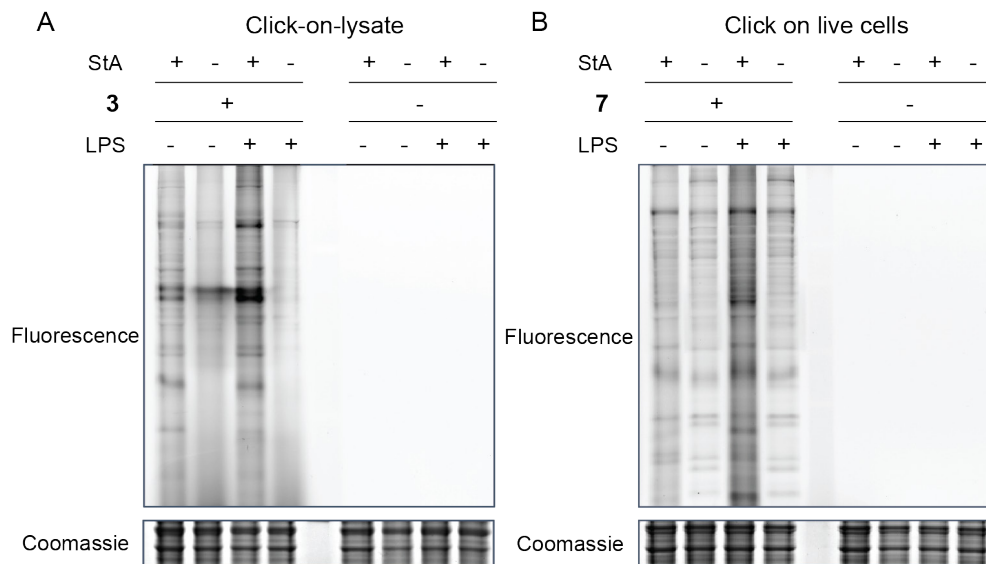
Figure 2: Proteins can be modified with sterculic acid (StA) as a post-translational modification. DC2.4 cells were immature or matured with LPS (100 ng/mL) for 24 h and treated with StA (100 μM) for 20 h. A) The cells were harvested and lysed before IEDDA reaction with tetrazine-modified fluorophore 3 (10 μM) or vehicle for 2 h at RT. B) Live cells were subjected to IEDDA reaction with tetrazine-modified fluorophore 7 (10 μM) for 2 h at 37°C, before being harvested and lysed. All lysates were resolved on SDS-PAGE (12.5% acrylamide gels) and were measured for in-gel fluorescence. Coomassie staining served as a protein loading control.

Chemical synthesis of library of tetrazine-modified biotin molecules

To further investigate these observed differences in lipidation pattern, a pull-down chemical proteomics approach was developed (Figure 3). A set of tetrazine-modified biotin molecules were designed and synthesised (as described below), which could be applied for the click reaction with StA. After StA uptake in DC2.4 cells (Figure 3A), the different tetrazine-modified biotins were added to the samples at different points in the protocol, either to the live cells or to the cell lysate (Figure 3B). The tetrazine

moiety could react with StA, whereas the biotin moiety allowed for pull-down of the lipidated proteins with streptavidin beads, followed by on-bead trypsin digestion and identification of the peptides by LC-MS/MS (Figure 3C). Thereby proteins that were modified with StA as a PTM could be quantitatively identified.
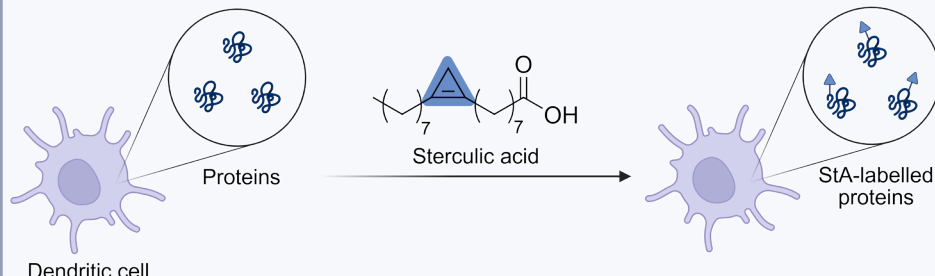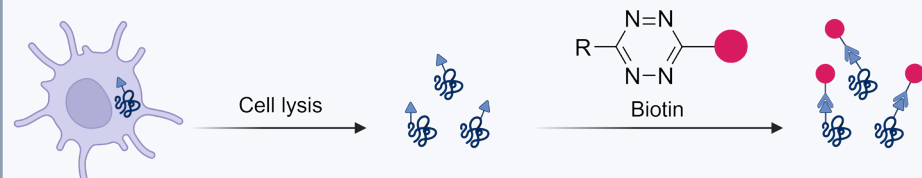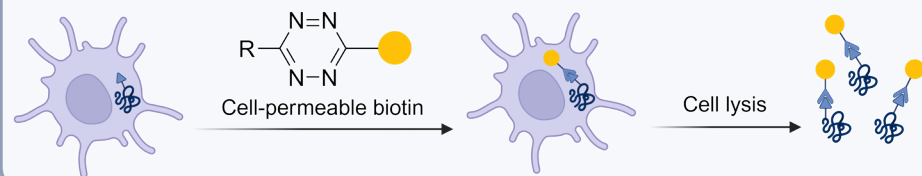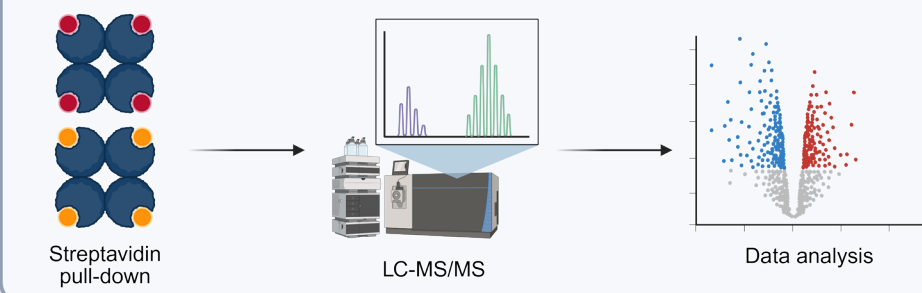
Figure 3: Illustration of the pull-down proteomics approach to study protein lipidation with sterculic acid (StA) in a dendritic cell line (DC2.4). The approach consists of A) StA labelling of proteins, followed by B) click reaction with tetrazine-modified biotins in lysate (1) or on live cells (2), and C) pull-down proteomics. The figure is made with BioRender.

To this end, several hydrophobic tetrazine-modified biotins (**16**-**21** and **29**-**31**) were synthesised (Scheme 1) and compared to the hydrophilic biotin-PEG4-tetrazine (Figure S1C) for their cell permeability under live cell conditions. For **16**-**21** and **29**-**31**, two different spacer lengths were chosen between the tetrazine and biotin moieties. One contains only the valeric acid moiety of biotin and is a short spacer (Biotin, Scheme 1). The other spacer contains an additional lysine group and is a medium length (LC-Biotin, Scheme 1). The synthesis of **16**-**21** (Scheme 1A) was based on the synthesis of previously published BODIPY-FL tetrazine conjugates.[44,45] Instead of the BODIPY fluorophores, a biotin moiety was coupled to the amine function of the tetrazines.

The synthetic route started from 4-(aminomethyl) benzonitrile of which the free amine was protected with a *tert*-butyloxycarbonyl (Boc) group using di-*tert*-butyl dicarbonate and DIPEA, yielding compound **9**. This compound was converted into *N*-Boc-protected aminoalkyl-tetrazines **10**-**12** by a Lewis acid-catalysed condensation of the nitrile with hydrazine, followed by oxidation with sodium nitrite under acidic conditions.[46] The protected amine of tetrazines **10**-**12** was deprotected using HCl/dioxane, and tetrazines **13**-**15** were immediately coupled to either the commercially available biotin or LC-biotin via an NHS coupling, resulting in tetrazine-modified biotins **16**-**21**. These compounds were all poorly soluble in DMSO, with solubility decreasing with increasing spacer length (**19**-**21**). Compounds **16**-**21** were attempted dissolved at 30 mM (in DMSO), but only **16**-**18** were soluble at this concentration. Compounds **19**-**21** were first soluble in DMSO at 10 mM concentrations.

To improve the solubility of these compounds, another set of tetrazine-modified biotins (**29**-**31**) were designed and synthesised (Scheme 1B). These compounds lacked the benzylic ring of **16**-**21** in an attempt to increase their solubility, while still retaining their cell-permeability. This synthetic route started with the Boc-protection of 3-aminopropionitrile to form **22**. Thereafter, similarly to the previous synthesis, the conversion into *N*-Boc-protected aminoalkyl-tetrazines **23**-**25**, followed by deprotection into tetrazines **26**-**28**, was performed. Lastly, an NHS coupling to biotin resulted in the tetrazine-modified biotins **29**-**31**. As expected, the solubility of these compounds had improved compared to that of **16**-**21**.

A
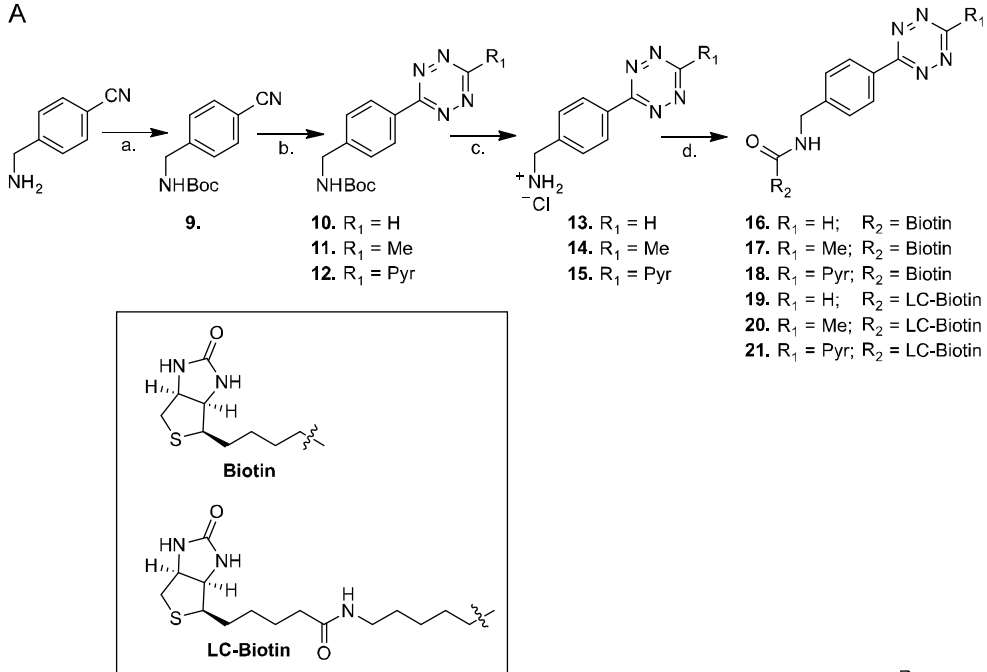
B
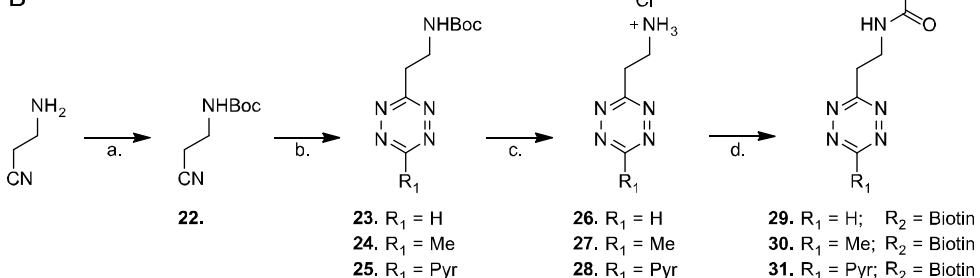
Scheme 1: *The synthesis of hydrophobic tetrazine-modified biotins* **16-21** *and* **29-31**. **A)** *a)* *Boc$_2$O, NaOH, H$_2$O, quant.; b) I) hydrazine monohydrate, Zn(OTf)$_2$, formamidine acetate/ acetonitrile/2-cyanopyridine, 60-80°C; II) NaNO$_2$, AcOH/DCM (1:1, v:v), 9-33% over two steps; c) 4 M HCl in dioxane, anhydrous DCM, 90-100%.; d) NHS-biotin/NHS-LC-biotin, DIPEA, DCM, 40-73%. **B)** a) Boc$_2$O, anhydrous DCM, 98%; b) I) hydrazine monohydrate, Zn(OTf)$_2$/ Ni(OTf)$_2$, formamidine acetate/acetonitrile/2-cyanopyridine, 20-60°C; II) NaNO$_2$, AcOH/DCM (1:1, v:v) or 4 M NaNO$_2$, 2 M HCl, 2-22%; c) 4 M HCl in dioxane, anhydrous DCM, 93-100%; d) NHS-biotin, DIPEA, DCM, 38%-73%.*

Testing permeability and reactivity of tetrazine-modified biotin library

To verify if the tetrazine-modified biotins were cell-permeable and could react with StA, live DC2.4 cells preloaded with StA were reacted with **16**-**21**, **29**-**31**, or biotin-PEG4-tetrazine. After the click reaction, any unreacted compound was washed away, and the cells were fixed and permeabilised. The addition of a streptavidin AZDye 647 conjugate was used to fluorescently label the biotin molecules that had entered the cells and reacted with StA. Lastly, the cells were imaged by fluorescence widefield microscopy (Figures 4 & S2).
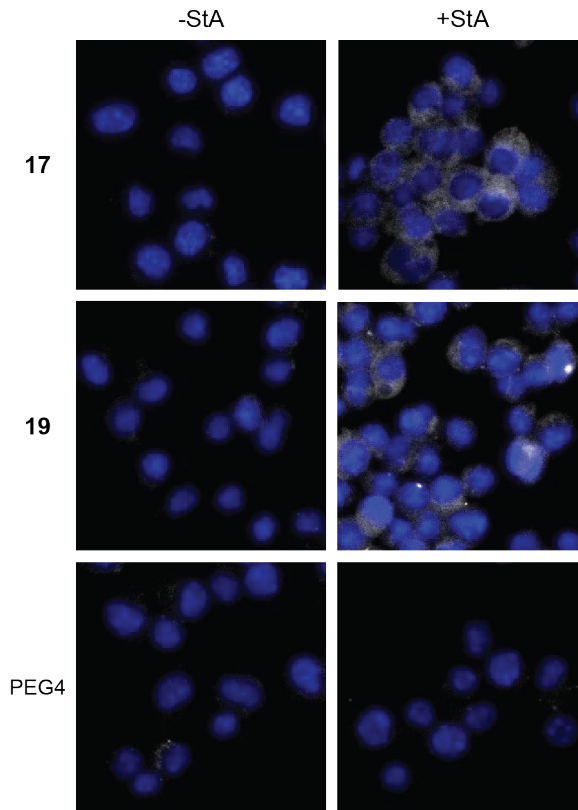
Figure 4: Fluorescent microscopy verifies that compounds *17* and *19* are cell-permeable and reactive with StA. Biotin-PEG4-tetrazine (PEG4) is used as a negative control. To allow uptake of the fatty acid, DC2.4 cells were incubated with sterculic acid (+StA, 100 µM) or vehicle control (-StA) for 1 h. The respective tetrazine-modified biotins (200 µM) were then added and incubated for 4 h, before unreacted compound was washed away. The cells were fixed and permeabilised, and a streptavidin AZDye 647 conjugate (grey) was added to visualise the location of the reacted biotins. The nuclei were counterstained with Hoechst 33342 (blue) for reference.

Compounds **17** and **19** showed detectable labelling over background, indicating that these two compounds are cell-permeable and able to react with StA. As expected, biotin-PEG4-tetrazine showed no signal in live cells, likely due to its hydrophilic PEG-spacer making it cell-impermeable (Figure 4). The rest of the compounds did

not show detectable labelling over background in live cells (Figure S2), indicating that these compounds are either cell-impermeable, or unable to react with StA.

The click reaction with the tetrazine-modified biotins **16-21** and **29-31** was also performed on fixed and permeabilised cells. The rationale was that the cell permeation with detergent after fixation would negate any cell-permeability factors for the probes. Therefore, a fluorescent signal would be expected from all compounds that can react with StA (Figure S3). Compounds **17** and **19**, as well as biotin-PEG4-tetrazine, showed detectable labelling over background. In addition, **29** and **30** showed labelling in the StA sample, indicating that they are StA reactive. Control samples showed no labelling of StA in live and fixed cells if the tetrazine-modified biotins were not present (Figures S4 & S5), as well as if the compounds were added and immediately washed away (Figures S6 & S7). This indicates that true signal-over-background was observed in Figures 4, S2, and S3. Based on these results, compounds **17** and **19** were credited with sufficient cell-permeability and StA reactivity qualities for further proteomic analysis.

Identification of oleoylated proteins with mass spectrometry

Compounds **17** and **19** were selected for the live-cell approach of pull-down chemical proteomics (outlined in Figure 3). However, due to the precious nature of these compounds, the mass spectrometry methodology was first optimised on lysates with biotin-PEG4-tetrazine. To this end, LPS-matured or untreated immature DC2.4 cells were incubated with StA to allow for its incorporation as a PTM. After cell lysis, the click reaction with biotin-PEG4-tetrazine was performed, and the modified proteins could be isolated with streptavidin beads. After on-bead enzymatic digestion, peptides from the lipidated proteins were detected by mass spectrometry and analysed. When biotin-PEG4-tetrazine was applied in this click-on-lysate approach in immature DC2.4 cells, 242 proteins were identified as significantly enriched with StA (Figure 5A), compared to control. For mature DC2.4 cells that were stimulated with LPS, 246 significantly enriched proteins were detected over control (Figure 5B). The UniProt protein database categorises protein entries into specific subsets based on for example biological function or cellular localisation.[47] As annotated by UniProt keyword KW-0472 77 (32%) and 83 (34%), respectively, of the identified proteins are known to be membrane proteins.

When comparing the StA-enriched proteins between LPS-treated mature and untreated immature DCs, 3 proteins were significantly enriched in the mature DC samples, and 2 proteins in the immature sample (Figure 5C). It is not clear whether these proteins are detected due to changes in their expression levels, increased protein lipidation, or a combination of these two factors. However, of the upregulated proteins, two (CD14[48,49], SLC15A3[50–52]) are known to be upregulated upon LPS stimulation, but nothing has been reported on their change in lipidation status. The downregulated protein TMEM176B, has also previously been shown to be downregulated in DCs upon LPS stimulation.[53,54] These results validate the described method as a robust way to study protein lipidation as a PTM, and again indicates that StA can be incorporated as a PTM in proteins.
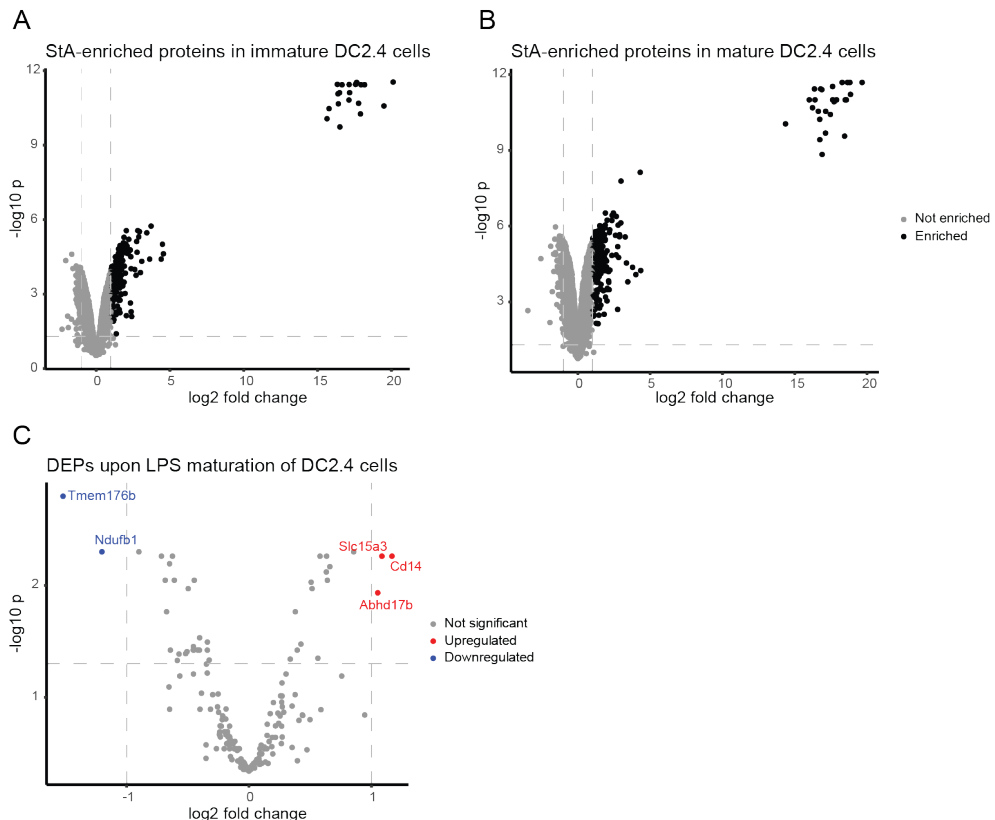
Figure 5: *Proteomic analysis of proteins modified with sterculic acid (StA) in DC2.4 cells by chemical proteomics. DC2.4 cells were immature or matured with LPS (100 ng/mL) for 24 h and treated with StA (10 µM) for 20 h. The cells were harvested and lysed, before IEDDA reaction with biotin-PEG4-tetrazine (200 µM) on the lysate. Shown are volcano plots of proteins identified in pull-down experiments in **A)** immature DC2.4 cells. **B)** LPS-matured DC2.4 cells. Proteins with a fold change >2 and p-value <0.05 are considered specifically enriched and are highlighted in black. **C)** Differentially StA-expressed proteins (DEPs) between mature and immature DC2.4 cells. LFQ-values of StA-enriched proteins were compared and proteins with significantly higher or lower LFQ abundance between the two conditions are marked in red and blue, respectively.*

Next, the pulldown protocol was applied to live cell labelling. Mature and immature DCs were labelled with StA for 20 hours at 10 µM, prior to the addition of **17** and **19**, followed by lysis, streptavidin-mediated retrieval, and mass spectrometry. For compound **17**, only 6 proteins were found to be StA-enriched in immature DCs (Figure 6A) and 10 proteins were found to be StA-enriched in mature DCs (Figure 6B). Of the enriched proteins, 2 (33%) and 2 (20%) proteins, respectively, were known membrane proteins (as annotated by UniProt keyword KW-0472[47]). Surprisingly, a completely different set of proteins than with the click-on-lysate approach with biotin-PEG4-tetrazine was retrieved for compound **17** in both mature and immature DCs (Table S1 & Figure S8).

For compound **19**, 11 proteins were found to be StA-enriched in immature DCs (Figure 6C) and 17 proteins were found to be StA-enriched in mature DCs (Figure 6D). Of the enriched proteins, 8 (73%) and 13 (76%) proteins, respectively, are known to be membrane proteins (as annotated by UniProt keyword KW-0472[47]). Only two proteins that were found to be significantly StA-enriched with **19** in immature DCs, were also detected with biotin-PEG4-tetrazine, whereas three common proteins were found in mature DCs (Table S1 & Figure S8).
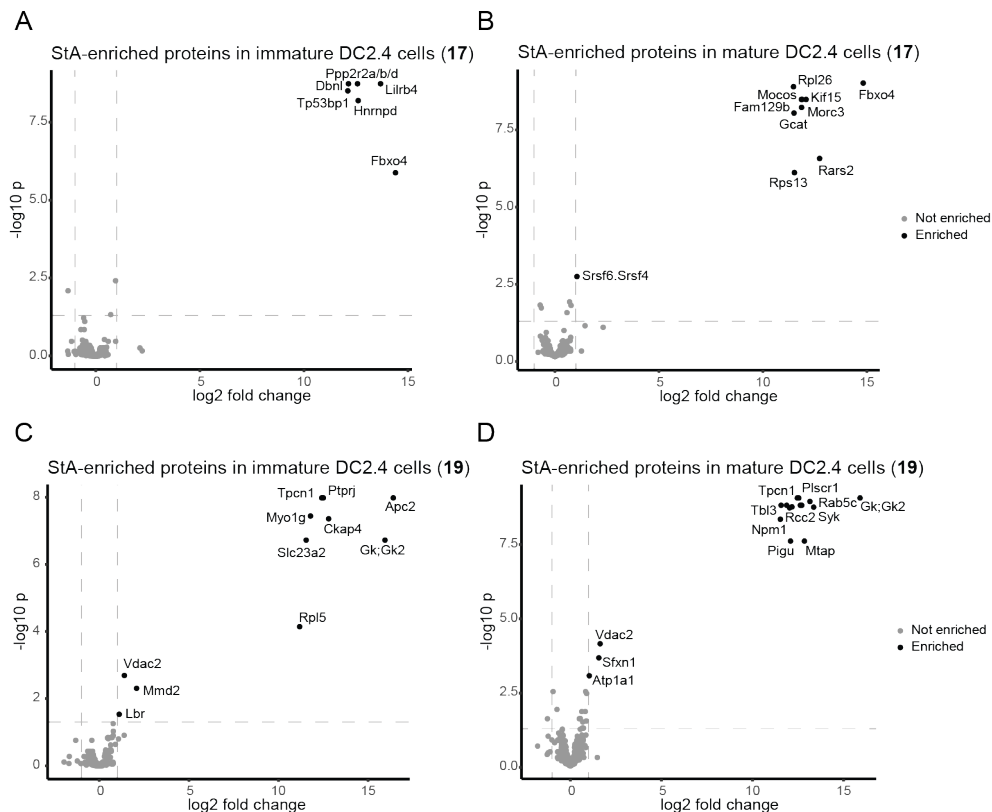

Figure 6: *Proteomic analysis of proteins modified with sterculic acid (StA) in DC2.4 cells by chemical proteomics. DC2.4 cells were immature or matured with LPS (100 ng/mL) for 24 h and treated with StA (10 μM) for 20 h. IEDDA reaction with **17** or **19** (200 μM) was performed on live cells, before the cells were harvested and lysed. Shown are volcano plots of proteins identified in pull-down experiments in **A)** immature DC2.4 cells with compound **17**. **B)** LPS-matured DC2.4 cells with compound **17**. **C)** immature DC2.4 cells with compound **19**. **D)** LPS-matured DC2.4 cells with compound **19**. All proteins with a fold change >2 and p-value <0.05 are considered specifically enriched and are highlighted in black.*

The lower numbers of StA-enriched proteins that were detected with the live-cell approach compared to the click-on-lysate approach could be caused by the need for **17** and **19** to diffuse through intact cells before encountering StA-lipidated proteins. It could also be affected by the hydrophobicity and poor solubility of the cell-permeable compounds **17** and **19**, causing them to be sticky. This could lead to more unspecific binding events, and thereby more noise in the MS data. In addition, the spacer

lengths between the biotin and tetrazine moieties in **17** (~13 Å) and **19** (~22 Å) are considerably shorter than the PEG4 spacer (~29 Å) of biotin-PEG4-tetrazine. These shorter spacers could lead to steric hindrance when the biotin-labelled proteins bind to the tetrameric streptavidin beads, impacting the number of proteins that can be pulled out. However, since the longer spacer in **19** also led to poorer solubility of the compound, further research is needed to fine-tune this relationship between solubility, cell-permeability, and spacer length.

The low amount of overlap between proteins detected with compound **19** and biotin-PEG4-tetrazine could indicate that tetrazine-modified biotins with different physicochemical properties might be preferential for certain proteins. As annotated by UniProt keyword KW-0472[47], ~75% of the proteins that were found to be StA-enriched with **19**, are known to be bound to or associated with membranes. For biotin-PEG4-tetrazine only ~30-35% of the StA-enriched proteins are known to be membrane proteins. Since membrane proteins generally are more hydrophobic than soluble proteins[42], and StA is likely embedded in the membrane as a lipid anchor[43], it could be that the more hydrophobic tetrazine-modified biotin (**19**) is more likely to react with these proteins. However, for compound **17** which is also more hydrophobic, only ~20-30% of the StA-enriched proteins are membrane proteins (as annotated by UniProt keyword KW-0472[47]). This could be explained by the shorter aliphatic linker between the hydrophilic biotin moiety and the reactive tetrazine moiety, making it more difficult for the tetrazine to reach StA embedded in the membranes. For compound **17**, a completely unique set of StA-enriched proteins were detected that were found with neither **19** nor biotin-PEG4-tetrazine, suggesting there might be an interesting application for this compound after all (Figure S8). It is not known which exact molecular properties of the tetrazine-modified biotins are responsible for the described discrepancies, and this would need to be elucidated by further research.

Previous research has highlighted an important role of protein lipidation in the regulation of a large number of immunological proteins.[8,12,55,56] From the significantly StA-enriched proteins that were detected with **17**, **19** and biotin-PEG4-tetrazine, all proteins with a reported immunological function (as annotated by UniProt keyword KW-0391[47]) are listed in Tables S2, S3, and S4, respectively. In addition, the proteins that are known to be lipidated (as annotated by UniProt keyword KW-0449[47]) or membrane proteins (as annotated by UniProt keyword KW-0472[47]) are marked. Several immunological proteins that have not been reported to be lipidated, or even membrane-bound, were identified using the described pull-down method. Most notably is SLC15A3, a transmembrane amino acid transporter located in endolysosomal membranes, that has not before been reported to be lipidated. Several recent reports have highlighted the important role of SLC15A3 in modulating anti-viral innate immune responses, among others in a TLR4-mediated inflammatory response[50], or by inducing type I and type III interferon responses via STING-mediated signalling pathways[57]. SLC15A3 has also been implicated in the escape of bacterially derived components from the endolysosomal system to the cytosol, which in turn activates the NOD2 signalling pathway.[51] SLC15A3 was also found to be upregulated in mature DCs (Figure 5C), again implicating its importance in modulating immune responses. Considering the powerful regulatory role protein lipidation can have, the oleoylation of SLC15A3 could therefore be a novel regulatory mechanism of this important immunomodulatory protein. However, the exact mechanism behind this regulation is not known, and further research is necessary to shine light on this complex interplay.

Conclusion

Here, it has been shown that proteins can be modified with StA as a PTM. This was confirmed by labelling StA-modified proteins with a fluorophore and resolving the proteins by SDS-PAGE, as well as labelling the proteins with tetrazine-modified biotins and performing pull-down chemical proteomics. A library of tetrazine-modified biotins was synthesised and assessed for their cell-permeability, as well as reactivity with StA. Two compounds (**17** and **19**) showed sufficient permeability and reactivity and were used in a live-cell click pull-down proteomics approach. This approach was compared to a click-on-lysate approach with biotin-PEG4-tetrazine. It appears that both the timing of the IEDDA reaction, and the physicochemical properties of the tetrazine-modified biotins affect which lipidated proteins are detected. The current research could not fully elucidate the underlying mechanisms of these discrepancies, and further research is needed to understand this. Several proteins with known immunological functions, that have never been reported to be lipidated, were also identified. The important innate immunoregulatory protein SLC15A3 was shown to be lipidated for the first time, indicating that this could be a regulatory mechanism for its activation.

Acknowledgements

Materials & Methods

Chemical synthesis

General

All reactions were performed using dried glassware and reagent grade solvents. All commercially available reagents used were obtained via Sigma-Aldrich and Merck and were used as received. Anhydrous solvents were prepared by keeping activated 4 Å molecular sieves in the solvents for at least 24 h. Flash chromatography was performed silica gel 60 (0.04-0.063 mm). TLC analysis was conducted on Merck aluminum sheets and silica gel 60 F254 sheets. TLC analyses were visualized using 254 nm UV absorption and by using ninhydrin staining followed by charring at ~150 ℃. ^{1}H and ^{13}C NMR spectra were recorded using the Bruker AV Liquid 400 MHz and Bruker AV WB 400 MHz spectrometer. Samples were measured in $CDCl_3$, MeOD DMSO-D_6 or D_2O. Chemical shifts (δ) are reported in ppm compared to either trimethyl silane (0 ppm) or the solvent residual peak as internal standard. Coupling constants are reported in Hz. Assigning individual signals of the final compounds was aided by HH-COSY.

9: tert-butyl (4-cyanobenzyl) carbamate
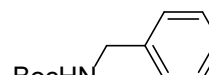
Di-tert-butyldicarbonate (22 mmol, 4.80 g, 1.1 eq) and NaOH (60 mmol, 2.40 g, 3 eq) were added to 40 mL H_2O. (4-aminomethyl)-benzonitrile (20 mmol, 3.37 g) was added and the reaction was stirred overnight at RT. The precipitate was filtered and concentrated under reduced pressure to yield compound **9** as a white solid (4.11 g, 17.7 mmol, 89%).

^{1}**H NMR** (400 MHz, $CDCl_3$) δ 7.61 (d, *J* = 8.3 Hz, 2H, CH $_{aromatic}$), 7.38 (d, *J*= 8.3 Hz, 2H, CH $_{aromatic}$), 5.03 (s, 1H, NH), 4.36 (d, *J* = 6.3 Hz, 2H, CH_2), 1.45 (s, 9H, $CH_{3\ Boc}$). ^{13}**C NMR** (101 MHz, $CDCl_3$) δ 146.8 ($C_{q\ aromatic}$), 144.7 ($C_{q\ boc\ carbonyl}$), 132.5 (CH $_{aromatic}$), 127.9 ($CH_{aromatic}$), 118.9 ($C_{q\ nitrile}$), 111.2 ($C_{q\ aromatic}$), 80.1 ($C_{q\ tbu}$), 44.3 (CH_2), 28.4-27.5 ($CH_{3\ Boc}$)

22: tert-butyl (2-cyanoethyl) carbamate
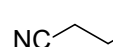
3-Amino propionitrile (10 mmol, 0.70 g) and Boc_2O (12 mmol, 2.76 mL, 1.2 eq.) were added to 20 mL anhydrous DCM. The reaction was stirred overnight at RT. The organic layer was washed with water and brine, dried over $MgSO_4$ and filtered. The organic layer was concentrated under reduced pressure to yield compound **22** as a clear oil (1.67 g, 9.8 mmol, 98%).

^{1}**H NMR** (400 MHz, $CDCl_3$) δ 5.05 (s, 1H, NH), 3.40 (q, *J* = 6.3 Hz, 2H, CH_2), 2.60 (t, *J* = 6.3 Hz, 2H, CH_2), 1.45 (d, *J* = 1.6 Hz, 9H, $CH_{3\ Boc}$). ^{13}**C NMR** (101 MHz, $CDCl_3$) δ 118.3 ($C_{q\ nitrile}$), 80.3 ($C_{q\ tBu}$), 36.9 (CH_2), 28.4-27.5 ($CH_{3\ Boc}$), 19.1 (CH_2).

General tetrazine synthesis (10-12 and 23-25)
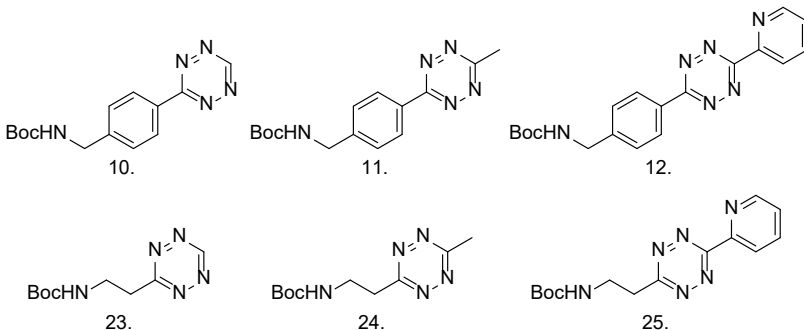
The N-Boc protected carbonitrile (compound **9** or **22**; 1 eq.) was added to a pressure tube. To this tube a Lewis acid catalyst (Zn(OTf)$_2$ or Ni(OTf)$_2$; 0.25 eq.), the corresponding carbonitrile (acetonitrile, formamidine acetate or 2-cyanopyridine; 5 eq.) and 64% hydrazine monohydrate (50 eq.) were added. If required, dry dioxane (1.6 mL/mmol) was added as an additional solvent and the pressure tube was sealed. The reaction mixture was heated and stirred overnight. After cooling down to RT the rubber seal was carefully punctured to release the NH$_3$ gas. For oxidation of the dihydrotetrazines, two different procedures were used as described below. After oxidation, column purification yielded tetrazines **10**-**12** and **23**-**25** as pink solids.

Procedure A: The suspension was slowly added to a mixture of AcOH/DCM (1:1, v:v, 20 mL/mmol). Next, NaNO$_2$ (20 eq.) was added over a period of 30 minutes. When gas formation ceased, the mixture was concentrated under reduced pressure, and the resulting mass was redissolved in EtOAc. The organic layer was washed three times with H$_2$O and three times with NaHCO$_3$ (sat.) and subsequently dried over MgSO$_4$, filtered, and concentrated in vacuo.

Procedure B: The suspension was added to an aqueous 4M NaNO$_2$ solution (80 eq., 20 mL/mmol). Next, aqueous 2M HCl (120 eq., 60 mL/mmol) was added dropwise until gas formation had ceased. The mixture was further diluted with aqueous 0.1M HCl (50 mL/mmol) was added, and the product was extracted three times with EtOAc (50 mL/mmol). The organic layer was dried over MgSO$_4$, filtered and concentrated under reduced pressure.

10: tert-butyl (4-(1,2,4,5-tetrazin-3-yl)benzyl)carbamate

Compound **9** (5 mmol, 1.16 g), Zn(OTf)$_2$ (1.25 mmol, 0.455 g, 0.25 eq) formamidine acetate (50 mmol, 5.20 g, 10 eq) and 64% hydrazine monohydrate (250 mmol, 12.1 mL, 50 eq) were used. The reaction was stirred overnight at 60°C. Oxidation procedure A was performed and column purification (1% -> 5%, EtOAc in DCM) yielded **10** as a pink solid (128 mg, 0.4 mmol, 9%).

^{1}H NMR (400 MHz, CDCl$_3$) δ 10.22 (s, 1H, tetrazine-H), 8.60 (d, J = 8.1 Hz, 2H, CH$_{aromatic}$), 7.53 (d, J = 8.1 Hz, 2H, CH$_{aromatic}$), 4.98 (s, 1H, NH), 4.46 (d, J = 6.2 Hz, 2H, CH$_2$), 1.48 (s, 9H, CH$_{3\ Boc}$). **^{13}C NMR** (101 MHz, CDCl$_3$) δ 166.4 (C$_{q\ tetrazine}$), 161.3 (C$_{q\ Boc\ carbonyl}$), 157.9 (CH$_{tetrazine}$), 144.8 (C$_{q\ aromatic}$), 130.7 (C$_{q\ aromatic}$), 128.7 (CH$_{aromatic}$),

128.3 (CH $_{aromatic}$), 44.5 (CH$_2$), 28.5 (CH$_{3\,Boc}$).

11: tert-butyl (4-(6-methyl-1,2,4,5-tetrazin-3-yl)benzyl)carbamate

Compound **9** (2 mmol, 0.464 g) was dissolved in acetonitrile (10 mmol, 0.522 mL, 5 eq) in a pressure tube. Zn(OTf)$_2$ (0.5 mmol, 0.182 g, 0.25 eq) and 64% hydrazine monohydrate (100 mmol, 4.84 mL, 50 eq) were added and the reaction was stirred overnight at 80°C. Oxidation procedure A was performed and column purification (2% -> 10%, EtOAc in DCM) yielded **11** as a pink solid (197 mg, 0.7 mmol, 33%).

¹H NMR (400 MHz, CDCl$_3$) δ 8.51 (d, *J* = 8.4 Hz, 2H, CH $_{aromatic}$), 7.48 (d, *J* = 8.4 Hz, 2H, CH $_{aromatic}$), 5.21 (s, 1H, NH), 4.43 (d, *J* = 6.1 Hz, 2H, CH$_2$), 3.09 (s, 3H, CH$_3$), 1.48 (s, 9H, CH$_{3\,Boc}$). **¹³C NMR** (101 MHz, CDCl$_3$) δ 167.2 (C$_{q\,tetrazine}$), 163.9 (C$_{q\,tetrazine}$), 156.1 (C$_{q\,Boc\,carbonyl}$), 144.1 (C$_{q\,aromatic}$), 130.8 (C$_{q\,aromatic}$), 128.2 (CH $_{aromatic}$), 128.1 (CH $_{aromatic}$), 79.8 (C$_{q\,Boc\,tBu}$), 44.4 (CH$_2$), 28.5 (CH$_{3\,Boc}$), 21.2 (CH$_3$).

12: tert-butyl (4-(6-(pyridin-2-yl)-1,2,4,5-tetrazin-3-yl)benzyl)carbamate

Compound **9** (2 mmol, 0.464 g) was dissolved in 2-cyanopyridine (10 mmol, 0.962 mL, 5eq) in a pressure tube. Zn(OTf)$_2$ (0.5 mmol, 0.182 g, 0.25 eq) and 64% hydrazine monohydrate (100 mmol, 4.84 mL, 50 eq) were added and the reaction was stirred overnight at 80°C. Oxidation procedure A was performed and column purification (2% -> 20%, EtOAc in DCM) yielded **12** as a pink solid (213 mg, 0.6 mmol, 29%).

¹H NMR (400 MHz, CDCl$_3$) δ 8.97 (d, *J* = 0.9 Hz, 1H, CH $_{pyr}$), 8.69 (d, *J* = 1.1 Hz, 1H, CH $_{pyr}$), 8.65 (d, 2H, CH $_{aromatic}$), 8.00 (td, *J* = 7.8, 1.8 Hz, 1H, CH $_{aromatic}$), 7.57 (dd, *J* = 4.8, 1.2 Hz, 1H, CH $_{pyr}$), 7.54 (d, *J* = 8.2 Hz, 2H, CH $_{aromatic}$), 5.12 (s, 1H, NH), 4.46 (d, *J* = 6.1 Hz, 2H, CH$_2$), 1.49 (s, 9H, CH$_{3\,Boc}$). **¹³C NMR** (101 MHz, CDCl$_3$) δ 164.3 (C$_q$ $_{tetrazine}$), 163.5 (C$_{q\,tetrazine}$), 156.1 (C$_{q\,Boc\,carbonyl}$), 151.0 (CH $_{pyr}$), 150.4 (C$_{q\,pyr}$), 144.7 (C$_q$ $_{aromatic}$), 137.6 (CH $_{pyr}$), 130.6 (C$_{q\,aromatic}$), 128.8 (CH $_{aromatic}$), 128.2 (CH $_{aromatic}$), 126.5 (CH $_{pyr}$), 124.0 (CH $_{pyr}$), 80.4 (C$_{q\,Boc\,tBu}$), 44.5 (CH$_2$), 28.5 (CH$_{3\,Boc}$).

23: tert-butyl (2-(1,2,4,5-tetrazin-3-yl)ethyl)carbamate

Compound **22** (1 mmol, 0.170 g), formamidine acetate (5 mmol, 0.521 g, 5 eq.), Zn(OTf)$_2$ (0.25 mmol, 0.090 g, 0.25 eq.) and dry dioxane (1.5 mL) were added to a pressure tube. 64% Hydrazine monohydrate (50 mmol. 2.42 mL, 50 eq.) was added dropwise and the reaction was stirred for 3 days at RT. Oxidation procedure B was performed, and column purification (5% EtOAc in DCM) yielded product **23** as a pink oil (6 mg, 0.02 mmol, 2%).

¹H NMR (400 MHz, CDCl$_3$) δ 10.24 (s, 1H, tetrazine-H), 5.01 (s, 1H, NH), 3.84 – 3.72 (m, 2H, CH$_2$), 3.57 (dd, *J* = 6.9, 5.4 Hz, 2H, CH$_2$), 1.38 (s, 9H, CH$_{3\,Boc}$).

24: tert-butyl (2-(6-methyl-1,2,4,5-tetrazin-3-yl)ethyl)carbamate

Compound **22** (1.65 mmol, 0.280 g), acetonitrile (19 mmol, 1 mL, 11 eq.), nickel triflate (0.25 mmol, 0.090 g, 0.15 eq.) and dry dioxane (2.6 mL) were added to a

pressure tube. 64% hydrazine monohydrate (76 mmol, 2.4 mL, 50 eq.) was added dropwise and the reaction was stirred overnight at 60°C. Oxidation procedure A was performed with 13 equivalents of $NaNO_2$. Column purification (3% → 10% EtOAc in DCM) yielded product **24** as a pink oil (7 mg, 0.03 mmol, 3%).

¹H NMR (400 MHz, CDCl$_3$) δ 5.02 (s, 1H, NH), 3.74 (td, J = 6.6, 5.5 Hz, 2H, CH$_2$), 3.51 (t, J = 6.2 Hz, 2H, CH$_2$), 3.06 (s, 3H, CH$_3$), 1.38 (s, 9H, CH$_{3 \, Boc}$). **¹³C NMR** (101 MHz, CDCl$_3$) δ 67.2 (C$_{q \, tBu}$), 38.4 (CH$_2$), 35.5 (CH$_2$), 28.4 (CH$_3$), 21.2 (CH$_{3 \, Boc}$).

25: tert-butyl (2-(6-(pyridin-2-yl)-1,2,4,5-tetrazin-3-yl)ethyl)carbamate

Compound **22** (1 mmol, 0.17 g), 2-cyanopyridine (5 mmol, 0.49 mL, 5 eq.) and zinc triflate (0.25 mmol, 0.09 g, 0.25 eq.) were added to nitrogen flushed flask. Hydrazine monohydrate (50 mmol, 2.5 g, 50 eq.) was added and the mixture was stirred overnight at 60°C under nitrogen atmosphere. Oxidation procedure B was performed and column purification (30% → 65% EtOAc in pentane) yielded product **25** as a pink oil (68 mg, 0.2 mmol, 22%).

¹H NMR (400 MHz, CDCl$_3$) δ 8.96 (d, J = 4.7 Hz, 1H, CH$_{pyr}$), 8.65 (d, J = 8.0 Hz, 1H, CH$_{pyr}$), 7.99 (td, J = 7.8, 1.9 Hz, 1H, CH$_{pyr}$), 7.57 (t, J = 6.3 Hz, 1H, CH$_{pyr}$), 4.34 (dt, J = 7.9, 3.9 Hz, 2H, CH$_2$), 3.56 – 3.47 (m, 2H, CH$_2$), 1.25 (s, 9H, CH$_{3, \, Boc}$). **¹³C NMR** (101 MHz, CDCl$_3$) δ 151.4 (CH$_{pyr}$), 137.9 (CH$_{pyr}$), 127.0 (CH$_{pyr}$), 124.5 (CH$_{pyr}$), 86.4 (C$_{q \, Boc}$), 33.1 (CH$_2$), 30.2 (CH$_2$), 28.4 (CH$_{3, \, Boc}$).

General Boc-deprotection (13-15 and 26-28)
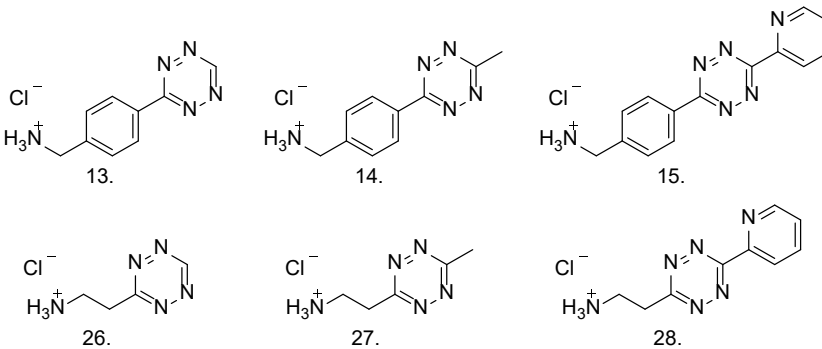
The Boc-protected tetrazine was dissolved in dry DCM (1 mL/30 mg) and 4M HCl in dioxane (1 mL / 30 mg) was added to the reaction mixture dropwise. The reaction was stirred for 2h at RT under N$_2$ atmosphere. The suspension was centrifuged, and the supernatant was removed. The pellet was washed two times via resuspension in 10 mL dry dioxane. The pellet was then resuspended in 5 mL dry dioxane and concentrated under reduced pressure yielding compounds **13**-**15** and **26**-**28** as colored N-Boc deprotected ammonium chloride salts. ¹H NMRs of synthesized compounds were consistent with previously reported NMR results of these compounds. Low concentrations and the instability of compounds **13**-**14** and

26-**28** caused not all ¹³C NMRs to be recorded.

13: (4-(1,2,4,5-tetrazin-3-yl)phenyl)methanamonium chloride

Compound **10** (0.1 mmol, 0.027 g) was used and resulted in the N-Boc deprotected product **13** as a pink hydrochloride salt (12 mg, 0.06 mmol, 55%).

¹H NMR (400 MHz, MeOD) δ 10.39 (s, 1H, tetrazine-H), 8.68 (d, J = 8.6 Hz, 2H, CH $_{aromatic}$), 7.75 (d, J = 0.6 Hz, 2H, CH $_{aromatic}$), 4.28 (s, 2H, CH$_2$). **¹³C NMR** (101 MHz, MeOD) δ 168.4 (C$_{q\ tetrazine}$), 167.7 (CH $_{tetrazine}$), 157.4 (C$_{q\ aromatic}$), 143.0 (C$_{q\ aromatic}$), 130.9 (CH $_{aromatic}$), 129.8 (CH $_{aromatic}$), 43.9 (CH$_2$).

14: (4-(6-methyl-1,2,4,5-tetrazin-3-yl)phenyl)methanamonium chloride

Compound **11** (0.1 mmol, 0.03 g) was used and resulted in the N-Boc deprotected product **14** as a pink hydrochloride salt (21 mg, 0.09 mmol, 87%).

¹H NMR (400 MHz, MeOD) δ 8.62 (d, J = 8.5 Hz, 2H, CH $_{aromatic}$), 7.74 (d, J = 8.4 Hz, 2H, CH $_{aromatic}$), 4.28 (s, 1H, NH), 3.05 (s, 3H, CH$_3$).

15: (4-(6-(pyridin-2-yl)-1,2,4,5-tetrazin-3-yl)phenyl)methanamonium chloride

Compound **12** (0.082 mmol, 0.03 g) was used and resulted in the N-Boc deprotected product **15** as a purple hydrochloride salt (24 mg, 0.08 mmol, 96%).

¹H NMR (400 MHz, MeOD) δ 9.16 (d, J = 8.1 Hz, 1H, CH $_{pyr}$), 9.08 (d, J = 4.6 Hz, 1H, CH $_{pyr}$), 8.80 (d, J = 8.4 Hz, 2H, CH $_{aromatic}$), 8.76 (dd, J = 8.0, 1.6 Hz, 1H, CH $_{pyr}$), 8.27 – 8.22 (m, 1H, CH $_{pyr}$), 7.82 (d, J = 8.6 Hz, 2H, CH $_{aromatic}$), 4.32 (s, 2H, CH$_2$). **¹³C NMR** (101 MHz, MeOD) δ 165.9 (C$_{q\ tetrazine}$), 161.7 (C$_{q\ tetrazine}$), 147.0 - 146.8 (m, CH $_{pyr,}$ C$_{q\ pyr}$), 140.1 (C$_{q\ aromatic}$), 133.5 (C$_{q\ aromatic}$), 131.2 (CH $_{aromatic}$), 130.4 (CH $_{pyr}$), 126.9 (CH $_{pyr}$), 43.9 (CH$_2$).

26: (4-(1,2,4,5-tetrazin-3-yl)phenyl)methanamonium chloride

Compound **23** (13 µmol, 3 mg) was used and resulted in the N-Boc deprotected product **26** as a pink hydrochloride salt (2 mg, 0.01 mmol, 93%).

¹H NMR (400 MHz, MeOD) δ 10.44 (s, 1H, tetrazine-H), 3.80 – 3.71 (m, 2H, CH$_2$), 3.67 (d, J = 10.4 Hz, 2H, CH$_2$).

27: 2-(6-methyl-1,2,4,5-tetrazin-3-yl)ethan-1-amonium chloride

Compound **24** (0.031 mmol, 7.3 mg) was used and resulted in the N-Boc deprotected product **27** as a pink hydrochloride salt (7 mg, 0.04 mmol, quant.).

28: 2-(6-(pyridin-2-yl)-1,2,4,5-tetrazin-3-yl)ethan-1-amonium chloride

Compound **25** (0.034 mmol, 0.01 g) was used and resulted in the N-Boc deprotected product **28** as a pink hydrochloride salt (9 mg, 0.04 mmol, quant.).

¹H NMR (400 MHz, MeOD) δ 9.13 (d, *J* = 8.1 Hz, 1H, CH $_{pyr}$), 9.07 (d, *J* = 5.5 Hz, 1H, CH $_{pyr}$), 8.74 (t, 1H, CH $_{pyr}$), 8.24 (t, *J* = 6.7 Hz, 1H, CH $_{pyr}$), 3.92 (t, *J* = 6.9 Hz, 2H, CH$_2$), 3.73 (t, *J* = 6.9 Hz, 2H, CH$_2$).

General synthesis biotin-tetrazines (16-21 and 29-31)
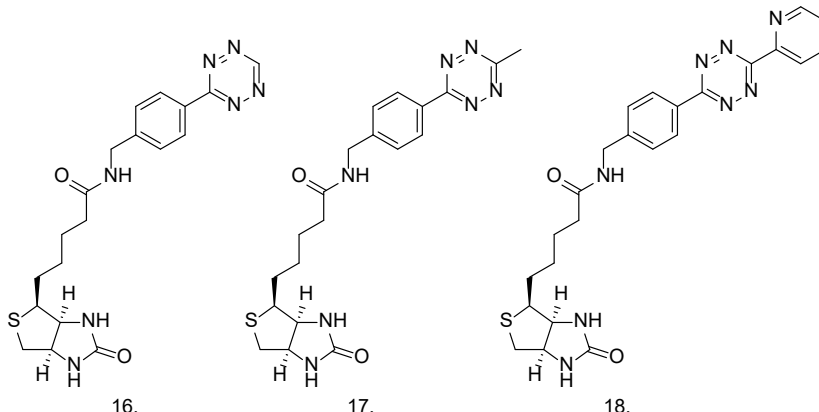
The NHS-biotins were dissolved in DCM after which the tetrazine ammonium salt (1.2 eq.) and DIPEA (2 eq.) were added. The reaction mixture was stirred for 3h at RT for tetrazines **13**-**15** and stirred for 24h at RT for tetrazines **26**-**28**. Completion of the reaction was checked with LC-MS and the mixture was concentrated. After purification by HPLC all fractions containing the product were pooled and lyophilized, which yielded the biotin-tetrazines **16-21** and **29-31** as pink solids. Final compounds were obtained in small amounts causing ^{13}C NMR signals to be too weak to be measured for some of the compounds.

16: N-(4-(1,2,4,5-tetrazin-3-yl)benzyl)-5-(2-oxohexahydro-1H-thieno[3,4-d]imidazol-4-yl)pentanamide

NHS-biotin (0.046 mmol, 0.016 g) was dissolved in 2.4 mL DCM. Compound **13** (0.055 mmol, 0.012 g, 1.2 eq) and DIPEA (0.092 mmol, 0.016 mL, 2 eq) were added to the reaction mixture. After purification compound **16** was obtained as a pink solid (14.0 mg, 0.03 mmol, 73%).

¹H NMR (400 MHz, DMSO-D$_6$, HH-COSY) δ 10.58 (s, 1H, tetrazine-H), 8.49 (d, *J* = 6.1 Hz, 1H, NH $_{amide}$), 8.46 (d, *J* = 8.3 Hz, 2H, CH $_{aromatic}$), 7.53 (d, *J* = 8.4 Hz, 2H, CH $_{aromatic}$), 6.44 (s, 1H, NH $_{biotin}$), 6.36 (s, 1H, NH $_{biotin}$), 4.39 (d, *J* = 6.0 Hz, 2H, CH$_2$), 4.33 – 4.27 (m, 1H, CH $_{biotin}$), 4.17 – 4.09 (m, 1H, CH $_{biotin}$), 3.14 – 3.07 (m, 1H, CH $_{biotin}$), 2.82 (dd, *J* = 12.5, 5.1 Hz, 1H, CH$_2$ $_{biotin}$), 2.57 (d, *J* = 21.2 Hz, 1H, CH$_2$ $_{biotin}$), 2.19 (t, *J* = 7.4 Hz, 2H, CH$_2$ $_{linker}$), 1.68 – 1.26 (m, 6H, CH$_2$ $_{linker}$).

HRMS: calculated for C$_{19}$H$_{24}$N$_7$O$_2$S [M+H]+ 414.17; found 414.17138

17: N-(4-(6-methyl-1,2,4,5-tetrazin-3-yl)benzyl)-5-(2-oxohexahydro-1H-thieno[3,4-d] imidazol-4-yl) pentanamide

NHS-biotin (0.073 mmol, 0.025 g) was dissolved in 3.75 mL DCM. Compound **14** (0.087 mmol, 0.021 g, 1.2 eq) and DIPEA (0.145 mmol, 0.025 mL, 2 eq) were added to the reaction. After purification compound **17** was obtained as a pink solid. (16.3 mg, 0.04 mmol, 53%).

^{1}H NMR (400 MHz, DMSO-D_6) δ 8.47 (t, J = 6.0 Hz, 1H, NH $_{amide}$), 8.42 (d, J = 8.4 Hz, 2H, CH $_{aromatic}$), 7.51 (d, J = 8.3 Hz, 2H, CH $_{aromatic}$), 6.44 (s, 1H, NH $_{biotin}$), 6.36 (s, 1H, NH $_{biotin}$), 4.38 (d, J = 6.0 Hz, 2H, CH_2), 4.30 (dd, 1H, CH $_{biotin}$), 4.16 − 4.09 (m, 1H, CH $_{biotin}$), 3.10 (dt, J = 8.7, 5.6 Hz, 1H, CH $_{biotin}$), 2.99 (s, 3H, CH_3), 2.82 (dd, J = 12.5, 5.1 Hz, 1H, CH_2 $_{biotin}$), 2.67 (q, J = 1.8 Hz, 1H, CH_2 $_{biotin}$), 2.18 (t, J = 7.4 Hz, 2H, CH_2 $_{linker}$), 1.67 − 1.29 (m, 6H, CH_2 $_{linker}$). **^{13}C NMR** (101 MHz, DMSO-D_6) δ 175.8 (C_q $_{carbonyl\ biotin}$), 163.2 (C_q $_{carbonyl\ amide}$), 148.2 (C_q $_{tetrazine}$), 144.6 (C_q $_{tetrazine}$), 134.7 (C_q $_{aromatic}$), 128.1 (CH $_{aromatic}$), 127.5 (CH $_{aromatic}$), 120.3 (C_q $_{aromatic}$), 61.1 (CH $_{biotin}$), 59.2 (CH $_{biotin}$), 55.5 (CH $_{biotin}$), 52.0 (CH_2 $_{biotin}$), 41.9 (CH_2), 31.3 (CH_2 $_{linker}$), 25.3 (CH_2 $_{linker}$), 11.6 (CH_3).

HRMS: calculated for $C_{20}H_{26}N_7O_2S$ [M+H]+ 428.19; found 428.18794

18: 5-(2-oxohexahydro-1H-thieno[3,4-d]imidazol-4-yl)-N-(4-(6-(pyridin-2-yl)-1,2,4,5-tetrazin-3-yl)benzyl)pentanamide

NHS-biotin (0.065 mmol, 0.022 g) was dissolved in 3.2 mL DCM. Compound **15** (0.079 mmol, 0.024 g, 1.2 eq) and DIPEA (0.131 mmol, 0.023 mL, 2 eq) were added to the reaction mixture. After purification, compound **18** was obtained as a purple solid. (12.7 mg, 0.03 mmol, 40%).

^{1}H NMR (400 MHz, DMSO-D_6, HH-COSY) δ 8.92 (d, J = 4.5 Hz, 1H, CH $_{pyr}$), 8.57 (d, J = 7.9 Hz, 1H, CH $_{pyr}$), 8.53 (d, J = 8.4 Hz, 2H, CH $_{aromatic}$), 8.49 (d, J = 6.0 Hz, 1H, NH $_{amide}$), 8.15 (td, J = 7.8, 1.8 Hz, 1H, CH $_{pyr}$), 7.72 (ddd, J = 7.6, 4.7, 1.2 Hz, 1H, CH $_{pyr}$), 7.56 (d, J = 8.4 Hz, 2H, CH $_{aromatic}$), 6.44 (s, 1H, NH $_{biotin}$), 6.37 (s, 1H, NH $_{biotin}$), 4.41 (d, J = 5.9 Hz, 2H, CH_2), 4.34 − 4.27 (m, 1H, CH $_{biotin}$), 4.17 − 4.09 (m, 1H, CH $_{biotin}$), 3.16 − 3.07 (m, 1H, CH $_{biotin}$), 2.83 (dd, J = 12.5, 5.1 Hz, 1H, CH_2 $_{biotin}$), 2.58 (d, J = 12.5 Hz, 1H, CH_2 $_{biotin}$), 2.20 (t, J = 7.4 Hz, 2H, CH_2 $_{linker}$), 1.66 − 1.31 (m, 6H, CH_2 $_{linker}$). **^{13}C NMR** (101 MHz, DMSO-D_6) δ 172.4 (C_q $_{carbonyl\ biotin}$), 163.2 (C_q $_{tetrazine}$), 150.6 (CH $_{pyr}$), 146.6 (C_q $_{pyr}$), 145.2 (C_q $_{aromatic}$), 137.9 (CH $_{pyr}$), 130.2 (C_q $_{aromatic}$), 128.2 (CH $_{aromatic}$), 128.0 (CH $_{aromatic}$), 124.0 (CH $_{pyr}$), 61.1 (CH $_{biotin}$), 59.3 (CH $_{biotin}$), 55.5 (CH $_{pyr}$), 41.9 (CH_2), 33.5 (CH_2 $_{linker}$), 28.1 (CH_2 $_{linker}$), 25.4 (CH_2 $_{linker}$).

HRMS: calculated for $C_{24}H_{27}N_8O_2S$ [M+H]+ 491.20; found 491.19836

19.   20.   21.
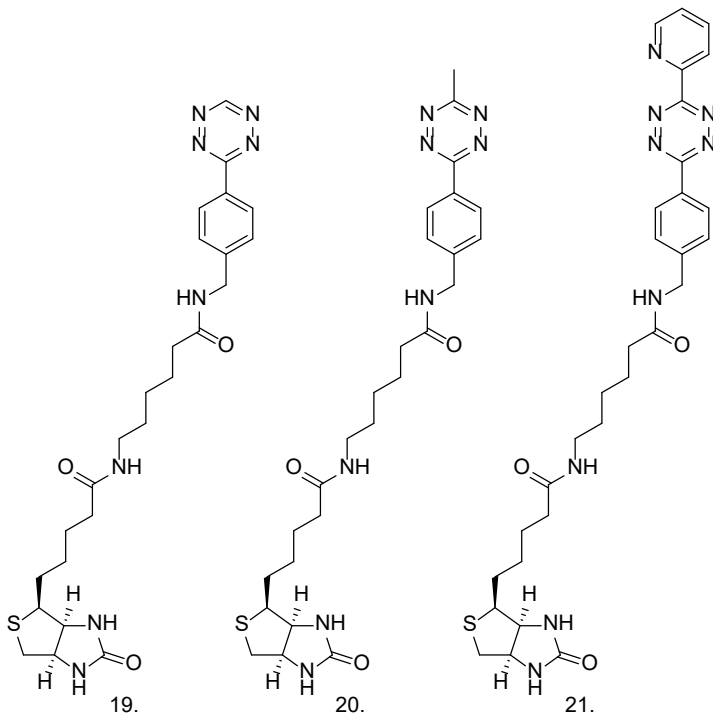
19: N-(4-(1,2,4,5-tetrazin-3-yl)benzyl)-6-(5-(2-oxohexahydro-1H-thieno[3,4-d]imidazol-4-yl)pentanamido)hexanamide

NHS-LC-biotin (0.075 mmol, 0.034 g) was dissolved in 3.75 mL DCM. Compound **13** (0.090 mmol, 0.020 g, 1.2 eq) and DIPEA (0.150 mmol, 0.026 mL, 2 eq) were added to the reaction mixture. After purification, compound **19** was obtained as a pink solid. (23.8 mg, 0.05 mmol, 60%).

^{1}H NMR (400 MHz, DMSO-D$_6$) δ 10.58 (s, 1H, tetrazine-H), 8.47 (d, J = 3.3 Hz, 2H, CH $_{tetrazine}$), 8.45 (t, J = 1.9 Hz, 1H, NH $_{amide}$), 7.76 (t, J = 5.6 Hz, 1H, NH $_{amide}$), 7.53 (d, J = 8.3 Hz, 2H, CH $_{tetrazine}$), 6.42 (s, 1H, NH $_{biotin}$), 6.36 (s, 1H, NH $_{biotin}$), 4.39 (d, J = 6.0 Hz, 2H, CH$_2$), 4.29 (dd, J = 7.8, 4.9 Hz, 1H, CH $_{biotin}$), 4.12 (dd, J = 7.8, 4.4 Hz, 1H, CH $_{biotin}$), 3.08 (dt, J = 8.7, 5.8 Hz, 1H, CH $_{biotin}$), 3.01 (q, J = 6.6 Hz, 2H, CH$_{2\ linker}$), 2.81 (dd, J = 12.5, 5.1 Hz, 1H, CH$_{2\ linker}$), 2.58 (s, 1H, CH$_2$ linker), 2.17 (t, J = 7.4 Hz, 2H, CH$_{2\ linker}$), 2.04 (t, J = 7.4 Hz, 2H CH$_{2\ linker}$), 1.67 – 1.19 (m, 12H, CH$_{2\ linker}$). **^{13}C NMR** (101 MHz, DMSO-D$_6$) δ 172.4 (C$_{q\ carbonyl\ amide}$), 171.9 (C$_{q\ carbonyl\ amide}$), 165.5 (CH$_{tetrazine}$), 162.8 (C$_{q\ carbonyl\ biotin}$), 145.1 (C$_{q\ aromatic}$), 130.4 (C$_{q\ aromatic}$), 128.1 (CH $_{aromatic}$), 127.9 (CH $_{aromatic}$), 61.1 (CH $_{biotin}$), 59.2 (CH $_{biotin}$), 55.5 (CH $_{biotin}$), 41.9 (CH$_2$), 38.4 (CH$_{2\ linker}$), 35.4 (CH$_{2\ linker}$), 35.3 (CH$_{2\ linker}$), 29.0-25.1 (CH$_{2\ linker}$).

HRMS: calculated for C$_{25}$H$_{35}$N$_8$O$_3$S [M+H]+ 527.26; found 527.25596

20: N-(4-(6-methyl-1,2,4,5-tetrazin-3-yl)benzyl)-6-(5-(2-oxohexahydro-1H-thieno[3,4-d]imidazol-4-yl)pentanamido)hexanamide

NHS-LC-biotin (0.083 mmol, 0.038 g) was dissolved in 4.15 mL DCM. Compound **14** (0.1 mmol, 0.025 g, 1.2 eq) and DIPEA (0.167 mmol, 0.029 mL, 2 eq) were added to the reaction mixture. After purification compound **20** was obtained as a pink solid. (23.2 mg, 0.04 mmol, 52%).

¹H NMR (400 MHz, DMSO-D$_6$) δ 8.46 (d, J = 5.9 Hz, 1H, NH $_{amide}$), 8.42 (d, J = 8.3 Hz, 2H, CH $_{aromatic}$), 7.76 (t, J = 5.6 Hz, 1H, NH $_{amide}$), 7.51 (d, J = 8.2 Hz, 2H, CH $_{aromatic}$), 6.42 (s, 1H, NH $_{biotin}$), 6.36 (s, 1H, NH $_{biotin}$), 4.38 (d, J = 6.0 Hz, 2H, CH$_2$), 4.29 (dd, J = 7.7, 4.9 Hz, 1H, CH $_{biotin}$), 4.12 (dd, J = 7.8, 4.4 Hz, 1H, CH $_{biotin}$), 3.11 – 3.05 (m, 1H, CH $_{biotin}$), 3.02 (dd, 2H, CH$_2$ $_{linker}$), 2.99 (s, 3H, CH$_3$), 2.81 (dd, J = 12.5, 5.1 Hz, 1H, CH$_2$ $_{biotin}$), 2.56 (d, J = 12.8 Hz, 1H, CH$_2$ $_{biotin}$), 2.17 (t, J = 7.4 Hz, 2H, CH$_2$ $_{linker}$), 2.03 (t, J = 7.4 Hz, 2H, CH$_2$ $_{linker}$), 1.59 – 1.20 (m, 12H, CH$_2$ $_{linker}$). **¹³C NMR** (101 MHz, DMSO-D$_6$) δ 172.4 (C$_{q \ carbonyl \ amide}$), 171.9 (C$_{q \ carbonyl \ amide}$), 167.1 (C$_{q \ tetrazine}$), 163.2 (C$_{q \ tetrazine}$), 162.8 (C$_{q \ carbonyl \ biotin}$), 144.6 (C$_{q \ aromatic}$), 130.4 (C$_{q \ aromatic}$), 128.1 (CH $_{aromatic}$), 127.5 (CH $_{aromatic}$), 61.1 (CH $_{biotin}$), 59.2 (CH $_{biotin}$), 55.5 (CH $_{biotin}$), 41.9 (CH$_2$), 38.4 (CH$_2$ $_{linker}$), 35.4 (CH$_2$ $_{linker}$), 35.3 (CH$_2$ $_{linker}$), 29.0-25.1 (CH$_2$ $_{linker}$), 20.9 (CH$_3$).

HRMS: calculated for C$_{26}$H$_{37}$N$_8$O$_3$S [M+H]+ 541.27; found 541.27139

21: 6-(5-(2-oxohexahydro-1H-thieno[3,4-d]imidazol-4-yl)pentanamido)-N-(4-(6-(pyridin-2-yl)-1,2,4,5-tetrazin-3-yl)benzyl)hexanamide

NHS-LC-biotin (0.062 mmol, 0.028 g) was dissolved in dry DCM (3.1 mL). Compound **15** (0.075 mmol, 0.022 g, 1.2 eq.) and DIPEA (0.124 mmol, 0.022 mL, 2 eq). were added to the reaction mixture. After purification compound **21** was obtained as a purple solid. (15.0 mg, 0.02 mmol, 40%).

¹H NMR (400 MHz, DMSO-D$_6$) δ 8.92 (ddd, J = 4.7, 1.8, 0.9 Hz, 1H, CH $_{pyr}$), 8.57 (dt, J = 8.0, 1.1 Hz, 1H, NH $_{amide}$), 8.56 – 8.51 (m, 2H, CH $_{aromatic}$), 8.48 (t, J = 6.0 Hz, 1H, CH $_{pyr}$), 8.15 (td, J = 7.8, 1.8 Hz, 1H, CH $_{pyr}$), 7.77 (t, J = 5.6 Hz, 1H, NH $_{amide}$), 7.72 (ddd, J = 7.6, 4.7, 1.2 Hz, 1H, CH $_{pyr}$), 7.56 (d, J = 8.3 Hz, 2H, Ch $_{aromatic}$), 6.43 (s, 1H, NH $_{amide \ biotin}$), 6.36 (s, 1H, NH $_{amide \ biotin}$), 4.41 (d, J = 6.0 Hz, 2H, CH$_2$), 4.29 (dd, J = 7.7, 4.9 Hz, 1H, CH $_{biotin}$), 4.11 (dd, J = 7.8, 4.4 Hz, 1H, CH $_{biotin}$), 3.12 – 3.05 (m, 1H, CH $_{biotin}$), 3.01 (q, J = 6.6 Hz, 2H, CH$_2$ $_{linker}$), 2.80 (dd, J = 12.4, 5.0 Hz, 1H, CH$_2$ $_{biotin}$), 2.70 – 2.64 (m, 1H, CH$_2$ $_{biotin}$), 2.53 (d, J = 8.8 Hz, 3H, CH$_3$), 2.18 (t, J = 7.4 Hz, 2H, CH$_2$ $_{linker}$), 2.04 (t, J = 7.4 Hz, 2H, CH$_2$ $_{linker}$), 1.65 – 1.19 (m, 12H, CH$_2$ $_{linker}$). **¹³C NMR** (101 MHz, DMSO-D$_6$) δ 176.1, 172.5, 171.9, 162.1, 151.6, 150.7, 145.2, 139.7, 130.2, 128.2, 128.0, 61.1, 59.2, 55.5, 41.9, 31.7, 28.1, 26.2, 25.4, 25.1.

HRMS: calculated for C$_{30}$H$_{38}$N$_9$O$_3$S [M+H]+ 604.28; found 604.28255

29. 30. 31.
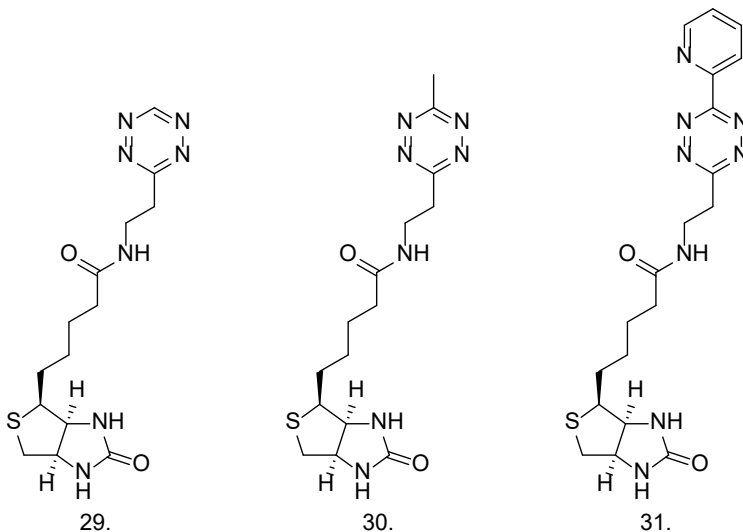
29: N-(2-(1,2,4,5-tetrazin-3-yl)ethyl)-5-(2-oxohexahydro-1H-thieno[3,4-d]imidazol-4-yl)pentanamide

NHS-biotin (0.01 mmol, 3.5 mg) was dissolved in dry DCM (0.7 mL). Compound **26** (0.012 mmol, 2 mg, 1.2 eq.) and DIPEA (0.021 mmol, 3.6 µL, 2 eq.) were added to the reaction mixture. After purification compound **29** was obtained as a pink solid (1.4 mg, 0.004 mmol, 38%).

¹H NMR (400 MHz, D_2O, HH-COSY) δ 10.39 (s, 1H, tetrazine-H), 4.59 (t, 1H, CH_{biotin}), 4.41 (t, 1H, CH_{biotin}), 3.77 (t, 2H, CH_2), 3.55 (t, J = 6.3 Hz, 2H, CH_2), 3.33 – 3.22 (m, 1H, CH_{biotin}), 2.98 (dd, 1H, $CH_{2\ biotin}$), 2.76 (d, J = 13.1 Hz, 1H, $CH_{2\ biotin}$), 2.14 (t, J = 7.3 Hz, 2H, $CH_{2\ linker}$), 1.78 – 1.22 (m, 6H, $CH_{2\ linker}$).

HRMS: calculated for $C_{14}H_{22}N_7O_2S$ [M+H]+ 352.16; found 352.15587

30: N-(2-(6-methyl-1,2,4,5-tetrazin-3-yl)ethyl)-5-(2-oxohexahydro-1H-thieno[3,4-d]imidazol-4-yl)pentanamide

NHS-biotin (0.026 mmol, 8.9 mg) was dissolved in dry DCM (1.8 mL). Compound **27** (0.031 mmol, 5.4 mg, 1.2 eq.) and DIPEA (0.052 mmol, 9 µL, 2 eq.) were added to the reaction mixture. After purification, compound **30** was obtained as a pink solid (7.0 mg, 0.02 mmol, 73%).

¹H NMR (400 MHz, D_2O) δ 4.59 (dd, J = 7.8, 5.2 Hz, 1H, CH_{biotin}), 4.39 (dd, J = 8.2, 4.4 Hz, 1H, CH_{biotin}), 3.74 (q, J = 5.2 Hz, 2H, CH_2), 3.48 (t, J = 6.4 Hz, 2H, CH_2), 3.27 (dt, J = 9.5, 5.0 Hz, 1H, CH_{biotin}), 3.02 (d, J = 1.7 Hz, 3H, CH_3), 3.00 – 2.93 (m, 1H, $CH_{2\ biotin}$), 2.75 (d, J = 13.1 Hz, 1H, $CH_{2\ biotin}$), 2.13 (t, J = 7.2 Hz, 2H, $CH_{2\ linker}$), 1.77 – 1.18 (m, 6H, $CH_{2\ linker}$).**¹³C NMR** (101 MHz, D_2O) δ 167.8, 62.1 (CH_{biotin}), 60.3 (CH_{biotin}), 55.3 (CH_{biotin}), 39.7 (CH_2).

HRMS: calculated for $C_{15}H_{24}N_7O_2S$ [M+H]+ 366.17; found 366.17139

31: 5-(2-oxohexahydro-1H-thieno[3,4-d]imidazol-4-yl)-N-(2-(6-(pyridin-2-yl)-1,2,4,5-tetrazin-3-yl)ethyl)pentanamide

NHS-biotin (0.033 mmol, 0.011 mg) was dissolved in dry DCM (2.2 mL). Compound **28** (0.039 mmol, 9.3 µg, 1.2 eq.) and DIPEA (0.065 mmol, 11 µL, 2 eq.) were added to the reaction mixture. After purification compound **31** was obtained as a pink solid (3.3 mg, 0.01 mmol, 35%).

¹H NMR (400 MHz, D$_2$O) δ 8.70 (s, 1H, CH$_{pyr}$), 8.52 (d, J = 8.0 Hz, 1H, CH$_{pyr}$), 8.09 (t, J = 7.9 Hz, 1H, CH$_{pyr}$), 7.66 (s, 1H, CH$_{pyr}$), 4.29 (s, 1H, CH$_{biotin}$), 4.10 (s, 1H, CH$_{biotin}$), 3.70 (d, J = 16.9 Hz, 2H, CH$_2$), 3.48 (s, 2H, CH$_2$), 2.97 (s, 1H, CH$_{2\,biotin}$), 2.77 – 2.59 (m, 1H, CH$_{2\,biotin}$), 2.51 – 2.37 (m, 1H, CH$_{biotin}$), 1.99 (t, J = 6.9 Hz, 2H, CH$_{2\,linker}$), 1.47 – 0.90 (m, 6H, CH$_{2\,linker}$)

HRMS: calculated for $C_{19}H_{25}N_8O_2S$ [M+H]+ 429.18; found 429.18243

Biological experiments

General. Sterculic acid (StA) was purchased from Cayman Chemical (#26735), and stored as 10 mM or 100 mM stock solutions in DMSO at -20°C. The tetrazine-fluorophore conjugates **3** and **7** were synthesised in-house (see Chapter 2 of this thesis), and were stored as 2 mM stock solutions in DMSO at -20°C. Biotin-PEG4-tetrazine was purchased from Conju-Probe (#CP-6001), and stored as an 80 mM stock solution in DMSO at -20°C. The other biotin-tetrazines (**16-21** and **29-31**) were synthesised in-house as described above, and stored as 10 mM stock solutions in DMSO at -80°C. Streptavidin AZDye 647 (Monovalent) labelling reagent was purchased from Abcam (#ab272190), and stored as delivered at 4°C.

Culturing of DC2.4 cells. DC2.4 cells were cultured in RPMI 1640 culture medium (Gibco, #31870025) supplemented with 10% FCS, GlutaMAX (2 mM), sodium pyruvate (1 mM), 1x non-essential amino acids (NEAA, Thermo Fisher Scientific), penicillin (100 I.U./mL), streptomycin (50 µg/mL), and 2-mercaptoethanol (50 µM, Thermo Fisher Scientific), and incubated at 37°C, 5% CO$_2$. The cells were grown to 70-80% confluency and passaged every 2-3 days by trypsinisation.

SDS-PAGE analysis of protein lipidation with sterculic acid. 3.4×10^5 cells were seeded per well in a 6-well plate (Sarstedt) and allowed to attach for 20 h at 37°C, 5% CO$_2$. Half the samples were stimulated with LPS-EB Ultrapure (100 mg/mL, InvivoGen) in fresh culture medium, while the other half got refreshed culture medium. All dishes were incubated 24 h at 37°C, 5% CO$_2$, and washed with medium x2. StA (100 µM) or DMSO vehicle (0.1%) in fresh culture medium were added to the dishes and incubated for 20 h at 37°C, 5% CO$_2$. The click-on-live-cell samples (Figure 2B) were washed with medium x2 before 10 µM of fluorophore **7** in fresh culture medium was added. The cells were incubated for 2 h at 37°C, 5% CO$_2$. Medium was aspirated and all cells were washed with PBS x2, harvested by scraping in ice-cold PBS, and centrifuged at 1000 *g*, 5 min. Supernatant was aspirated and cell pellets were lysed by resuspension in cold lysis buffer (sucrose

(250 mM) and $MgCl_2$ (1 mM) in PBS supplemented with 1x EDTA-free protease inhibitor (Roche)). Samples were incubated 10 min on ice with occasional vortexing, followed by sonication (Qsonica Q700 Microplate Sonicator, 2 x 10 s pulses, 10% amplitude, 0°C). Protein concentrations were measured by Qubit assay (Invitrogen) according to the manufacturer's protocol, and all samples were adjusted to 1 mg/mL in 10 µL lysis buffer. 5 µL of 3x concentrated click-mix (30 µM fluorophore **3** in PBS) were added to the click-on-lysate (Figure 2A) samples to give a final fluorophore concentration of 10 µM. Samples were incubated in the dark at RT for 2 h, before addition of 5 µL 4x Laemmli buffer (without 2-mercaptoethanol) to all samples and incubation at RT for 20 min to ensure all proteins were completely denatured. The samples were resolved by SDS-PAGE (12.5% acrylamide gel, ±80 min, 175 V) alongside protein marker (PageRuler Plus, Thermo Fisher Scientific) until the bromophenol blue had just come off the gel. In-gel fluorescence was measured in the AlexaFluor 488- Cy3-, and Cy5-channels on a Chemidoc MP imaging system (Bio-Rad), before subsequent staining with Coomassie, followed by destaining and imaging as a loading control.

Microscopy to verify cell-permeability of biotin-Tzs. $7x10^4$ DC2.4 cells were seeded per well in a flat-bottom 96-well plate. The plates were incubated at 37°C, 5% CO_2 overnight to let the cells attach. StA (100 µM) or DMSO vehicle (0.1%) in fresh culture medium were added to the dishes and incubated for 1 h at 37°C, 5% CO_2. All wells were washed with medium x2. For the live-cell click reaction, wells were treated with biotin-tetrazines **16-21** and **29-31** (200 µM), biotin-PEG4-tetrazine (200 µM) or DMSO vehicle (2%) in medium for 0 h or 4 h at 37°C, 5% CO_2. All live-click samples were washed with medium x3, followed by PBS x3. All wells were fixed with 4% PFA in PBS for 30 min. Samples were stored in 0.5% PFA in PBS for maximum one week at 4°C until further processing. All wells were washed with PBS x1, followed by glycine (20 mM) in PBS x1. The cells were permeabilised with saponin (0.01%) in PBS for 15 min and washed with PBS x2. All wells were blocked with BSA (1%) in PBS for 1 h. For the fixed-cell click reaction, wells were at this point treated with biotin-tetrazines **16**-**21** and **29**-**31** (200 µM), biotin-PEG4-tetrazine (200 µM) or DMSO vehicle (2%) in BSA (1%) in PBS for 0 h or 4 h at 37°C. The fixed-click samples were washed with BSA (1%) in PBS x6, and all wells were stained with streptavidin AZDye 647 (1:3000) at RT for 1 h. All wells were washed with PBS x4, before counterstaining the nuclei with Hoechst 33342 (2 µg/mL) in PBS for 10 min. The wells were washed with PBS x1 and glycerol/DABCO mounting medium was added. The samples were imaged with the 20x objective of an EVOS M7000 Imaging System (Thermo Fisher Scientific), using the DAPI and Cy5 channels.

Chemical proteomics on StA-treated DC2.4 cells. $7.5x10^5$ DC2.4 cells were seeded in 6 cm dishes in triplicate and allowed to attach for 20 h at 37°C, 5% CO_2. Cells were then either treated with LPS-EB Ultrapure (100 ng/mL, InvivoGen) or vehicle (PBS) in fresh medium for 24 h. Cells were then washed with medium twice and StA (10 µM) or vehicle (0.1% DMSO) was added. After 20 h of incubation, the medium was aspirated. Live-cell click samples were washed with fresh medium x2, before adding compound **17** or **19** (200 µM) diluted in fresh medium, and incubating the samples at 37°C, 5% CO_2 for 4 h to allow the compounds to react with StA. After the click reaction, the samples were washed with fresh medium x2 followed by DPBS x2. Simultaneously, the samples to be clicked-in-lysate were washed with DPBS x2, and all samples were harvested by scraping in ice-cold DPBS. Cells were pelleted by

centrifugation (1000 g, 5 min), supernatant was aspirated and cell pellets were lysed by resuspension in cold lysis buffer (Sucrose (250 mM) and MgCl$_2$ (1 mM) in PBS with 2x EDTA-free protease inhibitor (Roche)). Cells were lysed by vortexing followed by sonication (Qsonica Q700 Microplate Sonicator, 2x10 s pulses, 10% amplitude, 0°C). Protein concentration was measured by Qubit Protein assay (Invitrogen) and all samples were adjusted to the lowest protein concentration. To assist membrane solubility, 0.1% Triton X-100 was added to the click-on-lysate samples followed by click reaction with biotin-PEG4-tetrazine (200 µM) at 37°C for 4 h. The volume of all samples was adjusted to 520 µL with PBS and proteins were precipitated by addition of MeOH (666 µL), CHCl$_3$ (166 µL) and MilliQ (150 µL), vortexing after each addition. After spinning down (1500 g, 10 min) the upper and lower layer were aspirated and the protein pellet was resuspended in MeOH (600 µL) by sonication (Qsonica Q700 Microplate Sonicator, 2 x 10 s pulses, 10% amplitude). The proteins were spun down (20 000 g, 5 min) and the supernatant was discarded.

The proteins were redissolved in 500 µL PBS containing 0.5% SDS and 5 mM DTT by heating to 65°C for 15 minutes, allowed to cool to RT and alkylated by addition of IAA (15 µL, 0.5 M) for 30 min. Excess IAA was quenched with DTT (5 µL, 1 M) and samples were transferred to Eppendorf tubes containing 500 µL PBS and 25 µL prewashed Pierce™ High Capacity Streptavidin Agarose slurry (Thermo Fisher Scientific). Samples were agitated (1000 rpm) for 2 h to ensure binding to the beads, which were then spun down (3.000 g, 2 min). Supernatant was discarded and beads were washed with PBS containing 0.5% SDS (3X) and PBS (3X). Beads were resuspended in MilliQ, transferred to Protein LoBind tubes (Eppendorf), spun down (3000 g, 2 min) and supernatant was discarded. The beads were resuspended in digestion buffer (200 µL, 100 mM Tris pH 7.8, 100 mM NaCl, 1 mM CaCl$_2$, 2% (v/v) acetonitrile, sequencing-grade trypsin (Promega, 0.25 µg)) and incubated while shaking overnight (16 h, 37°C, 1000 rpm). Beads were spun down (3000 g, 2 min) and supernatant containing tryptic peptides were transferred to new Protein LoBind tubes. The beads were washed with a 10% formic acid solution (100 µL), which was transferred to the previously isolated peptides. Peptides were desalted using C18 StageTips preconditioned with 50 µL MeOH, 50 µL of 0.5% (v/v) FA in 80% (v/v) acetonitrile/MilliQ (solution B) and 50 µL 0.5% (v/v) FA in MilliQ (solution A) by centrifugation (600 g, 2 min). The peptides were washed with solution A (100 µL, 800 g, 3 min) and eluted into new Protein LoBind tubes using solution B (100 µL, 800 g, 3 min). Samples were concentrated using an Eppendorf SpeedVac (Eppendorf Concentrator Plus 5301 or 5305) and stored at -80°C until measurement.

Nano-LC-MS settings for pull-down samples. Desalted peptide samples were reconstituted in 25-35 µL LC-MS solution (97:3:0.1 H$_2$O, ACN, FA) containing 10 fmol/µL yeast enolase digest (cat. 186002325, Waters) as injection control. Injection amount was titrated using a pooled quality control sample to prevent overloading the nanoLC system and the automatic gain control (AGC) of the QExactive mass spectrometer. The desalted peptides were separated on a UltiMate 3000 RSLCnano system set in a trap-elute configuration with a nanoEase M/Z Symmetry C18 100 Å, 5 µm, 180 µm x 20 mm (Waters) trap column for peptide loading/retention and nanoEase M/Z HSS C18 T3 100 Å, 1.8 µm, 75 µm x 250 mm (Waters) analytical column for peptide separation. The column was kept at 40°C in a column oven. Samples were injected on the trap column at a flow rate of 15 µL/min for 2 min with 99% mobile phase A (0.1% FA in ULC-MS grade water (Biosolve)), 1% mobile

phase B (0.1% FA in ULC-MS grade acetonitrile (Biosolve)) eluent. The 85 min LC method, using mobile phase A and mobile phase B controlled by a flow sensor at 0.3 µL/min with average pressure of 400-500 bar (5500-7000 psi), was programmed as gradient with linear increment to 1% B from 0 to 2 min, 5% B at 5 min, 22% B at 55 min, 40% B at 64 min, 90% B at 65 to 74 min and 1% B at 75 to 85 min. The eluent was introduced by electro-spray ionization (ESI) via the nanoESI source (Thermo Fisher Scientific) using stainless steel Nano-bore emitters (40 mm, OD 1/32", ES542, Thermo Fisher Scientific).

The QExactive HF was operated in positive mode with data dependent acquisition without the use of lock mass, default charge of 2+ and external calibration with LTQ Velos ESI positive ion calibration solution (88323, Pierce, Thermo Fisher Scientific) every 5 days to less than 2 ppm. The tune file for the survey scan was set to scan range of 350 – 1400 m/z, 120,000 resolution (m/z 200), 1 microscan, automatic gain control (AGC) of 3e6, max injection time of 100 ms, no sheath, aux or sweep gas, spray voltage ranging from 1.7 to 3.0 kV, capillary temp of 250°C and an S-lens value of 80. For the 10 data dependent MS/MS events the loop count was set to 10 and the general settings were resolution to 15,000, AGC target 1e5, max IT time 50 ms, isolation window of 1.6 m/z, fixed first mass of 120 m/z and normalized collision energy (NCE) of 28 eV. For individual peaks the data dependent settings were 1.00e3 for the minimum AGC target yielding an intensity threshold of 2.0e4 that needs to be reached prior of triggering an MS/MS event. No apex trigger was used, unassigned, +1 and charges >+8 were excluded with peptide match mode preferred, isotope exclusion on and dynamic exclusion of 10 sec.

In between experiments, routine wash and control runs were done by injecting 5 µl LC-MS solution containing 5 µL of 10 fmol/µL BSA or enolase digest and 1 µL of 10 fmol/µL angiotensin III (Fluka, Thermo)/oxytocin (Merck) to check the performance of the platform on each component (nano-LC, the mass spectrometer (mass calibration/ quality of ion selection and fragmentation) and the search engine).

Data processing of pull-down samples. Raw files were analysed with MaxQuant (Version 2.0.1.0). The following changes were made to the standard settings of MaxQuant: Label-free quantification (LFQ) was chosen with an LFQ minimal ratio count of 1. Match between runs and iBAQ quantification was enabled. Searches were performed against a Uniprot database of the *Mus Musculus* proteome (UPID: UP000000589, downloaded April 13th, 2022) including the internal standard (yeast enolase P00924). The "proteinGroups.txt" file was used for further analysis in Microsoft Excel, and R Statistical Software[58] (Version 4.3.0). StA-enriched proteins were selected by filtering the proteins for detection by 2+ unique peptides, not found in the reverse decoy FASTA file. At most 1 missing LFQ value in the positive samples (+StA) was allowed, and missing values were imputed with the average value of the two remaining measurements. In cases where three values were missing from the negative samples (DMSO vehicle), the missing values were imputed with a negligible small number to allow for further processing and statistical calculations. Significantly StA-enriched proteins were determined using the empirical Bayes method in the Limma package[59] (Version 3.58.1) in R, and these proteins were determined to have a 2-fold difference between average LFQ values between StA- or vehicle-treated samples with an adjusted p-value of <0.05.

Supplementary Figures & Tables

A

Fluorophore **3**

B

Fluorophore **7**

C

Biotin-PEG4-tetrazine
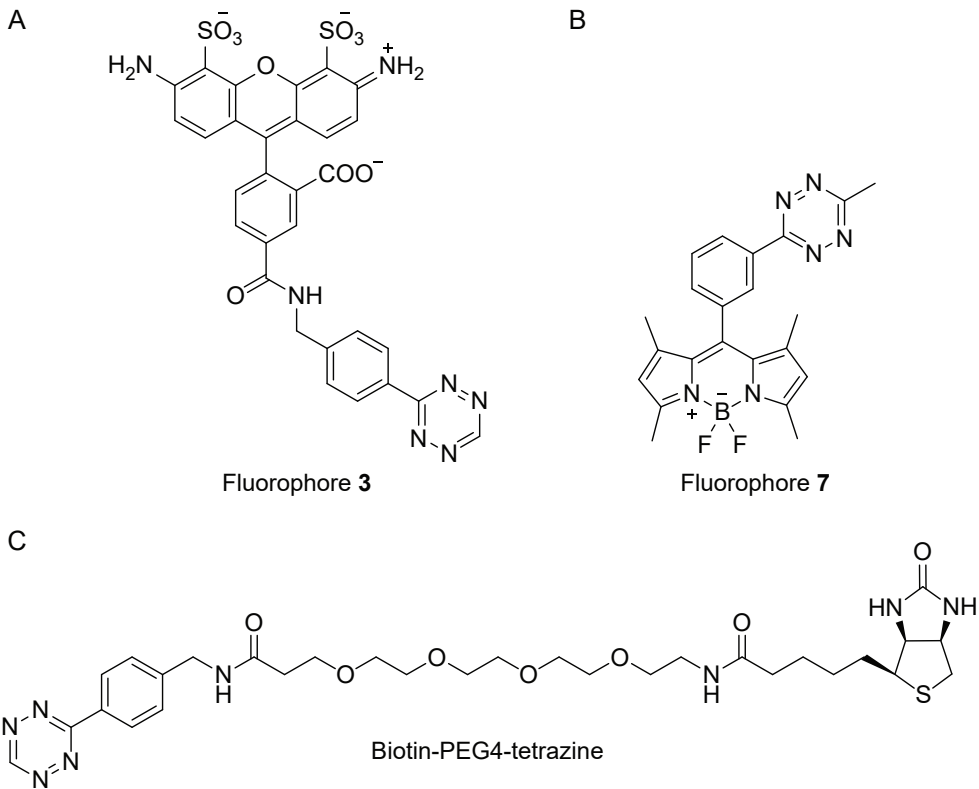
Figure S1: Structures of **A)** fluorophore **3** from Chapter 2, **B)** fluorophore **7** from Chapter 2, **C)** biotin-PEG4-tetrazine.
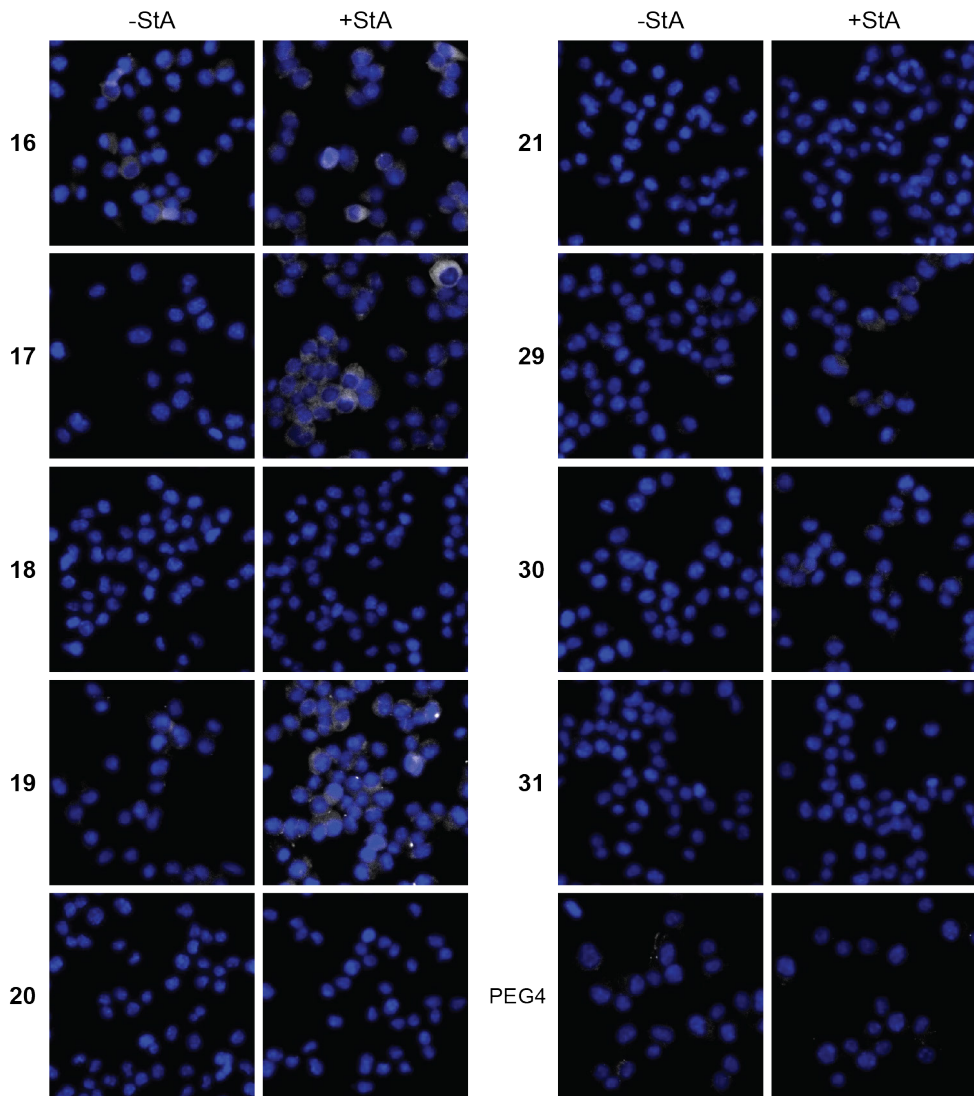
Figure S2: *Fluorescent microscopy to verify cell-permeability of tetrazine-modified biotins 16-21, 29-31, and biotin-PEG4-tetrazine in live DC2.4 cells. To allow uptake of the fatty acid, the cells were incubated with sterculic acid (+StA, 100 µM) or vehicle control (-StA) for 1 h. Then the respective tetrazine-modified biotins (200 µM) were added and incubated for 4 h, before unreacted compound was washed away. The cells were fixed and permeabilised, and a streptavidin AZDye 647 conjugate (grey) was added to visualise the location of the reacted biotins. The nuclei were counterstained with Hoechst 33342 (blue) for reference.*
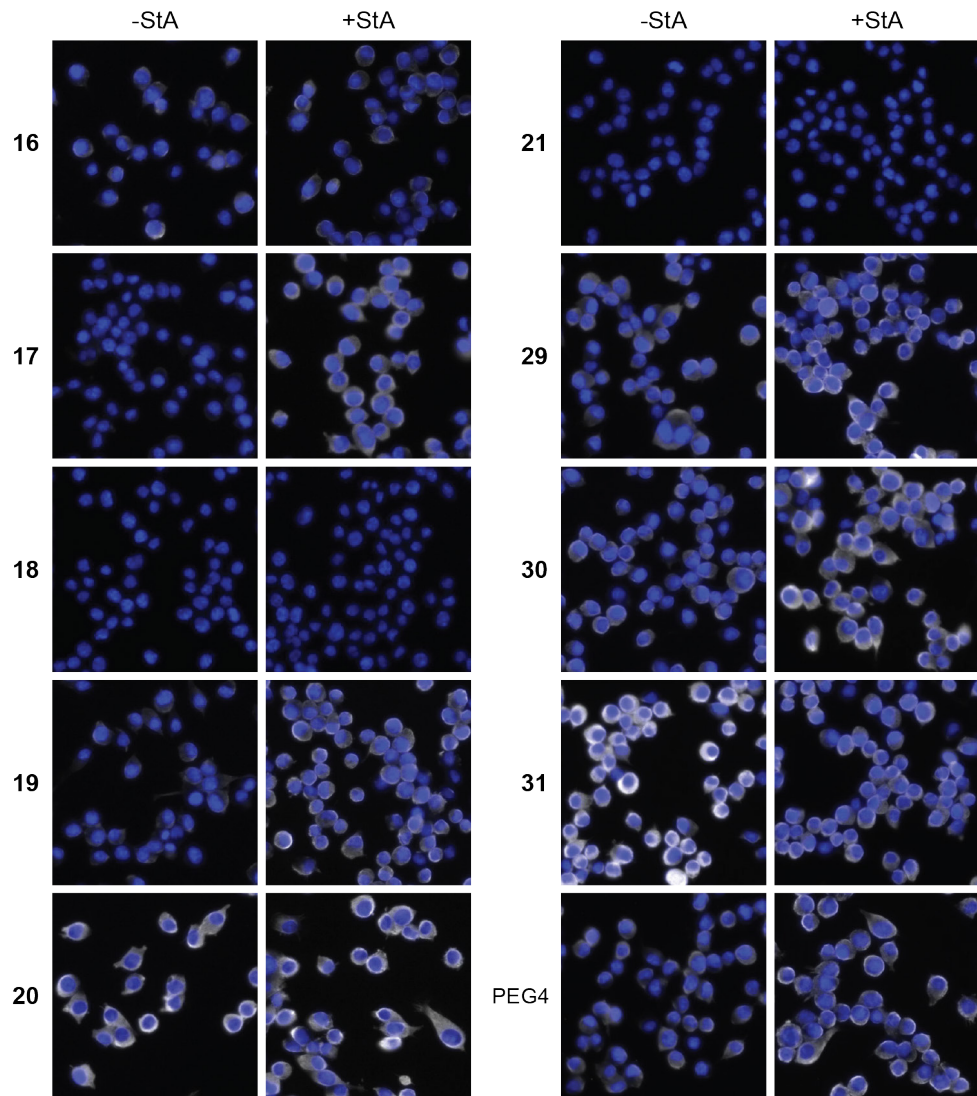
Figure S3: *Fluorescent microscopy to verify reactivity to sterculic acid (StA) of tetrazine-modified biotins **16-21**, **29-31**, and biotin-PEG4-tetrazine in fixed DC2.4 cells. To allow uptake of the fatty acid, the cells were incubated with StA (+StA, 100 µM) or vehicle control (-StA) for 1 h. The cells were fixed and permeabilised before the respective tetrazine-modified biotins (200 µM) were added and incubated for 4 h. Unreacted compound was washed away, and a streptavidin AZDye 647 conjugate (grey) was added to visualise the location of the reacted biotins. The nuclei were counterstained with Hoechst 33342 (blue) for reference.*
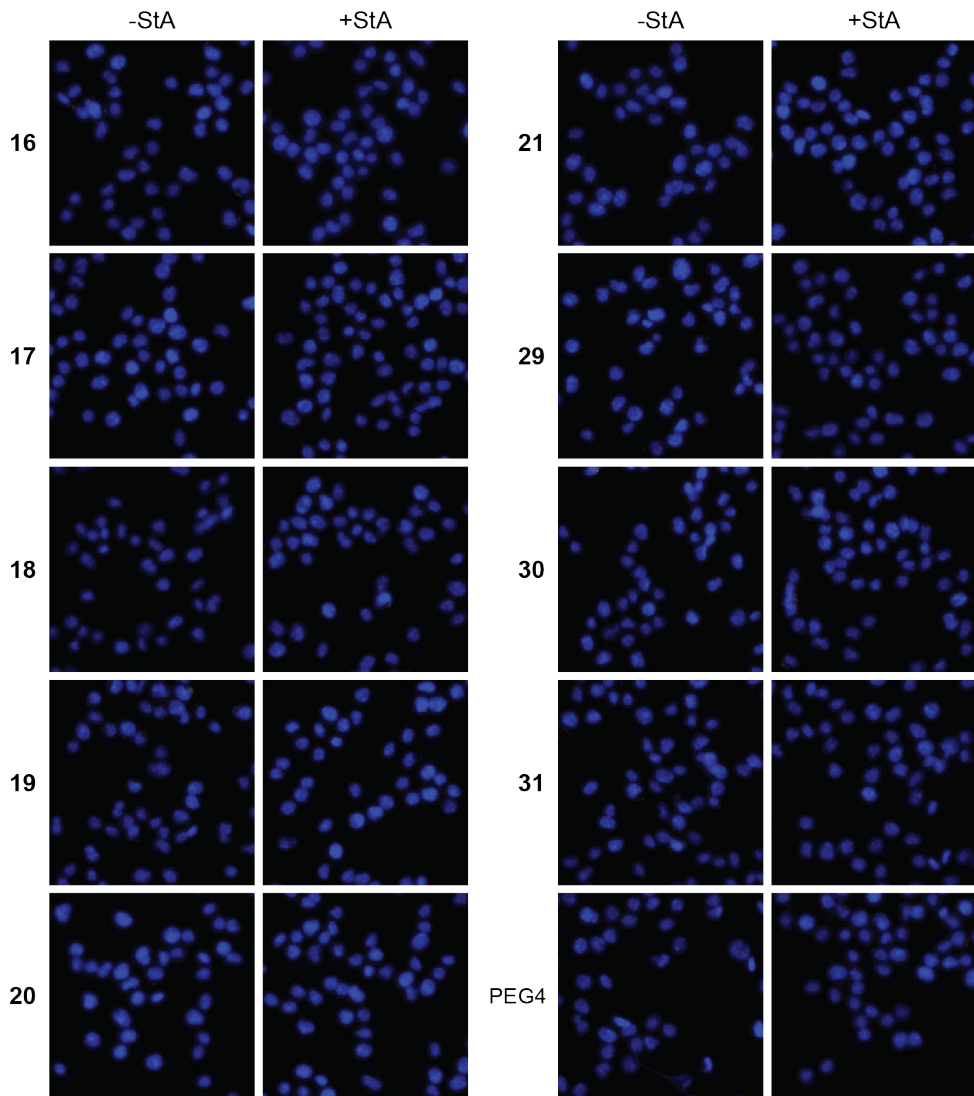
Figure S4: *Control fluorescent microscopy to ensure there is no background fluorescence when the tetrazine-modified biotins **16-21**, **29-31**, and biotin-PEG4-tetrazine are not added to live DC2.4 cells. To allow uptake of the fatty acid, the cells were incubated with sterculic acid (+StA, 100 µM) or vehicle control (-StA) for 1 h. Then vehicle control (for the tetrazine-modified biotins) was added and incubated for 4 h. The cells were fixed and permeabilised, and a streptavidin AZDye 647 conjugate (grey) was added to visualise the background fluorescence. The nuclei were counterstained with Hoechst 33342 (blue) for reference.*
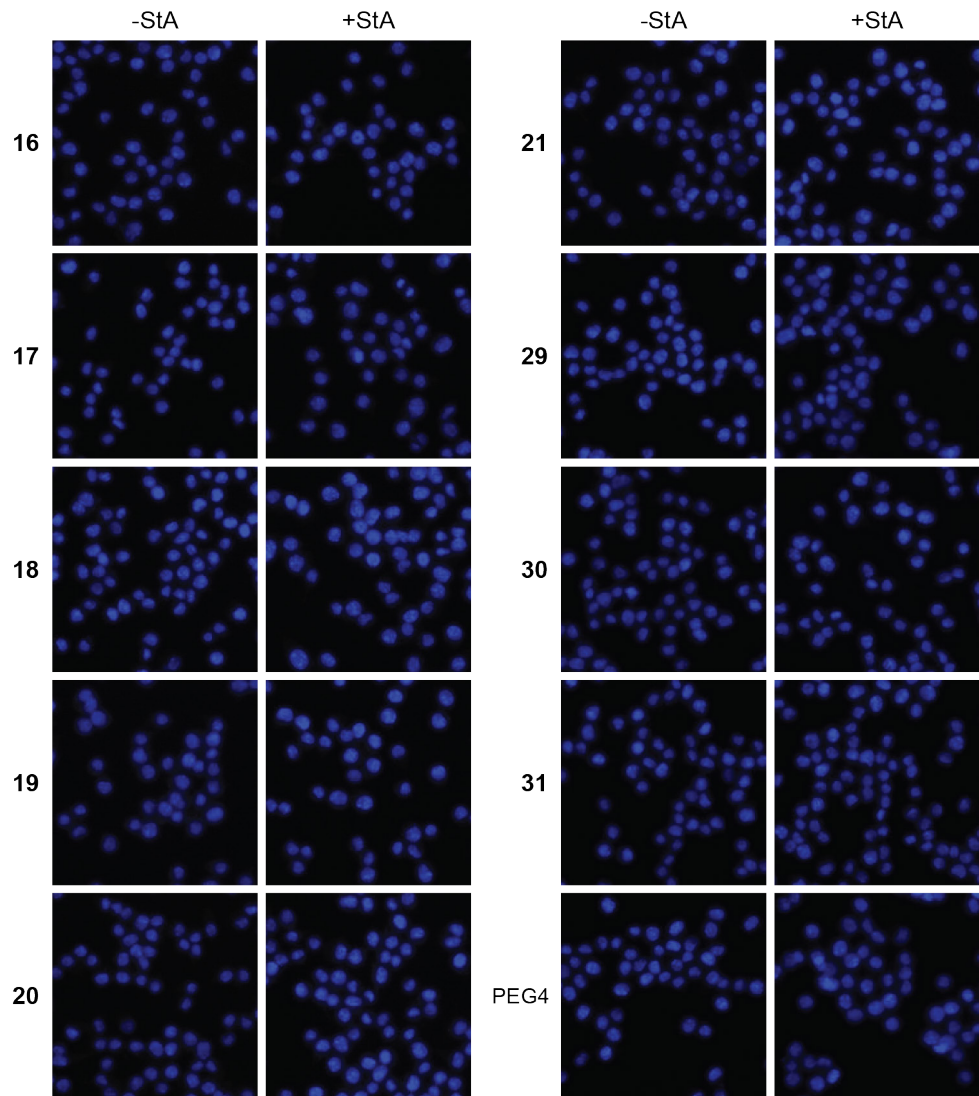
*Figure S5: Control fluorescent microscopy to ensure there is no background fluorescence when the tetrazine-modified biotins **16-21, 29-31**, and biotin-PEG4-tetrazine are not added to fixed DC2.4 cells. To allow uptake of the fatty acid, the cells were incubated with sterculic acid (+StA, 100 µM) or vehicle control (-StA) for 1 h. The cells were fixed and permeabilised, and the vehicle control (for the tetrazine-modified biotins) was added and incubated for 4 h. A streptavidin AZDye 647 conjugate (grey) was added to visualise the background fluorescence. The nuclei were counterstained with Hoechst 33342 (blue) for reference.*
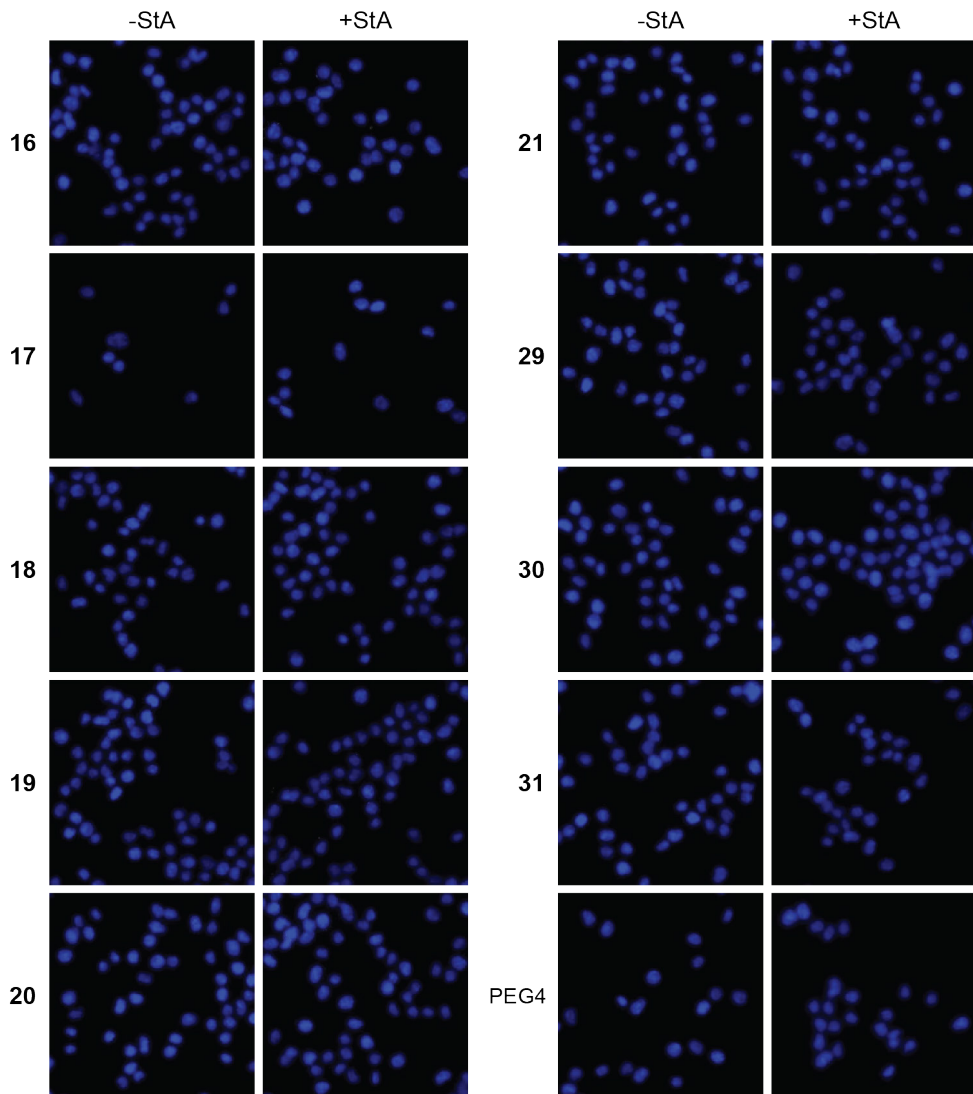
Figure S6: *Control fluorescent microscopy to ensure there is no background fluorescence when the tetrazine-modified biotins **16-21**, **29-31**, and biotin-PEG4-tetrazine are added to live DC2.4 cells but immediately washed away. To allow uptake of the fatty acid, the cells were incubated with sterculic acid (+StA, 100 μM) or vehicle control (-StA) for 1 h. Then vehicle control (for the tetrazine-modified biotins) was added and incubated for 4 h. The cells were fixed and permeabilised, and a streptavidin AZDye 647 conjugate (grey) was added to visualise the background fluorescence. The nuclei were counterstained with Hoechst 33342 (blue) for reference.*
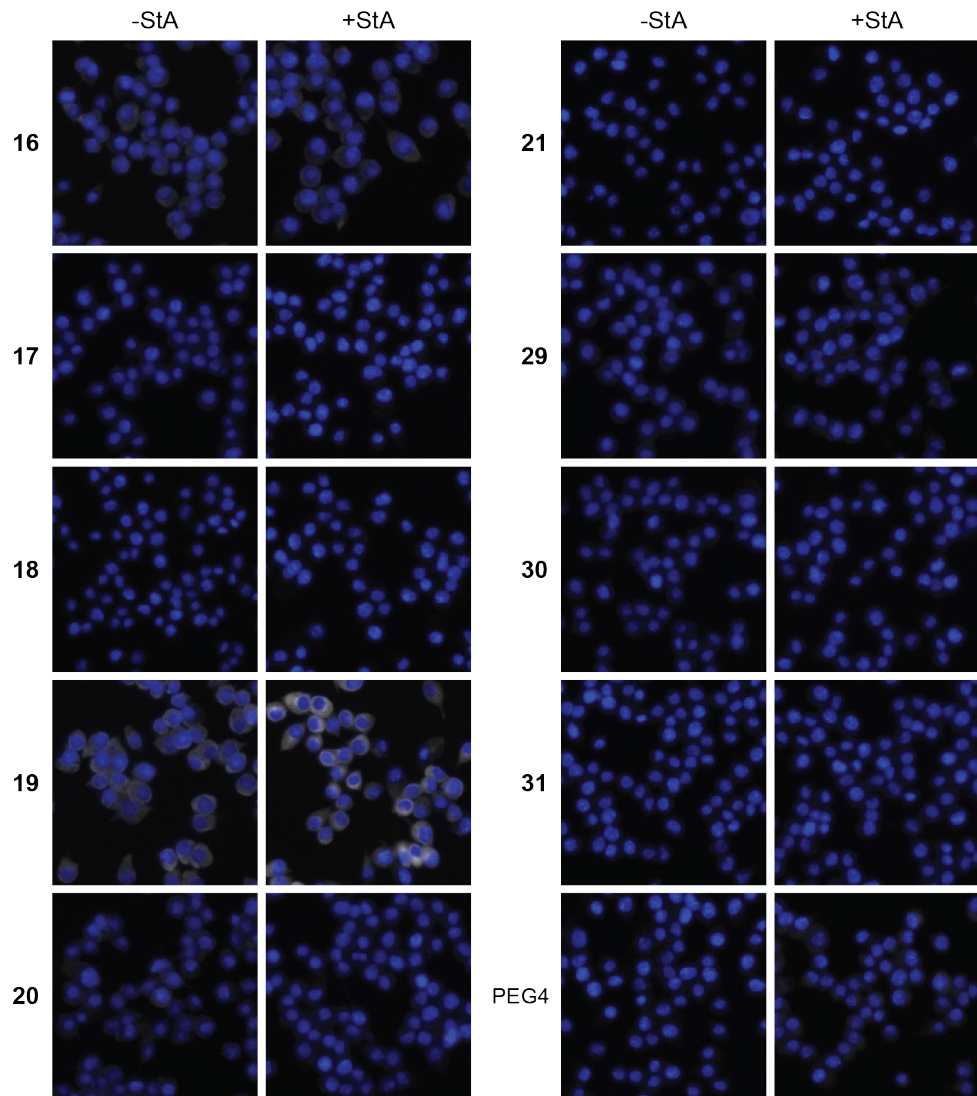
Figure S7: Control fluorescent microscopy to ensure there is no background fluorescence when the tetrazine-modified biotins *16-21*, *29-31*, and biotin-PEG4-tetrazine are added to fixed DC2.4 cells but immediately washed away. To allow uptake of the fatty acid, the cells were incubated with sterculic acid (+StA, 100 µM) or vehicle control (-StA) for 1 h. The cells were fixed and permeabilised, and the vehicle control (for the tetrazine-modified biotins) was added and incubated for 4 h. A streptavidin AZDye 647 conjugate (grey) was added to visualise the background fluorescence. The nuclei were counterstained with Hoechst 33342 (blue) for reference.

Table S1: *List of gene names of the proteins that were found to be significantly enriched with sterculic acid (StA) in immature or mature DC2.4 cells, using compounds 17 or 19. The proteins that were also found to be significantly StA-enriched with biotin-PEG4-tetrazine are underlined.*

Compound **17** in immature DC2.4s	Compound **17** in mature DC2.4s	Compound **19** in immature DC2.4s	Compound **19** in mature DC2.4s
Fbxo4	Fbxo4	_Gk_	_Gk_
Dbnl	Rpl26	Tpcn1	Tpcn1
Lilrb4	Kif15	_Vdac2_	_Vdac2_
Tp53bp1	Fam129b	Apc2	Plscr1
Hnrnpd	Mocos	Ptprj	Rab5c
Ppp2r2a/b/d	Morc3	Myo1g	Myo1c
	Gcat	Ckap4	Cds2
	Rars2	Slc23a2	Tbl3
	Rps13	Rpl5	_Tmem38b_
	Srsf4/6	Mmd2	Rdh11
		Lbr	Syk
			Rcc2
			Npm1
			Pigu
			Mtap
			Sfxn1
			Atp1a1

Immature DCs   **Mature DCs**

Compound **19**   Biotin-PEG4-tetrazine   Compound **19**   Biotin-PEG4-tetrazine
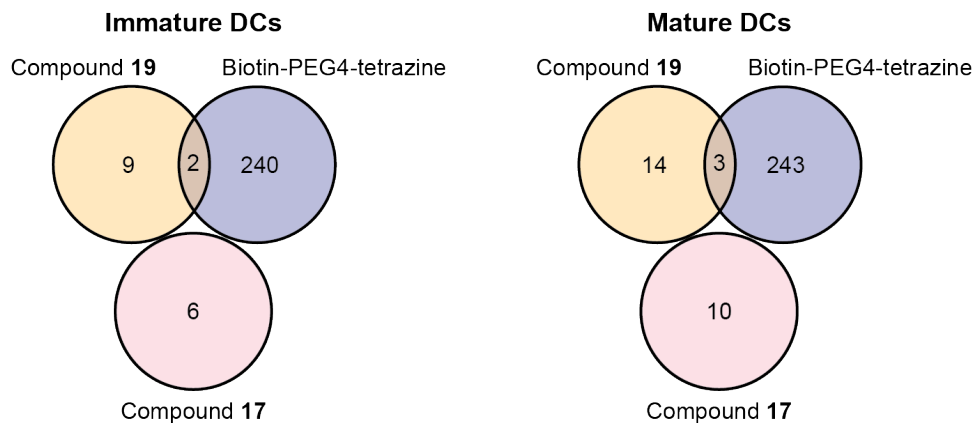
Figure S8: *Venn diagrams showing overlap in proteins that were found to be sterculic acid-enriched with compounds **17**, **19**, or biotin-PEG4-tetrazine in immature and mature DC2.4 cells.*

Table S2: *Significantly sterculic acid-enriched proteins with known immunological functions (as annotated by UniProt keyword KW-0391[47]), that were detected by compound **17** in immature or mature DC2.4 cells. Whether the proteins are known to be lipidated (as annotated by UniProt keyword KW-0449[47]) or membrane proteins (as annotated by UniProt keyword KW-0472[47]), is also indicated (with x).*

Immature			Mature		
	Lipidated	Membrane		Lipidated	Membrane
Dbnl		x	*Morc3*		
Lilrb4		x			

Table S3: *Significantly sterculic acid-enriched proteins with known immunological functions (as annotated by UniProt keyword KW-0391[47]), that were detected by compound **19** in immature or mature DC2.4 cells. Whether the proteins are known to be lipidated (as annotated by UniProt keyword KW-0449[47]) or membrane proteins (as annotated by UniProt keyword KW-0472[47]), is also indicated (with x).*

Immature			Mature		
	Lipidated	Membrane		Lipidated	Membrane
Myo1g		x	*Syk*		x

Table S4: *Significantly sterculic acid-enriched proteins with known immunological functions (as annotated by UniProt keyword KW-0391[47]), that were detected by biotin-PEG4-tetrazine in immature or mature DC2.4 cells. Whether the proteins are known to be lipidated (as annotated by UniProt keyword KW-0449[47]) or membrane proteins (as annotated by UniProt keyword KW-0472[47]), is also indicated (with x).*

Immature			Mature		
	Lipidated	Membrane		Lipidated	Membrane
Cd14	x	x	Cd14	x	x
Smpdl3b	x	x	Smpdl3b	x	x
Bst2	x	x	Bst2	x	x
Mavs	x	x	Mavs	x	x
Lat2	x	x	Lat2	x	x
Slc15a3		x	Slc15a3		x
Mcoln2		x	Mcoln2		x
Ctnnbl1			Ctnnbl1		
Bag6			Bag6		
Ppp6c			Irak4		
			Polr3c		

References

1. Ambrogelly, A., Palioura, S. & Söll, D. Natural expansion of the genetic code. *Nature Chemical Biology* **3**, 29–35 (2007).

2. Suazo, K. F., Park, K.-Y. & Distefano, M. D. A Not-So-Ancient Grease History: Click Chemistry and Protein Lipid Modifications. *Chem Rev* **121**, 7178–7248 (2021).

3. Resh, M. D. Fatty acylation of proteins: The long and the short of it. *Prog Lipid Res* **63**, 120–131 (2016).

4. Mann, R. K. & Beachy, P. A. Cholesterol modification of proteins. *Biochimica et Biophysica Acta (BBA) - Molecular and Cell Biology of Lipids* **1529**, 188–202 (2000).

5. Wang, M. & Casey, P. J. Protein prenylation: unique fats make their mark on biology. *Nature Reviews Molecular Cell Biology* **17**, 110–122 (2016).

6. Kinoshita, T. Biosynthesis and biology of mammalian GPI-anchored proteins. *Open Biology* **10**, 190290 (2020).

7. Yuan, Y. *et al.* Protein lipidation in health and disease: molecular basis, physiological function and pathological implication. *Signal Transduction and Targeted Therapy* **9**, 60 (2024).

8. Zhang, Y., Qin, Z., Sun, W., Chu, F. & Zhou, F. Function of Protein S-Palmitoylation in Immunity and Immune-Related Diseases. *Frontiers in Immunology* **12**, (2021).

9. Chesarino, N. M. *et al.* Chemoproteomics reveals Toll-like receptor fatty acylation. *BMC Biology* **12**, 91 (2014).

10. Kim, Y.-C. *et al.* Toll-like receptor mediated inflammation requires FASN-dependent MYD88 palmitoylation. *Nature Chemical Biology* **15**, 907–916 (2019).

11. Mukai, K. *et al.* Activation of STING requires palmitoylation at the Golgi. *Nature Communications* **7**, 11932 (2016).

12. Das, T., Yount, J. S. & Hang, H. C. Protein S-palmitoylation in immunity. *Open Biology* **11**, 200411 (2021).

13. Crise, B. & Rose, J. K. Identification of palmitoylation sites on CD4, the human immunodeficiency virus receptor. *Journal of Biological Chemistry* **267**, 13593–13597 (1992).

14. Balamuth, F., Brogdon, J. L. & Bottomly, K. CD4 Raft Association and Signaling Regulate Molecular Clustering at the Immunological Synapse Site1. *The Journal of Immunology* **172**, 5887–5892 (2004).

15. Arcaro, A. *et al.* Essential Role of CD8 Palmitoylation in CD8 Coreceptor Function1. *The Journal of Immunology* **165**, 2068–2076 (2000).

16. Kabouridis, P. S., Magee, A. I. & Ley, S. C. S-acylation of LCK protein tyrosine kinase is essential for its signalling function in T lymphocytes. *The EMBO Journal* **16**, 4983–4998 (1997).

17. Yurchak, L. K. & Sefton, B. M. Palmitoylation of Either Cys-3 or Cys-5 Is Required for the Biological Activity of the Lck Tyrosine Protein Kinase. *Molecular and Cellular Biology* **15**, 6914–6922 (1995).

18. Kosugi, A. *et al.* A pivotal role of cysteine 3 of Lck tyrosine kinase for localization to glycolipid-enriched microdomains and T cell activation. *Immunology Letters* **76**, 133–138 (2001).

19. Flores, J., White, B. M., Brea, R. J., Baskin, J. M. & Devaraj, N. K. Lipids: chemical tools for their synthesis, modification, and analysis. *Chem Soc Rev* **49**, 4602–4614 (2020).

20. Jao, C. Y., Roth, M., Welti, R. & Salic, A. Metabolic labeling and direct imaging of choline phospholipids in vivo. *Proceedings of the National Academy of Sciences* **106**, 15332–15337 (2009).

21. Jao, C. Y., Roth, M., Welti, R. & Salic, A. Biosynthetic Labeling and Two-Color Imaging of Phospholipids in Cells. *ChemBioChem* **16**, 472–476 (2015).

22. Martin, B. R. & Cravatt, B. F. Large-scale profiling of protein palmitoylation in mammalian cells. *Nature Methods* **6**, 135–138 (2009).

23. Charron, G. *et al.* Robust Fluorescent Detection of Protein Fatty-Acylation with Chemical Reporters. *J Am Chem Soc* **131**, 4967–4975 (2009).

24. Yap, M. C. *et al.* Rapid and selective detection of fatty acylated proteins using ω-alkynyl-fatty acids and click chemistry. *Journal of Lipid Research* **51**, 1566–1580 (2010).

25. Thinon, E. *et al.* Global profiling of co- and post-translationally N-myristoylated proteomes in human cells. *Nat Commun* **5**, 4919 (2014).

26. Wright, M. H. *et al.* Global Analysis of Protein N-Myristoylation and Exploration of N-Myristoyltransferase as a Drug Target in the Neglected Human Pathogen Leishmania donovani. *Chemistry & Biology* **22**, 342–354 (2015).

27. Boyle, P. C. *et al.* Detecting N-myristoylation and S-acylation of host and pathogen proteins in plants using click chemistry. *Plant Methods* **12**, 38 (2016).

28. Storck, E. M. *et al.* Dual chemical probes enable quantitative system-wide analysis of protein prenylation and prenylation dynamics. *Nature Chemistry* **11**, 552–561 (2019).

29. Kallemeijn, W. W. *et al.* Proteome-wide analysis of protein lipidation using chemical probes: in-gel fluorescence visualization, identification and quantification of N-myristoylation, N- and S-acylation, O-cholesterylation, S-farnesylation and S-geranylgeranylation. *Nature Protocols* **16**, 5083–5122 (2021).

30. Hang, H. C. *et al.* Chemical Probes for the Rapid Detection of Fatty-Acylated Proteins in Mammalian Cells. *J Am Chem Soc* **129**, 2744–2745 (2007).

31. Martin, D. D. O. *et al.* Rapid detection, discovery, and identification of post-translationally myristoylated proteins during apoptosis using a bio-orthogonal azidomyristate analog. *The FASEB Journal* **22**, 797–806 (2008).

32. Kostiuk, M. A. *et al.* Identification of palmitoylated mitochondrial proteins using a bio-orthogonal azido-palmitate analogue. *The FASEB Journal* **22**, 721–732 (2008).

33. Witten, A. J. *et al.* Fluorescent imaging of protein myristoylation during cellular differentiation and development. *Journal of Lipid Research* **58**, 2061–2070 (2017).

34. Greaves, J. *et al.* Molecular basis of fatty acid selectivity in the zDHHC family of S-acyltransferases revealed by click chemistry. *Proceedings of the National Academy of Sciences* **114**, E1365–E1374 (2017).

35. Wilson, J. P., Raghavan, A. S., Yang, Y.-Y., Charron, G. & Hang, H. C. Proteomic Analysis of Fatty-acylated Proteins in Mammalian Cells with Chemical Reporters Reveals S-Acylation of Histone H3 Variants. *Molecular & Cellular Proteomics* **10**, M110.001198 (2011).

36. Yount, J. S. *et al.* Palmitoylome profiling reveals S-palmitoylation–dependent antiviral activity of IFITM3. *Nature Chemical Biology* **6**, 610–614 (2010).

37. Cui L, Liu M, Lai S, Hou H, Diao T, Zhang D, Wang M, Zhang Y, W. J. Androgen upregulates the palmitoylation of eIF3L in human prostate LNCaP cells. *Onco Targets Ther.* **12**, 4451–4459 (2019).

38. Sobocińska, J., Roszczenko-Jasińska, P., Ciesielska, A. & Kwiatkowska, K. Protein

Palmitoylation and Its Role in Bacterial and Viral Infections. *Frontiers in Immunology* **8**, (2018).

39. Thinon, E., Percher, A. & Hang, H. C. Bioorthogonal Chemical Reporters for Monitoring Unsaturated Fatty-Acylated Proteins. *ChemBioChem* **17**, 1800–1803 (2016).

40. Montigny, C. *et al.* S-Palmitoylation and S-Oleoylation of Rabbit and Pig Sarcolipin. *Journal of Biological Chemistry* **289**, 33850–33861 (2014).

41. Nůsková, H. *et al.* Stearic acid blunts growth-factor signaling via oleoylation of GNAI proteins. *Nature Communications* **12**, 4590 (2021).

42. Schwartz, R. & King, J. Frequencies of hydrophobic and hydrophilic runs and alternations in proteins of known structure. *Protein Science* **15**, 102–112 (2006).

43. Ray, A., Jatana, N. & Thukral, L. Lipidated proteins: Spotlight on protein-membrane binding interfaces. *Progress in Biophysics and Molecular Biology* **128**, 74–84 (2017).

44. Bertheussen, K. *et al.* Live-Cell Imaging of Sterculic Acid—a Naturally Occurring 1,2-Cyclopropene Fatty Acid—by Bioorthogonal Reaction with Turn-On Tetrazine-Fluorophore Conjugates. *Angewandte Chemie International Edition* **61**, (2022).

45. Devaraj, N. K., Hilderbrand, S., Upadhyay, R., Mazitschek, R. & Weissleder, R. Bioorthogonal Turn-On Probes for Imaging Small Molecules inside Living Cells. *Angewandte Chemie International Edition* **49**, 2869–2872 (2010).

46. Sarris, A. J. C. *et al.* Fast and pH-Independent Elimination of trans-Cyclooctene by Using Aminoethyl-Functionalized Tetrazines. *Chemistry – A European Journal* **24**, 18075–18081 (2018).

47. UniProt: the Universal Protein Knowledgebase in 2023. *Nucleic Acids Research* **51**, 523–531 (2023).

48. Landmann, R. *et al.* Human monocyte CD14 is upregulated by lipopolysaccharide. *Infection and Immunity* **64**, 1762–1769 (1996).

49. Mahnke, K. *et al.* CD14 is Expressed by Subsets of Murine Dendritic Cells and Upregulated by Lipopolysaccharide BT - Dendritic Cells in Fundamental and Clinical Immunology: Volume 3. in (ed. Ricciardi-Castagnoli, P.) 145–159 (Springer US, Boston, MA, 1997). doi:10.1007/978-1-4757-9966-8_25.

50. Song, F. *et al.* Regulation and biological role of the peptide/histidine transporter SLC15A3 in Toll-like receptor-mediated inflammatory responses in macrophage. *Cell Death & Disease* **9**, 770 (2018).

51. Nakamura, N. *et al.* Endosomes are specialized platforms for bacterial sensing and NOD2 signalling. *Nature* **509**, 240–244 (2014).

52. Wang, Y. *et al.* Expression and Regulation of the Proton-Coupled Oligopeptide Transporter PhT2 by LPS in Macrophages and Mouse Spleen. *Molecular Pharmaceutics* **11**, 1880–1888 (2014).

53. Condamine, T. *et al.* Tmem176B and Tmem176A are associated with the immature state of dendritic cells. *Journal of Leukocyte Biology* **88**, 507–515 (2010).

54. Louvet, C. *et al.* Identification of a New Member of the CD20/FcεRIβ Family Overexpressed in Tolerated Allografts. *American Journal of Transplantation* **5**, 2143–2153 (2005).

55. Lin, H. Protein cysteine palmitoylation in immunity and inflammation. *The FEBS Journal* **288**, 7043–7059 (2021).

56. West, S. J., Boehning, D. & Akimzhanov, A. M. Regulation of T cell function by protein S-acylation. *Frontiers in Physiology* **13**, (2022).

57. He, L. *et al.* The Solute Carrier Transporter SLC15A3 Participates in Antiviral

Innate Immune Responses against Herpes Simplex Virus-1. *Journal of Immunology Research* **2018**, 5214187 (2018).

58. R Core Team. R: A Language and Environment for Statistical Computing. Preprint at (2023).

59. Ritchie, M. E. *et al.* limma powers differential expression analyses for RNA-sequencing and microarray studies. *Nucleic acids research* **43**, (2015).

60. Perez-Riverol, Y. *et al.* The PRIDE database resources in 2022: a hub for mass spectrometry-based proteomics evidences. *Nucleic acids research* **50**, 543–552 (2022).

4

Phenotypic and Multiomic Differences Between T cells with a Differential Sterculic Acid Uptake

Abstract

T cells undergo rapid metabolic reprogramming during activation to support the high energy demands of cell growth and proliferation. This metabolic shift is supported by the uptake of exogenous nutrients from the cells' environment. For certain nutrients, such as glutamine and glucose, the uptake mechanisms and biological effects of high or low uptake are well understood. This is less the case for fatty acids, where neither the uptake mechanism nor the precise biological effects of uptake have been characterized. Here this problem is addressed using bioorthogonal chemistry: by exposing splenocytes to sterculic acid, a bioorthogonal analogue of oleic acid, followed by fluorescent-activated cell sorting, a method was developed to multiplex nutrient uptake with phenotypic, proteomic, and transcriptomic differences on a single-cell level. Cells with a high uptake of exogenous sterculic acid took on a more effector-like phenotype and metabolism compared to low-uptake cells. Additionally, these cells upregulated the expression of key genes and proteins related to glucose metabolism, fatty acid synthesis, and the mevalonate pathway, also indicating a more effector-like state. These effects became more pronounced if the T cells were activated *in vitro* with αCD3/αCD28 antibodies prior to sterculic acid uptake.

Introduction

Upon activation, T cells undergo a rapid metabolic reprogramming to support their increased cell growth and proliferation. During the activation process, quiescent T cells, which mainly rely on catabolic metabolism and oxidative phosphorylation (OXPHOS) for their energy supply, shift their metabolism towards aerobic glycolysis and anabolism to support their high energetic and biosynthetic demands.[1–3]

Interestingly, this metabolic shift is heavily supported by an increased uptake of exogenous nutrients such as glucose and amino acids.[4,5] The uptake of exogenous free fatty acids (FFAs) are known to be essential for the activation and survival of several T cell subsets.[6,7] While fatty acids (FAs) in quiescent T cells are prone to degradation via fatty acid oxidation (FAO) to fuel ATP production via OXPHOS, T cells upregulate *de novo* fatty acid synthesis and fatty acid uptake upon activation.[6] Furthermore, activated T cells are known to upregulate other lipid biosynthetic pathways such as cholesterol biosynthesis, to support their increased need for membrane components.[8] A more detailed description of the metabolic reprogramming of T cells upon activation can be found in Chapter 1.

Previous work has shown that the exposure of T cells to oleic acid (OA) affects their survival, proliferation, activation, and differentiation.[9–15] However, since the use of the native form of OA in these experiments does not allow for the detection of intracellular OA, limited information about the actual cellular OA uptake on a single-cell level could be gathered. Additionally, it could not be determined if the observed effects were a result of extracellular exposure of OA in the culture medium, or cellular uptake of OA.

This thesis has demonstrated the effective manner by which the bioorthogonal OA analogue, sterculic acid (StA), can be used to study fatty acid uptake in cells. In this Chapter, the uptake of StA in primary cells isolated from mouse spleens was explored at a single-cell level. Murine splenocytes are a heterogenous population of immune cells, but contain a large portion of T cells (~30-35%).[16,17] It was therefore envisaged that the detection of StA, using the mild inverse electron-demand Diels-Alder (IEDDA) reaction, could be used to distinguish cells with a high and low FA uptake within the heterogenous splenocyte mixture. The focus was to identify factors governing the ability of a cell to take up FAs during activation. Differences between populations after short pulses of FA uptake, at times before or after activation, were deemed to be the most informative, rather than examining the phenotype of the cells long after immune activation to determine the functional effect of FA uptake on later phenotypes.

With these proof-of-principle experiments, the uptake of StA was monitored on a single-cell level by fluorescent detection with flow cytometry. Simultaneously, proteomic and transcriptomic differences between cells with differential StA uptake were explored. The transcriptomic differences were investigated using single-cell RNA sequencing (scRNAseq), to gain further insight into how the heterogeneous splenocyte population responded to the uptake of exogenous StA.

Results & Discussion

As a strategy to multiplex OA uptake with phenotypic and multiomic information, a workflow was developed where murine splenocytes were exposed to StA (Figure 1). In order to do this, the method described in Chapter 2 of this thesis was re-developed: Splenocytes – isolated from fresh mouse spleens by mechanical homogenization[18] – were incubated with a short pulse of StA (Figure 1A) and the cyclopropene group was used to perform an inverse electron-demand Diels-Alder (IEDDA) click reaction with fluorophore **7** (Figure 1B).

The cells were analysed by flow cytometry and a variation in fluorescent signal spanning one order of magnitude was observed in a single sample (Figure S1A), suggesting highly heterologous fatty acid uptake in this complex mixture of immune cells. In addition, the same experiment was performed after first activating the T cell population within the splenocytes. Incubation with αCD3/αCD28 antibodies[19] overnight, prior to lipid uptake analysis, would allow a comparative exploration of the fatty acid uptake in both naïve and activated T cells in comparison – all within the complex mixture of other immune cells of the spleen – to investigate potential differences in the response upon activation. Upon T cell activation with αCD3/αCD28, the variation in fluorescent signal during flow cytometry increased to almost two orders of magnitude (Figure S1B).

To determine whether any cell-type intrinsic factors were responsible for the differences in lipid uptake, the high and low uptake cells were isolated by fluorescence-activated cell sorting (FACS, Figure 1C). The fluorescence of **7** was used to separate the highest and lowest quartile of cells based on StA uptake for further analysis of their metabolism, transcriptomes, and proteomes (Figure 1D).

A) Sterculic acid uptake

B) IEDDA click reaction

Sterculic acid

Splenocytes

Low-uptake cell   High-uptake cell

Click!

Low fluorescence   High fluorescence

C) Cell sorting (FACS)

D) Analysis method

Single-cell RNAseq

Seahorse analysis

Proteomics
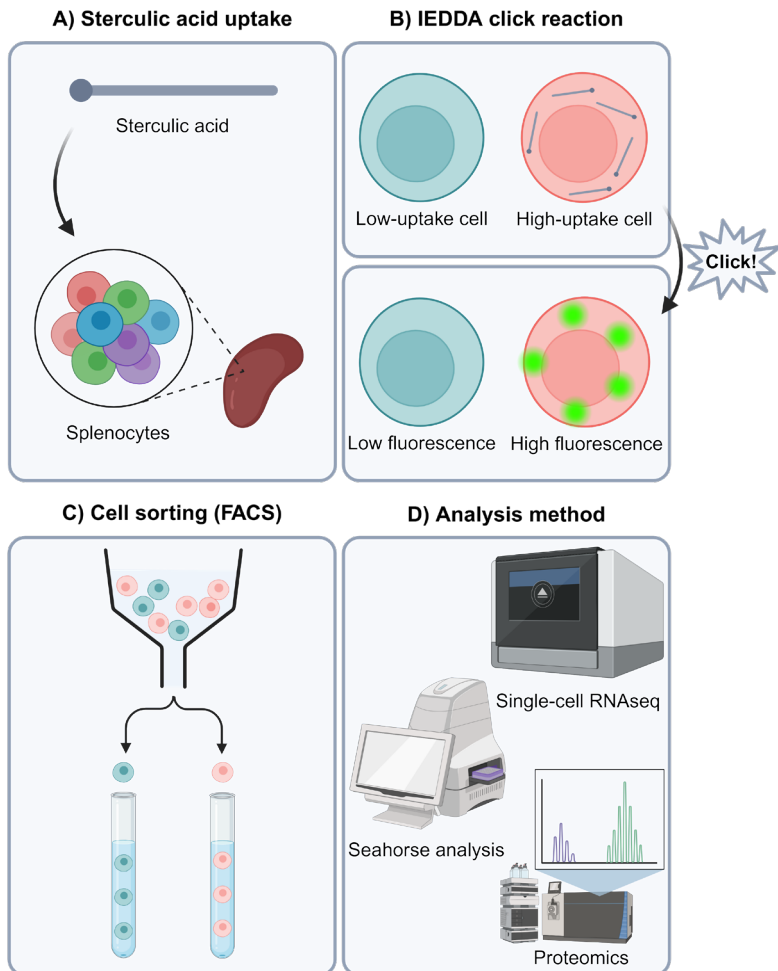
Figure 1: Illustration showing an overview of the workflow from ***A)*** *sterculic acid uptake in murine splenocytes,* ***B)*** *inverse electron-demand Diels-Alder (IEDDA) reaction,* ***C)*** *fluorescence-activated cell sorting (FACS), and* ***D)*** *the subsequent analysis methods. The figure is made with BioRender.*

Phenotypic differences between T cells with differential StA-uptake

To focus initially on a smaller subset of cells from the complex splenocyte mixture, the highest and lowest quartile of StA uptake in CD3+/CD4+ T cells were sorted by FACS according to the gating strategies shown in Figure S1. The well-known T cell activation markers CD44 and CD62L[20,21] were also included in the antibody panel.

Upon analysis of the cells with differential StA-uptake by flow cytometry, it was apparent that the size of the high-uptake cells was larger than the low-uptake cells, based on median forward scatter (FSC), for both naïve (Figures 2A & 2B) and

activated (Figures 2C & 2D) CD3+/CD4+ T cells. The activated T cells also showed increased cellular granularity, as measured by median side scatter (SSC), upon high StA-uptake (Figures 2C & 2D). However, no difference in cellular granularity was observed for the naïve T cells (Figures 2A & 2B). Increased cell size and granularity is known to occur in T cells upon activation[22,23], and the increased cell size has (partially) been attributed to an increase in activity of mammalian target of rapamycin (mTOR), a key regulator of many facets of cellular metabolism.[24] Therefore, these results could indicate that the high-uptake T cells are in a more effector-like state than the low-uptake cells, and that the differentiation of these cells affect their ability to take up exogenous FAs.
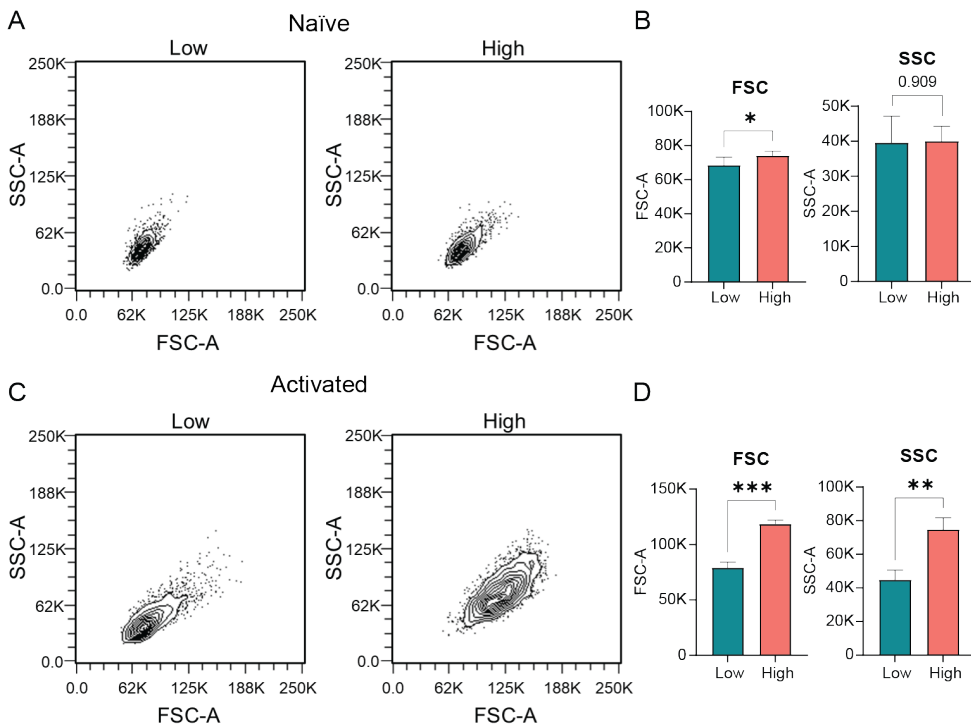
Figure 2: CD3+/CD4+ T cells with high StA-uptake are larger and more granulated than low-uptake cells, especially when activated. A) Forward scatter (FSC) and side scatter (SSC) plots of the low- and high-uptake populations of naïve T cells, and subsequent B) quantification of the median FSC and SSC (based on 5 biological replicates). C) Forward scatter (FSC) and side scatter (SSC) plots of the low- and high-uptake populations of activated T cells, and subsequent D) quantification of the median FSC and SSC (based on 3 biological replicates). Unpaired, two-way, student's T test. * = P ≤ 0.05, ** = P ≤ 0.01, *** = P ≤ 0.001

Upon further investigation of the FACS data it became clear that there was a shift in the expression of the CD44 and CD62L markers in the high-uptake population compared to the low-uptake population of naïve T cells, (Figure 3A). Upon quantification of the median fluorescence intensity (MFI), a trend of increased CD44 expression is observed, while CD62L expression was significantly decreased at the cell surface in the high-uptake population (Figure 3B). Again, this indicates that the

cells in the high-uptake population are in a more activated state than the low-uptake population. For the activated T cells, all cells were activated by a αCD3/αCD28 antibody cocktail prior to StA uptake and FACS. Interestingly, a similar pattern was observed for the activated T cells where a trend towards increased expression of CD44 and decreased expression of CD62L at the cell surface was observed (Figures 3C & 3D). This suggests that the T cell population after *in vitro* activation is still a heterogeneous mixture of T cell subsets, and that the high StA-uptake population appears to be dominated by more effector-like T cells. This is in accordance with the previous observation of increased cell size (and granularity) of high-uptake T cells.
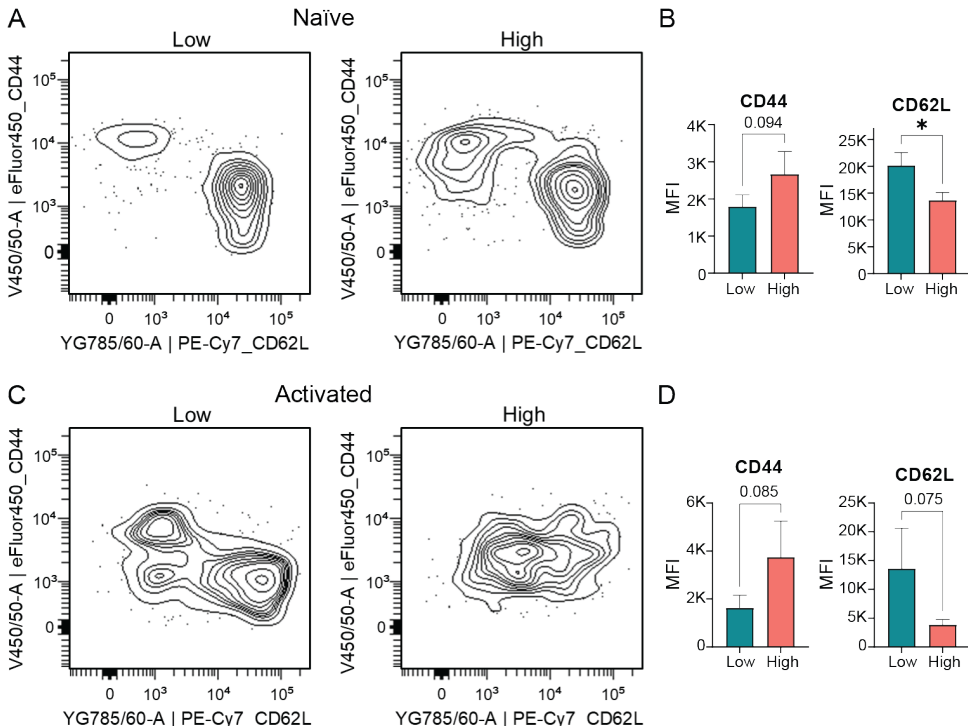
Figure 3: *CD3+/CD4+ T cells with a high StA-uptake show increased expression of CD44 and decreased expression of CD62L, compared to low-uptake cells, indicating T cell activation.* **A)** *Plots showing CD44 & CD62L expression of low- and high-uptake populations of naïve T cells, and subsequent* **B)** *quantification of median fluorescence intensity (MFI) of CD44 & CD62L expression (based on 3 biological replicates).* **C)** *Plots showing CD44 & CD62L expression of low- and high-uptake populations of activated T cells, and subsequent* **D)** *quantification of median fluorescence intensity (MFI) of CD44 & CD62L expression (based on 3 biological replicates). Unpaired, two-way, student's T test. * = P ≤ 0.05.*

Following cell sorting of CD3+/CD4+ T cells by FACS, the metabolic energetics of cells with low and high uptake of StA were also examined. The oxygen consumption rate (OCR) and extracellular acidification rate (ECAR) were measured using a Seahorse analyser[25], to assess changes in mitochondrial respiration and glycolysis, respectively. From these data, the percentage-wise reliance of these cells on oxidative phosphorylation (%OXPHOS) and glycolysis (%Glycolysis) were determined (Figure 4).

The metabolic energy map (Figure 4A) provides valuable insights into the metabolic phenotypes of both naïve and activated splenocytes and their T cell subsets. For naïve cells, both low- and high-uptake populations exhibit a quiescent metabolic phenotype. However, low-uptake cells appear more quiescent compared to their high-uptake counterparts. In contrast, the mixed, unsorted splenocyte population displays a more energetic phenotype, characterised by an overall higher metabolic capacity. Upon activation, the metabolic energy map reveals notable changes to the T cells energy profiles. Low-uptake T cells, while retaining a predominantly quiescent phenotype, show an increase in glycolytic capacity. High-uptake T cells exhibit an increase in both glycolytic and overall energetic capacities. Similarly, the mixed, unsorted splenocyte population demonstrates a more energetic phenotype, while maintaining a balance between glycolytic and oxidative pathways. These metabolic characteristics of naïve and activated T cells are in line with what is known from previous literature.[26–29]

For naïve cells (Figure 4B), low-uptake T cells show a minimal reliance on glycolysis, with approximately 3.3% of their energy resulting from glycolytic pathways. In contrast, high-uptake cells present with a significantly greater glycolytic reliance at around 66%. This increased glycolytic reliance of high-uptake T cells corresponds with the previous observations that these cells exist in an inherently more effector-like state than the low-uptake T cells.

In the activated cells (Figure 4C), the low-uptake T cells display a significant increase in glycolytic capacity compared to their naïve counterparts, rising to approximately 46.3%. High-uptake T cells maintain a similar reliance on glycolysis as in their naïve state, at around 47.8%, reflecting a metabolic phenotype characterised by an almost equal reliance on glycolysis and OXPHOS. Interestingly, no change in the glycolytic reliance for the high-uptake cells was observed here, indicating that the *in vitro* activation of these cells somehow overrides the metabolic differences observed in the naïve state.

While naïve cells show a more pronounced shift between OXPHOS and glycolysis, it's important to note that their energy maps display smaller differences between low and high uptake conditions. This apparent contradiction is due to the overall low metabolic output (both mitochondrial and glycolytic ATP) in naïve cells. Although the shift seems minor in absolute terms, it represents a significant percentage of the total ATP output. In contrast, activated cells present a different scenario. The apparent difference in energy maps between low and high uptake conditions primarily reflects the lower overall ATP production in low uptake cells, rather than fundamentally different metabolic patterns. Both high and low uptake activated cells maintain similar levels of OXPHOS and glycolysis. However, high uptake cells generate substantially more ATP, indicating higher metabolic activity.
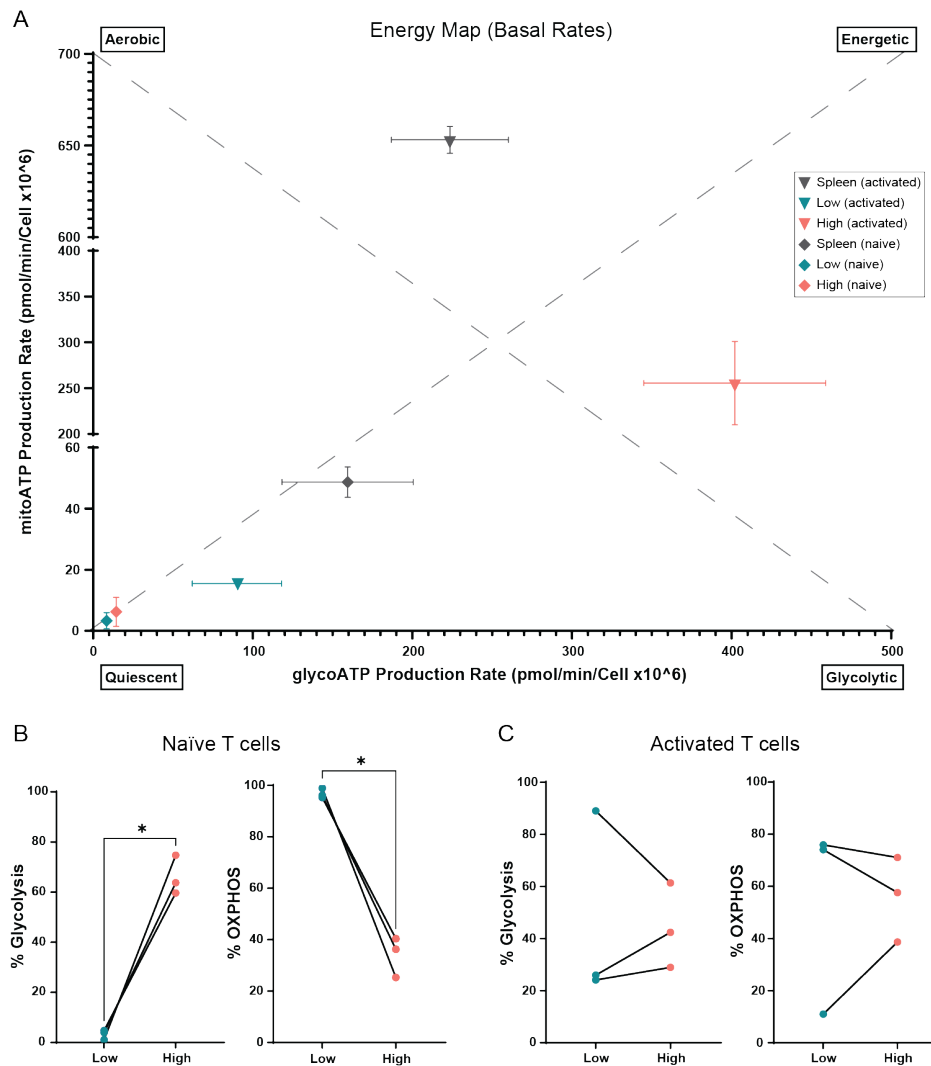
**Figure 4:** *Metabolic bioenergetics of CD3+/CD4+ T cells following StA uptake and cell sorting to high (pink) and low (blue) uptake. **A)** Energy map, MitoATP versus GlycoATP of the naïve and activated cells. **B)** Naïve T-cell high and low uptake of StA showing % glycolysis reliance, and % OXPHOS (Wilcoxons). **C)** Activated T-cell high and low uptake of StA showing % glycolysis reliance, and % OXPHOS (Wilcoxons).*

Proteomic differences between T cells with differential StA-uptake

It has already been suggested that CD4+ T cells with a high StA uptake have a more effector-like phenotype compared to low-uptake cells. This is exemplified by increased cell size (Figure 2), increased CD44 expression (Figure 3), decreased CD62L expression (Figure 3), as well as increased metabolic activity (Figure 4). To investigate if these phenotypic differences were rooted in differences at the proteomic level, a chemical proteomics approach was applied to study the T cells with a differential StA uptake. Similarly to the metabolic energetics, CD4+ T cells with differential StA uptake were sorted by FACS (Figure S1). The sorted cells were then lysed to isolate the cellular proteins, followed by tryptic digestion of the proteins into shorter peptide chains, and LC-MS/MS analysis.[30] The processed proteomics data were analysed using R Statistical Software.[31] Proteins were identified as significantly up- or downregulated in the high-uptake population if they had a log2 fold change >1 or <-1, respectively, as well as a p-value <0.05. To further investigate the metabolic bioenergetic shifts that were observed, proteins linked to metabolic alterations were focused upon.

At a first glance, the principal component analysis (PCA) based on the results from the naïve CD4+ T cells shows that the four replicates were quite different from each other (Figure 5A). Instead of the high- and low-uptake samples clustering together, there is a stronger tendency of the replicates clustering together. This indicates that most of the variance in the data is between replicates, and not between the experimental conditions (low- or high-uptake). Keeping this limitation in mind, the samples were assessed further, and a total of 4141 unique proteins were detected in the naïve samples. However, only 23 proteins were differentially expressed (22 upregulated and 1 downregulated in the high-uptake population, Table S1). The heatmap (Figure 5B) and volcano plot (Figure 5C) show the expression levels of the differentially expressed proteins (DEPs). The low number of DEPs could be explained by the discrepancies observed in the PCA.
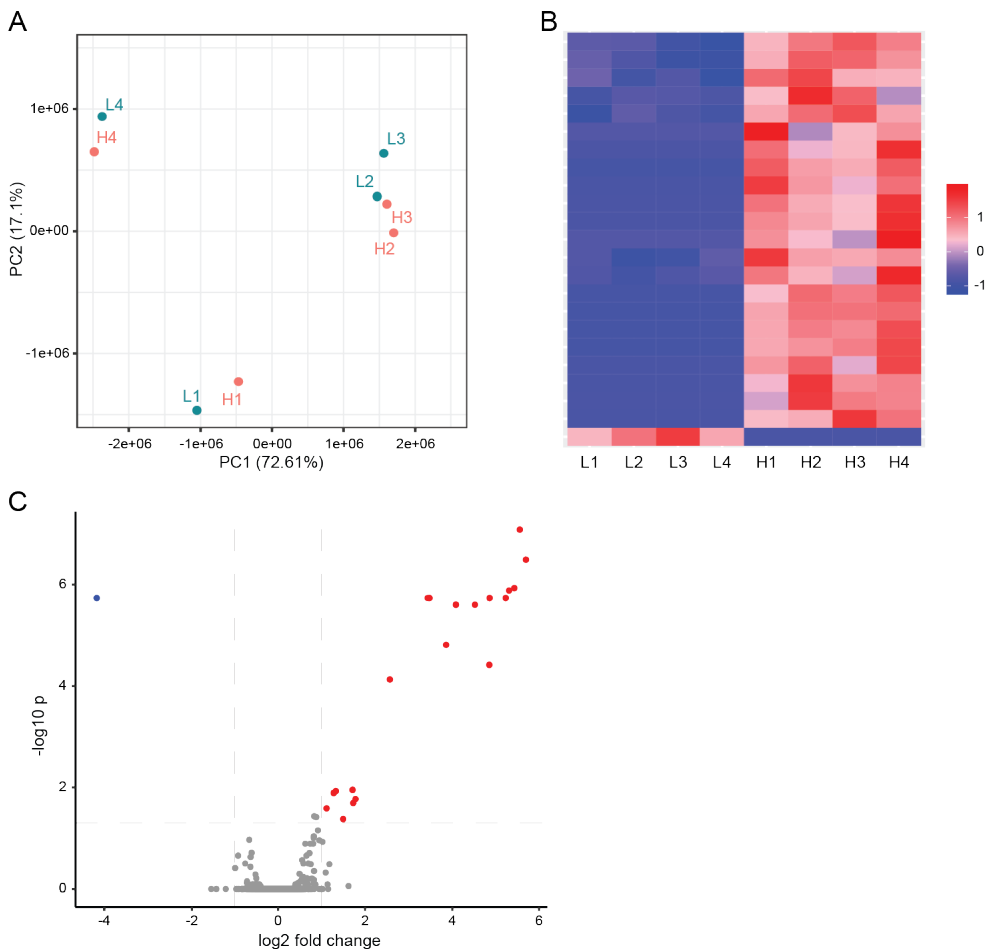
Figure 5: *Proteomics results from naïve CD3+/CD4+ T-cells, **A)** principal component analysis (PCA), **B)** heatmap, **C)** volcano plot. Red = upregulated, blue = downregulated. Based on 4 biological replicates.*

Among the DEPs, a few of the proteins were known to be involved in the proliferation and differentiation of CD4+ T cells. CDK1 and CD74 were upregulated in the high-uptake population (Figure 6A), where cyclin-dependent kinase 1 (CDK1) is a known regulator of the cell cycle, which drives cells through the G2 phase and mitosis.[32] In T cells, the CDK cascade has been proposed as a potential link between cell division and T cell differentiation via the phosphorylation of immunologically relevant transcription factors.[33] The upregulation of this protein in high StA-uptake T cells could indicate that the cells were in a more proliferative state than the low-uptake cells. While CD74 is mainly known as the invariant chain[34], which plays an important role in antigen presentation, recent research has also highlighted its role in T cell biology.[35–37] It has been shown to act as a receptor for the pleiotropic cytokine macrophage migration inhibitory factor (MIF), and is upregulated on the surface of activated CD4+ T cells supporting their migration.[38] CD74 has also been shown to be upregulated on tumour-infiltrating Tregs, where it facilitates accumulation and

function of these cells via stabilising FOXP3 expression.[39] The upregulation of CD74 in high-uptake CD4+ T cells could thereby indicate an increased proportion of activated cells, and potentially also Tregs, in this population. This is in line with previously observations from this Chapter.

Additionally, F-box only protein 7 (FBXO7), a known cell cycle regulatory protein[40], is downregulated in the high StA-uptake CD4+ T cells. The downregulation of FBXO7 has previously been shown to increase glycolysis in CD4+ T cells[41], which could help explain the observed increase in glycolysis in the high-uptake population (Figure 4B).

Looking at the other DEPs, no metabolic proteins related to glycolysis, the tricarboxylic acid (TCA) cycle, or lipid metabolism, as annotated by UniProt[42] keywords KW-0324, KW-0816, and KW-0443, respectively, were detected in the naïve samples. The UniProt protein database categorises protein entries into specific subsets based on for example biological function or cellular localisation.[42] From the pathway analysis (Figure 6B), using the clusterProfiler package[43] in R, it is clear that the proteins that were upregulated in the high-uptake T cells are mainly involved in chromosome condensation and segregation. This indicates that the high-uptake cells were in a more proliferative state where the chromosomes are duplicated and separated during mitosis, compared to the low-uptake cells.
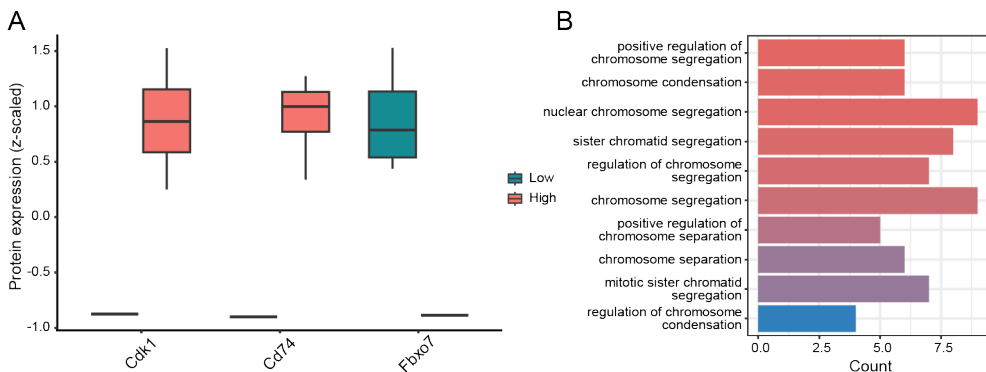
Figure 6: *Proteomics results from naïve CD3+/CD4+ T-cells,* **A)** *box plots of differentially expressed proteins that are involved in T cell biology,* **B)** *pathway analysis of all upregulated proteins (using the clusterProfiler package[43] in R). Based on 4 biological replicates.*

This data suggests two things. Firstly, the biology that underpins the changes in FA uptake in the naïve population may be stochastic in nature, rather than being fully reliant on pre-existing phenotypic differences between the cells. The second observation is that the naïve cells that take up more FA are in higher state of cell division, suggesting the presence of background T cell replication even in naïve unstimulated populations.

The same cell sorting and proteomic approach was applied to CD4+ T cells that had been activated in vitro using αCD3/αCD28 antibodies prior to StA uptake. The PCA following subsequent examination of the activated CD4+ T cells, shows a better separation between the low- and high-uptake conditions, and a better clustering of the respective replicates (Figure 7A). This is also reflected in the heatmap

(Figure 7B) and volcano plot (Figure 7C) where it is apparent that more proteins were differentially expressed than for the naïve samples. Of in total 4956 unique proteins that were detected, 358 were differentially expressed for the activated cells. Of the DEPs 204 were downregulated and 154 were upregulated in the high-uptake samples (Table S2).
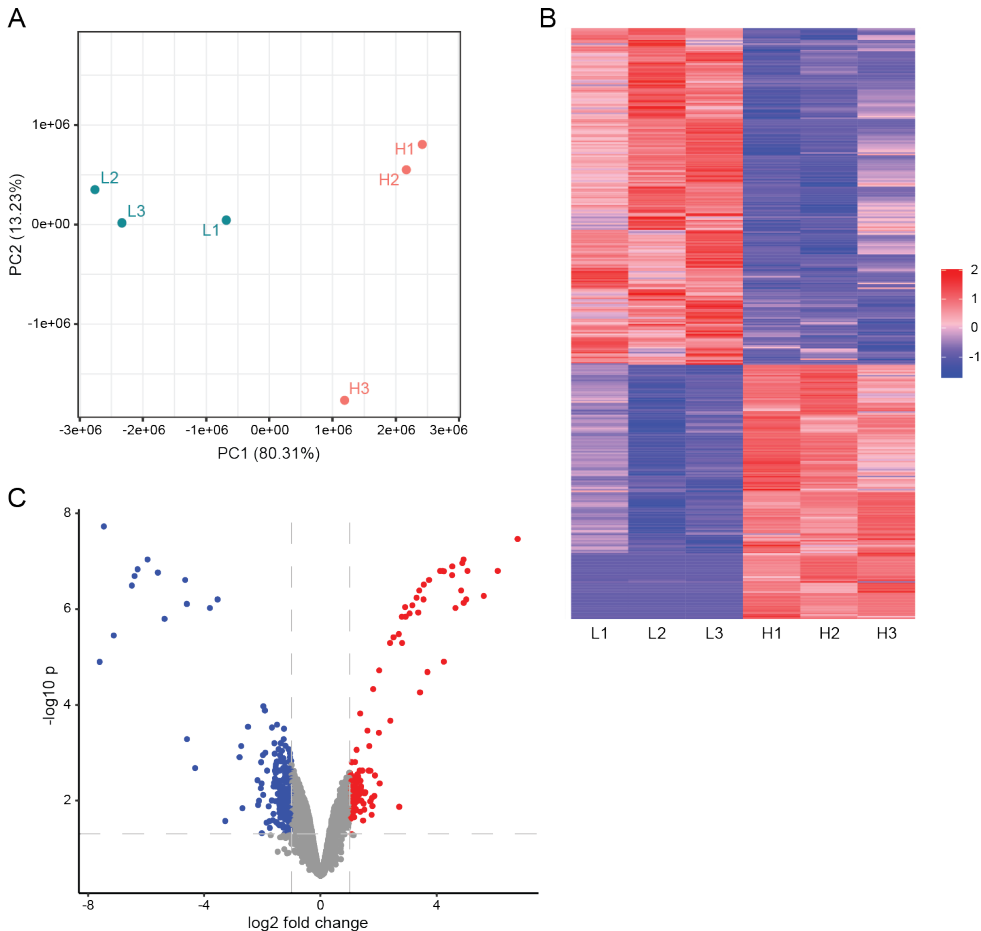
Figure 7: Proteomics results from αCD3/αCD28-activated CD3+/CD4+ T-cells, A) principal component analysis (PCA), B) heatmap, C) volcano plot. Red = upregulated, blue = downregulated. Based on 3 biological replicates.

Several proteins involved in cellular metabolism were identified as differentially expressed in the activated CD4+ T cells (Figure 8A). This includes HK2 and IRF4 which are involved in glucose metabolism. Hexokinase 2 (HK2) is the first rate-limiting step of glucose metabolism, phosphorylating glucose to glucose-6-phosphate.[44] Upon T cell activation, HK2 is known to be upregulated to support the increased metabolic requirements of these cells.[45–47] Interferon regulatory factor 4 (IRF4) has been implicated as an important transcription factor involved in the differentiation of T cell subsets upon activation, as well as controlling the metabolic shift of activated T cells.[48–51] It has even been proposed that IRF4 controls the expression of glycolytic

enzymes, there among HK2.[48]

Several proteins involved in fatty acid synthesis were also upregulated in the high StA-uptake, activated T cells (Figure 8A). The three proteins ATP citrate lyase (ACL, encoded by the gene *ACLY*), acetyl-CoA carboxylase (ACC1, encoded by the gene *ACACA*), and fatty acid synthase (FAS, encoded by the gene *FASN*) catalyse the *de novo* biosynthesis of palmitic acid from citrate, a product of the TCA cycle.[52,53] All three proteins were upregulated in the high StA-uptake T cells. The genes encoding these proteins have previously been reported to be upregulated in activated T cells[6,8,54], thereby supporting the current observations that the high-uptake CD4+ T cells take on a more activated phenotype.

The high StA-uptake T cells thereby appear to have an increased flux through glucose metabolism (as indicated by the upregulation of IRF4 and HK2), potentially to fuel the production of citrate and subsequent *de novo* fatty acid synthesis (via ACL, ACC1 and FAS), which fits the observations of the metabolic extracellular flux experiments (Figure 4).

Additionally, a number of proteins of the mevalonate pathway, where mevalonate is formed from HMG[55], were found to be upregulated in the high-uptake CD4+ T cells (Figure 8A). In the mevalonate pathway acetyl-CoA is turned into dimethylallyl pyrophosphate (DMAPP), which is further metabolised into geranyl pyrophosphate (GPP) and farnesyl pyrophosphate (FPP) via the enzyme farnesyl pyrophosphate synthase (FDPS).[56,57] FPP is a precursor for multiple other biosynthetic pathways such as cholesterol[58], ubiquinone[59], and dolichol[60] biosynthesis, as well as protein prenylation.[61] The proteins hydroxymethylglutaryl (HMG)-CoA synthase 1 (HMGCS1), phosphomevalonate kinase (PMVK), and isopentenyl-diphosphate delta isomerase 1 (IDI1) are all involved in different parts of this pathway. The mevalonate pathway is important for T cell activation and differentiation because it leads to increased cholesterol biosynthesis[62,63], ensuring sufficient production of an indispensable membrane component, especially during proliferation. Additionally, cholesterol is enriched in the immunological synapse and is essential for its proper function.[64–66] The upregulation of key enzymes in this pathway therefore further supports that high-uptake CD4+ T cells are more effector-like cells than the low-uptake cells.

The pathway analysis of DEPs in activated CD4+ T cells (Figure 8B), using the clusterProfiler package[43] in R, showed an upregulation of pathways involved in ribosomal biogenesis and protein translation in the high-uptake cells. This indicates a large general biosynthetic focus of these cells, which also fits with the previously described observations that the high-uptake cells were in a more effector-like or activated state.
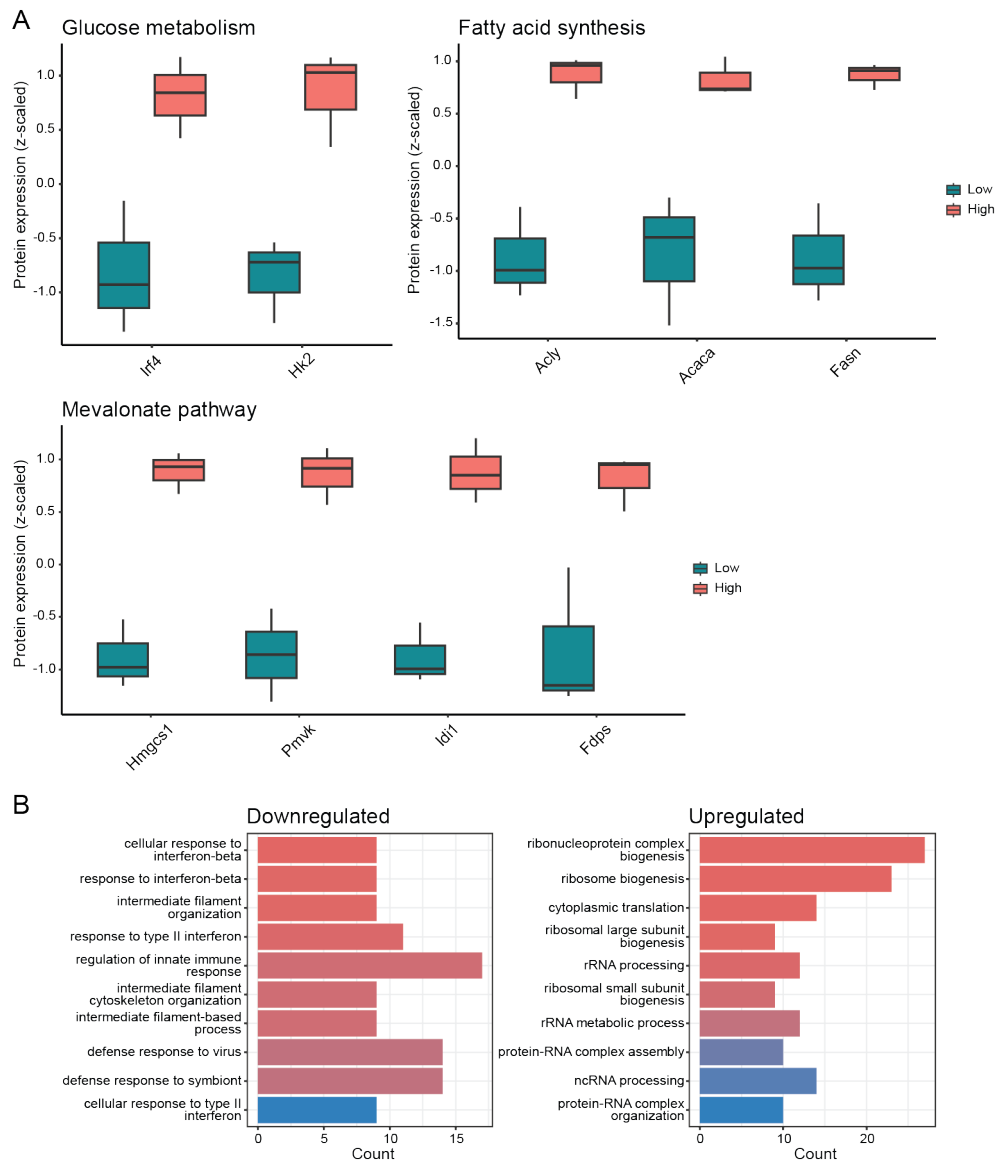
Figure 8: *Proteomics results from αCD3/αCD28-activated CD3+/CD4+ T-cells, **A)** box plots of significantly upregulated proteins that are involved in glucose metabolism, fatty acid synthesis, and the mevalonate pathway, **B)** pathway analysis of the downregulated and upregulated proteins separately (using the clusterProfiler package[43] in R). Based on 3 biological replicates.*

Single-cell RNA sequencing of splenocytes with differential StA-uptake

To complement the chemical proteomics data, and to gain further insight into how different immune cell subsets react to differential StA uptake, a single-cell RNA sequencing (scRNAseq) approach was also developed, using the 10x Genomics platform.[67] scRNAseq was chosen over bulk RNAseq due to the heterogeneity of the splenocyte population. However, since the splenocytes had to undergo an IEDDA click reaction prior to FACS, it was essential to ensure that the click reaction did not impact the integrity of the unstable RNA molecules.

Therefore, cells were treated with StA (or DMSO vehicle), before IEDDA reaction with fluorophore **7** was performed on either live, or fixed and permeabilised cells. The total cellular RNA was isolated from these samples and separated on agarose gel to visualise RNA integrity. Since cellular RNA consists mainly of ribosomal RNA (rRNA, 80-90%), the 28S and 18S rRNA subunits are the two bands that will be visible on the agarose gel, in a 2:1 ratio. When isolating RNA from fixed cells, a slight shift in the bands were visible compared to live cells, but there was no visible change in RNA integrity upon addition of StA, or after the IEDDA click reaction (Figure S2A). In contrast, the addition of oleic acid analogues containing alkyne or azide modifications (Figure S2D), and subsequent copper-catalysed azide-alkyne cycloaddition (CuAAC), showed visible RNA degradation (Figure S2B). To determine which component of the CuAAC mixture caused this degradation, each component was tested individually (Figure S2C). Only upon addition of the complete CuAAC mixture to the cells, RNA degradation occurred, implying that the active copper(I) species in the mixture, which is only present after reduction with sodium ascorbate, is responsible for the degradation. These results further demonstrate the benefits of using the IEDDA click reaction when studying unstable biomolecules such as RNA.

Taking advantage of the demonstrated RNA integrity after IEDDA click reaction, the scRNAseq approach was applied to study the transcriptomic differences on a complete splenocyte level, between the sorted high and low StA-uptake cells. The gating strategies for sorting naïve and αCD3/αCD28 activated splenocytes are shown in Figure S3.

The populations with the lowest and highest quartile of StA uptake, which were collected by FACS, were analysed using a 10x Genomics scRNAseq workflow in collaboration with the Leiden Genome Technology Center (LGTC). Upon quality control of the sequencing data, it was discovered that one sample, the high-uptake sample from naïve splenocytes, had significantly higher RNA counts per cell than the other samples (Figure S4). In fear of the high RNA counts from this sample skewing the data, the high- and low-uptake samples from naïve splenocytes were omitted from the remaining analysis. Further analysis was only performed on the high- and low-uptake samples from activated splenocytes.

The cells from the samples with activated splenocytes were clustered based on their gene expression. The resulting UMAP highlights substantial differences between the low- and high-uptake samples (Figure 9), where certain cell clusters are differentially present in the different uptake conditions.
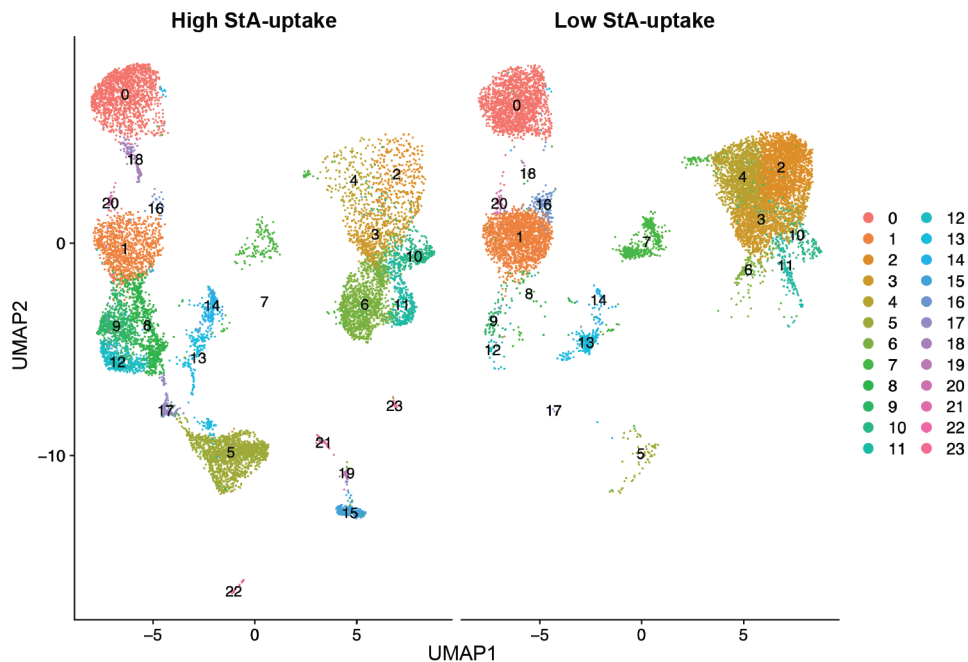
Figure 9: UMAP showing cell clustering based on gene expression from high- and low-StA uptake samples of activated splenocytes. The data is based on scRNAseq results.

Identification of the immune cell subsets corresponding to each cluster was done according to expression of relevant marker genes (Tables 1 & S3). This highlights that B cells (clusters 2-4, 6, 10-11) were mainly present in the low-uptake sample, whereas certain T, NKT, or NK cell clusters were mostly present in the high-uptake samples (clusters 5, 8-9, 12, 14, 18) or equally present in both low- and high-uptake samples (clusters 0-1, 13).

Table 1: Immune cell subsets corresponding to clusters identified from the scRNAseq analysis (from Figure 2). Relevant marker genes for the identification can be found in Table S3.

Cluster	Subset	Cluster	Subset	Cluster	Subset
0	CD4+ T cells	8	CD8+ T cells	16	CD8+ T cells
1	CD8+ T cells	9	CD8+ T cells	17	Mixed
2	B cells	10	B cells	18	CD4+ T cells
3	B cells	11	B cells	19	Monocytes
4	B cells	12	CD8+ NKT cells	20	Mixed
5	NK cells	13	CD4+ NKT cells	21	Monocytes
6	B cells	14	CD4+ Treg	22	NK cells
7	Mixed	15	Monocytes	23	Monocytes

From the FACS data, it was clear that the activated cells, and especially those taking up large amounts of StA, were larger (as seen by FSC) and more granulated (as seen by SSC), than the naïve and low-uptake cells (Figures 10A & 10B). Since the activated high-uptake population consists of a larger portion of NK cells and CD8+ T cells, and these cell types are known to match this morphology[22,23], this could help explain these differences. The low-uptake population consists of more B cells, which were not targeted by the αCD3/αCD28 activation, and could therefore explain why these cells appear smaller and less granulated. When the splenocytes were activated, the BODIPY signal is more widely distributed (Figure 10C), implying that there is more spread in the StA-uptake in these cells than for the naïve splenocytes.
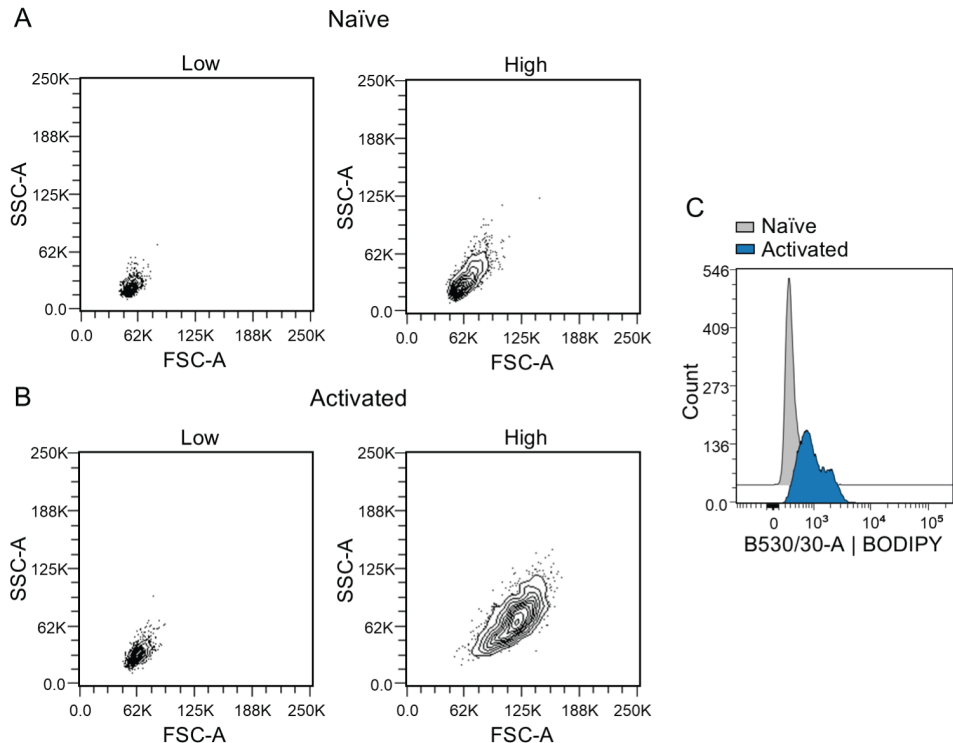
Figure 10: High-uptake cells are bigger and more granulated, especially in activated splenocytes. Based on forward scatter (FSC) and side scatter (SSC) of cells after sorting them into high- and low-StA uptake populations for scRNAseq of A) naïve splenocytes, B) αCD3/αCD28-activated splenocytes, C) Histogram showing the BODIPY signal (indicating StA uptake) of naïve or activated splenocytes (according to the gating strategies shown in Figure S2).

The focus of this section is on lymphocytes, and more specifically T cells, NKT cells, and NK cells. Superimposing the expression of the genes encoding the subunits of T cell co-receptor CD3 (*CD3E, CD3D*, and *CD3G*) onto the scRNAseq UMAP (Figure 11A), shows that different T cell subsets (CD4+, CD8+, Treg), as well as NKT cell subsets (CD4+, CD8+) express this pan T cell marker. Performing the same overlay with the T helper cell marker CD4 (*CD4*, Figure 11A), highlights the same clusters that were identified as CD4+ in Table 1, validating that approach. Focusing on the

clusters containing T, NKT, and NK cells (Figure 11B), again emphasises that NK cells, regulatory T cells (Tregs), and certain CD8+ T and NKT cell subsets were mainly present in the high-uptake population, CD4+ T cells and certain subsets of CD8+ T cells were similarly present in both, whereas CD4+ NKT cells were mainly present in the low-uptake population.
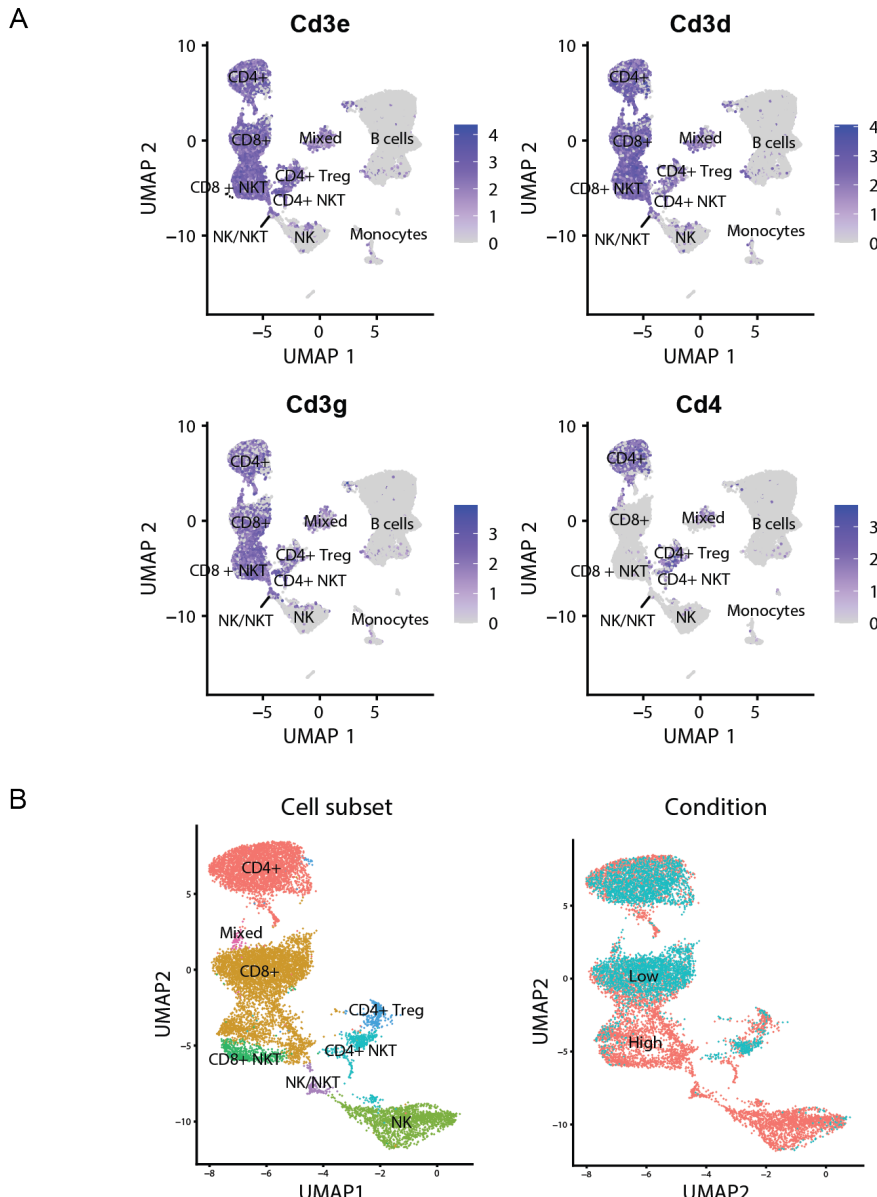
Figure 11: Subsections of the scRNAseq UMAP showing A) clusters expressing the genes encoding CD3 subunits (CD3E, CD3D, CD3G) and CD4, B) zoom-in on clusters of interest containing T, NKT, and NK cell (lymphocyte) subsets.

All the highlighted lymphocyte subsets can be categorized by their own distinct metabolic features to support their immunological functions. Conventional CD4+ or CD8+ T cells change their metabolic requirements upon activation.[3,68–71] While naïve or memory T cells rely heavily on FAO and OXPHOS to support their energetic needs, they undergo a switch to a highly glycolytic state, with increased *de novo* fatty acid synthesis, upon activation and differentiation into effector T cells. All these T cell subsets were included in the CD4+ and CD8+ clusters in Figures 9 & 11, and the wide metabolic range of these T cell subsets can explain the spread in observed StA-uptake by these cells.

NK cells are known to rely heavily on fatty acid uptake and FAO to fuel their effector functions[72,73], which could explain why they were mainly detected in the high StA-uptake population. Previous research has also put fatty acid uptake and FAO at the centre of Treg differentiation and function.[74–76] This is further supported by the localisation of Tregs mainly in the high StA-uptake population (Figures 9 & 11). While NKT cell development has been reported to require lipids[77], and *de novo* fatty acid synthesis is implicated in maintaining NKT cell homeostasis[78], not much is known about the uptake and metabolism of exogenous fatty acids in this cell type. No logical explanation can therefore be given to the observed discrepancy in StA-uptake between CD4+ (low uptake) and CD8+ (high uptake) NKT cells (Figures 9 & 11).

After selecting the clusters containing the lymphocyte subsets of interest, the focus was shifted to the expression of key metabolic genes involved in lipid metabolism and glycolysis in these clusters. These metabolic pathways were chosen because they are known to be differentially expressed, and utilised, by different lymphocyte subsets.[26–29] The expression of the relevant genes can be seen in Figures S5 & S6 and Figures S7 & S8, for lipid metabolism and glycolysis, respectively. It became clear that the expression of most of the genes were equally distributed across clusters, and show little differential expression based on differential StA uptake. However, some differentially expressed genes could be detected. For genes involved in fatty acid metabolism, *FASN*, *HMGCR*, and *CCR5* appear to be upregulated in the high-uptake cells (Figure 12A). This upregulation occurred across almost all the lymphocyte subsets (Figure 12B).

As previously explained, *FASN* encodes the enzyme fatty acid synthase (FAS) which catalyses the *de novo* synthesis of palmitic acid (C16:0) from acetyl-CoA and malonyl-CoA.[79] *De novo* fatty acid synthesis, and *FASN* specifically, has been shown to be necessary for the metabolic reprogramming of activated T cells.[6,8] *HMGCR* encodes HMG-CoA reductase, the enzyme catalysing the rate-limiting step of the mevalonate pathway, where mevalonate is formed from HMG.[55] *HMGCR* has been shown to be indispensable for T cell survival[80] and activation[81], and has also been shown to play a significant role in the cytotoxic activity of NK cells.[82] The upregulation of *FASN* and *HMGCR* could therefore indicate that the high StA-uptake cells were in a more activated state than the low-uptake cells. These results are in line with the observations that were made when looking at the proteomic differences between high and low StA-uptake populations (Figure 8A).

CCR5 encodes CC chemokine receptor 5, a receptor that can bind a number of chemokines such as CCL3, CCL4, and CCL5.[83] In NK and NKT cells, where this gene is mainly expressed (Figure 12B), *CCR5* has been shown to be important for

proper trafficking and function of these cells.[84,85]
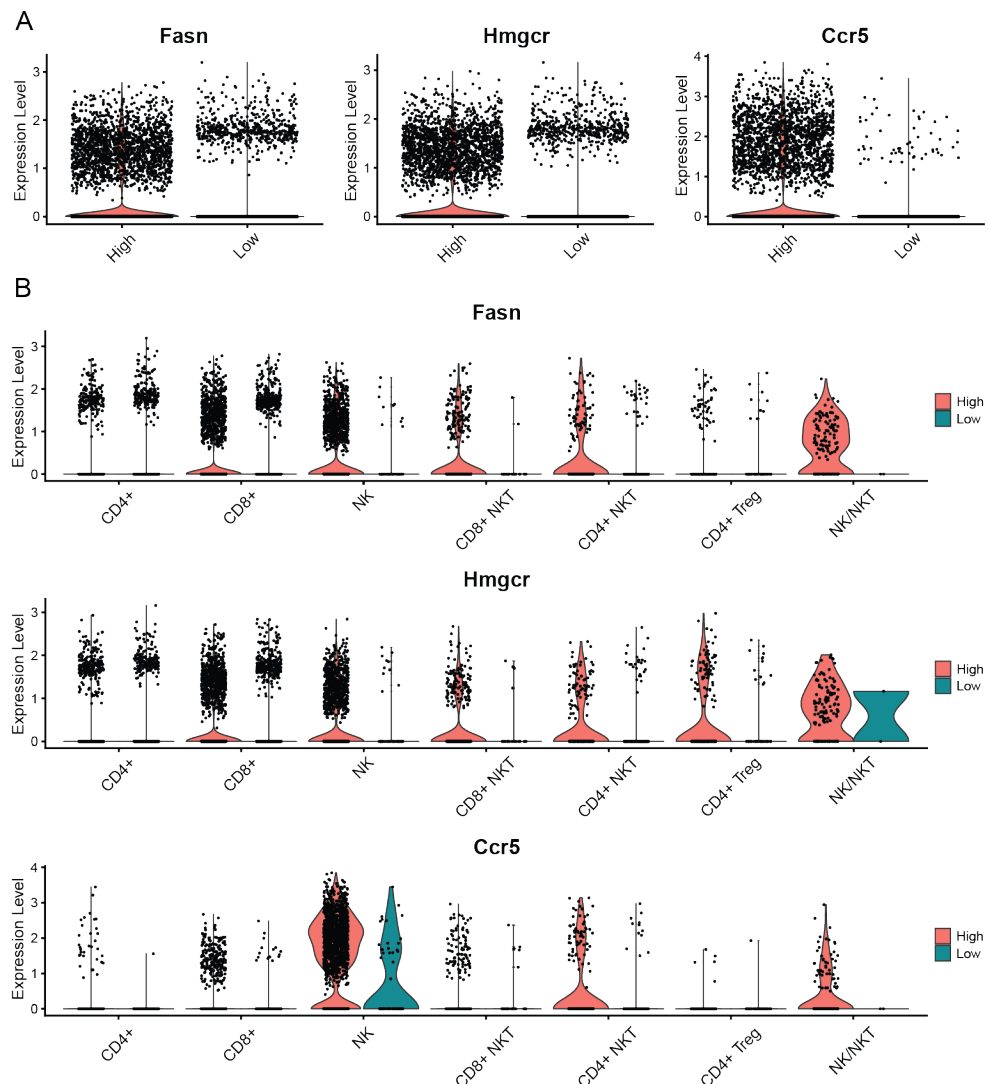
Figure 12: *Differentially expressed genes related to lipid metabolism from scRNAseq in the high- and low-uptake populations of T, NKT, and NK cells (lymphocytes), represented as violin plots. **A)** pooled data from all the relevant lymphocyte clusters, **B)** showing the data for the lymphocyte clusters separately.*

For the scRNAseq data presented here, it is important to note that the high-uptake cells were overrepresented in some clusters (e.g. CD8+ T cells, CD8+ NKT cells, and NK cells). This results in fewer data points for the low-uptake cells and could skew the data in the direction of genes appearing upregulated in the high-uptake cells. It can therefore not be said with certainty that the mentioned proteins were upregulated.

When focusing on genes involved in glycolysis, *LDHA*, *SREBF1*, *PIK3CA*, and *AKT2* appear to be upregulated in the high StA-uptake cells (Figure 13A). The upregulated genes were observed in almost all the lymphocyte subsets (Figure 13B).

LDHA encodes the enzyme lactate dehydrogenase A (LDHA) which is responsible for the last step of glycolysis where pyruvate is converted to lactate.[86] The deletion of *LDHA* has previously been shown to suppress glycolysis rates, as well as T cell proliferation and differentiation.[87] Similarly, effector T cells showed increased expression of *LDHA*, as a result of phosphoinositide-3-kinase (PI3K) signalling.[86] Here, the increased expression of *LDHA* could indicate an increased effector-like function of the high StA-uptake cells. This is further supported by the upregulation of *PIK3CA* and *AKT2*, genes encoding the catalytic PI3Kα subunit, and RAC-beta serine/threonine-protein kinase (AKT2), respectively. The PI3K-AKT axis has been implicated as an important signalling pathway for metabolic reprogramming in activating and differentiating T cells[88–90], and could explain the upregulation of *LDHA*, as well as indicating that the high-uptake cells have undergone this metabolic reprogramming into proliferating, highly glycolytically active cells. Interestingly, it appears that *PIK3CA* is downregulated in high StA-uptake Tregs, in contrast to all the other lymphocyte clusters where it is upregulated (Figure 13B). The reliance of Treg function and differentiation on PI3K is debated, and PI3K has been shown to both inhibit and support the development of this T cell subset.[91–94] Therefore, it is not clear what the downregulation of *PIK3CA* in Tregs mean for their function in this case. In addition, it is not clear why only *PIK3CA*, and not *PIK3CB* and *PIK3CD* encoding the PI3K β and δ subunits, respectively, is differentially expressed in this data (Figure S8), especially since *PIK3CD* is known to be the most prevalent subunit class in T cells.[95] It is also not clear why *AKT2* is differentially expressed, but not its isoforms *AKT1* and *AKT3* (Figure S8).[96] Downstream targets of the PI3K/AKT pathway, such as *MTOR*, *FOXO1*, and *MYC*[97], were also not differentially expressed upon StA uptake in this experiment.

SREBF1, a gene downstream of the PI3K/AKT signalling pathway[98,99], also plays an important role in the metabolic reprogramming in the activation phase of T cells.[8] The gene encodes the transcription factor sterol regulatory element-binding protein 1 (SREBP1), that induces the expression of all genes involved in *de novo* fatty acid and cholesterol synthesis.[8,100,101] The upregulation of this gene could help explain the observed increase in *FASN* and *HMGCR* (Figures 12A & 12B) that was described earlier. In addition, *SREBF1* has also been shown to influence the expression of glycolysis-related genes[102,103], and could together with the increase in *LDHA*, *PIK3CA*, and *AKT2* indicate that the high-uptake cells were more glycolytically active, and thereby more activated or effector-like, in line with the previous results discussed in this Chapter.

Thereby, the upregulation of the metabolic pathways appeared to be the result of increased expression of the PI3K-AKT signalling pathway, which in turn caused an upregulation of transcription factor SREBP1, known to modulate both glycolysis and lipid biosynthetic pathways.[8,104–107]
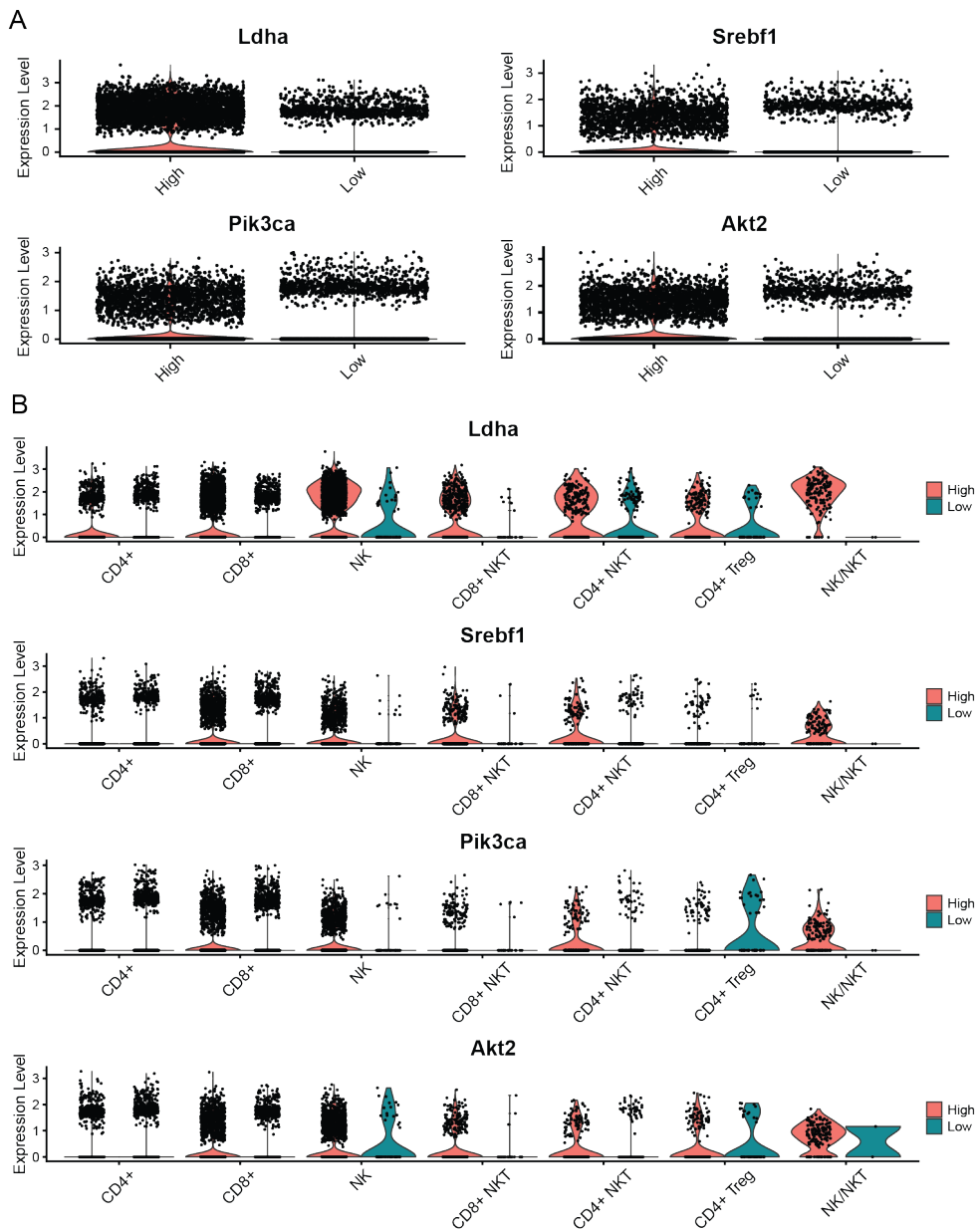
*Figure 13: Differentially expressed genes related to glycolysis from scRNAseq in the high- and low-uptake populations of T, NKT, and NK cells (lymphocytes), represented as violin plots. A) pooled data from all the relevant lymphocyte clusters, B) showing the data for the lymphocyte clusters separately.*

Since the scRNAseq data were based on only one biological replicate, it was not possible to do statistics on the expression levels of the relevant genes. To verify and strengthen the results, more replicates would be necessary. Due to cost- and time-restraints, this was not possible to accomplish within the scope of this project.

However, the results from the scRNAseq are in line with what was previously observed with proteomics, where glucose metabolism (via HK2), fatty acid synthesis (via ACL, ACC1, and FAS), and the mevalonate pathway (via FDPS, HMGCS1, PMVK, and IDI1) were also upregulated in the activated, high-uptake CD4+ T cells. This strengthens the observations made by the two different methods, increasing the reliability of the data.

While the metabolic energetics, as determined by Seahorse extracellular flux analysis, showed a significant increase in glycolytic reliance only in the naïve high StA-uptake cells (Figures 4B & 4C), proteomics (Figure 8A) and scRNAseq (Figures 12 & 13) also indicated an increased flux through glycolysis, as well as fatty acid synthesis and the mevalonate pathway, which are derived from side products from glucose metabolism. In combination, this could indicate that also the *in vitro* αCD3/αCD28 activated cells showed increased glycolytic activity upon high StA-uptake.

This proof-of-principle Chapter has highlighted a connection between increased exogenous FA uptake, and increased metabolic activity and an effector-like phenotype. Previously, genes involved in *de novo* FA synthesis (*ACACA*, *FASN*) and the mevalonate pathway (*HMGCR*, *HMGCS1*, *FDPS*), as well as their regulator *SREPF1*, have been reported to be upregulated in CD4+ T cells treated with OA.[15] However, a lot is still unclear as to the exact mechanism behind these observations. Firstly, no changes in known fatty acid transport proteins such as CD36[108] or fatty acid-binding protein 5 (FABP5)[109] were detected in neither the scRNAseq data (Figure S6), nor the proteomics data (Tables S1 & S2). It is therefore not clear how exogenous StA is taken up by the cells. Additionally, these experiments cannot determine if the increased effector-like phenotype of the high-uptake cells is an inherent property, or if it is a response to the increased FA availability in the culture medium of the cells. Since the cells in most cases are pulsed with StA for only 15 minutes, the former is deemed most probable. However, further research is necessary to support this hypothesis.

Conclusion

In this Chapter, a workflow for multiplexing the uptake of bioorthogonal OA analogue, StA, with single-cell analytical methods like flow cytometry, and a multiomics approach, was developed. Populations of naïve T cells and T cells activated *in vitro* with αCD3/αCD28, with a high uptake of StA, were shown to take on a more effector-like phenotype compared to low StA-uptake cells. This was demonstrated by increased cell size, increased CD44 expression, decreased CD62L expression, increased glycolytic activity, as well as the upregulation of key metabolic pathways of effector T cells. Key genes involved in glycolysis, fatty acid synthesis, and the mevalonate pathway were upregulated in high StA-uptake splenocytes, as detected by scRNAseq. This analysis was focused on T, NKT, and NK cells. In addition, proteins in the same pathways were upregulated in CD4+ T cells as determined by proteomics, indicating robust results. It is not clear whether certain cells take up more exogenous StA because of an inherently more effector-like state, or if the high StA-uptake is induced by the increased availability of FAs in the culture medium. Further research is necessary to answer these questions.

Acknowledgements

Materials & Methods

General. Sterculic acid was purchased from Cayman Chemical (#26735), and stored as 10 mM or 100 mM stock solutions in DMSO at -20°C. Oleic acid-alkyne (#900412E) and oleic acid-azide (#900415C) were purchased from Avanti, and stored as 10 mM stock solutions in DMSO at -80°C. Oleic acid was purchased from Sigma Aldrich (#O1383), and stored as 100 mM stock solution in DMSO at -80°C. AZDye 488 alkyne (#CCT-1277) and AZDye 488 azide (#CCT-1275) were purchased from Click Chemistry Tools (now VectorLabs), and stored as 2 mM stock solutions in DMSO at -20°C. Fluorophore **7** was synthesised in-house (see Chapter 2 of this thesis), and was stored as 2 mM stock solution in DMSO at -20°C. The murine RNase inhibitor was purchased from New England Biolabs (#M0314L), and stored as delivered at -20°C. Zombie NIR Fixable Viability kit was purchased from BioLegend (#423105), and stored as delivered at -20°C. DNase I was purchased from Thermo Fisher Scientific (#90083), and stored as delivered at -20°C. PE/Dazzle 594 anti-mouse CD3 antibody was purchased from BioLegend (#100246), and stored as delivered at 4°C. APC anti-mouse CD4 antibody was purchased from BioLegend (#100516), and stored as delivered at 4°C. eFluor450 anti-mouse CD44 antibody was purchased from Invitrogen (#48-0441-82), and stored as delivered at 4°C. PE-Cyanine7 anti-mouse CD62L antibody was purchased from Invitrogen (#25-0621-82), and stored as delivered at 4°C.

DC2.4 cell culturing. DC2.4 cells were cultured in RPMI 1640 culture medium (Gibco, #31870025) supplemented with 10% FCS, GlutaMAX (2 mM), sodium pyruvate (1 mM), 1x non-essential amino acids (NEAA, Thermo Fisher Scientific), penicillin (100 I.U./mL), streptomycin (50 µg/mL), and 2-mercaptoethanol (50 µM, Thermo Fisher Scientific), and incubated at 37°C, 5% CO_2. The cells were grown to 70-80% confluency and passaged every 2-3 days by trypsinisation.

Splenocyte isolation, stimulation and culturing. Spleens were harvested from naïve C57BL/6 mice. To obtain a single-cell suspension of splenocytes, the spleens were minced with the flat end of a syringe plunger over a 70 µm cell strainer. The strainer was washed with single-cell suspension buffer (SCSB, 2% FCS and 1 mM EDTA in PBS), and the process was repeated until no more red tissue was visible in the strainer. The cells were pelleted at 300 rcf and 4°C for 10 min, the supernatant was discarded, and the cells were resuspended in 2 mL ACK lysis buffer (Thermo Fisher Scientific) per spleen, to remove red blood cells. After 5 min in the lysis buffer, cold PBS was added until 40 mL and the cells were pelleted at 500 rcf and 4°C for 5 min. The supernatant was discarded, and the cells were resuspended in SCSB and passed over a 40 µm cell strainer. The cells were pelleted at 300 rcf and 4°C for 10 min, the supernatant was discarded, and the cells were resuspended in splenocyte medium (RPMI 1640 culture medium (Capricorn Scientific, #RPMI-HXA) supplemented with 10% FCS, GlutaMAX (2 mM), penicillin (100 I.U./mL), streptomycin (50 µg/mL), and 2-mercaptoethanol (50 µM)). The cells were counted using a haemocytometer before seeding. For experiments using solely unstimulated splenocytes, the cells were seeded directly for the respective experiments (see below).

For experiments using both stimulated and unstimulated splenocytes, half the wells of a Nunc™-treated 6-well plate (Thermo Fisher Scientific) were coated with Ultra-

LEAF purified anti-mouse CD3ε antibody (BioLegend, 5 µg/mL) in sterile PBS for 2 h at 37°C. After 2 h the antibody was removed, and 15×10^6 cells were seeded per well in 5 mL complete splenocyte medium supplemented with Ultra-LEAF purified anti-mouse CD28 antibody (BioLegend, 3 µg/mL) and recombinant murine IL2 (PeproTech, 10 U/mL). For unstimulated control cells, 15×10^6 cells were seeded per well in 5 mL complete splenocyte medium supplemented with recombinant murine IL2 (PeproTech, 10 U/mL). All cells were incubated at 37°C, 5% CO_2 overnight. The next day, the activated and naïve cells were scraped, combined in separate tubes and centrifuged at 300 rcf for 10 min. The cells were resuspended in fresh splenocyte medium before being counted using a haemocytometer and seeded for experiments (see below).

Cell sorting of naïve splenocytes for proteomics and Seahorse analysis. Three spleens were harvested, and splenocytes were isolated (as described above) to yield ~400-500x10⁶ unstimulated cells. These cells were seeded evenly over the wells of three Nunc™-treated 6-well plates (Thermo Fisher Scientific) in 2 mL fresh splenocyte medium per well. To each well, 2 mL sterculic acid (200 µM) in splenocyte medium was added, to give a final sterculic acid-concentration of 100 µM. The cells were incubated at 37°C, 5% CO_2 for 15 min, to allow for uptake of the fatty acid. All wells were harvested, combined in 50 mL tubes, and washed with fresh medium (x1) and PBS (x1). Each washing step consisted of spinning down (300 rcf, 5 min), aspirating supernatant, and resuspending in wash solution. After the last wash, the cells were resuspended in PBS supplemented with fluorophore **7** (1 µM) and incubated on ice for 35 min, to allow the fluorophore to react with sterculic acid. The cells were washed with cold PBS (x2), where each washing step consisted of spinning down (300 rcf, 5 min, 4°C), aspirating supernatant, and resuspending in wash solution. To perform a viability staining, the cells were resuspended in 750 µL of HBSS (Gibco, #14025092) supplemented with Zombie NIR (BioLegend, #423105, 1:500) and DNase I (Thermo Fisher Scientific, #90083, 30 U/mL), and incubated at RT for 15 min. The rest of the antibody cocktail was diluted in 250 µL HBSS and added to the cells to give a final volume of 1 mL. The following antibodies and dilutions (calculated with 1 mL final volume) were used: PE/Dazzle 594 anti-mouse CD3 (1:800), APC anti-mouse CD4 (1:400), eFluor450 anti-mouse CD44 (1:200), and PE-Cyanine7 anti-mouse CD62L (1:1000). The cells were incubated at RT for an additional 25 min, before addition of 10 mL FACS buffer (PBS with 0.2% BSA and 2 mM EDTA) and centrifugation at 300 rcf, 5 min. The cells were then washed with FACS buffer (x2), before being resuspended in ~1.5 mL FACS buffer. The samples were transported on ice and sorted using a BD FACS Aria III 4L (BD Biosciences, San Jose, CA, USA), following the gating strategy shown in Figure S1A. The experiment was repeated minimum as biological triplicates.

Cell sorting of activated splenocytes for proteomics and Seahorse analysis. Three spleens were harvested, and splenocytes were isolated and activated (as described previously). Subsequently, the same protocol as for sorting naïve splenocytes (described above) was used, except for the PE/Dazzle 594 anti-mouse CD3 antibody which was diluted at 1:200 instead of 1:800. The FACS gating strategy is shown in Figure S1B. The experiment was repeated as biological triplicates.

Seahorse analysis. 1-2x10⁶ sorted low- and high-uptake cells were used to perform the Seahorse Real-Time ATP Rate Assay. Inhibitors and uncouplers were prepared

in XF assay media, supplemented with 5 mM D-(+)-glucose for sequential addition at the appropriate final concentrations of oligomycin A (1.8 µM), and antimycin A (2 µM) (all Sigma-Aldrich). Cells were placed in a non-CO2 incubator at 37°C for 1 h prior to the assay. Basal respiration (OCR) and extracellular acidification rate (ECAR) were measured by the Seahorse Biosciences XFe24 Extracellular Flux Analyser (Agilent Technologies, Santa Clara, CA, USA). Oxygen consumption rates (OCR) and ECAR were measured and analysed using the Agilent online analysis tool. Values recorded were normalised to cell numbers seeded. Baseline readings were established, and the effects of specific inhibitors and uncouplers on OCR and ECAR were assessed using repeated measures ANOVA and plotted as bar charts, and scatter plots. Error bars indicating standard deviation were included to illustrate variability within the data.

Preparation of sorted samples for proteomics. From the sorted cells (described above), $2x10^5$ cells of each population were taken for total-digest proteomics. The samples were spun down at 300 rcf, 5 min, 4°C, and the supernatant was aspirated. The cell pellets were plunge frozen and stored at -80°C until further processing. Upon thawing of the samples, they were resuspended in 15 µL lysis buffer (250 mM sucrose, 5 mM EDTA, 1x cOmplete™ protease inhibitor (Roche) in PBS). The samples were lysed by sonication (Qsonica Q700 Microplate Sonicator, 4x10 s pulses, 10% amplitude, 0°C). Protein concentration was measured by Qubit Protein assay (Invitrogen) according to the manufacturer's protocol, and all samples were found to contain ~4 µg of protein. The proteins were precipitated by adding 500 µL cold (-80°C) acetone, vortexing, and incubating the samples at -80°C for 1 h. The samples were spun down at 20 000 rcf, 15 min, 4°C, and the supernatant was poured off. To wash, 300 µL acetone was added to each sample, followed by vortexing and sonication (2x10 s pulses, 10% amplitude, 0°C). The samples were incubated at -80°C overnight, before being spun down at 20 000 rcf, 15 min, 4°C. The supernatant was poured off, and the samples were airdried for 2 min to ensure all the acetone had evaporated. To redissolve and denature the proteins, 20 µL urea (8 M) in NH_4HCO_3 (100 mM), pH 8 was added, and the samples were shaken for 30 min at 37°C, 1000 rpm. The proteins were then reduced by addition of dithiothreitol (DTT, 5 mM) and the samples were shaken for 15 min at 65°C, 800 rpm. The samples were cooled down before addition of iodoacetamide (IAA, 10 mM) and incubation for 30 min at RT in the dark, to acetylate all proteins. Unreacted IAA was quenched by addition of DTT (7 mM). All samples were diluted with 170 µL $CaCl_2$ (1 mM) in NH_4HCO_3 (20 mM) to ensure urea concentrations <1 M. All samples were transferred to Protein LoBind tubes (Eppendorf), and sequencing-grade trypsin (Promega, 0.2 µg) was added. The trypsin digestion mixture was shaken at 37°C, 1000 rpm overnight, before being quenched by addition of 5 µL 50% trifluoroacetic acid (TFA) in MilliQ. Peptides were desalted using Empore™ C18 StageTips (CDS Analytical) preconditioned with 50 µL MeOH, 50 µL of 0.05% (v/v) TFA in 60% (v/v) acetonitrile/MilliQ (solution B) and 50 µL 0.05% (v/v) TFA in MilliQ (solution A) by centrifugation (600 rcf, 2 min). The peptides were washed with solution A (100 µL, 800 rcf, 3 min) and eluted into new Protein LoBind tubes using solution B (100 µL, 800 rcf, 3 min). The samples were concentrated using an Eppendorf SpeedVac (Eppendorf Concentrator Plus 5301 or 5305) and stored at -80°C until measurement. Upon measurement, desalted peptide samples were reconstituted in 40 µL LC-MS solution (97:3:0.05 MilliQ, acetonitrile, TFA).

LC-MS/MS measurements. Peptides (prepared as described above) were separated via nanoflow reversed-phase liquid chromatography using a nanoElute 2 LC system (Bruker Daltonics) coupled to a timsTOF HT mass spectrometer (Bruker) with 0.1% FA (solution A) and 0.1% FA/99.9% ACN (solution B) as the mobile phases. The samples were loaded on a trap column (PepMap C18, 5 mm x 0.3 mm, 5 µm, 100 Å, Thermo Scientific) followed by elution and separation on the analytical column (PepSep C18, 25 cm x 75 µm, 1.5 µm, 100 Å, Bruker) kept at 50 °C using a gradient of 2 - 25% solvent B in 25 min, 25 - 32% B in 5 min, 32 - 95% B in 5 min and 95% B for 10 min at a flow rate of 300 nL/min. Peptides were introduced to a TimsTOF HT (Bruker Daltonics) using a 20 µm ID fused silica emitter (Bruker Daltonics) installed in a nano-electrospray ion source (CaptiveSpray source, Bruker Daltonics) with spray voltage set to 1500 V.

For DIA acquisition, peptides were analysed with a TimsTOF HT (Bruker Daltonics) running in DIA-PASEF mode. The DIA-PASEF method was optimized for the specific sample type using the py_diAID tool.[110] The method covered an ion mobility range from 1.35 to 0.7 Vs cm-2 and an m/z range of 300 to 1300, using 10 DIA-PASEF scans with two isolation windows per scan, resulting in a cycle time of 1.1 s. Collision energy was linearly decreased from 59 eV at 1.6 Vs cm-2 to 20 eV at 0.6 Vs cm-2. For all experiments the ion mobility dimension was calibrated linearly using three selected ions of the Agilent ESI LC/MS Tuning Mix [m/z, 1/K0: (322.0481, 0.7318 Vs cm−2), (622.0289, 0.9848 Vs cm−2), (922.0097, 1.1895 Vs cm−2)]. Mass calibration was performed with sodium formate in HPC mode.

Proteomics data analysis. The raw files were analysed using DIA-NN (version 1.8.1). Searches were performed against a UniProt database of the mouse proteome (UPID: UP000000589, downloaded 17th March 2024).[42] The output file "report. unique_genes_matrix.tsv" from DIA-NN was used for further analysis in R Statistical Software.[31] At most 1 missing value in either the low- or high-uptake samples were allowed, and missing values were imputed with the average value of the remaining measurements. In cases where all values were missing from either the low- or high-uptake samples, the missing values were imputed with a negligible small number to allow for further processing and statistical calculations. Significantly differentially expressed proteins were determined using the empirical Bayes method in the Limma package[111] (Version 3.58.1) in R, and the significant proteins were determined to have a 2-fold difference between the expression levels of low- and high-uptake samples with an adjusted p-value of <0.05. Pathway analysis was performed using the clusterProfiler package in R.[43]

Checking integrity of RNA by 1% agarose gel after click reactions. $1x10^6$ DC2.4 cells were seeded per well in 6-well plates, and incubated at 37°C, 5% CO_2 overnight to allow the cells to attach. The samples shown in Figures S2A & S2B were treated with either sterculic acid (50 µM), oleic acid-alkyne (50 µM), oleic acid-azide (50 µM) or DMSO-vehicle (0.5%) in fresh DC2.4 medium for 1 h at 37°C, 5% CO_2, followed by a wash with DC2.4 medium x1 and PBS x1. The samples shown as "Live" in Figure S2A were reacted with fluorophore **7** (5 µM) or DMSO vehicle (0.25%) in fresh DC2.4 medium for 1 h at 37°C, 5% CO_2. The medium was aspirated and the cells were resuspended in 500 µL TRIzol reagent (Invitrogen) per well, before being transferred to 1.5 mL Eppendorf tubes. The samples were plunge frozen in liquid nitrogen and stored at -80°C until further processing. Simultaneously, the samples shown as

"Fixed" in Figures S2A & S2B were fixed with 4% PFA in PBS for 15 min at RT. The fixed cells were washed with PBS x2, and permeabilised with PBS supplemented with saponin (0.1%) and RNase inhibitor (40 U/mL). After permeabilization, the cells were again washed with PBS x2, followed by click reaction with complete IEDDA cocktail, complete CuAAC cocktail, or DMSO vehicle (0.25%) in PBS for 1 h at RT in the dark. The IEDDA cocktail consisted of fluorophore **7** (5 µM) in PBS. The complete CuAAC cocktail consisted of $CuSO_4$ (1 mM), sodium ascorbate (10 mM), THPTA ligand (1 mM), amino-guanidine (10 mM), HEPES pH 7.2 (100 mM), and AZDye 488 alkyne/azide (5 µM). The fixed cells were then washed with PBS x2, before addition of 500 µL TRIzol reagent (Invitrogen) per well. The fixed cells were scraped to loosen them from the plate and transferred to 1.5 mL Eppendorf tubes. To all the fixed samples, proteinase K (40 U/mL, New England Biolabs, #P8197S) was added, and the samples were incubated at 56°C for 1 h, followed by 10 min at RT and 5 min on ice. All fixed cell samples were plunge frozen in liquid nitrogen and stored at -80°C until further processing.

For the samples shown in Figure S2C, a similar protocol was followed as described above. The only differences were that there was no oleic acid analogues added to these samples, and the separate components of the CuAAC cocktail (diluted in 100 mM HEPES, pH 7.2) were also added to the cells.

All the prepared samples were thawed, 100 µL chloroform was added to each, and they were vortexed vigorously for 15 s. After centrifugation at 20 000 rcf for 5 min, the supernatant (aqueous phase, ~200 µL) was transferred to new tubes. To the new tubes, 100 µL chloroform was added, they were vortexed vigorously, and spun down at 20 000 rcf for 5 min. The supernatant (~180 µL) was transferred to new tubes, 180 µL isopropanol was added, and the samples were vortexed. RNA precipitation occurred by incubating the samples for 20 min at RT, followed by centrifugation at 20 000 rcf for 15 min. The pellets were washed twice with ethanol (70%), and airdried for 5 min. RNA isolated from live cells was reconstituted in 15 µL MilliQ, whereas RNA from fixed cells was reconstituted in 10 µL MilliQ. The RNA concentration was measured with a DeNovix DS-11 spectrophotometer, and 1 µg RNA from each sample was mixed with RNA loading dye (Thermo Fisher Scientific, #R0641, 1x) supplemented with GelRed and loaded on 1% agarose gels in TAE buffer. As a reference, RiboRuler High Range RNA ladder (Thermo Fisher Scientific, #SM1821) was also added to the gels. The gels were run at 80 V for 45 min and were imaged on a Chemidoc MP imaging system (Bio-Rad).

Cell sorting of splenocytes for single-cell RNA sequencing. One spleen was harvested, and the splenocytes were isolated and stimulated as described above. The stimulated cells were scraped from the 6-well plate and counted using a haemocytometer. 8×10^6 cells were seeded in 800 µL splenocyte medium in one well of an uncoated 12-well plate. To the same well, 800 µL sterculic acid (50 µM) in splenocyte medium was added, to give a final sterculic acid-concentration of 25 µM. The cells were incubated at 37°C, 5% CO_2 for 1 h, to allow for uptake of the fatty acid. The cells were harvested, transferred to a 15 mL tube, and washed with fresh medium (x2). Each washing step consisted of spinning down (300 rcf, 5 min), aspirating supernatant, and resuspending in wash solution. The cells were resuspended in 1.6 mL fresh medium supplemented with fluorophore **7** (1 µM) and seeded in a well in an uncoated 12-well plate. The cells were incubated at 37°C, 5%

CO_2 for 1 h, to allow the fluorophore to react with sterculic acid, followed by being harvested, transferred to a 15 mL tube, and washed with fresh medium (x1) and PBS (x1). To perform a viability staining, the cells were resuspended in 1 mL Zombie NIR (1:1000) in PBS, and incubated at RT for 20 min. After staining, two washing steps with fresh medium (x1) and PBS (x1) were performed. The cells were fixed with 2% paraformaldehyde (PFA) in PBS for 30 min, before unreacted PFA was quenched with PBS supplemented with glycine (20 mM) and RNase inhibitor (40 U/mL). A last wash with FACS buffer was performed, before the cells were resuspended in 600 µL FACS buffer supplemented with RNase inhibitor (40 U/mL). The samples were transported on ice and sorted using a BD FACS Aria III 4L (BD Biosciences, San Jose, CA, USA), according to the gating strategy shown in Figure S3.

scRNAseq workflow & data analysis. $4x10^5$ cells of the low and high StA-uptake populations were collected by FACS (as described above) and were handed over to the Leiden Genome Technology Centre (LGTC) for processing, measurement, and data analysis. The samples were analysed using the Chromium Fixed RNA Kit (10x Genomics).

Supplementary Figures & Tables
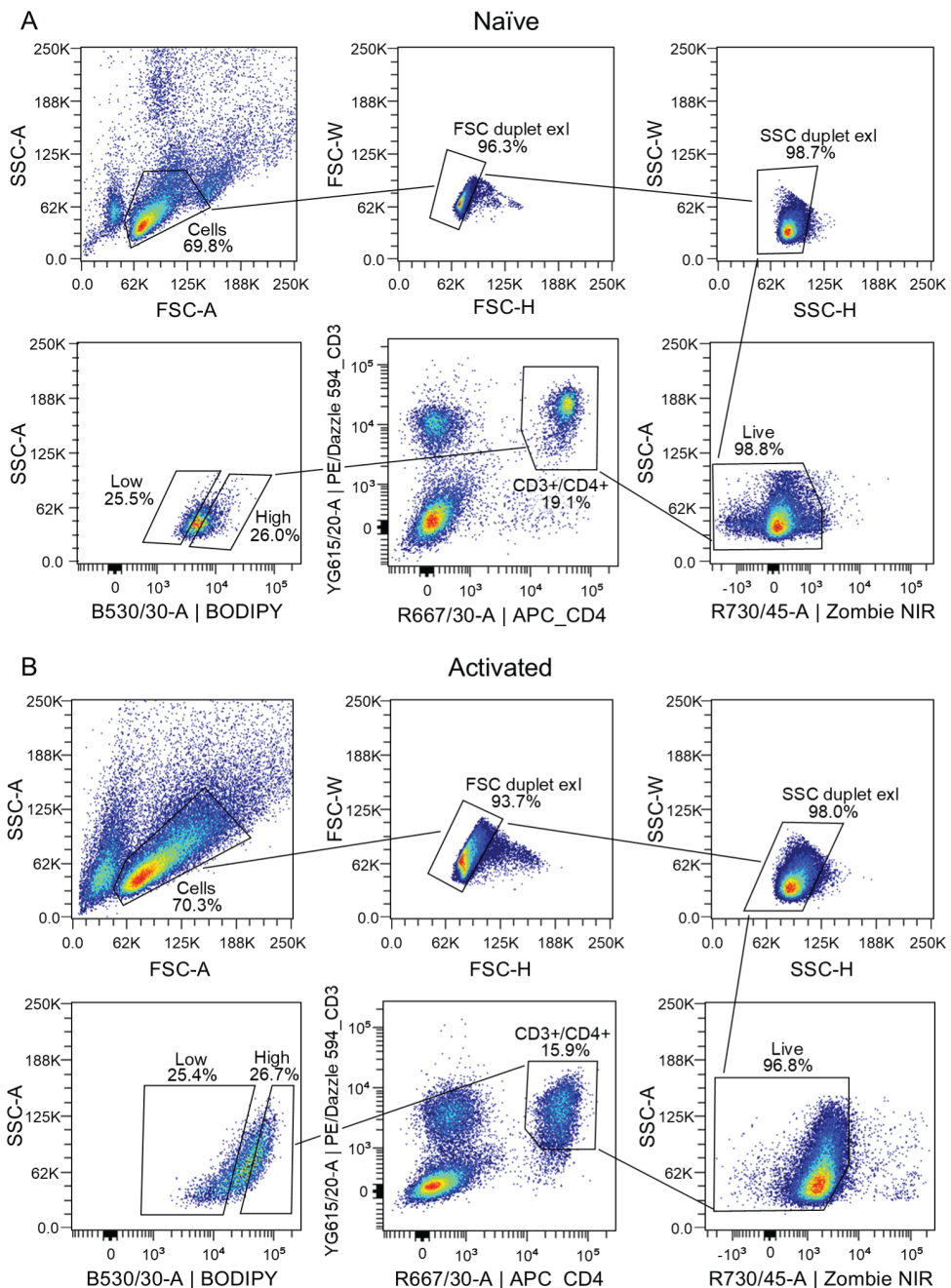
Figure S1: *Example of FACS gating strategy for proteomics and Seahorse analysis of **A)** naïve splenocytes, **B)** αCD3/αCD28-activated splenocytes.*

Table S1: *List of significantly up- and downregulated proteins (in the high-uptake population) after proteomics analysis of naïve CD3+/CD4+ T cells upon high or low uptake of StA.*

Upregulated	Downregulated
Cd74	Fbxo7
Ncapg	
Ncapd2	
Cdk1	
Ncaph	
Kif2c	
Swap70	
Pygm	
Kif4	
Pld4	
Incenp	
Tbc1d4	
Supt20h	
Mafg	
Dut	
Rbfa	
Top2a	
Marcksl1	
Stmn1	
Smc2	
Anxa2	
Dhfr	

Table S2: *List of significantly up- and downregulated proteins (in the high-uptake population) after proteomics analysis of αCD3/αCD28-activated CD3+/CD4+ T cells upon high or low uptake of StA. The table continues on the next page.*

Upregulated			Downregulated		
Mapkapk5	Dut	Rps25	Fbxl22	Plp2	Tra2b
Smad4	Btf3	Ipo5	Irf1	H1-5	Dok2
Mtg2	Psat1	Pdcd2	Rnf13	Cd3d	Atp2a1
Tsnaxip1	Srm	Shmt2	Ifngr1	Pecam1	Kdsr
Kcna6	Rps17	Ddx3x	Depdc1b	S100a6	Tmub1
Heatr9	Cdca7	Acaca	Pkp1	Anxa1	Krt17
Maff	Gpatch4	Nudt5	Endod1	Gimap3	Nqo2
Cops7a	Impdh2	Noc2l	Ifit1bl1	Phf11b	Cap2
Fem1aa	Rpl22	Rps11	Frmd4b	Cox6c	Fam98c
Zc3h7b	Stard4	Aimp2	Krt4	Ahnak	Syne3
Uqcc6	Ifrd2	Hells	Adap1	Trafd1	Tiam1
Ccdc97	Cyp51a1	Grwd1	Tmem71	Prkab1	Eeig1
Nexmif	Rps3	Gemin8	H2-DMb2	Cnst	Cd247
Akirin2	Smyd5	Surf2	Mbtd1	Hide1	Rasa3
Zeb1	Znhit3	Aprt	Trbv19	Cd48	Slc28a2
Smg7	Colgalt1	Acly	Ifit2	Fgd3	Tgm2
Klhl9	Nolc1	Dph6	Ecm1	Sp100	Hmgn1
Ctnna1	Hk2	Rrp15	Cdkn1b	Dsp	Ets1
Dhrs11	Fdps		Prss59	Aldh3a2	Dop1b
Aasdhppt	Snrpb		Oasl2	H2bc14	Hsdl2
Pprc1	Fasn		S100a4	Iigp1	Znf710
Trim26	Larp4		Vmn2r3	Tmem245	H2bc3
Pmf1	Spin4		Cep76	Cybc1	Tm9sf3
Crcp	Eif4a1		Ing1	Chdh	Cyria
Sar1b	Rpsa		Krt76	Kif1b	Vps13c
Ccdc127	Eif4e2		Cd3e	H2-M3	Nfatc2ip
Polr2d	Nob1		Lamtor5	Hist1h2bp	Arl6ip4
Tatdn2	Abcf2		Sell	Il4r	Itgb3
Lhpp	Psmg4		Cirbp	Fbxo6	Trbv1
Gga2	Hspbp1		Rtp4	Cd47	Elmo2
Crabp2	Gzmb		Slfn5	Trim14	Tdrp
Arl1	Dohh		Pdcd4	S100a11	Kctd12
Snapc1	Heatr3		Hba	Ubac2	H2ax

Upregulated (cont.)		Downregulated (cont.)		
Atf6	Hat1	Dapl1	Krt5	Elf1
Nedd9	Aven	Try10	Sipa1l1	Dennd1c
Gal3st4	Mrto4	Krt16	Mdm1	Creb1
Ogfod1	Cluh	Nucks1	Saraf	Sigirr
Bcat1	Pcna	Dpys	Cmc2	Rcsd1
Hmgcs1	Mtrr	Ifit1	Cytip	Cd84
Kpna2	Ppat	Krt42	Zbtb2	As3mt
Eif5a	Acbd6	H2bc26	Irf7	Map3k3
Lss	Rpap2	S100a13	Ifi203	Sfxn3
Znhit6	Znrd2	Ighg1	Itm2b	Galm
Znf583	Ltv1	Sun2	Sh3bgrl	Zbp1
Ntmt1	Fam98a	Ltb	Amacr	Ccdc71
Ybx3	Mthfd2	Casp1	Tma7	Gvin1
Psmb5	Rps24	Clec2d	Mndal	Itgb7
Rpl22l1	Rps23	H1-2	Cd3g	Anxa5
Cdc45	Dtd2	Trp53i11	Alb	Gbp7
Psmg3	Orc6	Ms4a6b	Bles03	Fchsd1
Slfn2	Nufip1	Epsti1	H1-0	Plgrkt
Dnajc15	Edrf1	Ifi204	Anxa2	Ddah2
Eef1akmt4	Acsl4	Inppl1	Znf551	Col4a2
Fpgs	Naa50	Cd74	Cmpk2	Rab22a
Pmvk	Cdc123	H1-1	Cstb	Tmx4
Idi1	Rpl35	Tbc1d8b	Vkorc1	Fam3c
Mak16	Rplp0	Abcg3	Arid5a	Coq9
Etf1	Ipo4	Ephx1	Atp2a3	Myo15a
Nap1l1	Hypk	Hist2h2bb	Cfap20	Zfp512b
Uck2	Ubap2	Abraxas1	Lmna	Smarca2
Pabpc4	Cks2	Gimap1	Srsf2	Hmgb2
Ttc27	Irf4	H2bu2	Sting1	Esyt2
Rpl30	C1d	Adgre5	Gsn	Gbp9
Gxylt1	Pwp1	Stat2	Capg	Rnf169
Mcm10	Rps12	Krt12	Pafah1b3	Arhgef18
Pla2g12a	Serpinb6b	Ctse	Msh3	Hsd11b1
Aen	Umps	Ptms	Sit1	Igtp
Cars1	Blm	Srd5a3	Zfp362	Hp1bp3

A

B

C

Tz = fluorophore **7**
alk = AZDye 488 alkyne
az = AZDye 488 azide
C = Copper(II) sulfate
N = Sodium ascorbate
T = THPTA ligand
A = Aminoguanidine
M = CuAAC click mix

D

Sterculic acid (StA)

Oleic acid alkyne (OAalk)

Oleic acid azide (OAaz)
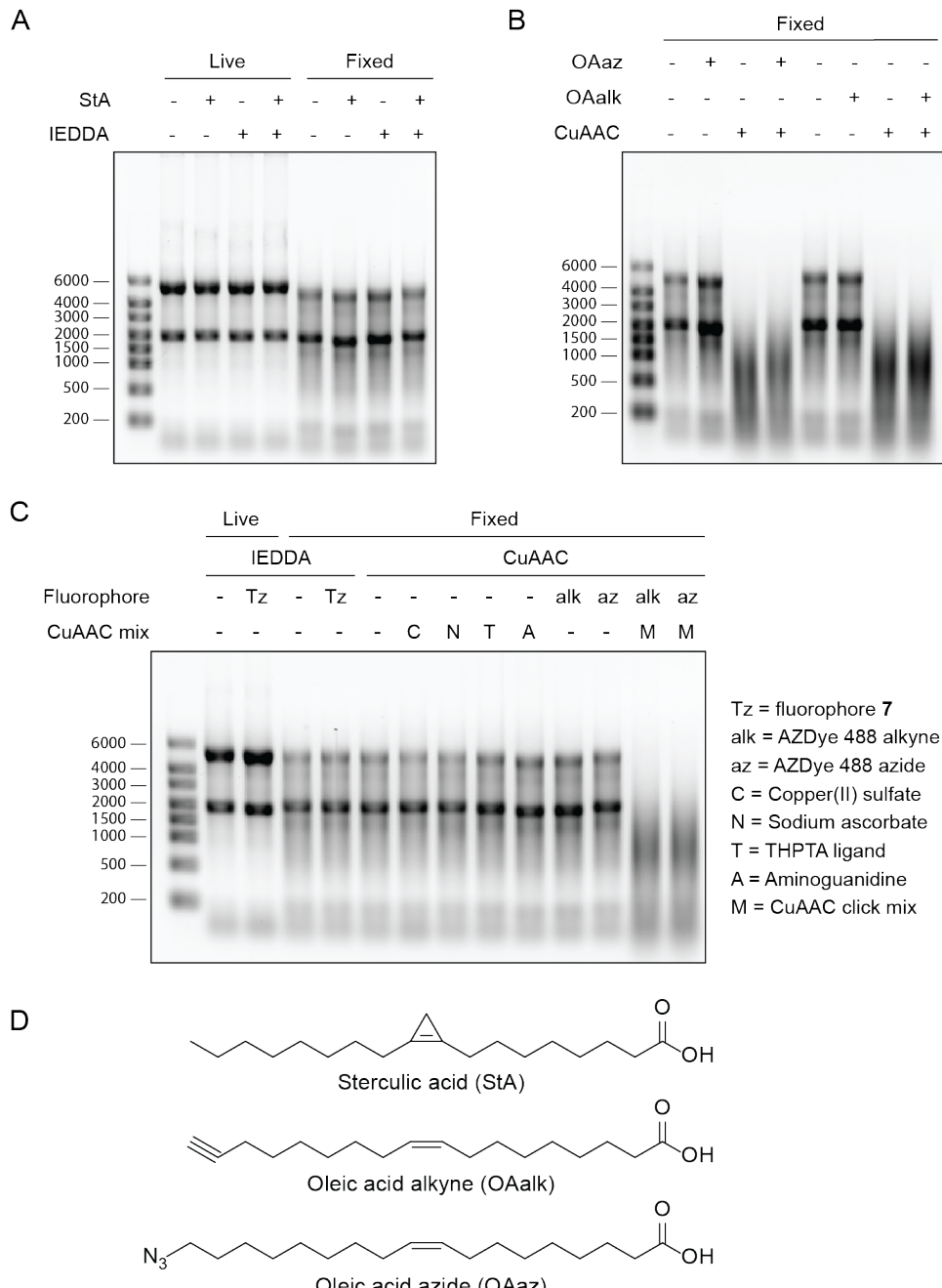
Figure S2: *RNA gels showing intact RNA after IEDDA, but not after CuAAC. **A)** IEDDA in live and fixed cells. **B)** CuAAC in fixed cells. **C)** IEDDA and CuAAC with each individual click mix component. **D)** Structures of oleic acid analogues with cyclopropene (sterculic acid, StA), alkyne (oleic acid alkyne, OAalk) and azide (oleic acid azide, OAaz) click handles.*
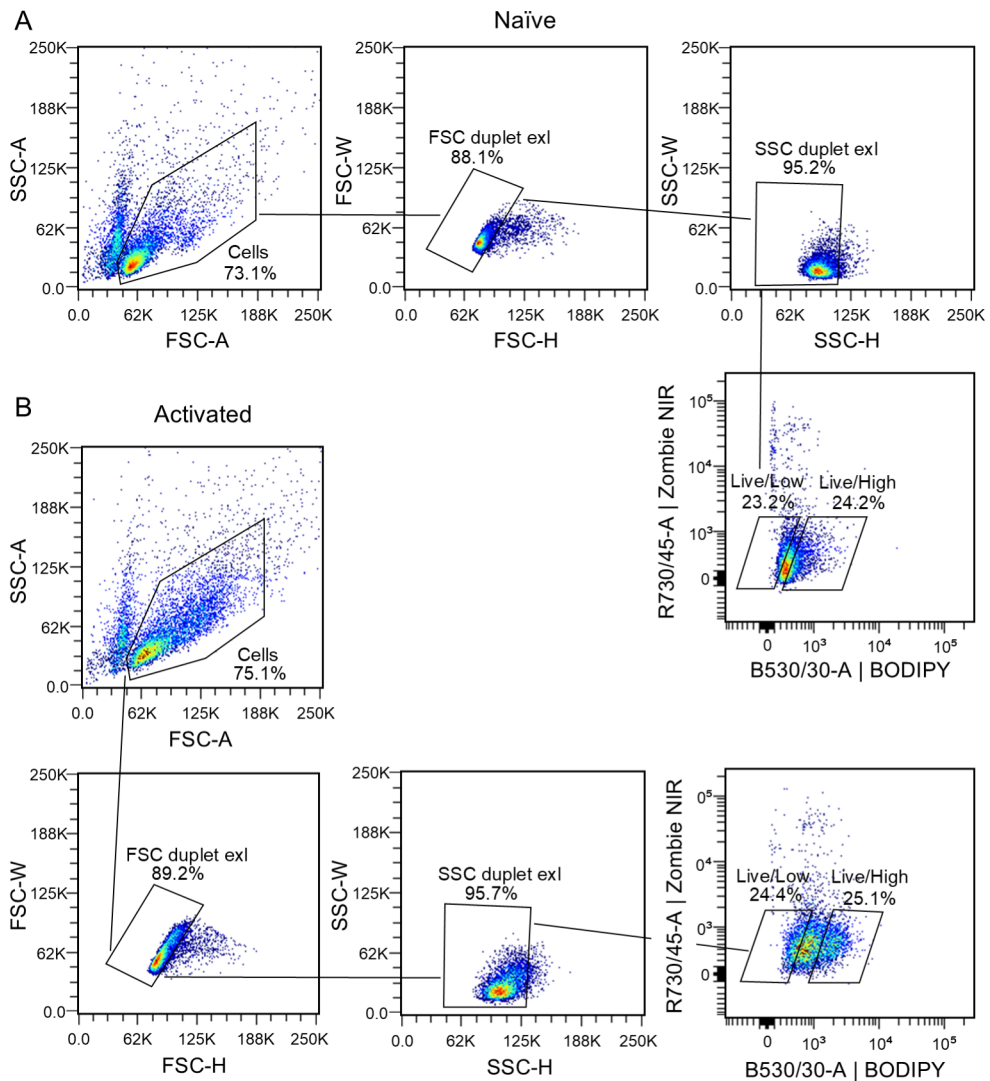
Figure S3: *Example of FACS gating strategy for scRNAseq of* ***A)*** *naïve splenocytes,* ***B)*** *αCD3/ αCD28-activated splenocytes.*
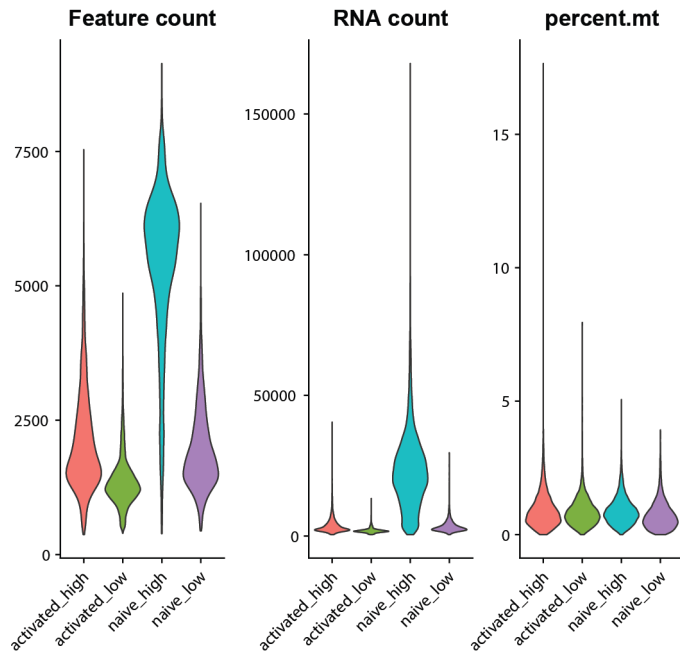
Figure S4: *Quality control analysis of all samples submitted for scRNAseq showing that the high-uptake sample of naïve splenocytes is quite different from the other samples. It contains more feature and RNA counts than the other samples.*

Table S3: *Immune cell subsets corresponding to clusters identified from the scRNAseq analysis (from Figure 2). The immune cell subsets were determined based on expression of relevant marker genes from the scRNAseq data.*

| Cluster	Immune subset	Relevant marker genes
0	CD4+ T cells	*CD3E, CD3D, CD3G, CD3Z, CD4*
1	CD8+ T cells	*CD3Z, CD8A, CD8B1*
2	B cells	*CD19, IGHM, IGHD, IGHE*
3	B cells	*CD19, IGHM, IGHD, IGHE*
4	B cells	*CD19, IGHM, IGHD, IGHE*
5	NK cells	*CD16, CD27, CD161, KLRK1, NCR1*
6	B cells	*CD19, IGHM, IGHD, IGHE, IGHG*
7	Mixed (T & B cells)	*CD3Z, CD4, CD8B1, CD19, IGHD, IGHE*
8	CD8+ T cells	*CD3Z, CD8A, CD8B1*
9	CD8+ T cells	*CD3Z, CD8A, CD8B1*
10	B cells	*CD19, IGHM, IGHD, IGHE*
11	B cells	*CD19, IGHM, IGHG*
12	CD8+ NKT cells	*CD3Z, CD8A, CD16, CD161, CD122, KLRK1*
13	CD4+ NKT cells	*CD3Z, CD4, CD161, CD122, KLRK1, NCR1*
14	CD4+ Treg	*CD3Z, CD4, FOXP3*
15	Monocytes	*CD68, CD172A, CD86, CD40, CD80*
16	CD8+ T cells	*CD8A, CD8B1*
17	Mixed	*CD8A, CD8B1, CD161, CD122, KLRK1, NCR1*
18	CD4+ T cells	*CD3Z, CD4*
19	Monocytes	*CD11B, CD14, CD16, CD68, CD172A, CD40, CD80*
20	Mixed	*CD3Z, CD4, CD8A, CD8B1*
21	Monocytes	*CD11B, CD14, CD16, CD172A, CD80*
22	NK cells	*CD56, CD49B*
23	Monocytes	*CD68, CD172A*
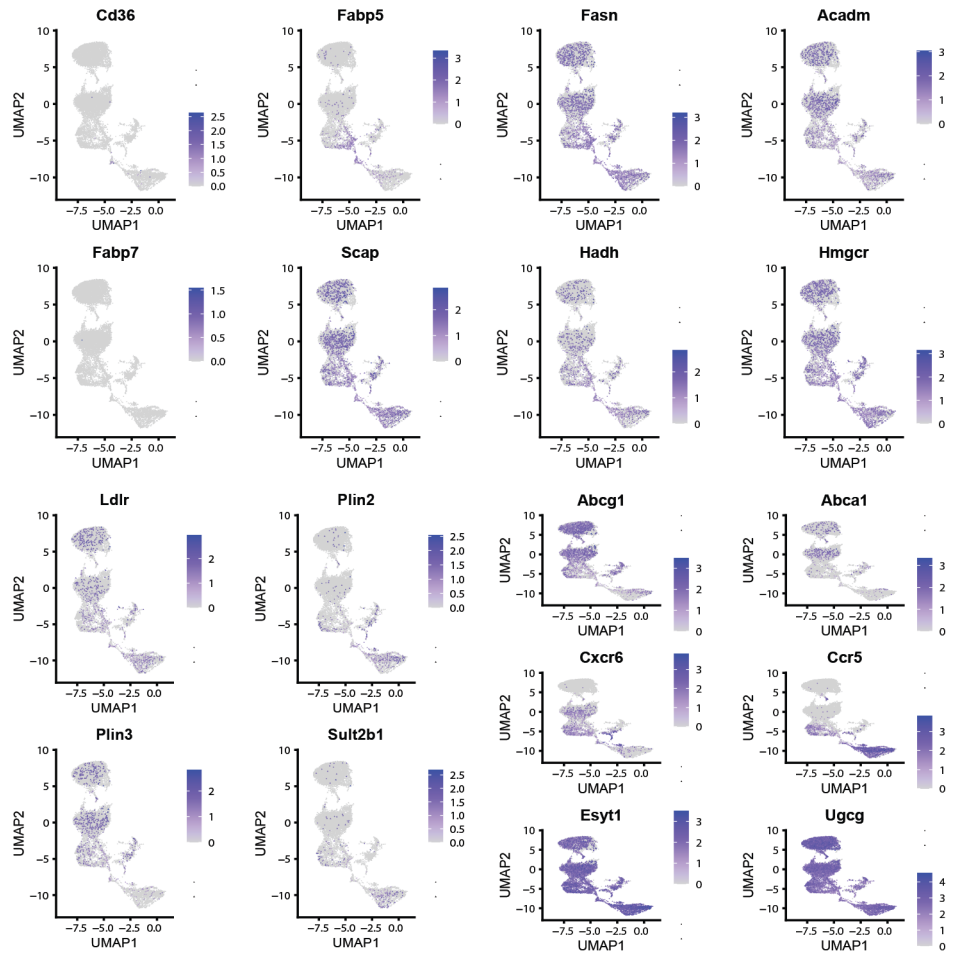
Figure S5: *Gene expression distribution from scRNAseq of genes related to lipid metabolism. The expression distribution is highlighted in clusters containing all T, NKT, and NK cells.*
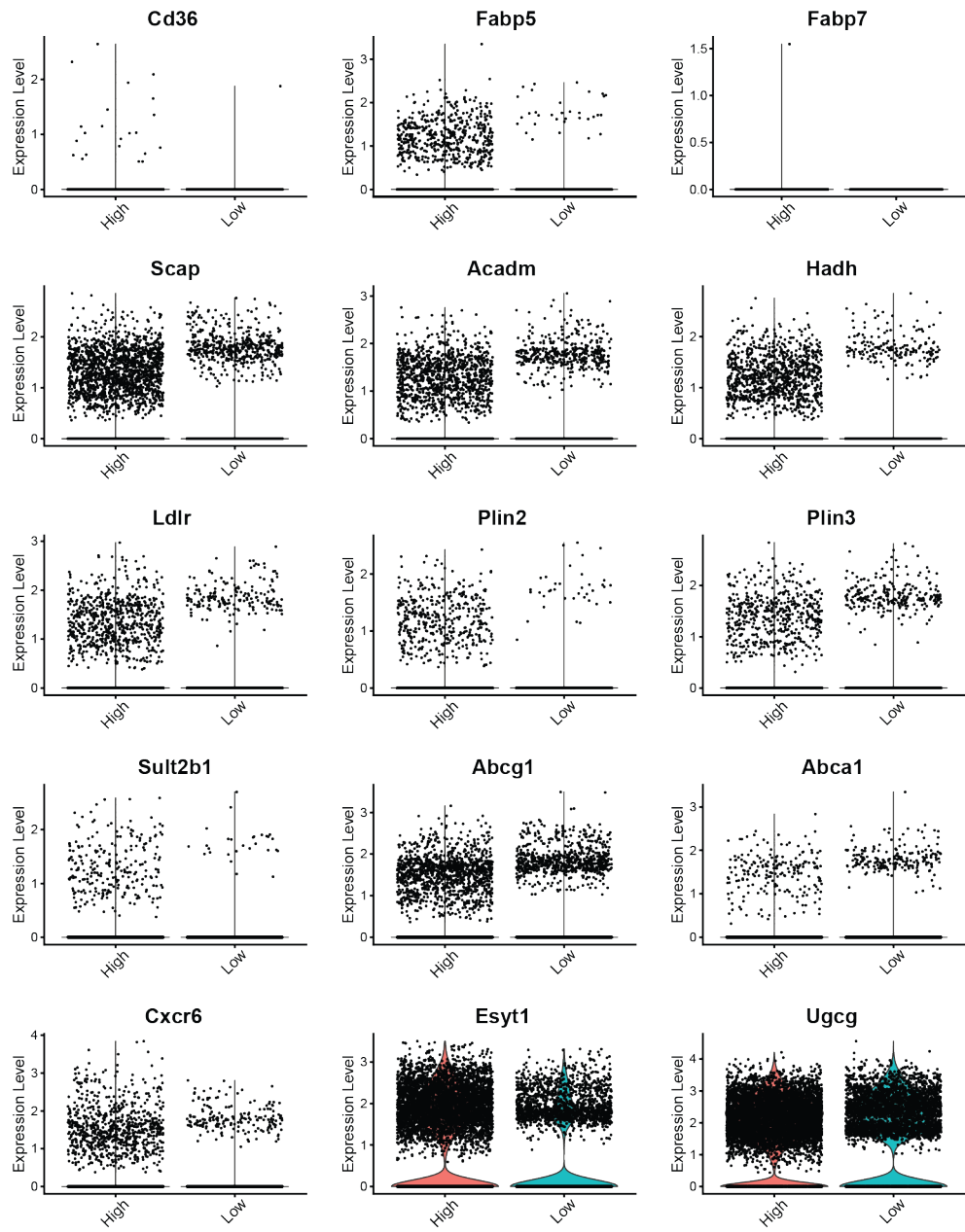
Figure S6: *Expression of genes related to lipid metabolism from scRNAseq in the high- and low-uptake populations of T, NKT, and NK cells, represented as violin plots.*
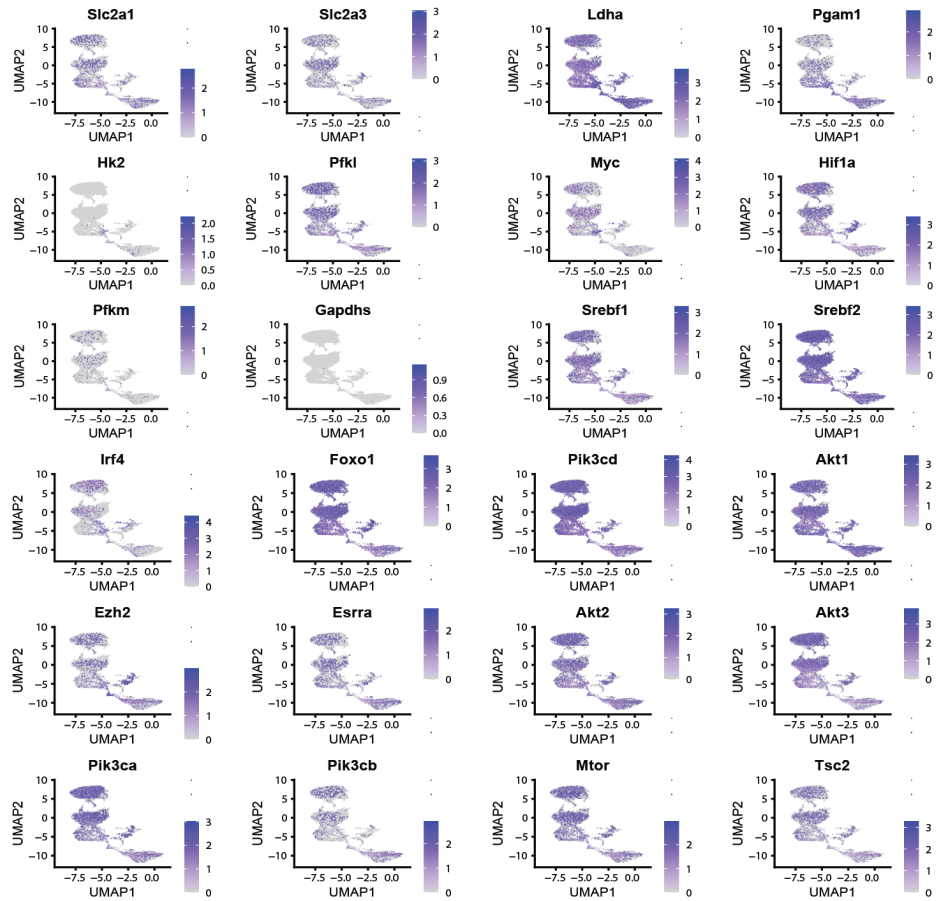
**Figure S7:** *Gene expression distribution from scRNAseq of genes related to glycolysis and glucose metabolism. The expression distribution is highlighted in clusters containing all T, NKT, and NK cells.*
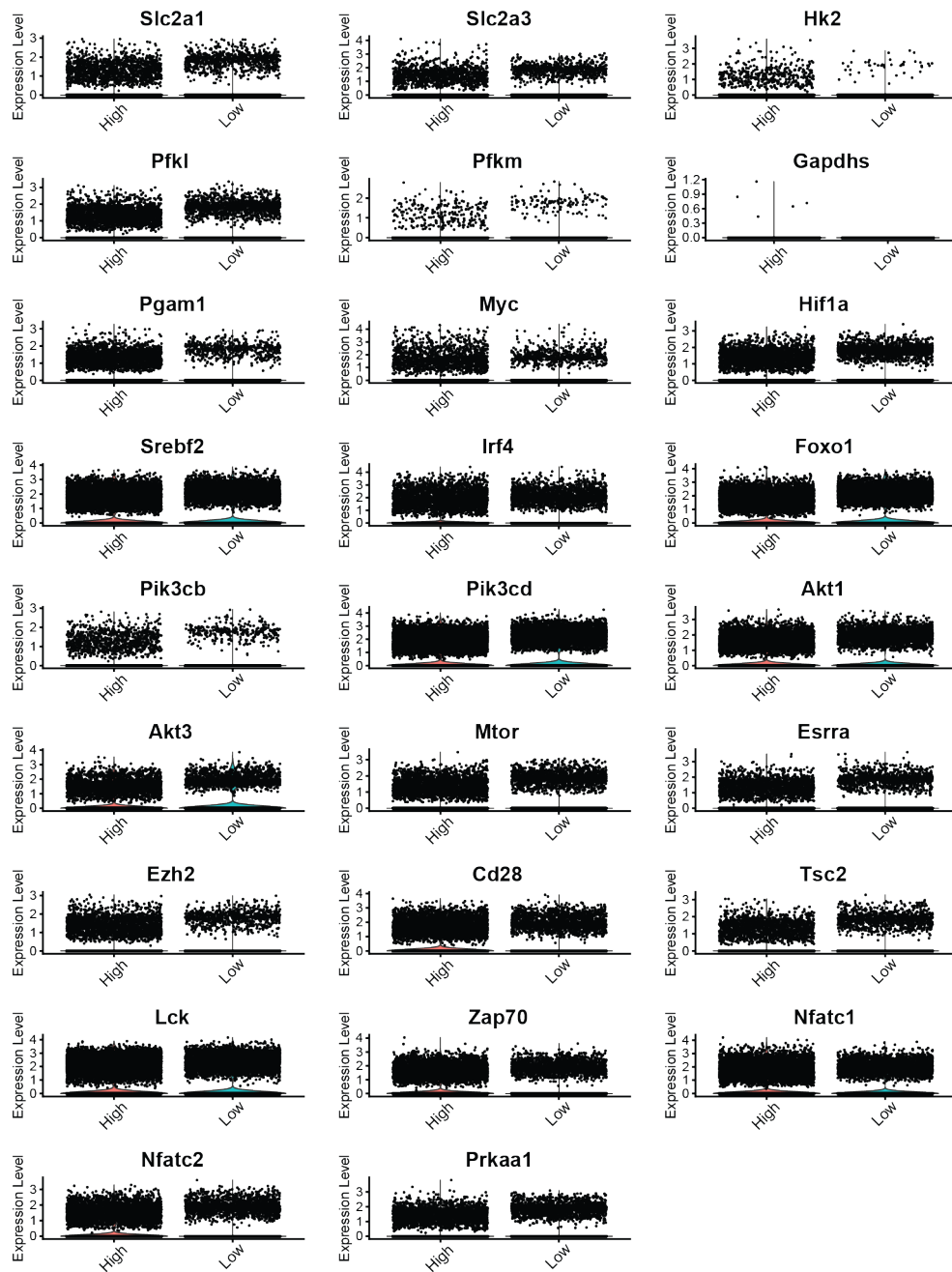
Figure S8: *Expression of genes related to glycolysis and glucose metabolism from scRNAseq in the high- and low-uptake populations of T, NKT, and NK cells, represented as violin plots.*

References

1. Fox, C. J., Hammerman, P. S. & Thompson, C. B. Fuel feeds function: energy metabolism and the T-cell response. *Nature Reviews Immunology* **5**, 844–852 (2005).

2. MacIver, N. J., Michalek, R. D. & Rathmell, J. C. Metabolic Regulation of T Lymphocytes. *Annu Rev Immunol* **31**, 259–293 (2013).

3. Buck, M. D., O'Sullivan, D. & Pearce, E. L. T cell metabolism drives immunity. *Journal of Experimental Medicine* **212**, 1345–1360 (2015).

4. Jacobs, S. R. *et al.* Glucose Uptake Is Limiting in T Cell Activation and Requires CD28-Mediated Akt-Dependent and Independent Pathways. *The Journal of Immunology* **180**, 4476–4486 (2008).

5. Geiger, R. *et al.* L-Arginine Modulates T Cell Metabolism and Enhances Survival and Anti-Tumor Activity. *Cell* **167**, 829–842 (2016).

6. Angela, M. *et al.* Fatty acid metabolic reprogramming via mTOR-mediated inductions of PPARγ directs early activation of T cells. *Nat Commun* **7**, (2016).

7. Pan, Y. *et al.* Survival of tissue-resident memory T cells requires exogenous lipid uptake and metabolism. *Nature* **543**, 252–256 (2017).

8. Kidani, Y. *et al.* Sterol regulatory element–binding proteins are essential for the metabolic programming of effector T cells and adaptive immunity. *Nat Immunol* **14**, 489–499 (2013).

9. Gorjão, R., Cury-Boaventura, M. F., de Lima, T. M. & Curi, R. Regulation of human lymphocyte proliferation by fatty acids. *Cell Biochem Funct* **25**, 305–315 (2007).

10. Passos, M. E. P. *et al.* Differential effects of palmitoleic acid on human lymphocyte proliferation and function. *Lipids Health Dis* **15**, 217 (2016).

11. von Hegedus, J. H. *et al.* Oleic acid enhances proliferation and calcium mobilization of CD3/CD28 activated CD4+ T cells through incorporation into membrane lipids. *Eur J Immunol* **54**, (2024).

12. Miura, S. *et al.* Increased proliferative response of lymphocytes from intestinal lymph during long chain fatty acid absorption. *Immunology* **78**, 142–146 (1993).

13. Ioan-Facsinay, A. *et al.* Adipocyte-derived lipids modulate CD4+ T-cell function. *Eur J Immunol* **43**, 1578–1587 (2013).

14. Zhu, Y. *et al.* Oleic acid causes apoptosis and dephosphorylates Bad. *Neurochem Int* **46**, 127–135 (2005).

15. Reilly, N. A. *et al.* Oleic acid triggers metabolic rewiring of T cells poising them for T helper 9 differentiation. *iScience* **27**, (2024).

16. Hensel, J. A., Khattar, V., Ashton, R. & Ponnazhagan, S. Characterization of immune cell subtypes in three commonly used mouse strains reveals gender and strain-specific variations. *Laboratory Investigation* **99**, 93–106 (2019).

17. Wang, H. *et al.* Analysis of spleen histopathology, splenocyte composition and haematological parameters in four strains of mice infected with Plasmodium berghei K173. *Malaria Journal* **20**, 249 (2021).

18. Grosjean, C. *et al.* Isolation and enrichment of mouse splenic T cells for ex vivo and in vivo T cell receptor stimulation assays. *STAR Protocols* **2**, 100961 (2021).

19. Riddell, S. R. & Greenberg, P. D. The use of anti-CD3 and anti-CD28 monoclonal antibodies to clone and expand human antigen-specific T cells. *Journal of Immunological Methods* **128**, 189–201 (1990).

20. Schumann, J., Stanko, K., Schliesser, U., Appelt, C. & Sawitzki, B. Differences in CD44

Surface Expression Levels and Function Discriminates IL-17 and IFN-γ Producing Helper T Cells. *PLOS ONE* **10**, (2015).

21. Bajnok, A., Ivanova, M., Rigó Jr., J. & Toldi, G. The Distribution of Activation Markers and Selectins on Peripheral T Lymphocytes in Preeclampsia. *Mediators of Inflammation* **2017**, (2017).

22. Wu, T. *et al.* Cell Granularity Reflects Immune Cell Function and Enables Selection of Lymphocytes with Superior Attributes for Immunotherapy. *Advanced Science* **10**, (2023).

23. Waugh, R. E., Lomakina, E., Amitrano, A. & Kim, M. Activation effects on the physical characteristics of T lymphocytes. *Frontiers in Bioengineering and Biotechnology* **11**, (2023).

24. Pollizzi, K. N., Waickman, A. T., Patel, C. H., Sun, I. H. & Powell, J. D. Cellular Size as a Means of Tracking mTOR Activity and Cell Fate of CD4+ T Cells upon Antigen Recognition. *PLOS ONE* **10**, (2015).

25. Yoo, I., Ahn, I., Lee, J. & Lee, N. Extracellular flux assay (Seahorse assay): Diverse applications in metabolic research across biological disciplines. *Molecules and Cells* **47**, 100095 (2024).

26. Ma, S., Ming, Y., Wu, J. & Cui, G. Cellular metabolism regulates the differentiation and function of T-cell subsets. *Cell Mol Immunol* **21**, 419–435 (2024).

27. Wang, R. & Green, D. R. Metabolic reprogramming and metabolic dependency in T cells. *Immunological Reviews* **249**, 14–26 (2012).

28. Slack, M., Wang, T. & Wang, R. T cell metabolic reprogramming and plasticity. *Molecular Immunology* **68**, 507–512 (2015).

29. Hu, C. *et al.* Immune cell metabolism and metabolic reprogramming. *Molecular Biology Reports* **49**, 9783–9795 (2022).

30. Wright, M. H. & Sieber, S. A. Chemical proteomics approaches for identifying the cellular targets of natural products. *Natural Product Reports* **33**, 681–708 (2016).

31. R Core Team. R: A Language and Environment for Statistical Computing. Preprint at (2023).

32. Diril, M. K. *et al.* Cyclin-dependent kinase 1 (Cdk1) is essential for cell division and suppression of DNA re-replication but not for liver regeneration. *Proceedings of the National Academy of Sciences* **109**, 3826–3831 (2012).

33. Wells, A. D. & Morawski, P. A. New roles for cyclin-dependent kinases in T cell biology: linking cell division and differentiation. *Nature Reviews Immunology* **14**, 261–270 (2014).

34. Schröder, B. The multifaceted roles of the invariant chain CD74 — More than just a chaperone. *Biochimica et Biophysica Acta (BBA) - Molecular Cell Research* **1863**, 1269–1281 (2016).

35. Westmeier, J. *et al.* Macrophage migration inhibitory factor receptor CD74 expression is associated with expansion and differentiation of effector T cells in COVID-19 patients. *Frontiers in Immunology* **14**, (2023).

36. Bonnin, E. *et al.* CD74 supports accumulation and function of regulatory T cells in tumors. *Nature Communications* **15**, 3749 (2024).

37. Zhang, L. *et al.* CD74 is a functional MIF receptor on activated CD4+ T cells. *Cellular and Molecular Life Sciences* **81**, 296 (2024).

38. Zhang, L. *et al.* CD74 is a functional MIF receptor on activated CD4+ T cells. *Cellular and Molecular Life Sciences* **81**, 296 (2024).

39. Bonnin, E. *et al.* CD74 supports accumulation and function of regulatory T cells in tumors. *Nature Communications* **15**, 3749 (2024).

40. Nelson, D. E., Randle, S. J. & Laman, H. Beyond ubiquitination: the atypical functions of Fbxo7 and other F-box proteins. *Open Biology* **3**, (2013).

41. Harris, R. *et al.* Fbxo7 promotes Cdk6 activity to inhibit PFKP and glycolysis in T cells. *Journal of Cell Biology* **221**, (2022).

42. UniProt: the Universal Protein Knowledgebase in 2023. *Nucleic Acids Res* **51**, 523–531 (2023).

43. Yu, G., Wang, L.-G., Han, Y. & He, Q.-Y. clusterProfiler: an R Package for Comparing Biological Themes Among Gene Clusters. *OMICS: A Journal of Integrative Biology* **16**, 284–287 (2012).

44. Roberts, D. J. & Miyamoto, S. Hexokinase II integrates energy metabolism and cellular protection: Akting on mitochondria and TORCing to autophagy. *Cell Death & Differentiation* **22**, 248–257 (2015).

45. Varanasi, S. K., Jaggi, U., Hay, N. & Rouse, B. T. Hexokinase II may be dispensable for CD4 T cell responses against a virus infection. *PLOS ONE* **13**, (2018).

46. Gerriets, V. A. *et al.* Metabolic programming and PDHK1 control CD4+ T cell subsets and inflammation. *The Journal of Clinical Investigation* **125**, 194–207 (2015).

47. Shi, L. Z. *et al.* HIF1α–dependent glycolytic pathway orchestrates a metabolic checkpoint for the differentiation of TH17 and Treg cells. *Journal of Experimental Medicine* **208**, 1367–1376 (2011).

48. Man, K. *et al.* The transcription factor IRF4 is essential for TCR affinity–mediated metabolic programming and clonal expansion of T cells. *Nature Immunology* **14**, 1155–1165 (2013).

49. Schmidt, C. *et al.* IRF4 is required for migration of CD4+ T cells to the intestine but not for Th2 and Th17 cell maintenance. *Frontiers in Immunology* **14**, (2023).

50. Mahnke, J. *et al.* Interferon Regulatory Factor 4 controls TH1 cell effector function and metabolism. *Scientific Reports* **6**, 35521 (2016).

51. Huber, M. & Lohoff, M. IRF4 at the crossroads of effector T-cell fate decision. *European Journal of Immunology* **44**, 1886–1895 (2014).

52. Lochner, M., Berod, L. & Sparwasser, T. Fatty acid metabolism in the regulation of T cell function. *Trends Immunol* **36**, 81–91 (2015).

53. Mashima, T., Seimiya, H. & Tsuruo, T. De novo fatty-acid synthesis and related pathways as molecular targets for cancer therapy. *British Journal of Cancer* **100**, 1369–1372 (2009).

54. Osinalde, N. *et al.* Nuclear Phosphoproteomic Screen Uncovers ACLY as Mediator of IL-2-induced Proliferation of CD4+ T lymphocytes*. *Molecular & Cellular Proteomics* **15**, 2076–2092 (2016).

55. Goldstein, J. L. & Brown, M. S. Regulation of the mevalonate pathway. *Nature* **343**, 425–430 (1990).

56. Mullen, P. J., Yu, R., Longo, J., Archer, M. C. & Penn, L. Z. The interplay between cell signalling and the mevalonate pathway in cancer. *Nature Reviews Cancer* **16**, 718–731 (2016).

57. Guerra, B. *et al.* The Mevalonate Pathway, a Metabolic Target in Cancer Therapy. *Frontiers in Oncology* **11**, (2021).

58. Cerqueira, N. M. F. S. A. *et al.* Cholesterol Biosynthesis: A Mechanistic Overview. *Biochemistry* **55**, 5483–5506 (2016).

59. Stefely, J. A. & Pagliarini, D. J. Biochemistry of Mitochondrial Coenzyme Q Biosynthesis. *Trends in Biochemical Sciences* **42**, 824–843 (2017).

60. Wilson, M. P. *et al.* A pseudoautosomal glycosylation disorder prompts the revision of dolichol biosynthesis. *Cell* **187**, 3585–3601 (2024).

61. Manaswiyoungkul, P., de Araujo, E. D. & Gunning, P. T. Targeting prenylation inhibition through the mevalonate pathway. *RSC Medicinal Chemistry* **11**, 51–71 (2020).

62. Gruenbacher, G. & Thurnher, M. Mevalonate Metabolism in Immuno-Oncology. *Frontiers in Immunology* **8**, (2017).

63. Gruenbacher, G. & Thurnher, M. Mevalonate metabolism governs cancer immune surveillance. *OncoImmunology* **6**, (2017).

64. Robinson, G. A., Waddington, K. E., Pineda-Torra, I. & Jury, E. C. Transcriptional Regulation of T-Cell Lipid Metabolism: Implications for Plasma Membrane Lipid Rafts and T-Cell Function. *Frontiers in Immunology* **8**, (2017).

65. Bietz, A., Zhu, H., Xue, M. & Xu, C. Cholesterol Metabolism in T Cells. *Frontiers in Immunology* **8**, (2017).

66. Aguilar-Ballester, M., Herrero-Cervera, A., Vinué, Á., Martínez-Hervás, S. & González-Navarro, H. Impact of Cholesterol Metabolism in Immune Cell Function and Atherosclerosis. *Nutrients* **12**, (2020).

67. Janesick, A. *et al.* High resolution mapping of the tumor microenvironment using integrated single-cell, spatial and in situ analysis. *Nature Communications* **14**, 8353 (2023).

68. O'Neill, L. A. J., Kishton, R. J. & Rathmell, J. A guide to immunometabolism for immunologists. *Nat Rev Immunol* **16**, 553–565 (2016).

69. Loftus, R. M. & Finlay, D. K. Immunometabolism: Cellular Metabolism Turns Immune Regulator. *Journal of Biological Chemistry* **291**, 1–10 (2016).

70. Lim, S. A., Su, W., Chapman, N. M. & Chi, H. Lipid metabolism in T cell signaling and function. *Nat Chem Biol* **18**, 470–481 (2022).

71. Raud, B., McGuire, P. J., Jones, R. G., Sparwasser, T. & Berod, L. Fatty acid metabolism in CD8+ T cell memory: Challenging current concepts. *Immunological Reviews* **283**, 213–231 (2018).

72. Sheppard, S. *et al.* Fatty acid oxidation fuels natural killer cell responses against infection and cancer. *Proceedings of the National Academy of Sciences* **121**, (2024).

73. Schimmer, S. *et al.* Fatty acids are crucial to fuel NK cells upon acute retrovirus infection. *Frontiers in Immunology* **14**, (2023).

74. Pacella, I. *et al.* Fatty acid metabolism complements glycolysis in the selective regulatory T cell expansion during tumor growth. *Proceedings of the National Academy of Sciences* **115**, 6546–6555 (2018).

75. Field, C. S. *et al.* Mitochondrial Integrity Regulated by Lipid Metabolism Is a Cell-Intrinsic Checkpoint for Treg Suppressive Function. *Cell Metabolism* **31**, 422–437 (2020).

76. Endo, Y., Kanno, T. & Nakajima, T. Fatty acid metabolism in T-cell function and differentiation. *Int Immunol* **34**, 579–587 (2022).

77. Tiwary, S., Berzofsky, J. A. & Terabe, M. Altered Lipid Tumor Environment and Its Potential Effects on NKT Cell Function in Tumor Immunity. *Frontiers in Immunology* **10**, (2019).

78. Koh, J. *et al.* De novo fatty-acid synthesis protects invariant NKT cells from cell death, thereby promoting their homeostasis and pathogenic roles in airway

hyperresponsiveness. *eLife* **12**, (2023).

79.	Wakil, S. J. Fatty acid synthase, a proficient multifunctional enzyme. *Biochemistry* **28**, 4523–4530 (1989).

80.	Lacher, S. M. *et al.* HMG-CoA reductase promotes protein prenylation and therefore is indispensible for T-cell survival. *Cell Death Dis* **8**, (2017).

81.	Blank, N. *et al.* Atorvastatin Inhibits T Cell Activation through 3-Hydroxy-3-Methylglutaryl Coenzyme A Reductase without Decreasing Cholesterol Synthesis1. *The Journal of Immunology* **179**, 3613–3621 (2007).

82.	Poggi, A., Boero, S., Musso, A. & Zocchi, M. R. Selective Role of Mevalonate Pathway in Regulating Perforin but Not FasL and TNFalpha Release in Human Natural Killer Cells. *PLOS ONE* **8**, (2013).

83.	Mueller, A. & Strange, P. G. The chemokine receptor, CCR5. *The International Journal of Biochemistry & Cell Biology* **36**, 35–38 (2004).

84.	Khan, I. A. *et al.* CCR5 Is Essential for NK Cell Trafficking and Host Survival following Toxoplasma gondii Infection. *PLOS Pathogens* **2**, (2006).

85.	Ajuebor, M. N. *et al.* Lack of Chemokine Receptor CCR5 Promotes Murine Fulminant Liver Failure by Preventing the Apoptosis of Activated CD1d-Restricted NKT Cells1. *The Journal of Immunology* **174**, 8027–8037 (2005).

86.	Xu, K. *et al.* Glycolysis fuels phosphoinositide 3-kinase signaling to bolster T cell immunity. *Science* **371**, 405–410 (2021).

87.	Chen, X., Liu, L., Kang, S., Gnanaprakasam, J. N. R. & Wang, R. The lactate dehydrogenase (LDH) isoenzyme spectrum enables optimally controlling T cell glycolysis and differentiation. *Science Advances* **9**, (2025).

88.	Finlay, D. K. Regulation of glucose metabolism in T cells: new insight into the role of Phosphoinositide 3-kinases. *Frontiers in Immunology* **3**, (2012).

89.	Shyer, J. A., Flavell, R. A. & Bailis, W. Metabolic signaling in T cells. *Cell Research* **30**, 649–659 (2020).

90.	Kim, E. H. & Suresh, M. Role of PI3K/Akt signaling in memory CD8 T cell differentiation. *Frontiers in Immunology* **4**, (2013).

91.	Sauer, S. *et al.* T cell receptor signaling controls Foxp3 expression via PI3K, Akt, and mTOR. *Proceedings of the National Academy of Sciences* **105**, 7797–7802 (2008).

92.	Soond, D. R., Slack, E. C., Garden, O. A., Patton, D. T. & Okkenhaug, K. Does the PI3K pathway promote or antagonize regulatory T cell development and function? *Frontiers in Immunology* **3**, (2012).

93.	Handi, J., Patterson, S. J. & Levings, M. The Role of the PI3K Signaling Pathway in CD4+ T Cell Differentiation and Function. *Frontiers in Immunology* **3**, (2012).

94.	Chellappa, S. *et al.* The PI3K p110δ Isoform Inhibitor Idelalisib Preferentially Inhibits Human Regulatory T Cell Function. *The Journal of Immunology* **202**, 1397–1405 (2019).

95.	Johansen, K. H., Golec, D. P., Thomsen, J. H., Schwartzberg, P. L. & Okkenhaug, K. PI3K in T Cell Adhesion and Trafficking. *Frontiers in Immunology* **12**, (2021).

96.	Abdullah, L., Hills, L. B., Winter, E. B. & Huang, Y. H. Diverse Roles of Akt in T cells. *Immunometabolism* **3**, (2021).

97.	Glaviano, A. *et al.* PI3K/AKT/mTOR signaling transduction pathway and targeted therapies in cancer. *Molecular Cancer* **22**, 138 (2023).

98.	Portsmann, T. *et al.* SREBP Activity Is Regulated by mTORC1 and Contributes to Akt-Dependent Cell Growth. *Cell Metabolism* **8**, 224–236 (2008).

99. Li, L.-Y. *et al.* Interplay and cooperation between SREBF1 and master transcription factors regulate lipid metabolism and tumor-promoting pathways in squamous cancer. *Nature Communications* **12**, 4362 (2021).

100. Horton, J. D. *et al.* Combined analysis of oligonucleotide microarray data from transgenic and knockout mice identifies direct SREBP target genes. *Proceedings of the National Academy of Sciences* **100**, 12027–12032 (2003).

101. Howie, D., Ten Bokum, A., Necula, A. S., Cobbold, S. P. & Waldmann, H. The Role of Lipid Metabolism in T Lymphocyte Differentiation and Survival. *Frontiers in Immunology* **8**, (2018).

102. Ruiz, R. *et al.* Sterol Regulatory Element-binding Protein-1 (SREBP-1) Is Required to Regulate Glycogen Synthesis and Gluconeogenic Gene Expression in Mouse Liver. *Journal of Biological Chemistry* **289**, 5510–5517 (2014).

103. Toriyama, K. *et al.* T cell-specific deletion of Pgam1 reveals a critical role for glycolysis in T cell responses. *Communications Biology* **3**, 394 (2020).

104. Horton, J. D. *et al.* Combined analysis of oligonucleotide microarray data from transgenic and knockout mice identifies direct SREBP target genes. *Proceedings of the National Academy of Sciences* **100**, 12027–12032 (2003).

105. Howie, D., Ten Bokum, A., Necula, A. S., Cobbold, S. P. & Waldmann, H. The Role of Lipid Metabolism in T Lymphocyte Differentiation and Survival. *Front Immunol* **8**, (2018).

106. Ruiz, R. *et al.* Sterol Regulatory Element-binding Protein-1 (SREBP-1) Is Required to Regulate Glycogen Synthesis and Gluconeogenic Gene Expression in Mouse Liver. *Journal of Biological Chemistry* **289**, 5510–5517 (2014).

107. Toriyama, K. *et al.* T cell-specific deletion of Pgam1 reveals a critical role for glycolysis in T cell responses. *Communications Biology* **3**, 394 (2020).

108. Chen, Y., Zhang, J., Cui, W. & Silverstein, R. L. CD36, a signaling receptor and fatty acid transporter that regulates immune cell metabolism and fate. *Journal of Experimental Medicine* **219**, (2022).

109. Jin, R. *et al.* Role of FABP5 in T Cell Lipid Metabolism and Function in the Tumor Microenvironment. *Cancers* **15**, (2023).

110. Skowronek, P. *et al.* Rapid and In-Depth Coverage of the (Phospho-)Proteome With Deep Libraries and Optimal Window Design for dia-PASEF. *Molecular & Cellular Proteomics* **21**, (2022).

111. Ritchie, M. E. *et al.* limma powers differential expression analyses for RNA-sequencing and microarray studies. *Nucleic Acids Res* **43**, (2015).

5

Summary & Future Prospects

Summary

The cellular metabolism of immune cells constitutes an important part of their proper function and activation.[1] Using T cells as an example, this phenomenon is highlighted by the metabolic reprogramming that occurs in these cells upon activation. The metabolism of quiescent T cells mainly revolves around catabolic pathways where glucose (for naïve T cells) or fatty acids (for memory T cells) are broken down to feed the tricarboxylic acid (TCA) cycle and oxidative phosphorylation (OXPHOS) pathways to generate energy via mitochondrial respiration.[2] Upon activation and differentiation, effector T cells shift their metabolism from mitochondrial respiration to aerobic glycolysis. Glycolysis is an important pathway to generate building blocks for the synthesis of complex biomolecules, so the metabolic reprogramming is accompanied by a shift towards anabolic pathways, generating the necessary biomaterials for increased growth and proliferation.[3] The metabolic reprogramming is further supported by an increased uptake of exogenous nutrients, such as glucose, amino acids, and fatty acids (FAs). The availability of these nutrients in the cell's environment is essential for the proper activation and differentiation of effector T cells.[4–8] The ability to unravel this complex interface between the immune system and cellular metabolism relies on the development of appropriate chemical tools. The aim of this thesis was to develop sterculic acid (StA) as a bioorthogonal analogue of the immunomodulatory FA oleic acid (OA), and to use this as a tool to study the uptake of StA in different immune cells.

Chapter 1 gave a detailed description of the current understanding of T cell metabolism and how it is connected to their immunological functions. A special focus was given to FA and lipid metabolism, explaining how pathways like fatty acid β-oxidation (FAO), fatty acid synthesis (FAS), and FA uptake are regulated in different T cell subsets. Furthermore, a deep dive into the function of the monounsaturated OA (C18:1, ω-9) as an immunomodulatory FA was given, where OA has been shown to influence immunological functions in diseases like asthma, sepsis, and cancer. Specifically for T cells, OA has been shown to affect their proliferation, metabolism and differentiation. Chapter 1 continues by describing molecular tools that are available for studying cellular uptake of exogenous FAs. Historically, either radioactively or fluorescently labelled FAs have been used for this purpose, but here it is suggested that bioorthogonal chemistry is more suitable for studying FA uptake. By incorporating a small chemical modification with a unique bioorthogonal functional group into the FA molecule, treating cells with this bioorthogonal FA analogue, and subsequently adding a reporter molecule (e.g. a fluorophore) with the complementary functionality, the FA analogue is covalently labelled in the cells. Chapter 1 proposed the naturally occurring plant metabolite StA as a novel live-cell compatible bioorthogonal analogue of OA and hypothesised that the cyclopropene moiety of StA would allow for an inverse electron-demand Diels-Alder (IEDDA) reaction with a tetrazine modified reporter molecule.

Chapter 2 described the initial exploration of StA as a bioorthogonal OA analogue. It focused on a library of eight quenched tetrazine-conjugated fluorophores and evaluated their abilities to react with StA via an IEDDA reaction. Their stability, as well as their turn-on ratio and reaction kinetics, were evaluated upon ligation with StA. These assays indicated that the IEDDA reaction between StA and the tetrazine-conjugated fluorophores could occur with varying efficiency in solution. Subsequently,

it was demonstrated by confocal microscopy that StA could be taken up by live cells, and the IEDDA reaction could be successfully performed on either live or fixed cells. Fluorophore **6,** a BODIPY FL-based conjugate with a H-substitution on the tetrazine, was deemed best for fixed-cell imaging, whereas fluorophore **7**, a BODIPY-based conjugate with a methyl-substitution on the tetrazine, was deemed best for live-cell imaging. The turn-on ratio of fluorophore **7** was sufficient to perform live-cell confocal imaging without washing away unreacted fluorophore, a big advantage to reduce cell loss during washing steps. Lastly, the labelling of StA *in cellulo* was multiplexed with two other bioorthogonal reactions to label several biomolecules simultaneously, emphasising the strength and flexibility of this novel bioorthogonal OA analogue.

Chapter 3 further delved into the diversity of StA as a bioorthogonal OA analogue by investigating its incorporation into proteins as a post-translational modification (PTM). Protein lipidation as a PTM is important for correct protein function, signalling, transportation and regulation, and can also have immunomodulatory properties. It was shown by fluorescent gel electrophoresis that StA could be incorporated into proteins as a PTM, and that the protein lipidation could be visualised by IEDDA reaction with tetrazine-conjugated fluorophores. However, the detected proteins depended on which fluorophore was used and whether the IEDDA reaction was performed on live cells or on cell lysate. To further investigate these observed differences in lipidation pattern, a pull-down chemical proteomics approach was applied. A library of cell-permeable tetrazine-modified biotin molecules were synthesised with different spacer lengths and substitutions on the tetrazine, and was compared to the commercially available, cell-impermeable biotin-PEG4-tetrazine. With fluorescent microscopy, it was demonstrated that biotins **17**, with a short spacer and methyl-substituted tetrazine, and **19**, with a longer spacer and H-substituted tetrazine, were cell-permeable and reactive with StA. Comparing the lipidated proteins that were recovered with **17**, **19**, or biotin-PEG4-tetrazine in a pull-down chemical proteomics approach showed little to no overlap between detected proteins. This further supported the previous observation that the timing of the IEDDA reaction makes a difference, but it also implied that chemical properties of the biotin molecules, such as spacer length, could also influence the pool of proteins that were detected. The developed method detected several proteins with known immunological functions, that have never been known to be lipidated as a PTM. Among them is SLC15A3, a transmembrane amino acid transporter with immunomodulatory properties. These results could indicate modification with OA as a novel regulatory mechanism for this protein.

In **Chapter 4**, the use of StA as a bioorthogonal OA analogue was applied to study the uptake of exogenous FAs in a heterogeneous, primary T cell population. After StA uptake and IEDDA reaction with fluorophore **7**, the cells were differentiated based on low or high uptake of StA by fluorescence-activated cell sorted (FACS). Comparing the low- and high-uptake populations with each other revealed remarkable phenotypic, metabolic, proteomic, and transcriptomic differences. The high-uptake cells took on a more effector-like phenotype with larger and more granulated cells, increased expression of CD44, and decreased expression of CD62L, compared to the low-uptake cells. These differences were observed in naïve T cells as well as *in vitro* activated T cells. It was also demonstrated that the high-uptake cells are more metabolically active than the low-uptake cells, in line with existing literature about effector T cell metabolism. The metabolic differences were also reflected

on a proteomic and transcriptomic level where key proteins and genes involved in glycolysis, fatty acid synthesis and the mevalonate pathway were significantly upregulated in the high-uptake cells. The upregulation of these pathways is closely connected to the metabolic reprogramming that occurs during effector T cell differentiation (described in Chapter 1) and further supported the observation that high StA-uptake T cells exhibited a more effector-like state. However, it could not be determined if the high-uptake cells are inherently dispositioned for a more effector-like state, or if this is induced by increased availability of FAs in the culture medium.

In conclusion, this thesis reports the first use of StA as a bioorthogonal analogue of OA. StA was readily taken up *in vitro* by a plethora of immune cells and could react with tetrazine-modified reporter molecules (e.g. fluorophores) via an IEDDA reaction, presenting a non-toxic, live-cell compatible alternative to other commonly used bioorthogonal reactions. The versatility of this approach allowed for multiplexing with other bioorthogonal reactions, permitting the simultaneous study of multiple biomolecules. The workflow could further be adapted and applied to study the lipidation of proteins as a PTM, as well as to investigate phenotypic and multiomic differences between T cells with a differential StA-uptake. The adaptability of the workflow emphasises its strength and applicability as a chemical tool to study FA uptake.

Future Prospects

Effects of different spacer lengths on pull-down of oleoylated proteins

In Chapter 3, a library of cell-permeable tetrazine-modified biotins were synthesised. Of these, compounds **17** and **19** were found to be cell-permeable and reactive with StA. However, the compounds had two different spacers between the biotin moiety and the tetrazine, with either a short (~13 Å, biotin) or medium (~22 Å, LC-biotin) spacer length (Figure 1A). These cell-permeable biotins were compared to the cell-impermeable biotin-PEG4-tetrazine which has a long (~29 Å) spacer between the biotin and tetrazine moieties (Figure 1A). In the chapter it was postulated that the short and medium spacer lengths of **17** and **19** could lead to increased steric hindrance upon binding of the tetrameric streptavidin beads during pull-down, leading to fewer proteins being detected. This effect was not observed for biotin-PEG4-tetrazine, further supporting the hypothesis that spacer length plays a role in protein retrieval.

In view of these findings, an expansion of the library of cell-permeable tetrazine-modified biotins is envisioned, where an additional spacer length similar to that of PEG4 is added (Figure 1B, LC-LC-biotin). However, increasing spacer length also appeared to negatively impact the compounds' solubility, so this would need to be optimised further. A cell-impermeable biotin-PEG2-tetrazine could also be used as a control, since it also has a medium spacer length (Figure 1B). If a drastic drop in detected proteins occurs compared to biotin-PEG4-tetrazine, spacer length is likely implicated, and a longer spacer would lead to less steric hindrance.

A

B
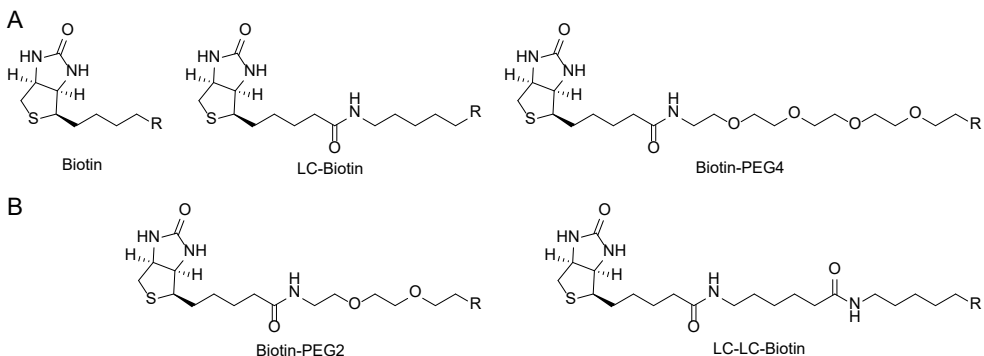
Figure 1: *Structures of biotin molecules with different spacer lengths.* ***A)*** *biotin, LC-biotin and biotin-PEG4,* ***B)*** *biotin-PEG2 and LC-LC-biotin.*

Incorporating fatty acid uptake into the single-cell RNAseq workflow

Chapter 4 described how information about fatty acid uptake was multiplexed with a single-cell RNA sequencing (scRNAseq) workflow by using StA. Cells were treated with StA, and subsequent IEDDA reaction with a fluorophore, before being sorted into high- and low-uptake populations by FACS. The two resulting populations were subjected to scRNAseq and were compared to each other. However, this strategy requires a sorting step during which information of nutrient uptake *per individual cell* is lost, preventing the correlation of sequencing information to nutrient uptake on a per-cell basis.

A different strategy was therefore also attempted, with the idea that the StA-uptake information could be incorporated directly as a readable parameter in the scRNAseq workflow. For this purpose, an oligonucleotide barcode system was developed that was inspired by the TotalSeq™ B barcoding technology. This technology was developed to be compatible with 10x Genomics' scRNAseq platform and consists of an antibody conjugated to the 5' end of an oligonucleotide (Figure 2A). The antibody is specific for a cell surface marker of interest, and the oligonucleotide firstly consists of a capture sequence which is implemented in the 10x Genomics workflow. In addition, a PCR handle is included for amplification, as well as the barcode sequence itself which is unique to each TotalSeq™ B antibody used.

The newly developed oligonucleotide described here consisted of a TotalSeq™ barcode conjugated to a methyltetrazine at the 5' end, rather than to an antibody (Figures 2B & 2C). This would allow for it to react in an inverse electron-demand Diels-Alder (IEDDA) click reaction to StA, thereby allowing the quantification of StA in the same sequencing run that would analyse the per-cell transcriptome.

The initial experiments with the tetrazine-conjugated oligonucleotide were performed with the murine dendritic cell line DC2.4, which had been prelabelled with StA, before being fixed and permeabilised. The perforation of the cell membrane allowed for the tetrazine-conjugated oligonucleotide to enter the cells to react with StA. As a negative control, cells prelabelled with native OA were used. After the IEDDA

reaction, unreacted oligonucleotide was washed away. The cells were then prepared according to 10x Genomics' provided instructions, and the PCR product was analysed on an Agilent Bioanalyzer chip. Unfortunately, no substantial difference in the amount of PCR product was observed between the StA- and OA-treated cells (Figure 2D). Some optimisation was attempted. For example, by increasing the cell numbers, or increasing the number of wash steps after the IEDDA click reaction. However, nothing appeared to affect the amount of PCR product detected in the StA sample compared to the OA sample (data not shown).

It was hypothesised that since FAs are not covalently crosslinked upon fixation with paraformaldehyde, and the water solubility of StA is massively increased upon click reaction with the oligonucleotide, the entire StA-oligonucleotide complex could potentially be washed away during the wash steps after the click reaction. It is also not known what effect the conjugation of the oligonucleotide to the tetrazine has on its reactivity with cyclopropenes, and it is possible that the kinetics of the tetrazine-conjugated oligonucleotide are so slow that one hour incubation for the click reaction was not sufficient. It was shown in Chapter 3 that the addition of bulky groups to the tetrazine can largely impact its ability to react with StA. Due to these major unanswered technological questions, as well as time- and cost-constraints, this approach was abandoned for the time being.

Although the initial tests with the tetrazine-conjugated oligonucleotide in combination with StA did not show positive results, it would be interesting to try this approach with other nutrients, e.g. amino acids, that are covalently crosslinked upon fixation. This would remove the uncertainty of washing away the nutrient after IEDDA reaction with the oligonucleotide and would better demonstrate the feasibility of the approach.

Effects of starvation prior to fatty acid uptake

To build further on the data described in Chapter 4, there are several new angles that could be interesting to explore. T cells undergo metabolic reprogramming upon activation, which renders effector T cells reliant on uptake of exogenous nutrients (see Chapter 1). Upon nutrient deficiency, for example by metabolic competition for glucose in the tumour microenvironment, effector T cell differentiation and function are negatively impacted.[9,10] Glucose deficiency could also skew T cell differentiation in favour of regulatory T cells over effector T cells.[11] While the StA uptake in Chapter 4 was performed in complete culture medium, it would be interesting to see how the T cells would react to starvation, e.g. by using glucose-depleted culture medium, prior to StA uptake, and if this would affect the observed effector-like state of the high-uptake T cells (see Chapter 4).

3' - AACGATCCTGGCCGGAATTTCG ACACCATGTACATGC TCTAGCCTTCTCGTGTGCAGACTTGAGGTCAGTG - 5'
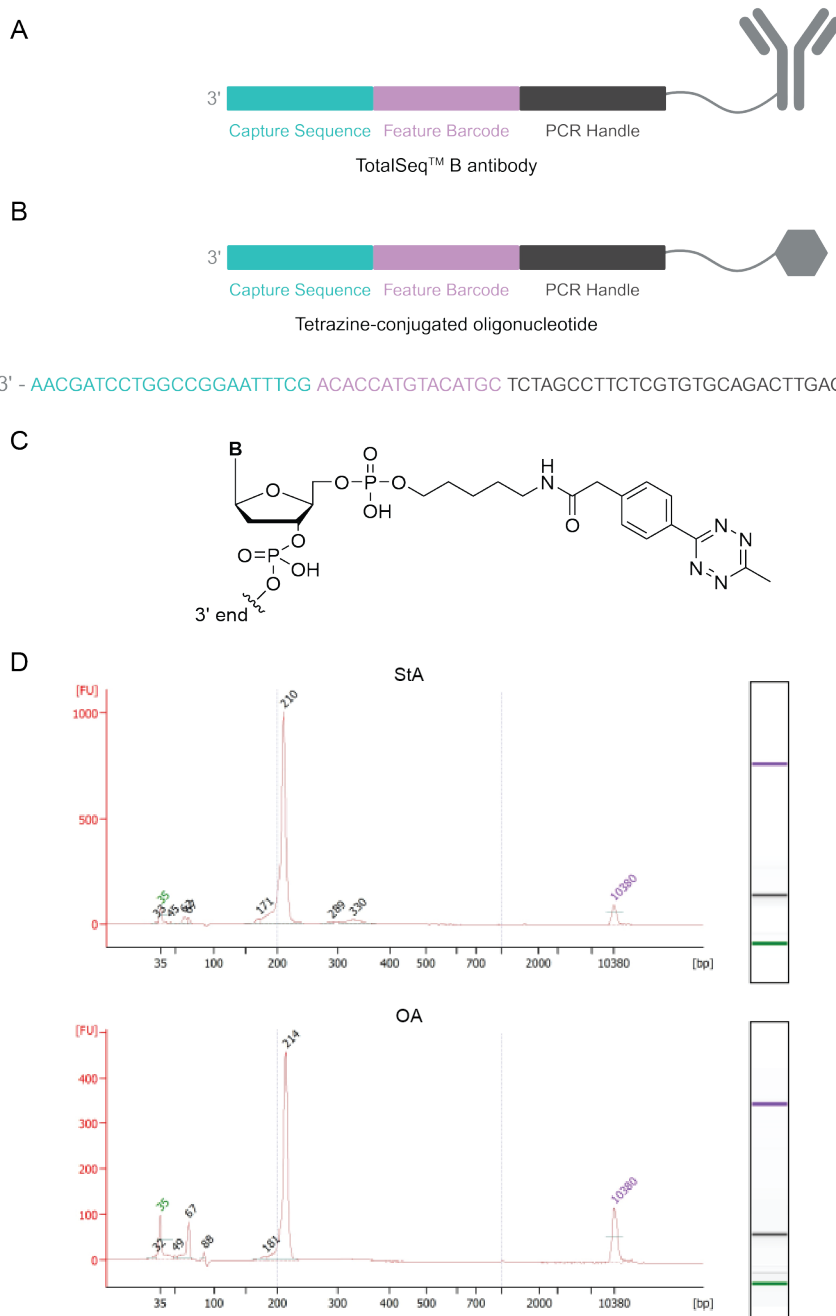
Figure 2: A) *TotalSeq™ B feature barcoding technology developed for antibody labelling of surface markers to be implemented into the 10x Genomics workflow.* **B)** *TotalSeq™ B-inspired oligonucleotide barcode with tetrazine modification at 5' end, and the oligonucleotide sequence.* **C)** *Structure of 5' tetrazine modification on the oligonucleotide.* **D)** *example of PCR results after StA uptake and IEDDA reaction with the tetrazine-modified oligonucleotide.*

Further classifications of T cell subsets upon differential FA uptake

It would also be interesting to further analyse and classify which T cell subsets are present in the high and low StA-uptake populations after FACS (see Chapter 4). The cytokine production of the two different populations could be analysed by enzyme-linked immunosorbent assays (ELISAs), or the populations could be subjected to further flow cytometry analysis with a more elaborate and thorough antibody panel. This could help determine the present T cell subsets in more detail and further verify if the high-uptake population contains a higher proportion of effector T cells.

To investigate the differentiation potential of the high and low StA-uptake populations of naïve splenocytes, the cells could be activated *in vitro* with αCD3/αCD28 antibodies after FACS. After the *in vitro* activation, a similar combination of ELISAs and flow cytometry as described above could be applied to determine which T cell subsets are predominantly present, and if there are differences between cells with differential FA uptake capacities.

Multiplexing nutrients in the single-cell RNAseq workflow

In Chapter 2 it was demonstrated that the IEDDA reaction with StA can be multiplexed with other bioorthogonal reactions and used to study multiple biomolecules at once. This could be extrapolated to the scRNAseq workflow described in Chapter 4, where a second bioorthogonal nutrient analogue, and subsequent bioorthogonal reaction, could be added. The bioorthogonal amino acid analogue azidohomoalanine, which has been shown to mimic glutamine uptake in T cells[12], could for example be used. However, a bioorthogonal reaction must be chosen that does not utilise a copper catalyst, since the copper catalyst was shown to degrade RNA (Chapter 4, Figure S2). For this purpose, a strain-promoted azide-alkyne cycloaddition (SPAAC)[13] or Staudinger ligation[14] could be used, although some further optimisations would be necessary to incorporate this into the scRNAseq workflow. Since T cells also increase their amino acid uptake upon differentiation into effector T cells (see Chapter 1), it is likely that cells with a high FA uptake will also show a high amino acid uptake. However, there could be populations of cells with a high FA uptake combined with a low amino acid uptake and vice versa. It would be interesting to determine which phenotypic, metabolic, and transcriptomic profile these cells have, and what differentiate them from the other T cell populations.

Acknowledgements

Materials & Methods

General. Sterculic acid was purchased from Cayman Chemical (#26735), and stored as 10 mM or 100 mM stock solutions in DMSO at -20°C. Oleic acid was purchased from Sigma Aldrich (#O1383), and stored as 100 mM stock solution in DMSO at -80°C. The murine RNase inhibitor was purchased from New England Biolabs (#M0314L), and stored as delivered at -20°C. The RNase-free PBS (10x) was purchased from Thermo Fisher Scientific (#J62851.AP**)** and stored as delivered at room temperature (RT). The PBS was diluted to 1x with MilliQ water prior to use. The custom-made oligonucleotide sequence with a 5' tetrazine modification (Figures 2B & 2C) was ordered from Biomers.net. Upon delivery, the oligonucleotide was dissolved in MilliQ water (1 mM), and stored at -20°C.

DC2.4 cell culturing. DC2.4 cells were cultured in RPMI 1640 culture medium (Gibco, #31870025) supplemented with 10% FCS, GlutaMAX (2 mM), sodium pyruvate (1 mM), 1x non-essential amino acids (NEAA, Thermo Fisher Scientific), penicillin (100 I.U./mL), streptomycin (50 µg/mL), and 2-mercaptoethanol (50 µM, Thermo Fisher Scientific), and incubated at 37°C, 5% CO_2. The cells were grown to 70-80% confluency and passaged every 2-3 days by trypsinisation.

Click reaction with ssDNA barcode modified with tetrazine. 2.5×10^6 DC2.4 cells were seeded per 60 mm dish, and incubated at 37°C, 5% CO_2 overnight to allow the cells to attach. The samples were treated with either sterculic acid or the native oleic acid (50 µM) in fresh DC2.4 medium, and incubated for 1 h at 37°C, 5% CO_2, to allow for uptake of the FAs. The cells were washed with fresh medium x1, followed by PBS x1, before they were scraped in PBS and transferred to Eppendorf tubes. The cells were spun down at 400 rcf for 5 min, and were fixed in 4% PFA in PBS for 15 min at RT. The cells were spun down at 400 rcf for 5 min, before unreacted PFA was quenched with PBS supplemented with glycine (20 mM) and RNase inhibitor (40 U/mL). The cells were spun down at 900 rcf for 5 min, and washed with RNase-free PBS x1 before permeabilisation with RNase-free PBS supplemented with saponin (0.1%) for 15 min at RT. The tubes were filled up with RNase-free PBS before being spun down at 850 rcf for 5 min. The custom-made tetrazine-conjugated oligonucleotide (5 µM, see Figures 2B & 2C) in RNase-free PBS, supplemented with RNase inhibitor (40 U/mL), was added to the cells and reacted for 1 h at RT with shaking (800 rpm). The cells were spun down at 850 rcf for 5 min and was washed with RNase-free PBS between 2 and 5 times. The cells were resuspended in RNase-free PBS and was transported on ice to collaborators from the Leiden Genome Technology Center (LGTC) at Leiden University Medical Center (LUMC). The samples were thereafter prepared according to the 10x Genomics user guide (CG000477), until having been analysed on an Agilent Bioanalyser (see results in Figure 2D).

References

1.	O'Neill, L. A. J., Kishton, R. J. & Rathmell, J. A guide to immunometabolism for immunologists. *Nat Rev Immunol* **16**, 553–565 (2016).

2.	Buck, M. D., O'Sullivan, D. & Pearce, E. L. T cell metabolism drives immunity. *Journal of Experimental Medicine* **212**, 1345–1360 (2015).

3.	MacIver, N. J., Michalek, R. D. & Rathmell, J. C. Metabolic Regulation of T Lymphocytes. *Annu Rev Immunol* **31**, 259–293 (2013).

4.	Jacobs, S. R. *et al.* Glucose Uptake Is Limiting in T Cell Activation and Requires CD28-Mediated Akt-Dependent and Independent Pathways. *The Journal of Immunology* **180**, 4476–4486 (2008).

5.	Geiger, R. *et al.* L-Arginine Modulates T Cell Metabolism and Enhances Survival and Anti-Tumor Activity. *Cell* **167**, 829–842 (2016).

6.	Sinclair, L. V *et al.* Control of amino-acid transport by antigen receptors coordinates the metabolic reprogramming essential for T cell differentiation. *Nat Immunol* **14**, 500–508 (2013).

7.	Carr, E. L. *et al.* Glutamine Uptake and Metabolism Are Coordinately Regulated by ERK/MAPK during T Lymphocyte Activation. *The Journal of Immunology* **185**, 1037–1044 (2010).

8.	Angela, M. *et al.* Fatty acid metabolic reprogramming via mTOR-mediated inductions of PPARγ directs early activation of T cells. *Nat Commun* **7**, (2016).

9.	Chang, C.-H. *et al.* Metabolic Competition in the Tumor Microenvironment Is a Driver of Cancer Progression. *Cell* **162**, 1229–1241 (2015).

10.	Ho, P.-C. *et al.* Phosphoenolpyruvate Is a Metabolic Checkpoint of Anti-tumor T Cell Responses. *Cell* **162**, 1217–1228 (2015).

11.	Feuerer, M. *et al.* Lean, but not obese, fat is enriched for a unique population of regulatory T cells that affect metabolic parameters. *Nature Medicine* **15**, 930–939 (2009).

12.	Pelgrom, L. R. *et al.* QUAS-R: An SLC1A5-mediated glutamine uptake assay with single-cell resolution reveals metabolic heterogeneity with immune populations. *Cell Rep* **42**, (2023).

13.	Agard, N. J., Prescher, J. A. & Bertozzi, C. R. A Strain-Promoted [3 + 2] Azide−Alkyne Cycloaddition for Covalent Modification of Biomolecules in Living Systems. *Journal of the American Chemical Society* **126**, 15046–15047 (2004).

14.	Kiick, K. L., Saxon, E., Tirrell, D. A. & Bertozzi, C. R. Incorporation of azides into recombinant proteins for chemoselective modification by the Staudinger ligation. *Proceedings of the National Academy of Sciences* **99**, 19–24 (2002).

A

Appendices

Nederlandse Samenvatting

Bio-orthogonale technieken voor het bestuderen van de vetzuuropname in immuuncellen

Het cellulaire metabolisme van immuuncellen vormt een belangrijk onderdeel van hun functie en activatie. Aan de hand van T-cellen wordt dit fenomeen geïllustreerd door de metabole herprogrammering die optreedt bij activatie van deze cellen. Het metabolisme van rustende T-cellen bestaat voornamelijk uit katabole routes, waarbij glucose (voor naïeve T-cellen) of vetzuren (voor T-geheugencellen) worden afgebroken om de tricarbonzuurcyclus en oxidatieve fosforylering te voeden, waarmee energie wordt gegenereerd via mitochondriale respiratie. Na activatie en differentiatie schakelen effector-T-cellen hun metabolisme om van mitochondriale respiratie naar aerobe glycolyse. Glycolyse is een belangrijke route voor de aanmaak van bouwstenen die nodig zijn voor de synthese van complexe biomoleculen. Deze metabole herprogrammering gaat daarom gepaard met een verschuiving naar anabole routes, die de noodzakelijke biomaterialen produceren voor verhoogde groei en proliferatie. De metabole herprogrammering wordt verder ondersteund door een verhoogde opname van exogene nutriënten, zoals glucose, aminozuren en vetzuren. De beschikbaarheid van deze nutriënten in de extracellulaire omgeving is essentieel voor de correcte activatie en differentiatie van effector-T-cellen. Het ontrafelen van dit complexe samenspel tussen het immuunsysteem en het cellulaire metabolisme vereist de ontwikkeling van de juiste chemische hulpmiddelen. Het doel van dit proefschrift was om sterculinezuur te ontwikkelen als een bio-orthogonaal analoog van het immunomodulerende vetzuur oliezuur, en dit te gebruiken als hulpmiddel om de opname van sterculinezuur in verschillende immuuncellen te bestuderen.

Hoofdstuk 1 geeft een gedetailleerde beschrijving van de huidige kennis over het metabolisme van T-cellen en de relatie met hun immunologische functies. Hierbij werd speciale aandacht besteed aan vetzuur- en lipidenmetabolisme, met uitleg over hoe processen als vetzuur bèta-oxidatie, vetzuursynthese en vetzuuropname worden gereguleerd in verschillende T-cel-subtypen. Vervolgens wordt ingegaan op de rol van het enkelvoudig onverzadigde oliezuur (C18:1, ω-9) als immunomodulerend molecuul, dat invloed heeft op immuunfuncties bij ziekten zoals astma, sepsis en kanker. Voor T-cellen specifiek is aangetoond dat oliezuur hun proliferatie, metabolisme en differentiatie beïnvloedt. Daarnaast worden moleculaire hulpmiddelen beschreven die gebruikt worden om de opname van exogene vetzuren te onderzoeken. Traditioneel werd dit gedaan met radioactief of fluorescent gelabelde vetzuren, maar hier wordt voorgesteld dat bio-orthogonale chemie geschikter is voor dit doel. Door een kleine chemische modificatie met een unieke bio-orthogonale functionele groep in het vetzuur aan te brengen, cellen met dit analoog te behandelen en vervolgens een rapporteermolecuul (bijv. een fluorofoor) toe te voegen met de complementaire functionaliteit, kan het vetzuuranaloog covalent worden gelabeld in de cel. Hoofdstuk 1 stelt het plantaardige metaboliet sterculinezuur voor als een nieuw, 'live-cell'-compatibel bio-orthogonaal analoog van oliezuur, en veronderstelt dat de cyclopropeenring van sterculinezuur een 'inverse electron-demand Diels-Alder' (IEDDA)-reactie mogelijk maakt met een tetrazine-gemodificeerd rapporteermolecuul.

Hoofdstuk 2 beschrijft de eerste verkenning van sterculinezuur als bio-orthogonaal

oliezuur-analoog. Een bibliotheek van acht 'quenched' tetrazine-geconjugeerde fluoroforen werd getest op hun vermogen om via een IEDDA-reactie met sterculinezuur te reageren. Hun stabiliteit, 'turn-on'-ratio en reactiesnelheid werden geëvalueerd. Deze testen toonden aan dat de IEDDA-reactie tussen sterculinezuur en de fluoroforen met verschillende efficiëntie kon plaatsvinden in oplossing. Vervolgens werd met confocale microscopie aangetoond dat sterculinezuur door levende cellen kan worden opgenomen en dat de IEDDA-reactie succesvol kon worden uitgevoerd op zowel levende als gefixeerde cellen. Fluorofoor **6** (een op BODIPY FL gebaseerd conjugaat met H-substitutie op de tetrazine) bleek het meest geschikt voor gefixeerde cellen, terwijl fluorofoor **7** (een op BODIPY gebaseerd conjugaat met methylsubstitutie op de tetrazine) het meest geschikt was voor levende cellen. De 'turn-on'-ratio van fluorofoor **7** was zelfs hoog genoeg om 'live-cell' confocale microscopie uit te voeren zonder niet-gereageerde fluorofoor uit te wassen, wat een groot voordeel is om verlies van cellen tijdens wasstappen te voorkomen. Tot slot werd aangetoond dat het labelen van sterculinezuur in cellen kon worden gecombineerd met twee andere bio-orthogonale reacties om meerdere biomoleculen gelijktijdig te labelen, waarmee de veelzijdigheid van dit nieuwe oliezuur-analoog werd benadrukt.

Hoofdstuk 3 gaat dieper in op de diversiteit van sterculinezuur als bio-orthogonaal oliezuur-analoog door te onderzoeken of het kan worden ingebouwd in eiwitten als posttranslationele modificatie (PTM). Eiwitlipidatie als PTM is belangrijk voor een correcte eiwitfunctie, signaaloverdracht, transport en regulatie, en kan ook immunomodulerende eigenschappen hebben. Met fluorescente gelelektroforese werd aangetoond dat sterculinezuur in eiwitten kan worden ingebouwd, en dat deze lipidatie kan worden gevisualiseerd via een IEDDA-reactie met tetrazine-geconjugeerde fluoroforen. De gedetecteerde eiwitten verschilden echter afhankelijk van de gebruikte fluorofoor en of de reactie werd uitgevoerd in levende cellen of in cellysaten. Om deze verschillen verder te onderzoeken, werd een 'pull-down' chemoproteomicsbenadering toegepast. Een bibliotheek van cel-permeabele tetrazine-gemodificeerde biotine-moleculen met verschillende spacerlengtes en substituties op de tetrazine werd gesynthetiseerd en vergeleken met de commercieel beschikbare, cel-impermeabele biotine-PEG$_4$-tetrazine. Met fluorescentie-microscopie werd aangetoond dat biotines **17** (met een korte spacer en een methylsubstitutie op de tetrazine) en **19** (met een langere spacer en een H-substitutie op de tetrazine) cel-permeabel waren en reageerden met sterculinezuur. Vergelijking van de gelipideerde eiwitten die met **17**, **19** of biotine-PEG$_4$-tetrazine werden geïsoleerd, toonde weinig overlap tussen de gedetecteerde eiwitten. Dit bevestigde dat het moment van de IEDDA-reactie van invloed is, maar suggereerde ook dat de chemische eigenschappen van de biotine (zoals de spacerlengte) de detectie van verschillende eiwitten beïnvloeden. Met deze methode werden verschillende eiwitten met bekende immunologische functies gedetecteerd die niet eerder als gelipideerd bekend stonden, waaronder SLC15A3, een transmembraan aminozuurtransporter met immunomodulerende eigenschappen. Dit kan wijzen op een nieuw regulatiemechanisme voor dit eiwit via oliezuur-modificatie.

Hoofdstuk 4 beschrijft het gebruik van sterculinezuur als bio-orthogonaal oliezuur-analoog om de opname van exogene vetzuren te bestuderen in een heterogene, primaire T-celpopulatie. Na opname van sterculinezuur en IEDDA-reactie met fluorofoor **7** werden cellen op basis van lage of hoge sterculinezuur-opname

gescheiden met 'fluorescence-activated cell sorting' (FACS). Vergelijking van de populaties met lage en hoge opname onthulde opvallende fenotypische, proteomische en transcriptomische verschillen. De cellen met hoge opname vertoonden een meer effectorachtig fenotype, met grotere en meer gegranuleerde cellen, verhoogde expressie van CD44 en verlaagde expressie van CD62L. Deze verschillen werden waargenomen in zowel naïeve als *in vitro* geactiveerde T-cellen. Bovendien bleken de cellen met hoge opname een hogere metabolisch activiteit te hebben, overeenkomstig met bestaande literatuur over effector-T-celmetabolisme. De metabole verschillen kwamen ook tot uiting op proteomisch en transcriptomisch niveau, waarbij belangrijke eiwitten en genen betrokken bij glycolyse, vetzuursynthese en de mevalonaatroute significant waren opgereguleerd in de cellen met hoge opname. Deze opregulatie sluit nauw aan bij de metabole herprogrammering die optreedt tijdens effector-T-celdifferentiatie (zoals beschreven in Hoofdstuk 1), en ondersteunt de observatie nog verder dat T-cellen met hoge sterculinezuur-opname een meer effectorachtige toestand vertonen. Het kon echter niet worden geconcludeerd of deze cellen van nature voorbestemd zijn tot een effectorachtig profiel, of dat dit wordt geïnduceerd door een verhoogde beschikbaarheid van vetzuren in het medium.

Concluderend rapporteert dit proefschrift het eerste gebruik van sterculinezuur als bio-orthogonaal analoog van oliezuur. Sterculinezuur werd *in vitro* gemakkelijk opgenomen door diverse immuunceltypen en kon reageren met tetrazine-gemodificeerde rapporteermoleculen (zoals fluoroforen) via een IEDDA-reactie, waarmee een niet-toxisch, 'live-cell'-compatibel alternatief wordt geboden voor andere bio-orthogonale reacties. De veelzijdigheid van deze aanpak maakte 'multiplexing' met andere bio-orthogonale reacties mogelijk, waardoor gelijktijdige studie van meerdere biomoleculen kon plaatsvinden. De workflow kon bovendien worden aangepast om eiwitlipidatie als PTM te onderzoeken, evenals de fenotypische en multi-omische verschillen tussen T-cellen met verschillende sterculinezuur-opname te bestuderen. De flexibiliteit van deze methode benadrukt haar kracht en bruikbaarheid als chemisch hulpmiddel voor de studie van vetzuuropname.

Curriculum Vitae

Kristine Bertheussen was born on October 26th, 1994 in Bergen, Norway. She obtained her high school diploma from Bergen Katedralskole in 2013. In 2014, she moved to Trondheim to start her studies at the Norwegian University of Science and Technology, where she completed three years of a five-year master's program in Biotechnology, equivalent to a bachelor's program.

She continued her academic studies in 2018 at Leiden University with a master's program in Biology with a specialisation in Molecular Genetics and Biotechnology. During this program, she conducted two research internships at the Institute of Biology Leiden. The first internship was performed in the group of Prof.dr. Nathaniel Martin, under the supervision of Dr. Thomas Wood and Dr. Jaco Slingerland, and focused on the synthesis of novel lipopeptide antibiotic analogues and assessment of their abilities to kill drug-resistant bacterial strains. The second internship was performed in the group of Prof.dr. Gilles van Wezel, under the supervision of Dr. Mariana Avalos Garcia, and focused on metabolic network analysis of volatile terpene compounds and other secondary metabolites in the bacterial genus *Streptomyces*. She completed her master's studies in 2020 and graduated with a *cum laude* distinction.

In November 2020, she started her doctoral studies in the group of Chemical Biology & Immunology at Leiden University under the supervision of Prof.dr. Sander van Kasteren, where the work described in this thesis was conducted. As part of the graduate program and the Institute for Chemical Immunology (ICI) PhD program, she followed courses in scientific conduct, personal and professional development, and communication.

Parts of the work described here were presented as a poster at the ICI Conference (Leiden, 2022). Oral presentations were given at the Bioorthogonal & Bioresponsive Symposium (online, 2021), the ICI Conference (online, 2021), the Reedijk Symposium (Leiden, 2023), the IUPAC CHAINS Conference (The Hague, 2023), the European Immunometabolism Conference (Køge, Denmark, 2024), and the Immunometabolism in Health and Disease Gordon Research Seminar and Conference (GRS/GRC, Smithfield, Rhode Island, 2024).

List of Publications

A Novel Cyclopropenyl Fatty Acid Library Reveals Tissue-Specific Preferences for Regulatory T Cell Uptake Through Click-Chemistry

Heieis, G.; Reinalda, L.; Bogue, L. I.; Steuten, K.; Corrigan, C.; Wang, X.; <u>Bertheussen, K.</u>; el Boujadayni, M.; Sinclair, L. V.; van der Stelt, M.; Everts, B.; Finlay, D. K.; van Kasteren S. I. *bioRxiv*. https://doi.org/10.1101/2025.07.11.664320

Live-Cell Imaging of Sterculic Acid — a Naturally Occurring 1,2-Cyclopropene Fatty Acid — by Bioorthogonal Reaction with Turn-On Tetrazine-Fluorophore Conjugates

<u>Bertheussen, K.</u>; van de Plassche, M.; Bakkum, T.; Gagestein, B.; Ttofi, I.; Sarris, A. J. C.; Overkleeft, H. S.; van der Stelt, M.; van Kasteren, S. I. *Angew. Chem. Int. Ed.* 61 (2022).

Mechanistic insights into the C_{55}-P targeting lipopeptide antibiotics revealed by structure–activity studies and high-resolution crystal structures

Wood, T. M.; Zeronian, M. R.; Buijs, N.; <u>Bertheussen, K.</u>; Abedian, H. K.; Johnson, A. V.; Pearce, N. M.; Lutz, M.; Kemmink, J.; Seirsma, T.; Hamoen, L. W.; Janssen, B. J. C.; Martin, N. I. *Chem. Sci.* 13, 2985-2991 (2022).

Thrombin-Derived Peptides Potentiate the Activity of Gram-Positive-Specific Antibiotics against Gram-Negative Bacteria

Wesseling, C. M. J.; Wood, T. M.; Slingerland, C. J.; <u>Bertheussen, K.</u>; Lok, S.; Martin, N. I. *Molecules*. 26, 1954 (2021).

The contribution of achiral residues in the laspartomycin family of calcium-dependent lipopeptide antibiotics

Wood, T. M.; <u>Bertheussen, K.</u>; Martin, N. I. *Org. Biomol. Chem.* 18, 514-517 (2020).

Acknowledgements

First, thank you **Sander** for trusting in me at the beginning and welcoming me as a PhD candidate in your group. From the panic before my first presentation at a conference, to the marathon of writing my thesis, you have supported and motivated me and have shown me my true potential. Even though I'm no longer one of your PhDs, I hope our encounters in the bouldering hall will continue. To **Kim**, thank you for being my second promotor and for your insightful and helpful feedback during the writing of my thesis.

To my paranymphs **Laura** and **Thijmen**, thank you for standing by my side on the last day of my PhD journey and for all the lovely coffee meetups we've had in the last months. **Laura**, you came into the group towards the end of my PhD, but it feels like you've been there since day one. Thank you for helping me with my final experiments and for letting me rant to you about my frustrations while writing my thesis. Your support has gotten me through it, and I'm so happy to call you my friend. **Thijmen**, thank you for being a true inspiration. You are smart and caring, and with your immense knowledge and dedication to your work I know you will accomplish great things.

I would also like to thank all the remaining members of the group, both current and former. **Amber**, **Amit**, **Charlotte**, **Diana**, **Don**, **Eva**, **Hans**, **Heleen**, **Kas**, **Leonard**, **Luuk**, **Merel**, **Nina**, **Thomas**, **Tyrza**, **Ward**, and **Yixuan**, in one way or another you have all contributed to making the last 5 years an enjoyable experience. However, I must extend extra gratitude to some of you. **Thomas**, thank you for taking time during the last months of your PhD to teach me how to master CLEM. Although no CLEM images ended up in my thesis in the end, your help was invaluable. **Diana**, thank you for being my office buddy. Whether we were complaining about the microscope not working or eating spicy Mexican candy, I always felt accepted and supported by you. And lastly, **Nina** and **Tyrza**, thank you for all the warmth and joy you spread, you made my PhD a happier time. I hope the future will bring more parties and BioScience Park lunches for us.

An additional thank you to the remaining members of the **CBI group** and all members of the **MolPhys group** for creating a fun, including, and inspiring work environment. It has been a pleasure sharing lab, office, and lunch spaces with you.

Thank you to the students I had the pleasure of supervising. **Maxime**, **Charlotte**, and **Dieke**, you all did great work and I'm sure the future will hold many exciting opportunities for you.

Outside of work, I want to thank all my friends and family. You have been a huge support, and I could not have done this without you.

Først og fremst, kjære familien min, **mamma**, **pappa**, **Erlend** og **Håvard**. Tusen takk for all støtten deres, og for at dere har skapt rom der jeg har fått avbrekk fra en stressende hverdag. Jeg føler meg utrolig heldig som alltid har kunnet komme på besøk til Bergen, København eller Senja, og hatt muligheten til å slappe av og roe ned sammen med dere. Det har vært gull verdt.

Til Bergens beste jenter, **Maren**, **Siri**, **Hilde**, **Vilde**, **Vilde**, **Vilde**, **Sofie**, **Elisabeth** og

Ane, tenk så heldig jeg er som fortsatt har så gode venner hjemmefra. Tusen takk for alle de fine stundene vi har hatt. Selvom vi har vokst opp og har ulike meninger, interesser og karrierer, har alle en gjensidig respekt og forståelse for hverandre. Det er unikt, og noe jeg setter veldig stor pris på. Og **Anna**, takk for at du er du. Støtten din har betydd uendelig mye i den siste tiden. Du er sterk, god og klok, og vil alltid være min Bory.

Then, to all my friends I've met during my time in the Netherlands, **Niels**, **Doro**, **Tobi**, **Ned**, **Floor**, **Carolien**, **Lisa**, **Shaun**, **Marco**, **Mitchell**, **Savannah**, **Marta**, **Dimi**, **Stephan**, **Elma, Noortje**, and **Shiv**. Thank you for all the dinners, holidays, parties, bouldering sessions, concerts, and festivals we have shared. You have kept me sane and have shown me how fun life can be.

And finally, **Mathijs**, how can I begin to explain what you mean to me. I got to know you at the beginning of my PhD, and you have been there through laughter, tears, frustrations, and joy. Although our path hasn't always been easy, I'm certain we'll come out stronger on the other side. Thank you for being my person.